

UNIVERSIDADE DE SANTIAGO DE COMPOSTELA

Departamento de Física de Partículas

New physics implications and searches at LHCb

Miriam Lucio Martínez

Tese de Doutoramento



Programa de Doutoramento
en Física Nuclear e de Partículas

Contents

| | | |
|----------|--|-----------|
| 1 | Introduction | 1 |
| 1.1 | Higgs Mechanism | 1 |
| 1.1.1 | Coupling to fermions | 3 |
| 1.1.2 | Coupling to photons and gluons | 3 |
| 1.2 | Particle Content | 3 |
| 1.3 | CKM Matrix | 5 |
| 1.4 | Need for New Physics | 5 |
| 1.4.1 | Matter-antimatter imbalance | 5 |
| 1.4.2 | Dark matter and dark energy | 6 |
| 1.4.3 | Unification of forces | 6 |
| 2 | Supersymmetry | 10 |
| 2.1 | Introduction | 10 |
| 2.2 | Points addressed by SUSY | 11 |
| 2.3 | Supersymmetry breaking | 11 |
| 2.4 | Minimal Supersymmetrical Standard Model (MSSM) | 12 |
| 2.4.1 | Dark Matter in the MSSM | 12 |
| 2.4.2 | MSSM Lagrangian | 13 |
| 2.4.3 | CMSSM | 15 |
| 2.4.4 | AMSB | 16 |
| 2.4.4.1 | mAMSB | 16 |
| 2.4.5 | Renormalization Group equations | 18 |
| 2.5 | RPV Models | 20 |
| 2.5.1 | Consequences of RPV | 21 |
| 2.6 | Experimental searches | 22 |
| 3 | Low E in SUSY (MFV) | 24 |
| 3.1 | Motivation for MFV | 24 |
| 3.2 | MFV EFT | 24 |
| 3.3 | MFV SUSY | 25 |
| 3.4 | MFV R-parity | 26 |
| 3.5 | Characteristics | 27 |
| 3.6 | CMFV | 27 |

| | | |
|----------|--|-----------|
| 3.7 | Experimental bounds | 27 |
| 3.8 | Unitarity Triangle | 28 |
| 4 | LHCb | 30 |
| 4.1 | LHC | 30 |
| 4.2 | LHCb | 31 |
| 4.2.1 | Beam pipe, vacuum chamber and BCM | 32 |
| 4.2.2 | Magnet | 32 |
| 4.2.3 | Tracking | 33 |
| 4.2.3.1 | VELO | 34 |
| 4.2.3.2 | ST | 34 |
| 4.2.3.3 | OT | 35 |
| 4.2.4 | PID | 36 |
| 4.2.4.1 | RICH | 36 |
| 4.2.4.2 | Calorimeters | 37 |
| 4.2.4.3 | Muon System | 38 |
| 4.2.5 | Trigger | 39 |
| 4.2.5.1 | L0 | 39 |
| 4.2.5.2 | HLT | 40 |
| 4.2.5.3 | HLT1 | 41 |
| 4.2.5.4 | HLT2 | 42 |
| 4.2.6 | Tracking and Vertexing performance | 42 |
| 4.2.7 | PID performance | 46 |
| 4.2.8 | Trigger performance | 48 |
| 4.2.8.1 | L0 hardware trigger | 48 |
| 4.2.8.2 | High Level Trigger | 49 |
| 4.2.9 | The LHCb Upgrade | 51 |
| 4.2.9.1 | Trigger Upgrade | 51 |
| 4.2.9.2 | VELO Upgrade | 52 |
| 4.2.9.3 | PID Upgrade | 52 |
| 4.2.9.4 | Tracking Upgrade | 53 |
| 4.2.10 | Analysis workflow | 54 |
| 5 | $\Delta F=2$ | 56 |
| 5.1 | Introduction | 56 |
| 5.2 | ϕ_s experimental | 57 |
| 5.2.1 | Phenomenology | 58 |
| 5.2.2 | Samples and event selection | 58 |
| 5.2.2.1 | Data sample | 59 |
| 5.2.2.2 | Simulation samples | 59 |
| 5.2.2.3 | Stripping selection | 60 |
| 5.2.2.4 | Trigger selection | 60 |
| 5.2.2.5 | Corrections | 61 |

| | | |
|----------|---|-----------|
| 5.2.3 | Mass fit and computation of signal sWeights | 62 |
| 5.2.4 | C_{SP} factors | 64 |
| 5.2.5 | Decay time resolution | 66 |
| 5.2.6 | Angular acceptance | 66 |
| 5.2.7 | Decay time acceptance | 67 |
| 5.2.7.1 | Measurement of $\tau(B^0)$ | 69 |
| 5.2.8 | Flavour tagging | 70 |
| 5.2.9 | Data fitting | 72 |
| 5.2.10 | Baseline fit | 72 |
| 5.2.11 | Coverage of the uncertainty with the sFit | 73 |
| 5.2.11.1 | Simulation | 73 |
| 5.2.11.2 | Signal and background simulation | 74 |
| 5.2.11.3 | Data | 75 |
| 5.3 | ϕ_s pheno | 76 |
| 5.3.1 | Observables | 76 |
| 5.4 | ϕ_s MultiNest | 76 |
| 5.4.1 | MultiNest | 84 |
| 5.4.1.1 | Bayesian inference | 84 |
| 5.4.1.2 | Nested sampling | 85 |
| 5.4.1.3 | Ellipsoidal nested sampling | 86 |
| 5.4.1.4 | The MultiNest algorithm | 86 |
| 6 | Kaon Physics | 87 |
| 6.1 | Introduction | 87 |
| 6.2 | $K_s^0 \rightarrow \pi^0 \mu^+ \mu^-$ Sensitivity study | 88 |
| 6.2.1 | Analysis strategy | 89 |
| 6.2.2 | Reconstruction and selection | 90 |
| 6.2.3 | Background sources | 92 |
| 6.2.4 | Fit model | 93 |
| 6.2.5 | Expected sensitivity | 93 |
| 6.2.6 | Conclusions | 94 |
| 6.3 | Probing SUSY effects in $K_s^0 \rightarrow \mu^+ \mu^-$ | 96 |
| 6.3.1 | Formalism | 96 |
| 6.3.1.1 | Observables | 97 |
| 6.3.1.2 | $K_s^0 \rightarrow \mu^+ \mu^-$ | 98 |
| 6.3.1.3 | $\varepsilon'_K/\varepsilon_K$ | 104 |
| 6.3.1.4 | ε_K and ΔM_K | 106 |
| 6.3.2 | Parameter scan | 108 |
| 6.3.3 | Results | 109 |
| 6.3.3.1 | Effects from $\left(\delta_d^{LL(RR)}\right)_{12}$ separately | 110 |
| 6.3.3.2 | Floating LL and RR MIs simultaneously | 110 |
| 6.3.3.3 | Non degenerate Higgs masses | 113 |
| 6.3.4 | Conclusions | 114 |

| | |
|---|------------|
| 7 CMSSM | 121 |
| 7.1 MasterCode framework | 121 |
| 7.2 Sampling algorithm | 122 |
| 7.3 Scan Ranges | 122 |
| 7.4 Method | 122 |
| 7.4.1 Gaussian Constraints | 123 |
| 7.4.2 Non-Gaussian Constraints | 124 |
| Appendices | 126 |
| A MasterCode observables | 127 |
| A.1 Mass Spectrum | 127 |
| A.2 Dark Matter Relic Density | 128 |
| A.3 Neutralino Scattering off Nuclei | 129 |
| A.3.1 Spin-Independent Term | 129 |
| A.3.2 Spin-Dependent Term | 130 |
| A.4 Anomalous Magnetic Moment of the Muon | 130 |
| A.5 Electroweak Precision Observables | 131 |
| A.6 Flavour Physics Observables | 132 |
| B Coverage of the uncertainty with the sFit | 133 |
| Bibliography | 138 |

¹ Chapter 1

² Introduction

³ The Standard Model (hereafter SM) of Particle Physics, mainly formulated in the [1970s](#),
⁴ is the quantum field theory that describes the strong and electroweak interactions. It is
⁵ represented in Group Theory by [\[1\]](#):

$$SU(3)_C \bigotimes SU(2)_T \bigotimes U(1)_Y \quad (1.1)$$

⁶ Where the strong interaction, described by Quantum Chromodynamics (QCD), is con-
⁷ tained in the $SU(3)_C$ group (a symmetry group of *color*, C), and $SU(2)_T \bigotimes U(1)_Y$, where
⁸ T and Y stand for weak isospin and hypercharge respectively, relates to the electroweak
⁹ interaction (EW). The SM fermions (described in [1.2](#)) consist of three families with two
¹⁰ $SU(2)_L$ doublets (Q_L and L_L) and three $SU(2)_L$ singlets (U_R , D_R and E_R). In order
¹¹ to preserve the electroweak gauge invariance (and so, keep the SM renormalizable), the
¹² particles predicted by this lagrangian have to be massless. This leads to the necessity of a
¹³ spontaneously breaking of the symmetry into $SU(3)_C \bigotimes U(1)_{EM}$. Such breaking is done
¹⁴ by the vacuum expectation value (VEV) of a scalar isospin doublet, with hypercharge
¹⁵ 1/2, called *Higgs* [\[2\]](#). More details on this mechanism are given in [1.1](#).

$$G_{SM} \xrightarrow{Higgs(1,2)_{1/2}} SU(3)_C \bigotimes U(1)_{EM} \quad (1.2)$$

¹⁶ 1.1 Higgs Mechanism

¹⁷ Similarly to what happens in the Ginzburg-Landau theory for superconductivity, the
¹⁸ Higgs mechanism arises from the need of EWSB, together with the requirement that
¹⁹ gauge invariance is preserved in \mathcal{L}_{SM} . The Higgs field interacts with the particles corre-
²⁰ sponding to the elementary field, including gauge bosons. Resulting of this interaction,
²¹ these particleless acquire mass. As for the others, the Higgs field has associated at least one
²² particle in the SM, the Higgs boson, a scalar particle with spin zero. Within the SM, it
²³ is not possible to make a prediction of its mass (other than setting loose upper and lower
²⁴ limits), since it depends on a parameter that needs to be determined experimentally.

²⁵ The term in the SM lagrangian that accounts for the self-interaction of the Higgs field
²⁶ is the following:

$$\mathcal{L}_{Higgs} = \mu^2 \phi^\dagger \phi - \lambda (\phi^\dagger \phi)^2, \quad \mu^2 < 0, \lambda > 0 \quad (1.3)$$

²⁷ Where ϕ denotes the (complex) Higgs Field :

$$\phi = \begin{pmatrix} \phi^+ \\ \phi^0 \end{pmatrix} \quad (1.4)$$

²⁸ A scalar isospin doublet with hypercharge $+1/2$. The initial symmetry of the system is
²⁹ broken for a non-zero value of this field:

$$\phi = \frac{1}{\sqrt{2}} \begin{pmatrix} 0 \\ v \end{pmatrix}, \quad v = \frac{\mu}{\sqrt{\lambda}} \quad (1.5)$$

³⁰ Leading to the Higgs particle, with mass $\sqrt{2\lambda v^2}$, neutral charge and hypercharge 1. It
³¹ was discovered in 2012 by 2 detectors at LHC, ATLAS [3] and CMS [4]. Its mass was
³² measured to be 125.09 ± 0.24 GeV.

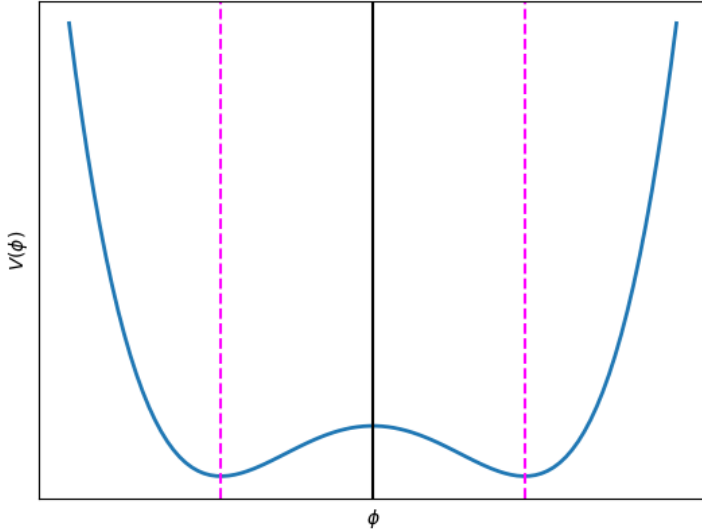


Figure 1.1: Higgs mechanism. The dashed-magenta vertical line indicate the two vacuum states. The black vertical line is located at the origin. The minimum is not at 0, and therefore the potential has a VEV.

³³ The gauge fields W^\pm and Z acquire mass through their interaction with the Higgs
³⁴ boson. Thus:

$$W^\pm = \frac{1}{\sqrt{2}} (W^{(1)} \mp W^{(2)}), \quad Z = \frac{1}{\sqrt{g_I^2 + g_Y^2}} (g_I W^{(3)} - g_Y B) \quad (1.6)$$

³⁵ Where Z and W^\pm are linear combinations of the weak and hypercharge bosons (3 and 1,
³⁶ respectively). Then:

$$m_{W^\pm} = \frac{vg_I}{\sqrt{2}}, m_Z = v\sqrt{\frac{g_I^2 + g_Y^2}{2}} \quad (1.7)$$

³⁷ Notice that the relation between both masses is given by the so-called *weak-mixing angle*,
³⁸ θ_W

$$\frac{m_W^\pm}{m_Z} = \frac{g_I}{\sqrt{(g_I + g_Y)}} = \cos \theta_W \quad (1.8)$$

³⁹ Measured experimentally to be $\theta_W \sim 0.50$ rad [1].

⁴⁰ 1.1.1 Coupling to fermions

⁴¹ The lagrangian term corresponding to the Higgs (H)-fermions (f) interaction can be
⁴² written as follows:

$$\mathcal{L}_{H\{f\}} = -\lambda_e \bar{E}_L \phi E_R - \lambda_d \bar{Q}_L \phi D_R - \lambda_u \varepsilon^{ab} \phi_b^\dagger U_R + \text{h.c.} \quad (1.9)$$

⁴³ Where λ_e , λ_d and λ_u are the respective coupling constants (*Yukawa couplings*), different
⁴⁴ for each fermion. Substituting in this expression the Higgs field with the result obtained
⁴⁵ before:

$$m_e = \frac{v\lambda_e}{\sqrt{2}}, m_u = \frac{v\lambda_u}{\sqrt{2}}, m_d = \frac{v\lambda_d}{\sqrt{2}} \quad (1.10)$$

⁴⁶ The fermion masses are therefore proportional to the Yukawa couplings.

⁴⁷ 1.1.2 Coupling to photons and gluons

⁴⁸ Both gluons and photons are gauge bosons of the strong and electromagnetic interactions,
⁴⁹ respectively. They have zero mass and spin 1. For the gluons, given that the color
⁵⁰ symmetry $SU(3)$ is not modified by the Higgs mechanism, they don't directly interact
⁵¹ with the Higgs boson. The only way this interaction can happen is via quark loops.
⁵² Contrary to what happens with the gluons, the photons can interact directly with the
⁵³ Higgs field. Nevertheless, they don't acquire mass as a result of this interaction, $m_\gamma = 0$.

⁵⁴ 1.2 Particle Content

⁵⁵ The particle content of the SM is categorized as a function of the intrinsic angular mo-
⁵⁶ mentum of each particle, or *spin*. Particles with half-integer spin are called *fermions*,
⁵⁷ while those with an integer value for the spin are *bosons*. The latter ones are the carriers
⁵⁸ of the different interactions that enter the SM lagrangian:

$$\mathcal{L} = \mathcal{L}_{kin} + \mathcal{L}_{Higgs} + \mathcal{L}_{Yuk} \quad (1.11)$$

59 Where the first term accounts for the kinetic part of the interaction, and the two others
 60 describe the Higgs mechanism (described in 1.1) and its interaction with the fermions.
 61 Regarding the fermions, a further classification can be made depending on whether they
 62 are affected (*quarks*) or not (*leptons*) by the strong interaction. If affected, a quantum
 63 number, color, further characterizes the particle. Note that the electroweak interaction
 64 affects all the particles.

65 An additional quantum number, *flavour*, is used to label the different elementary
 66 particles. There are three flavour families of quarks and leptons in the SM, represented in
 67 1.2. Each lepton (electron, i , muon, μ , tauon, τ) has associated a neutral particle, called
 68 the *neutrino*: ν_e , ν_μ , ν_{tau} . Even though they are predicted to be massless within the SM
 69 (so that there are not right-handed neutrinos in the SM and, equivalently, there are not
 70 left-handed antineutrinos), they are known to have mass [5].

71 The elementary particles of the SM are represented in 1.2. For each of this particles,
 72 there exists another one with the same mass but opposite physical charges. Those are
 73 called *antiparticles*. Notice that some particles (e.g. the photon) are their own antiparticle.

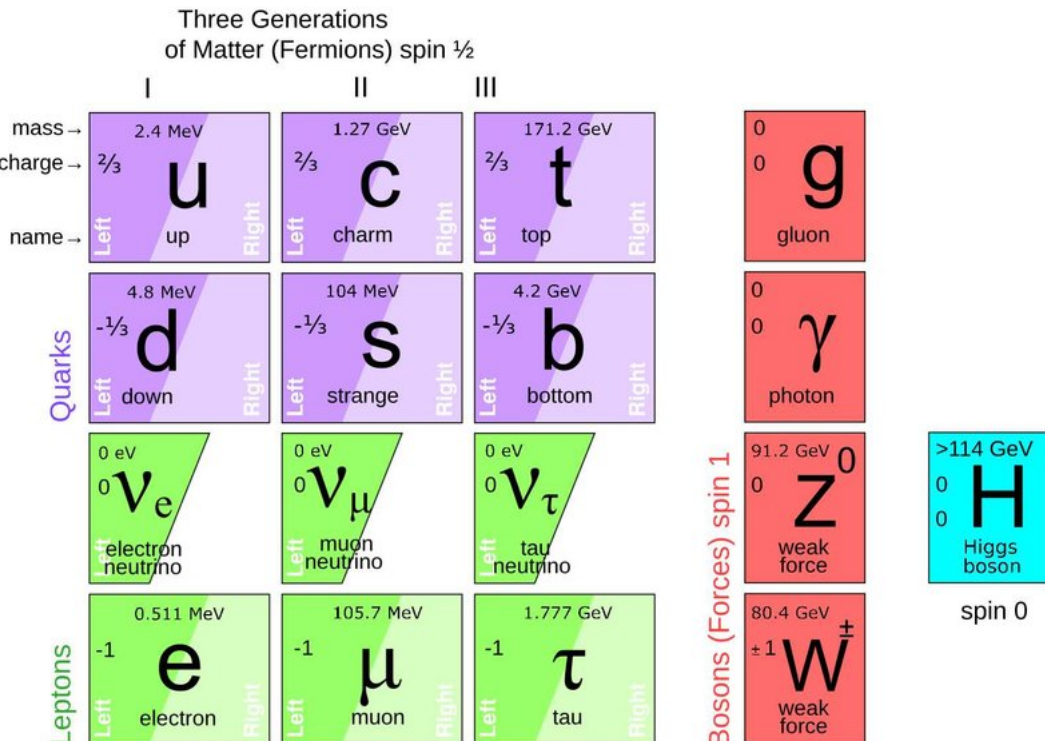


Figure 1.2: The SM particle content [6].

74 Quarks form bound states named *hadrons* that have a quantum number associated
 75 called the baryonic number, \mathcal{B} . They are composed either by a quark and an antiquark
 76 (forming *mesons*, with $\mathcal{B} = 0$) or by three quarks (*baryons*, with $\mathcal{B} = 1$). Given the spin

77 that results of the *sum* of the quarks, baryons are fermions and mesons are bosons.

78 1.3 CKM Matrix

79 The Yukawa couplings, seen in 1.1, generate off-diagonal terms that allow for the quarks
80 to *mix* between the three generations. Diagonalizing the quark mass matrices, 4 unitary
81 matrices are obtained, $V_{L,R}^{u,d}$, that determine the coupling of the W^\pm bosons to the different
82 quarks.

83 This diagonalization can be seen as the rotation from one basis (q) to another, hereafter
84 called *mass basis* or *physical basis*, q' . These are related by the aforementioned matrices
85 [7]:

$$\small{86} \quad u_L^i = V_u^{ij} u_L'^j \quad d_L^i = V_d^{ij} d_L'^j \quad (1.12)$$

87 With this, the weak current transforms from $\bar{u}_L^i \gamma^\mu d_L^i$ to $\bar{u}_L'^i \gamma^\mu (V_u^\dagger V_d)_{ij} d_L'^j \equiv$
88 $\bar{u}_L'^i \gamma^\mu V_{\text{CKM}} d_L'^i$, where V_{CKM} is a non-diagonal, unitary matrix called the *Cabibbo-Kobayashi-*
89 *Maskawa* (CKM) matrix. The most up-to-date measured values of its elements can be
90 found in [1].

$$\small{91} \quad V^{\text{CKM}} = \begin{pmatrix} V_{ud} & V_{us} & V_{ub} \\ V_{cd} & V_{cs} & V_{cb} \\ V_{td} & V_{ts} & V_{tb} \end{pmatrix} \quad (1.13)$$

92 This matrix is the responsible for the transitions between different quark generations,
93 that allow for processes in which there is change in the quark flavour but not in the electric
94 charge to happen. These are known as Flavour Changing Neutral Currents (FCNC). Most
95 of the rare decays are of this type. It also causes CP violation, that will be discussed in
96 the following sections. It is worth noticing that this matrix is not necessarily restricted
97 to being 3x3, thus extra quark generations (not discovered yet) can exist [7].

98 1.4 Need for New Physics

99 Even though the SM has shown to be a very successful theory, it lacks explanation for
100 several phenomena present in nature.

101 1.4.1 Matter-antimatter imbalance

102 In order to have an excess of matter over antimatter in the early universe (process known
103 as *baryogenesis* [8], three requirements have to be fulfilled. These are known as the
104 *Sakharov conditions* [8], and include a large CP-violation. The SM predicts a rate of the
105 CP-violation smaller than the one needed, thus, a new source is required.

106 1.4.2 Dark matter and dark energy

107 Several experimental evidences, such as the rotational speed of spiral galaxies, gravitational
 108 lensing, or observed fluctuations in the Cosmic Microwave Background radiation
 109 (see for example [9], [10]) have lead to discovery of dark matter and dark energy, that
 110 take up the vast majority of the Universe composition and don't interact with light. The
 111 possible baryonic (MACHOs, MAssive Compact Halo Objects, such as black holes, and
 112 RAMBOs, Robust Association of Massive Baryonic Objects) percentage of dark matter is small.
 113 The rest cannot be explained within the SM, it is *non baryonic cold dark matter*, where cold refers to its non-relativistic nature, or neutrinos. Possible candidates
 114 for cold dark matter entail weakly interacting sub-eV particles (WISPs), such as axions([11], [12], [13]), primordial black holes ref and weakly interacting massive particles
 115 (WIMPs).
 116

118 1.4.3 Unification of forces

119 The behavior of the three coupling constants at the order of TeV, *naturalness* ,(figure1.3,
 120 left) suggests the existence of a *primary* interaction, represented by a higher symmetry
 121 group (e.g. SU(5) or SO(10)). Spontaneous symmetry breaking of this interaction would
 122 lead to the existence of the electromagnetic, weak, and strong interactions at lower energy
 123 scales. Nevertheless, in order for this to happen, there should be a matching of these
 124 coupling constants for such high energies, which is not perfectly achieved in the SM. This
 125 hints the existence of new symmetries or fields (figure1.3, right). Some of these suggestions
 126 will be discussed in the following chapter.

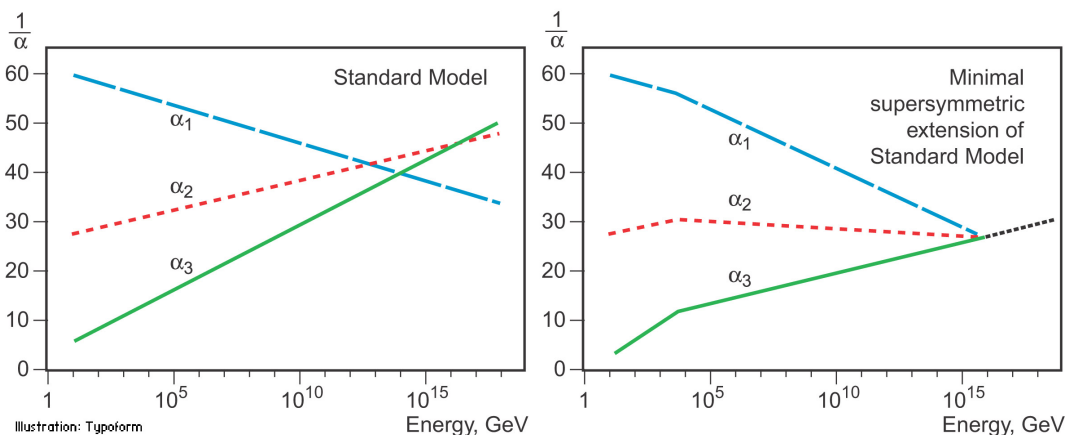


Figure 1.3: Running coupling constants as a function of the energy scale, for the SM (left) and in the context of supersymmetry (right) [14]

- 127 • The number of fermion families. As mentioned earlier, the number of fermion fami-
 128 lies is not an observable, but rather an input for the theory. More generations could
 129 in principle be accommodated as part of the SM particle content.

- The gauge hierarchy problem. This is intrinsically related to the mass of the Higgs boson. Apart from the fact that it is not predicted by the theory, it requires fine-tuning in order not to diverge, leading to the enlargement of the EW scale. Also, it is very small compared to the gravity scale, given by the Planck mass: $M_{Pl} = \sqrt{\hbar c/G_N} = 1.2 \times 10^{19}$ GeV, which is not fully understood.
- Inclusion of gravity. The SM fails to include gravity as one of the interactions, as there is no quantum theory for it.
- Neutrino masses. As it was already mentioned before, neutrinos are massless within the SM model. Nevertheless, experimental observations such as the oscillations of solar neutrinos [5] prove this prediction wrong. Thus, a Beyond the SM (BSM) mechanism to give neutrinos mass is required. There are several proposals for this, such as the seesaw mechanism or the Majorana theory [15].
- Charge quantisation. The fact that the electron charge and the proton charge are of the same magnitude but opposite sign has no explanation in the SM.
- Fermion masses and mixing angles. Similarly to what happened with the number of fermion families, these quantities are not predicted by the SM. Moreover, the mass of the top quark, much bigger than the other quark masses, is an intriguing fact not explained by this theory.
- The magnetic dipole moment of the muon, whose experimental measurement [16] deviates more than 3σ from the SM predictions.

In addition to this, several results provided by the LHCb collaboration refs on flavour anomalies and lepton flavour universality studies contribute to the motivation of the search for BSM physics.

Several theories have been proposed to cope with the SM problems, that make this model look more like an effective low energy theory than a model itself. Among these, Supersymmetry and Minimal Flavour Violation (MFV) are of special importance and will be discussed in the following chapters. However, there are other alternatives, some of which are briefly discussed below.

- **Majorana neutrinos:** in the SM, neutrinos are supposed to be massless *Dirac* particles. However it's been suggested that they are instead its own antiparticle, *Majorana neutrinos*. Within this theory, they are allowed to acquire mass. Several experiments search for a neutrinoless double beta decay that would prove this [17], [18].
- **Axions:** axions are hypothetical particles that compose DM, including the Peccei-Quinn mechanism [11] to solve the **strong CP problem** [19]. They would have been massively produced soon after the Big Bang. The couplings and masses axions can cover several orders of magnitudes.

- 167 • **Two Higgs Doublet Models (THDM):** in this scenario, there are two Higgs
 168 fields populating the vacuum instead of one.

$$\langle \phi_a \rangle_0 = \begin{pmatrix} 0 \\ \frac{v_1}{\sqrt{2}} \end{pmatrix}, \quad \langle \phi_b \rangle_0 = \begin{pmatrix} 0 \\ \frac{v_2}{\sqrt{2}} \end{pmatrix} \quad (1.14)$$

169 Where v_1 and v_2 follow the relation:

$$v \equiv (v_1^2 + v_2^2)^{1/2} \quad (1.15)$$

170 The ratio between these two VEVs, $\tan \beta \equiv \frac{v_2}{v_1}$ is the most important parameter
 171 in this model. It describes the diagonalization of the mass-squared matrices of the
 172 charged scalars and of the pseudoscalars, resulting in 4 fields

$$\begin{aligned} \phi_1 &= \sin \beta \phi_b + \cos \beta \phi_a & \phi_2 &= -\sin \beta \phi_a + \cos \beta \phi_b \\ \langle \phi_1 \rangle_0 &= \begin{pmatrix} 0 \\ \frac{v_{SM}}{\sqrt{2}} \end{pmatrix}, \quad \langle \phi_2 \rangle_0 = \begin{pmatrix} 0 \\ 0 \end{pmatrix} \end{aligned} \quad (1.16)$$

173 The spontaneous symmetry breaking leads in this case to 5 physical Higgs particles:
 174 two neutral scalars linear combinations of $Re(\phi_1^0)$ and $Re(\phi_2^0)$, H^0 and h^0 ; a neutral
 175 pseudoscalar, $A^0 \propto Im(\phi_2^0)$ and two charged scalars $H^\pm = \phi_2^\pm$.

- 176 • **Models with extra dimensions:** models with extra dimensions (apart from the
 177 usual 4 from the observed spacetime) are motivated by the attempts made to unify
 178 electromagnetism and gravity within the Kaluza-Klein theory [20], [21]. There are
 179 several proposals, such as *string theory* or the *Randall-Sundrum model* [22], that
 180 gives explanation to hierarchy using 5 dimensions and predicts the existence of the
 181 *graviton*.
- 182 • **SM with fourth generation (SM4):** adding a fourth generation of fermions
 183 requires the corresponding neutrino to be heavy, $m_{\nu_4} > M_Z/2$, to match the current
 184 experimental constraints [23].
- 185 • **Little Higgs Models:** in these models, the Higgs is realised as a light pseudo-
 186 Nambu Goldstone boson of a broken global symmetry. They attempt to solve the
 187 gauge hierarchy problem. The minimal version of such models include 4 new heavy
 188 vector bosons, (W'^\pm, Z', B') , coupled to SM fermions, mixed with the SM W^\pm
 189 and Z ; light Higgs doublet(s), with possibility of extra light scalar multiplets; heavy
 190 Higgs multiplets, coupled to Higgs/Goldstone pairs, decoupled from fermions, mixed
 191 with light Higgses, and heavy up-type quark(s), t' . An example spectrum can be
 192 seen in 1.4. Updated constraints in this model can be found in [24].

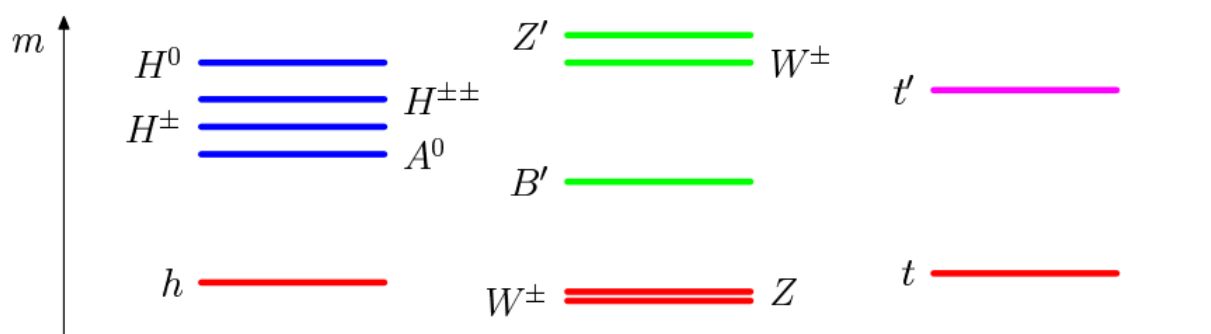


Figure 1.4: Example spectrum for LHM [ref?](#)

193 **Chapter 2**

194 **Supersymmetry**

195 **2.1 Introduction**

196 Supersymmetry (henceforth SUSY) is a framework that constitutes one of the main alter-
197 natives for BSM Physics. Postulated in the 70s as a graded Lie algebra (with commutators
198 and anticommutators), allowed by the Coleman-Mandula theorem [25], possess a unique
199 mathematical nature that allows for the solution of several of the SM caveats that were
200 discussed in the chapter before. It is being searched for in several experiments, and not
201 yet discovered. Lower limits are set in the scale of SUSY breaking, the so-called scale of
202 new physics. current bounds?

203 SUSY can be seen as a generalization of space-time symmetries in QFT, establishing
204 an invariance under the transformations of fermions to bosons, requiring their number
205 to be the same in nature. Hence, for each boson (fermion) there is a superpartner of
206 fermionic (bosonic) nature. If SUSY wasn't broken, the symmetry would be exact and
207 the masses of the particles would coincide with those of their respective superpartners,
208 which is not observed in nature. Moreover, none of the particles known to date fulfills
209 the quality to be a superpartner, which leads to the conclusion that for Supersymmetry
210 to exist there must be more particles than those seen so far (the double, in the simplest
211 supersymmetric extension of the SM).

212 A new quantity number can be introduced within SUSY, R-parity, defined as:

$$R = (-1)^{3B+L+2S} \tag{2.1}$$

213 Where B is the baryon number, L the lepton number (both quantities conserved in the
214 SM) and S the spin. Particles with R = 1 are SM particles, while their superpartners
215 have R = -1. Models where R-Parity is conserved (hence, B-L invariance) predict the
216 production of superparticle in pairs, and at least one stable supersymmetric particle, the
217 Lightest Supersymmetric Particle (LSP), thus providing a good candidate for dark matter.
218 There are also SUSY models where R-parity is violated, allowing the LSP to decay to SM
219 particles. An example of a RPV model is the bilinear RPV CMSSM [26].

220 2.2 Points addressed by SUSY

221 As mentioned earlier, the success of SUSY lies in the coverage of SM most important
222 **pitfalls**. A summary of this is discussed in this section.

- 223 • **Unification of forces:** as explained in the 2.1, gravity is not included in the SM.
224 Nevertheless, given that SUSY algebra is a generalization of Poincaré algebra, it is
225 therefore invariant under general coordinate transformation if it is local. With this,
226 a theory including gravity (*supergravity*) can be obtained from SUSY.
- 227 • **Gauge hierarchy problem:** Supersymmetry (and supersymmetric partners) lead
228 to the cancellation of quadratic mass terms causing divergences up to the SUSY
229 breaking scale, M_{SUSY} , given the relation

$$\sum_{bosons} m^2 - \sum_{fermions} m^2 = M_{SUSY}^2 \quad (2.2)$$

230 The origin of EWSB can also be explained from radiative electroweak symmetry
231 breaking within SUSY, also explaining the difference between the scales (M_{SUSY}
232 and the Higgs mass).

- 233 • **Unification of forces:** as mentioned earlier, the behavior of the coupling constants
234 at high energies hints a *great unification* of forces. This match, while not perfect in
235 the SM, is obtained in a supersymmetric scenario, as it can be seen in figure 1.3,
236 thanks to the change in the parameters of the renormalization group equations.
- 237 • **Matter-antimatter imbalance:** leptogenesis (a scenario in which there is an
238 asymmetry between leptons and antileptons in the early universe) can happen in
239 RPV models, being able to accommodate the total matter-antimatter imbalance.
- 240 • **Dark matter and dark energy:** as pointed out in 1.4.2, most of the origin of
241 dark matter and dark energy remains unexplained in the SM. Supersymmetry can
242 provide several candidates for this, provided R-parity is conserved. More details on
243 the possibilities are discussed in [ref](#).

244 2.3 Supersymmetry breaking

245 Supersymmetry breaking is inferred from experimental observation. Without it, the abundance
246 and mass of partners and superpartners would be equal, as said in 2.1. Moreover,
247 experimental constraints can help reducing the arbitrariness of the MSSM parameters.

248 All global continuous symmetries can be broken with an *extra* component of the Lagrangian
249 that breaks the symmetry of the larger part (Heisenberg-Wigner mode), with
250 spontaneous symmetry breaking and the resulting appearance of Goldstone particles, or
251 with a combination of these two methods. The Minimal Supersymmetric Standard Model
252 is an example of the former, and will be discussed in more detail in the following section.

253 **2.4 Minimal Supersymmetrical Standard Model**
 254 **(MSSM)**

255 The Minimal Supersymmetrical Standard Model is the simplest supersymmetric extension
 256 of the SM, containing some general features that do not depend on the choice of model.
 257 Among said features is the fact that for each SM partner there is a *superpartner* (*gauginos*
 258 for bosons and *sfermions* for fermions), with spin differing 1/2. The particle content is
 259 summarized in 2.1.

Table 2.1: Particle content of the MSSM

| SM | MSSM | Spin |
|-------------------------------|--|------|
| gluon (g) | gluino \tilde{g} | 1/2 |
| Hypercharge & Weak bosons | $\tilde{W}^0, \tilde{W}^\pm, \tilde{B}^0$ | 1/2 |
| leptons ($(\nu, l)_L, e_R$) | sleptons ($(\tilde{\nu}, \tilde{l})_L, \tilde{e}_R$) | 0 |
| quarks (q) | squarks (\tilde{q}) | 0 |
| Higgs field | Higgsinos ($\tilde{H}_u^\pm, \tilde{H}_d^\pm, \tilde{H}_u^0, \tilde{H}_d^0$) | 1/2 |

260 Notice that in the MSSM, as in any supersymmetric scenario, it is required the presence
 261 of 2 Higgs bosons in the SM with hypercharge -1 and 1, compatible with FCNC constraints,
 262 as it fulfills the Glashow-Weinberg/Paschos condition([?], [?]). Gauginos have spin zero
 263 in order to be matter scalars and not gauge bosons. As for the sfermions, the only
 264 consistent interacting field theory of spin 3/2 has to include gravity [27], hence they have
 265 spin 1/2. This theory, known as *supergravity*, includes the superpartner of the *graviton*,
 266 known as *gravitino*. It is also worth mentioning that the MSSM, like the SM, fails to
 267 explain the number of fermion families.

268 The MSSM has some interesing features, such as the improvement in the unification
 269 of gauge coupling constants at some high energy scale, Λ , still undetermined but known
 270 to be in the order of 2×10^{16} GeV. This unification is kept if SUSY isbroken at a scale
 271 $M_S \leq \mathcal{O}(1\text{TeV})$. Even if gravity is included, its coupling constant seems to roughly point
 272 to the same value at the same Λ .

273 The soft-explicit breaking of the MSSM (or the electroweak symmetry breaking itself)
 274 allows for mixing between different sparticles with the same charge and color to happen.
 275 This leads to the existence of *charginos* ($\tilde{\chi}_{1,2}^\pm$) and *neutralinos* ($\tilde{\chi}_{1,2,3,4}^0$), as a combination
 276 of gauginos and higgsinos for the former and neutral gauginos for the latter. Sfermion
 277 mixing can also happen. The mixing patterns and mass values of sparticle mass eigenstates
 278 depend crucially on the manner of supersymmetry breaking.

279 **2.4.1 Dark Matter in the MSSM**

280 As said before, within the SUSY framework there are several candidates to constitute
 281 DM. A common feature they share is their stability. These candidates are:

- 282 ● Sneutrino: ruled out in the MSSM because of the current limits on the interaction
 283 cross section of dark matter particles with ordinary matter as measured by direct
 284 detection experiments
- 285 ● Lightest neutralino: the LSP for models conserving R-parity. Depending on its
 286 composition it can be of different natures. Said composition comes determined by a
 287 unitary 4x4 matrix that diagonalize the neutralino mass matrix, N , as seen in 2.3.
 288 2.4.
- 289 1. Bino-like: when the term N_{11} dominates the neutralino diagonalization matrix,
 290 N , fulfilled for $M_1 < \mu$
- 291 2. Higgsino-like: when the off-diagonal elements in the mixing matrix ($N_{13}^2 + N_{14}^2$)
 292 dominate, for $\mu < M_1$
- 293 3. Wino-like: when the term N_{12} dominates the neutralino diagonalization matrix,
 294 N , fulfilled for $\mu, M_{1,3} < M_2$
- 295 4. Mixed states of the above

- 296 ● Gravitino

$$\begin{pmatrix} N_{11} & N_{12} & N_{13} & N_{14} \\ N_{21} & N_{22} & N_{23} & N_{24} \\ N_{31} & N_{32} & N_{33} & N_{34} \\ N_{41} & N_{42} & N_{43} & N_{44} \end{pmatrix} \quad (2.3)$$

$$\chi_1^0 = N_{11}\tilde{B} + N_{12}\tilde{W} + N_{13}\tilde{H}_d^0 + N_{14}\tilde{H}_u^0 \quad (2.4)$$

2.4.2 MSSM Lagrangian

The MSSM lagrangian consists of two parts:

$$\mathcal{L}_{\text{MSSM}} = \mathcal{L}_{\text{SUSY}} + \mathcal{L}_{\text{SOFT}} \quad (2.5)$$

Where the first part is just a generalization of the SM lagrangian, and the second part contains the supersymmetry breaking mechanism. The corresponding *superpotential* used in $\mathcal{L}_{\text{rmSUSY}}$ is of the form:

$$W = \epsilon_{ij}(y_{ab}^U Q_a^j U_b^c H_2^i + y_{ab}^D Q_a^j D_b^c H_1^i + y_{ab}^L L_a^j E_b^c H_1^i + \mu H_1^i H_2^j) \quad (2.6)$$

Where Q , U and D represent the squark superfields, L and E the **slepton** ones, $y^{U,D,L}$ are the Yukawa couplings and $H_{1,2}$ the Higgs superfields. The only qualitative difference with respect to \mathcal{L}_{SM} is the last term, that accounts for the Higgs mixing. Additional lepton violating leptonic or baryonic number can be added to this superpotential in RPV models.

311 Because of gauge invariance, supersymmetry breaking in the MSSM cannot happen
 312 spontaneously. Thus, an explicit term accounting for this breaking appears in the la-
 313 grangian, $\mathcal{L}_{\text{SOFT}}$, where *soft* refers to the dimension 2 and 3 of the operators. This
 314 breaking is the responsible for the SM particles not to be degenerate with their respective
 315 superpartners, as mentioned earlier, having these larger masses. **Nonetheless this SUSY**
 316 **breaking, some properties from it remain.**

317 A possible alternative to the soft-explicit supersymmetry breaking explained before
 318 consists in spontaneous symmetry breaking for a given scale, Λ_s , with a sector of fields
 319 that belong to a *hidden* sector and communicates with the *observable* sector with the
 320 exchange of fields known as *messengers*, as represented schematically in 2.1. This type of
 321 supersymmetry has been extensively searched for in several experiments, with negative
 322 results so far REFERENCES.

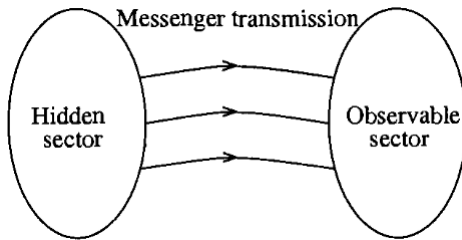


Figure 2.1: Schematic view of the hidden sector

323 The MSSM has 124 free parameters, namely:

- 324 • 18 SM parameters
- 325 • 1 Higgs sector parameter, analogue to the SM Higgs mass
- 326 • 5 real and 3 CP violating phases in the gaugino/higgsino sector
- 327 • 21 squark and slepton masses
- 328 • 36 real mixing angles for squark and slepton mass eigenstates
- 329 • real mixing angles for squark and slepton mass eigenstates

330 The complex phases are usually considered small. Some experiments are capable
 331 of measuring some of these parameters individually. Nevertheless, in general this large
 332 amount of degrees of freedom spoil the predictive power of the model. In order to reduce
 333 it, *mass universality* is imposed to some particular cases that will be further discussed
 334 in the next section. This implies that all spin 0 (1/2) sparticle masses are equal to
 335 a universal value m_0 ($m_{1/2}$). Another way of reducing the number of parameters is
 336 specifying the mechanism that breaks the symmetry, either with gauge fields (Gauge
 337 Mediated Supersymmetry Breaking, GMSB)[40] or as a consequence of a dominating
 338 super-Weyl anomaly (Anomaly Mediated Supersymmetry Breaking, AMSB). Some of
 339 this models will be explained in more detail later.

340 2.4.3 CMSSM

341 The *constrained* MSSM (hereafter CMSSM) is one of the most popular subversions of
 342 the MSSM. In this model, the concept introduced earlier of mass universality is imposed,
 343 meaning that for a given GUT scale $\Lambda \sim 2 \times 10^{16}$ GeV:

- 344 • All scalar masses are set to m_0

$$345 M_l^2(\Lambda) = M_{\tilde{q}}^2(\Lambda) \equiv m_0^2 I_3 \quad (2.7)$$

$$346 M_{\tilde{u}}^2(\Lambda) = M_{\tilde{e}}^2(\Lambda) = M_{\tilde{d}}^2(\Lambda) \equiv m_0^2 I_3 \quad (2.8)$$

$$m_{H_u}^2 = m_{H_d}^2 = m_0^2 \quad (2.9)$$

347 Where I_3 represents the 3x3 identity matrix

- 348 • All gaugino masses are set to $m_{1/2}$

$$m_{\tilde{B}}(\Lambda) = m_{\tilde{W}}(\Lambda) = m_{\tilde{g}}(\Lambda) \equiv m_{1/2} \quad (2.10)$$

- 349 • The trilinear couplings are set to A_0

$$A_{\tilde{u}}(\Lambda) = A_{\tilde{e}}(\Lambda) = A_{\tilde{d}}(\Lambda) \equiv A_0 I_3 \quad (2.11)$$

350 These requirements lead to the following relation between the gaugino masses at the TeV
 351 scale:

$$M_1 = \frac{\alpha_s}{\alpha} \sin \theta_W^2 M_2 = \frac{3}{5} \cos \theta_W^2 M_1 \quad (2.12)$$

352 Which translates into the ratios:

$$M_1 : M_2 : M_3 \approx 1 : 2 : 6 \quad (2.13)$$

353 With these conditions, the CMSSM ends up with a set of 5 free parameters: $(m_0,$
 354 $m_{1/2}, A_0, \tan \beta = \frac{v_1}{v_2}, \text{sign}(\mu))$. The last one refers to the sign of the Higgs self-coupling
 355 in the superpotential, while $\tan \beta = \frac{v_u}{v_d}$ is the ratio of the vevs from the Higgs doublet.
 356 Since gaugino masses run in the same way as the gauge couplings, within the CMSSM
 357 the LSP is generally the lightest neutralino. The status of CMSSM in light of current
 358 experimental constraints will be reviewed in chapter 2.4.3.

359 A more restrictive version of CMSSM exists, mSUGRA, where supersymmetry breaking
 360 is gravity-mediated. Within this model, the gravitino mass is equal to the scalar
 361 mass, $m_{3/2} = m_0$, thus adding a new constraint on the parameters. On the contrary,
 362 there are models with more relaxed conditions. An example of these is when the univer-
 363 sality condition on the Higgs masses is not applied, hence having Non Universal Higgs
 364 Masses (NUHM1 and NUHM2 [28]). This adds two extra free parameters, M_A , the mass
 365 of the CP-odd neutral higgs, A^0 , and μ , the Higgs self-coupling.

366 2.4.4 AMSB

367 In the Anomaly Mediated SUSY Breaking (AMSB), the supersymmetry breaking occurs
 368 mainly via a loop-induced super-Weyl anomaly. In some scenarios, such breaking is
 369 assumed to take place in a different *brane* from respect to the *observable* sector, within
 370 the context of *Extra Dimensions*. The anomaly-mediated SUSY breaking parameters are
 371 RG-invariant, being the corresponding masses given as functions of the gauge and Yukawa
 372 coupling constants. This helps avoiding a SUSY flavor problem.

373 To generate the weak scale masses of the sparticles, the gravitino mass, $m_{3/2}$ must be
 374 fairly heavy (of the order of tens of TeV). Ths, it's not affected by Big-Bang nucleosyn-
 375 thesis bounds. The gaugino masses $M_{1,2,3}$ are suppressed by loop factors relative to this
 376 gravitino mass, and the wino-like states are lighter than the bino-like ones. The following
 377 approximate ratios hold:

$$|M_1| : |M_2| : |M_3| \approx 2.8 : 1 : 7.1 \quad (2.14)$$

378 Within this model, the soft supersymmetry breaking terms can be computed from the
 379 gravitino mass, and the soft terms are real and both flavor and renormalization group
 380 invariant. Despite its many advantages, AMSB has a strong drawback: renormalization
 381 leads to negative squared masses for sleptons. There are several proposals to cope with
 382 this, like the *minimal* AMSB (mAMSB), that will be discussed further in 2.4.4.1.

383 2.4.4.1 mAMSB

384 In mAMSB, with the purpose of avoiding *tachyonic* sleptons in AMSB models, a constant
 385 contribution (m_0^2) is added to all squared scalar masses at the grand unified theory (GUT)
 386 scale, $\Lambda_{GUT} \sim 2^{16}\text{GeV}$. This addition can be mostly related to the presence of extra
 387 field(s)in the bulk [29], and destroys the aforementioned RG invariance, desirable in order
 388 to fulfill the **Flavour-Changing-Neutrl-Current (FCNC)** constraint. Nevertheless some
 389 characteristics are inherited.

390 Both the μ term and the to match soft bilinear Higgs coupling, B_μ are parameters of
 391 this model too. Given that they determine the Higgs potential:

$$G_F = [2\sqrt{2}(v_2^2 + v_1^1)]^{-1} \simeq 1.7 \times 10^{-5}\text{GeV}^{-2} \quad (2.15)$$

392 The minimization of 2.15 leads to the determination of such paramaters as a function
 393 of $\tan\beta$. Therefore, the mAMSB model has 3 continuous free parameters, $(m_0, m_{3/2},$
 394 $\tan\beta)$. In addition, the sign of the Higgsino mixing parameter, μ , is also free. The
 395 trilinear soft SUSY-breaking mass terms, like the gaugino masses, are determined by
 396 anomalies, therefore they are proportional to the gravitino mass.

397 This model has some interesting features, such as:

- 398 • The left and right sleptons are nearly degenerate ($m_{\tilde{l}_R} \approx m_{\tilde{l}_L}$), being stau the
 399 lightest slepton. As a consequence, the third and second generation *L-R* mixing
 400 angles become significantly larger, reaching the maximal limit at large $\tan\beta$.

- The lightest chargino and neutralino are also almost degenerate ($m_{\tilde{\chi}_1^\pm} \approx m_{\tilde{\chi}_1^0}$). This induces to a relatively long-lived $\tilde{\chi}_1^\pm$, that decays to a soft charged pion.
- Sfermion masses increase linearly with m_0 , but also depend on the precise value of $m_{3/2}$.
- The mass hierarchy between sleptons and gauginos depends on the input parameters.
- The squark masses are typically very heavy, as they grow with $g_3^4 m_{3/2}^2$.
- The stop masses are relatively high, because of the Higgs mass and the relatively low values of the trilinear couplings.
- The LSP (lightest neutralino) can be wino-, Higgsino-like or mixed-

The most up-to-date likelihood analysis of this model in light of current constraints can be found in [30]. A complete spectra at the best-fit points for the two signs of μ are shown in Fig. 2.2 in the wino-LSP case, where branching ratios exceeding 20% are indicated by dashed lines. As it can be seen, a relatively heavy spectrum is favoured in the global fit.

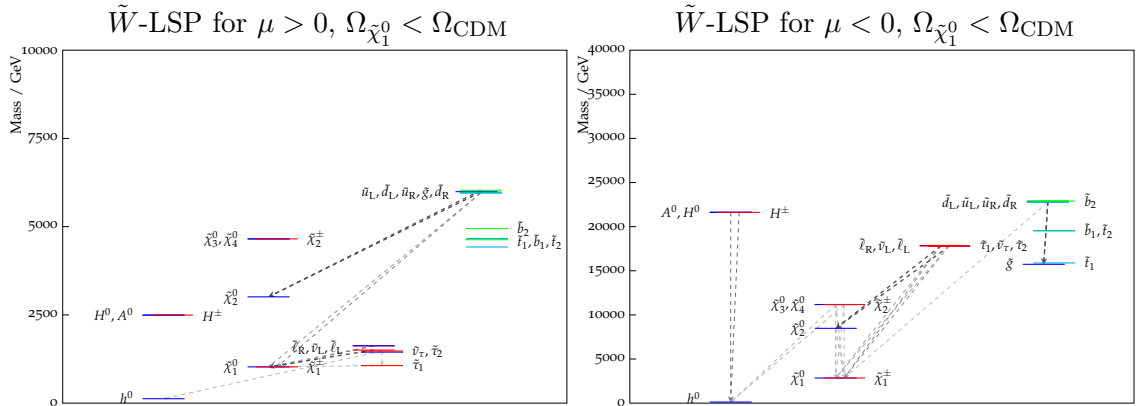


Figure 2.2: The spectra of the best-fit points for $\mu > 0$, allowing the LSP to contribute only part of the cold dark matter density. The wino-like LSP (lower) best-fit point is shown, indicating all the decay modes with branching ratios (BRs) above 20%, with darker shading for larger BRs, and the colours of the horizontal bars reflect particles' electric charges.

The preferred regions of the $(m_0, m_{3/2})$ planes for $\mu > 0$ (left panel) and $\mu < 0$ (right panel) are shown in the upper panels of Fig 2.3¹. It is seen that the wino region allowed at the 95% CL extends to smaller $m_{3/2}$ for both signs of μ , and also to larger m_0 at $m_{3/2} \gtrsim 300$ TeV when $\mu < 0$. The 68% CL region extends to much larger m_0 and $m_{3/2}$

¹The sharp boundaries at low m_0 in the upper panels of Fig 2.3 are due to the stau becoming the LSP, and the narrow separation between the near-horizontal portions of the 68 and 95% CL contours in the upper right panel of Fig. 2.3 is due to the sharp upper limit on the CDM density.

419 when $\mu < 0$, and the best-fit point also moves to larger masses than for $\mu > 0$, though
420 with smaller $\tan \beta$.

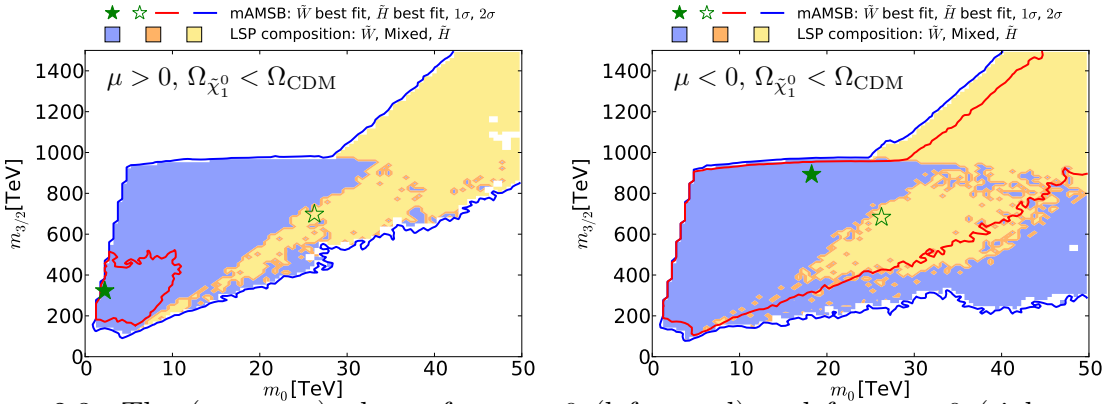


Figure 2.3: The $(m_0, m_{3/2})$ planes for $\mu > 0$ (left panel) and for $\mu < 0$ (right panel), allowing the $\tilde{\chi}_1^0$ to contribute only part of the CDM density. The best-fit points for the two signs of μ are indicated by green stars, closed in the wino-like region and open in the Higgsino-like region.

421 Fig 2.4 displays the cross section for spin-independent scattering on a proton, σ_p^{SI} ,
422 versus the neutralino mass, for the case in which the LSP is allowed to contribute only
423 a fraction of the CDM density. As previously, the left plane is for $\mu > 0$, the right plane
424 is for $\mu < 0$, the 1 and 2σ CL contours are shown as red and blue lines, and the wino-
425 and Higgsino-LSP regions are shaded in pale blue and yellow. The pale-green-shaded
426 region represents the range of σ_p^{SI}) excluded at the 95% CL by a combination of the latest
427 PandaX and LUX results [?, ?], while the purple and blue lines show the prospective
428 sensitivities of the LUX-Zeplin (LZ), XENON1T and XENONnT experiments [?, ?]. Also
429 shown, as a dashed orange line, is the neutrino ‘floor’, below which astrophysical neutrino
430 backgrounds would dominate any DM signal [?] (grey region). The plot shows good
431 prospects for future DM direct detection experiments when $\mu > 0$, with only a small
432 fraction of the parameter space lying below the neutrino ‘floor’. However, when $\mu < 0$
433 σ_p^{SI}) may fall considerably below the ‘floor’, because of cancellations [?] in the scattering
434 matrix element.

435 2.4.5 Renormalization Group equations

436 The renormalization group equations(RGE) are applied within the MSSM to describe the
437 evolution of gauge couplings, superpotential parameters and soft terms from a given *input*
438 scale up to near the *electroweak* scale. The method used in the SM (dimensional regu-
439 larization, DREG) cannot be used within SUSY, as it introduces a spurious violation of
440 this symmetry. The most common method for it is the dimensional reduction, DRED,
441 with modified minimal subtraction ($\overline{\text{DR}}$), as opposed to DREG with modified minimal
442 subtraction ($\overline{\text{MS}}$). Figure 2.5 compares the RG evolution of the coupling constants both

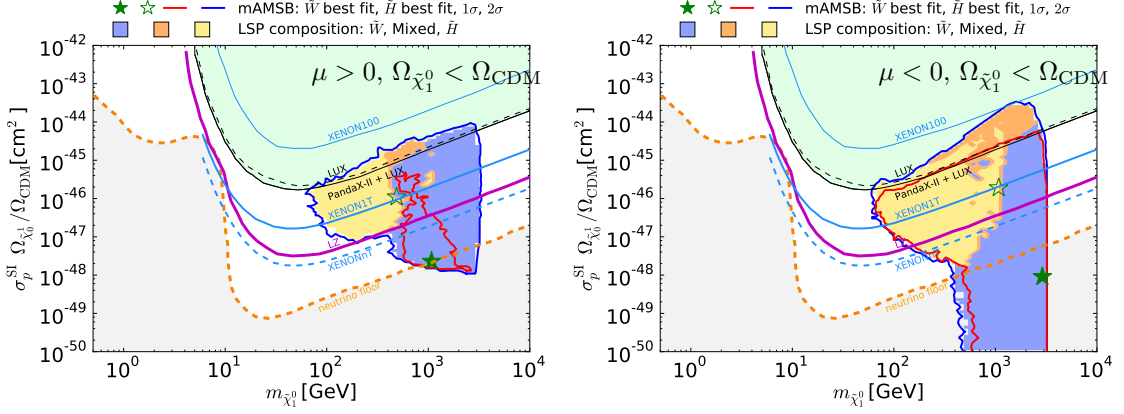


Figure 2.4: The $(m_{\tilde{\chi}_1^0}, \sigma_p^{SI})$ planes in the mAMSB for $\mu > 0$ (left) and $\mu < 0$ (right) in the case when the LSP only accounts for a fraction of the CDM density. The best-fit points for the two signs of μ are indicated by green stars, closed in the wino-like region and open in the Higgsino-like region.

in the SM and in the MSSM. As it can be seen, a better match at the electroweak scale is achieved within the MSSM, as discussed in 2.1.

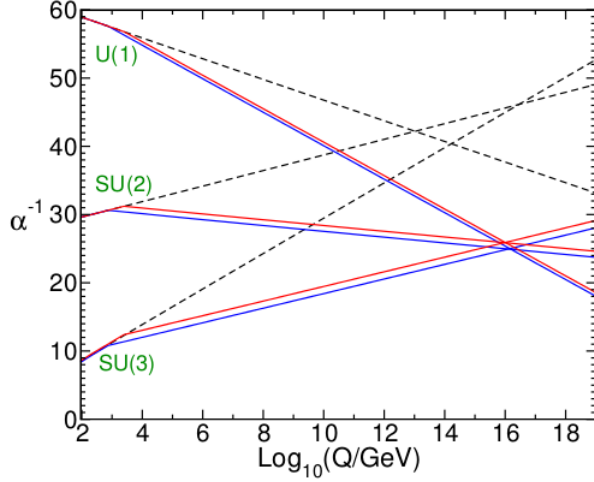


Figure 2.5: Two-loop renormalization group evolution of the inverse gauge couplings $\alpha_a^{-1}(Q)$ in the SM (dashed lines) and the MSSM (solid lines). In the MSSM case, the sparticle masses are treated as a common threshold varied between 750 GeV and 2.5 TeV, and $\alpha_3(m_Z)$ is varied between 0.117 and 0.120 [31].

The RGE are derived using what is known as the *supersymmetric non-renormalization theorem*, that implies that the logarithmically divergent contribution to a particular pro-

cess can always be written in terms of wave-function renormalizations [31]. One consequence derived from this is that for a given value of μ at tree-level, RG corrections to it will be proportional to the parameter itself and some combinations of dimensionless couplings, thus avoiding very large radiative corrections that could greatly enhance μ .

Within this framework, it is assumed that gauge couplings unify at a given scale, Λ . Hence, gaugino masses are considered to be unified near that scale as well (which come naturally in GUT models):

$$\frac{M_1}{g_1^2} = \frac{M_2}{g_2^2} = \frac{M_3}{g_3^2} = \frac{m_{1/2}}{g_\Lambda^2} \quad (2.16)$$

where g_Λ is the unified gauge coupling at Λ , and $m_{1/2}$ the unification value for the gaugino masses.

Some more consequences of the RGE are listed below.

1. Because they are not protected by the supersymmetric non-renormalization theorem, the soft parameters that describe the Yukawa couplings don't vanish at the electroweak scale, even if they are zero at the input scale.
2. The scalar squared masses will be almost diagonal, with the second family squarks and sleptons very nearly degenerate. The third-family squarks and sleptons will get normalized differently
3. The scalar squared-mass parameters grow as they are RG-evolved, due to the gaugino masses effect on the RGE. Therefore, large masses can be obtained at the electroweak scale even if these are small or even zero at the weak scale.
4. Because of the contributions they receive from the RGE, the Higgs squared masses generally decrease at the electroweak scale with respect to the input scale. This can lead to a negative value of $m_{H_u}^2$, with the consequence of a non-zero Higgs vev. This effect increases as the top Yukawa coupling does.
5. If the gaugino mass parameters M_1 , M_2 and M_3 have non-zero values for a given input scale, all the soft terms will be generated via RGE. Otherwise, gauginos would be extremely light, causing the model to be inviable due to experimental measurements.

2.5 RPV Models

R-parity (or matter parity) conservation can be justified in terms of a grand unified theory or as a consequence of a residual symmetry of a superstring vacuum. However, it is not necessarily the existing scenario. Additional terms can be added to the superpotential in 2.6 that violate baryon number (B) or lepton number (L), namely: **check consistency with other equation**

$$W_{\Delta L=1} = \frac{1}{2} \lambda^{ijk} L_i L_j \bar{e}_k + \lambda'^{ijk} L_i Q_j \bar{d}_k + \mu'^i L_i H_u \quad (2.17)$$

480

$$W_{\Delta B=1} = \frac{1}{2} \lambda''^{ijk} \bar{u}_i \bar{d}_j \bar{d}_k \quad (2.18)$$

481 Where $i = 1, 2, 3$, depending on the fermionic family. Terms in 2.17 (??) violate lepton
 482 (baryon) number by 1 unit. If both terms accompanying λ' and λ'' were to exist (without
 483 suppression), proton decays to final products such as $e^+ \pi^0$ would be feasible. Nevertheless,
 484 the lifetime for the proton is known to be $> 10^{34}$ years [32]. This, together with more
 485 experimental evidence , leads to the conclusion that one of these couplings must be zero or
 486 very small, being RPV models either B-violating or L-violating, with experimental upper
 487 bounds existing for both couplings.

488 One example of such type of RPV model is a scenario where R-parity is replaced by
 489 a *baryon triality*, defined in 2.19.

$$Z_3^B = \exp 2\pi i[B - 2Y]/3 \quad (2.19)$$

490 The corresponding symmetry establishes that the product of the baryon trialities of the
 491 particles in any term in the superpotential must be 1. With this, proton decay and
 492 neutron-antineutron oscillation are forbidden processes, as they would violate triality.
 493 This symmetry does allow the LSP to decay.

494 Another alternative is the spontaneous R-parity symmetry breaking by particles, like
 495 sneutrinos in the context of MSSM([33], [34]). Strong experimental bounds exist on
 496 this ref?. Either way, RPV scenarios greatly change the SUSY signatures in colliders,
 497 allowing processes like single sfermion production or exchange of sfermions to happen.

498 2.5.1 Consequences of RPV

499 Numerous consequences can be derived in the different possible RPV models. Some of
 500 them are briefly addressed below.

- 501 1. Within some of these models, there can be *leptogenesis* (asymmetry between leptons and antileptons in the early Universe), that would lead to the current matter-
 502 antimatter asymmetry discussed in 2.1.
- 503 2. The LSP can have color/charge, while fulfilling current constraints, and no longer
 504 needs to be stable.
- 505 3. Some RPV models include a seesaw mechanism that provides neutrinos with mass,
 506 while including sterile neutrinos [35].
- 507 4. A possible candidate for DM is the heavy gravitino, superpartner of the graviton.
 508 Even though it is unstable, its decay is heavily suppressed by the gravitational
 509 coupling, resulting in a lifetime bigger than the age of the Universe.

511 2.6 Experimental searches

512 Many experimental efforts have been done in the search for supersymmetry, both via direct
 513 searches of supersymmetric particles and by looking for indirect effects. A summary of
 514 the former is represented in figures 2.6 and 2.7, where bounds on the masses are set for
 515 different models, with data from ATLAS and CMS experiments, described in chapter 4.

516 With these experimental constraints, together with other experimental measurements,
 517 such as DM direct detection results ?? global fits can be made for different SUSY mod-
 518 els. A specific case will be discussed in chapter 7. More of these fits can be found
 519 in [36], [37], [38], [39], [30], [40], [41].

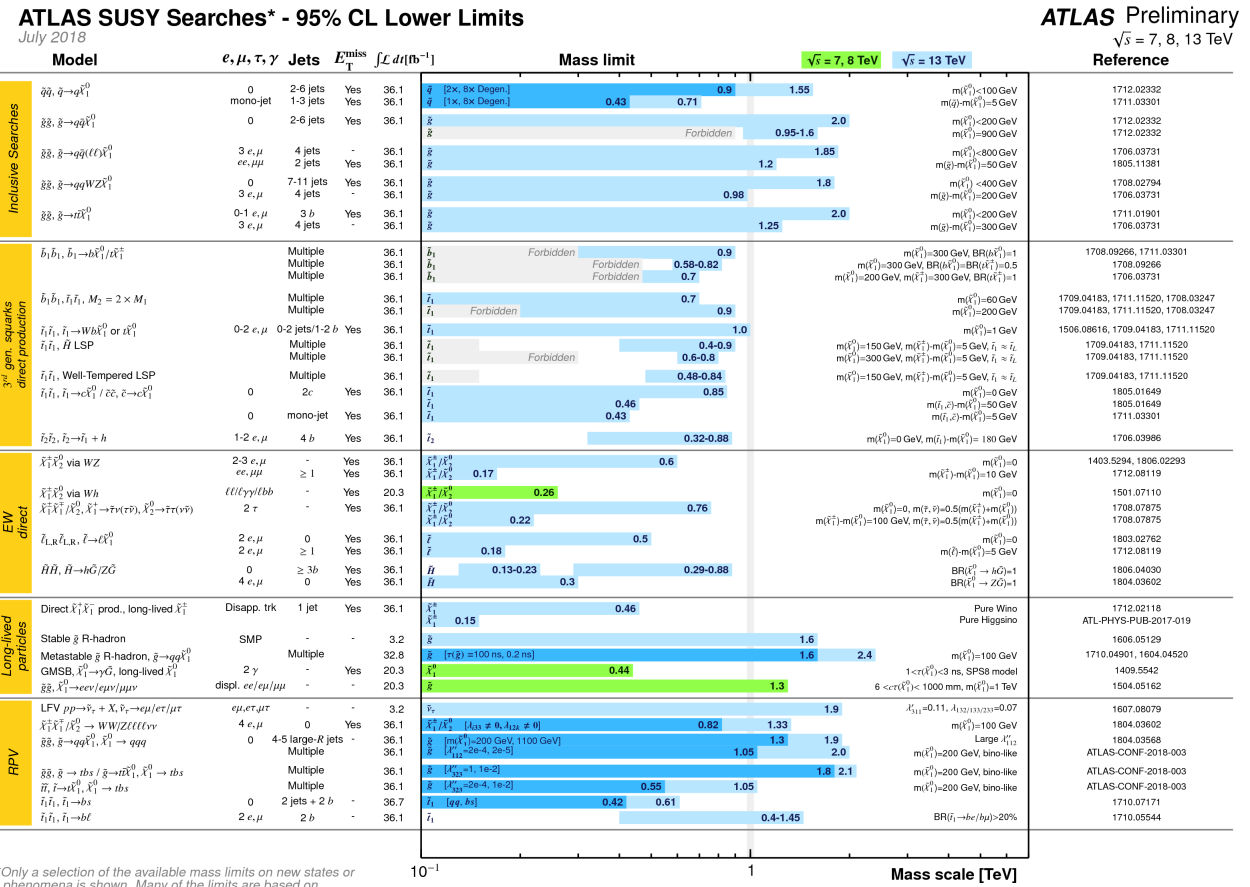


Figure 2.6: Experimental status of SUSY searches in ATLAS ref

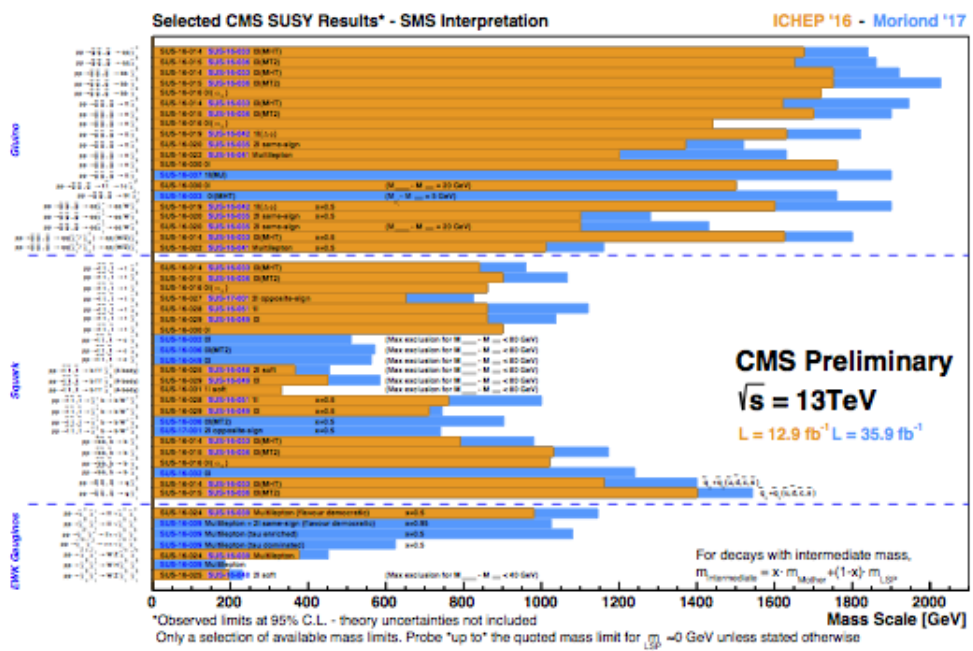


Figure 2.7: Experimental status of SUSY searches at CMS [ref](#)

520 Chapter 3

521 Low E in SUSY (MFV)

522 3.1 Motivation for MFV

523 The success of the SM in predicting flavour and CP violation effects leads to thinking
524 that NP has to follow its pattern. Otherwise, experimental evidence of additional flavour
525 violating structures should have appeared by now. Additionally, the hierarchy problem
526 suggests $\Lambda < \text{TeV}$, while in the case in which flavour violation is generated generically in
527 SUSY, $\Lambda \sim \mathcal{O}(\text{TeV})$ [42]. An effective field theory (henceforth, EFT) becomes necessary in
528 order to address the favour problem in SUSY, where the flavour violation predictions can
529 largely exceed the experimental constraints and are *a priori* unrelated to the SM sources
530 [43]. Minimal Flavour Violation (hereafter MFV) requires all flavour and CP-violating
531 interactions to be governed by the known structure of the SM Yukawa couplings [44]
532 in the low-energy regime. Hence, in any SM extension the amount of FCNC and CP
533 violating process should be ruled by these. As for supersymmetry, MFV holds under
534 the assumption of *mass universality*, and if the trilinear soft terms are proportional to
535 the Yukawa couplings at the GUT scale. This MFV can be seen as the remnant of an
536 underlying favor symmetry at the Λ scale [42].

537 3.2 MFV EFT

538 Minimal Flavour Violation (hereafter MFV) is constructed as a low-energy EFT [44],
539 within which the SM is contained. Its main feature is that the only source of $SU(3)^5$
540 flavour symmetry breaking are the background values of fields transforming under the
541 flavour group like the ordinary Yukawa couplings [44]. In the SM, the $U(3)^5$ flavour
542 symmetry is the largest group of unitary field transformations that commutes with the
543 gauge group. This can be decomposed [44] as: $U(3)^5 = [SU(3) \otimes U(1)]^5$.

$$G_F \equiv \bigotimes [SU(3) \otimes U(1)]_F, \quad F = Q, U, D, L, E \quad (3.1)$$

544 Notice that the baryon, lepton and hypercharge numbers are not modified by Yukawa
545 interactions. The $U(3)^5 = [SU(3) \otimes U(1)]^5$ group is broken by Yukawa interactions.

546 Flavour invariance is recovered introducing dimensionless auxiliary fields, Y_U , Y_D and Y_E
 547 transforming under $SU(3)_q^3 \otimes SU(3)_l^3$ promoting to spurion fields in order for flavour vio-
 548 lation to appear [43], thus leading to the Yukawa interaction terms of the SM lagrangian
 549 as discussed in 2.1, consistent with flavour symmetry. These terms can be rotated such
 550 that:
 551

$$Y_d = \hat{Y}_d, Y_e = \hat{Y}_e, Y_u = V^\dagger \hat{Y}_u \quad (3.2)$$

552 denoting \hat{Y} diagonal matrices, and V being the CKM matrix. The notation in [44] is
 553 followed.
 554

In MFV all higher-dimensional operators are constructed from SM and Y fields, and
 555 are invariant under CP and the flavour group G_F . Therefore, they can be rewritten
 556 in terms of the SM Yukawa couplings [43]. Given that the top Yukawa coupling is
 557 considerably large with respect to the others, the only relevant non-diagonal structure in
 558 the low $\tan\beta$ regime is obtained contracting two Y_u , hence having:
 559

$$(\lambda_{FC})_{ij} = \begin{cases} (Y_u Y_u^\dagger)_{ij} \approx \lambda_t^2 V_{3i}^* V_{3j} & i \neq h \\ 0 & i = j \end{cases} \quad (3.3)$$

559 where $\lambda_t = (\hat{Y}_u)_{33}$ and subleading effects on the r.h.s of 3.3 are suppressed by powers of
 560 m_c/m_t [43] as the effective coupling ruling all FCNC processes with external down-type
 561 quarks. Such processes are governed by $\Delta F = 2$ and $\Delta F = 1$ (Higgs field, gauge fields
 562 and four-fermion) operators. Further details on this operators can be found in [44].
 563

3.3 MFV SUSY

564 Consider the MSSM (where R-parity is conserved) as a low-energy EFT. Differently to
 565 what happens in other non-supersymmetric MFV scenarios, there are renormalizable
 566 terms with non-trivial flavour structure, besides the ordinary Yukawa couplings. Within
 567 MFV, the off-diagonal entries in the soft terms (the genuinely new sources of flavour
 568 violation in the MSSM) are CKM-like [43].
 569

The squark mass matrices after the electroweak breaking and using the soft terms, 3.9
 570 and 3.10 have the form
 571

$$\tilde{M}_U^2 = \begin{pmatrix} \tilde{m}_{Q_L}^2 + Y_u Y_u^\dagger v_u^2 + (1/2 - 2/3 \sin \theta_W^2) M_Z^2 \cos 2\beta & (A_u - \mu Y_u \cot \beta) v_u \\ (A_u - \mu Y_u \cot \beta)^\dagger v_u & \tilde{m}_{U_R}^2 + Y_U^\dagger Y_u v_u^2 + 2/3 \sin \theta_W^2 M_Z^2 \cos 2\beta \end{pmatrix} \quad (3.4)$$

572

$$\tilde{M}_D^2 = \begin{pmatrix} \tilde{m}_{Q_L}^2 + Y_d Y_d^\dagger v_d^2 + (1/2 - 1/3 \sin \theta_W^2) M_Z^2 \cos 2\beta & (A_d - \mu Y_d \tan \beta) v_d \\ (A_d - \mu Y_d \tan \beta)^\dagger v_d & \tilde{m}_{D_R}^2 + Y_D^\dagger Y_d v_d^2 - 1/3 \sin \theta_W^2 M_Z^2 \cos 2\beta \end{pmatrix} \quad (3.5)$$

573 According to MFV, the squark masses and trilinear couplings in 3.4,3.5 can be written
 574 as follows [44]:

$$\tilde{m}_{Q_L}^2 = \tilde{m}^2(a_1\mathbb{I} + b_1Y_uY_u^\dagger + b_2Y_dY_d^\dagger + b_3Y_dY_d^\dagger Y_uY_u^\dagger + b_4Y_uY_u^\dagger Y_dY_d^\dagger) \quad (3.6)$$

$$\tilde{m}_{U_R}^2 = \tilde{m}^2(a_2\mathbb{I} + b_5Y_uY_u^\dagger) \quad (3.7)$$

$$\tilde{m}_{D_R}^2 = \tilde{m}^2(a_3\mathbb{I} + b_6Y_dY_d^\dagger) \quad (3.8)$$

$$A_U = A(a_4\mathbb{I} + b_7Y_dY_d^\dagger)Y_u \quad (3.9)$$

$$A_D = A(a_5\mathbb{I} + b_8Y_uY_u^\dagger)Y_d \quad (3.10)$$

579 Where \tilde{m} and A set the mass scale of the soft terms, a_i and b_i are numerical coefficients
 580 and \mathbb{I} is the 3x3 identity matrix. Quadratic terms of the first two families of Yukawas
 581 have been neglected. In the limit of low $\tan\beta$ the terms quadratic in Y_d can be dropped
 582 too.

583 Under the assumption of mass universality and proportionality of trilinear terms, the
 584 b_i coefficients are zero at the GUT scale Λ and generated via RGE.

585 It is worth noticing from 3.4, 3.5 the physical squark masses are not degenerate under
 586 the MFV assumption, but the mass splitting is severely constrained.

587 The mass matrices in 3.5 and 3.4 are then diagonalized using the expansions in
 588 3.6,3.7,3.8,3.9 and 3.10. Analogously to the SM case, it is possible to change to a *super-*
 589 *CKM* basis, where:

$$\hat{m}_u = \frac{v_d}{\sqrt{2}}\hat{Y}_u, \quad \hat{m}_d = -\frac{v_u}{\sqrt{2}}\hat{Y}_d \quad (3.11)$$

591 Notice that in this basis the Yukawa matrices are diagonal, but the trilinear couplings
 592 and the mass-matrices are still non-diagonal. Unitary matrices Z_U and Z_D are needed in
 593 order to change to a mass eigenstate basis. In the MFV scenario the off-diagonal entries
 594 of this matrices are not zero, but CKM-like [43].

595 3.4 MFV R-parity

596 MFV can be used instead of the R-parity conservation assumption [45]. Under this
 597 scenario the baryon number can be violated, while the lepton number violation is strongly
 598 suppressed and only possible with massive neutrinos. This is strongly discouraged by the
 599 proton lifetime, and bounds from $n - \bar{n}$ oscillation and dinucleon decay. In some specific
 600 models, extra suppression from the neutrino sector can help further alleviate this bounds.
 601 Under this models R-parity is obtained as an approximate symmetry as a side effect. The
 602 LSP decays fast and is not necessarily neutral, it can be a stop or sbottom (decaying to 2
 603 bodies), a neutralino or chargino (decaying to 3 bodies) or a slepton (with the subsequent
 604 4 body decay). A possible DM candidate is the gravitino.

605 3.5 Characteristics

606 Given that the top Yukawa coupling is much larger than the others, in MFV all flavour-
607 changing effective operators are proportional to the same non-diagonal structure. This
608 greatly affects the predictability of this model, as will be discussed in 3.7. Within this
609 approach, the squark masses in the physical eigenbasis are not degenerate, but the induced
610 flavour violation is described in terms of the usual CKM parameters [44].

611 Strong assumptions need to be made in order to maintain MFV within different SUSY
612 scenarios, such as supergravity. Other models with different susy-breaking mechanism
613 (such as AMSB) can alleviate this conundrum [44].

614 As will be discussed in 3.8, the Universal Unitarity Triangle does not necessarily hold
615 within the MFV scenario.

616 Within MFV, both the gaugino masses $M_{1,2}$ and the Higgs mixing parameter μ . Otherwise,
617 given that they appear in the neutralino and chargino mixing matrices, they would
618 induce new sources of CP violation, thus violating MFV. An alternative approach [46]
619 consists in assuming the soft SUSY breaking sector to be CP conserving only in the limit
620 of flavour blindness, while allowing CP violation to happen by the MFV-compatible terms.
621 In this scenario, μ and the gaugino masses are real at low energies and the trilinear cou-
622 pings ([the only sources of CP-violation](#)) are strongly hierarchical, being the Electric Dipole
623 Moments (EDMs) the most important experimental constraints [42]. Nevertheless, in the
624 case in which this *ansatz* holds not at the low scale, but at the GUT scale (determined
625 by Λ), complex parameters can be generated via RGE [42], [46].

626 3.6 CMFV

627 The *constrained* MFV (cMFV) is a phenomenological definition of MFV, that uses the
628 CKM matrix (instead of the Yukawa couplings) as the only source of flavour violation and
629 restricts the set of relevant operators in the low-energy effective Hamiltonian to the SM
630 ones [43] (\mathcal{Q}_1). Contrarily to the more general definition of MFV proposed in [44], it is
631 not model-independent. In the limit in which $b_i \rightarrow 0$ in 3.6-3.10, the cMFV is recovered
632 from the general MFV. Nevertheless, it is worth mentioning that not all the scenarios are
633 \mathcal{Q}_1 -dominated, as it is assumed in cMFV. Indeed, in the limit of low $\tan \beta$ it is not always
634 the case [43].

635 3.7 Experimental bounds

636 Generic flavour-violating interactions at $\Lambda \simeq$ TeV are known to be experimentally ex-
637 cluded. Within a MFV scenario, it is possible to relate various flavour-changing neutral
638 current (FCNC) processes, such as rare B and K decays. Furthermore, CP-violation in
639 the B_s system provide an excellent probe where to look for non-CKM sources of flavour
640 and CP-violation [43]. Besides, this constraint in the soft sector helps further reduce the

641 number of parameters of the MSSM, thus improving its predictivity.

642 Experimental bounds to the generic MFV approach come mainly from:

- 643 • $\Delta F = 2$ processes that help further improve the precision for CKM matrix elements
- 644 • The inclusive rare decay $B \rightarrow X_s \gamma$ to constraint the scale of the FCNC operators
- 645 • Rare FCNC decays into a lepton pair, e.g. $K_L(B) \rightarrow l^+ l^-$, $K^+ \rightarrow \pi^+ \nu \bar{\nu}$, that
646 provide constraints on several Wilson coefficients
- 647 • Non-leptonic decays, provided electroweak contributions can be properly disentangled
648 from the dominant effects coming from tree-level and gluon-penguin amplitudes

649 3.8 Unitarity Triangle

650 The *universal unitarity triangle* [47] (henceforth, UUT) represented in 3.1 is characterized
651 by not having any new operators beyond those present in the SM, hence only valid for
652 cMFV models 3.6. Depending on the mass regime and the value of $\tan \beta$, variations up to
653 the percent level can be found in a general MFV scenario [43]. In this triangle, no phases
654 are beyond the CKM phase, hence they are not polluted by new physics contributions
655 (since the quantities only depend on the CKM parameters). A virtue of the universal
656 triangle is that it allows to separate the determination of the CKM parameters from the
657 determination of new parameters present in the extensions of the SM. As an example,
658 new phases could affect α , β and γ .

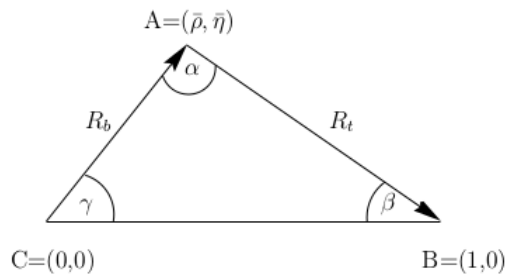


Figure 3.1: Unitarity Triangle, using the Wolfenstein parametrization [ref](#), [PDG](#)

659 Experimental measurements help determining the different values for the elements
660 that define the triangle in 3.1. Some of these measurements are $(\Delta M)_d / (\Delta M)_s$ (for R_t),
661 $\sin 2\beta$, $B_d^0 \rightarrow \phi K_S^0$ (for β) and tree-level decays (for γ). As said before, NP contributions
662 can affect these values, hence hinting the existence of BSM Physics.

663 In order for this triangle to be *universal* to any SM extension, the requirement that
664 new operators don't exist has to be fulfilled. Also, FCNC transitions should be ruled
665 by the CKM elements. Hence, only the values of the functions describing top-mediated
666 contributions to box and penguin diagrams can be modified by this new physics [47].

667 Under these conditions, the CKM matrix can be determined without further assumption
 668 on the unknown BSM parameters, with the possibility of disentangling SM contributions
 669 from NP ones, looking for inconsistencies in the universal triangle or disagreements of the
 670 data with respect to the predictions made based on the UUT. As an extra feature, these
 671 parameters are not affected by hadronic uncertainties [47].

The most up-to-date determination of the elements of the UUT can be found in 3.2.

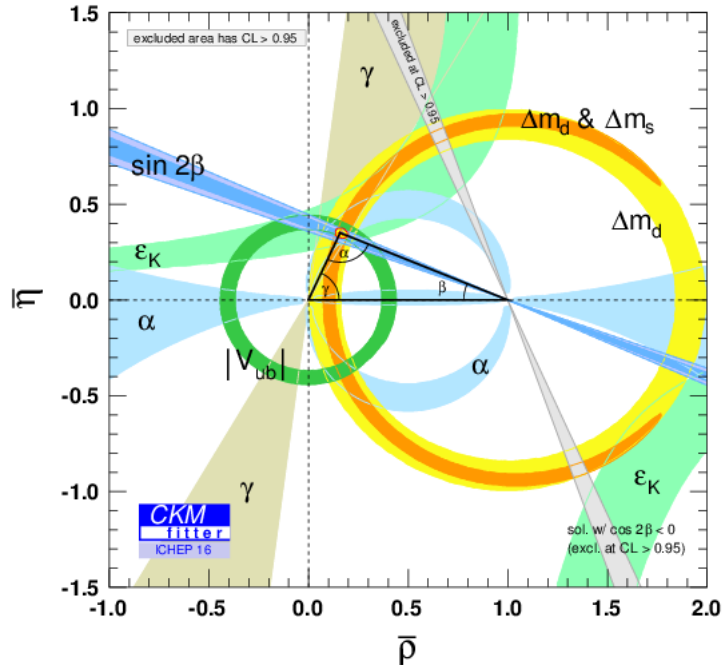


Figure 3.2: Experimental constraints on the UUT, using the Wolfenstein parametrization [48]

673

Chapter 4

674

LHCb

675

4.1 LHC

676 The Large Hadron Collider (LHC) is the world's largest and most powerful particle ac-
677 celerator. Located at CERN (*European Organization for Nuclear Research*), it consists of
678 a 27 km ring of superconducting magnets with a number of accelerating structures, that
679 boost the energy of the particles along the way.

680 Two proton beams travelling in opposite directions collide at different points of the
681 ring. These are extracted from ion sources, and accelerated in a chain of preaccelerators,
682 being the lat stage of such chain the Super Proton Synchrotron (SPS) (see Fig. 4.1). They
683 are accelearted to produce collisions at energy in the center of mass (\sqrt{s}) of the order
684 of the TeV, in order to test the Standard Model and look for New Physics. One of its
685 main achievements has been the discovery of the Higgs boson, introduced in [49], [50],
686 the last piece of the Standard Model puzzle. Protons are sent on bunches containing up
687 to 1.5×10^{11} particles, and corssing with a rate of 40 MHz. Special runs with heavy ions
(e.g. lead) are also made periodically.

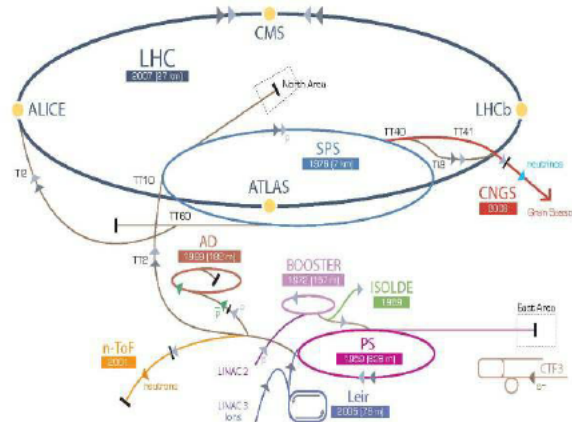


Figure 4.1: The LHC injection complex.

688 Since it first started operating in 2008, it has recorded data with different center of
689 mass energies, corresponding to 2 data-taking periods: Run 1 (2009-2013, $\sqrt{s} = 7, 8$ TeV),
690 and Run 2 (2013-present, $\sqrt{s} = 13, 14$ TeV). An upgrade of the detectors was made in
691 between the runs.

692 There are four interaction points within the LHC ring, corresponding to the four main
693 experiments. In these points, the beams cross over to the other beam pipe and collide
694 under a small angle. These four experiments are:

- 695 • **ATLAS** (*A Toroidal LHC ApparatuS*) [51]: a general-purpose 4π detector, focused
696 mainly in the search of New Physics via direct searches and responsible of the Higgs
697 boson discovery.
- 698 • **CMS** (*Compact Muon Solenoid*) [52]: also a general-purpose detector, with a
699 physics program similar to ATLAS and a more compact layout.
- 700 • **ALICE** (*A Large Ion Collider Experiment*) [53]: the smallest of the four detector,
701 it focuses in heavy-ion studies.
- 702 • **LHCb** (*Large Hadron Collider beauty*) [54]: a single-arm forward spectrometer,
703 initially designed for the study of particles containing b or c quarks, now converted
704 into a general-purpose detector. It is described in more detail in the following
705 section.

706 4.2 LHCb

707 The LHCb detector [55, 56] is a single-arm forward spectrometer covering the
708 pseudorapidity range $2 < \eta < 5$, designed for the study of particles containing b or c
709 quarks. The detector includes a high-precision tracking system consisting of a silicon-
710 strip vertex detector surrounding the pp interaction region [?]*, a large-area silicon-strip
711 detector located upstream of a dipole magnet with a bending power of about 4 Tm, and
712 three stations of silicon-strip detectors and straw drift tubes [?]* placed downstream
713 of the magnet. The tracking system provides a measurement of the momentum, p , of
714 charged particles with a relative uncertainty that varies from 0.5% at low momentum
715 to 1.0% at $200\text{ GeV}/c$. The minimum distance of a track to a primary vertex (PV), the
716 impact parameter (IP), is measured with a resolution of $(15 + 29/p_T)\mu\text{m}$, where p_T is
717 the component of the momentum transverse to the beam, in GeV/c . Different types of
718 charged hadrons are distinguished using information from two ring-imaging Cherenkov
719 detectors [?]*. Photons, electrons and hadrons are identified by a calorimeter system
720 consisting of scintillating-pad and preshower detectors, an electromagnetic calorimeter
721 and a hadronic calorimeter. Muons are identified by a system composed of alternating
722 layers of iron and multiwire proportional chambers [?]*. The online event selection is
723 performed by a trigger [?]*, which consists of a hardware stage, based on information
724 from the calorimeter and muon systems, followed by a software stage, which applies a full
725 event reconstruction.

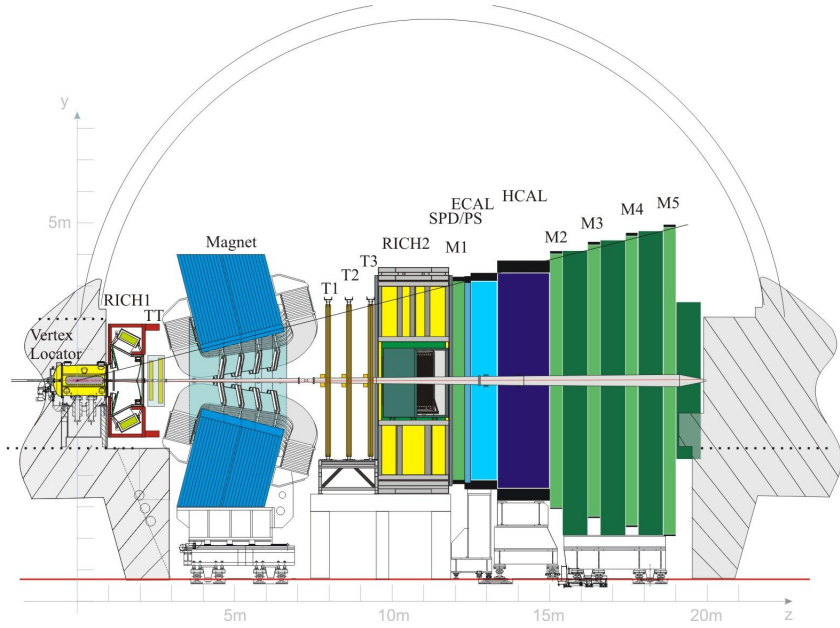


Figure 4.2: LHCb detector

4.2.1 Beam pipe, vacuum chamber and BCM

The design of the beampipe (4.3) is especially delicate, given the pseudorapidity region at which LHCb operates, where there is a high particle density. It is of 19m long and includes the forward window of the VELO and four main conical sectors. The three closer to the interaction point are made of beryllium, as it is highly transparent to particles resulting from collisions. The one left is made of stainless steel because of its good mechanical and vacuum properties. The beampipe support system consists of one fixed and one movable support, in order to reduce the background as much as possible. Two sector valves located at the cavern entrances isolate the experiment beam vacuum from the LHC.

The Beam Conditions Monitor (BCM) takes care of possible problems with the LHC beam conditions, requesting a beam dump if necessary. It monitors the particle flux at two locations close to the vacuum chamber (so as to protect the sensitive LHCb tracking devices). It is connected to the LHCb experiment control system and to the beam interlock controller of the LHC. The two stations consist of eight diamond sensors, with the same dimensions as those of ATLAS and CMS.

4.2.2 Magnet

LHCb contains a dipole magnet that bends charged particles in order to measure their momenta. The measurement covers the forward acceptance of $\pm 250\text{mrad}$ vertically and of $\pm 300\text{mrad}$ horizontally. Two identical conical saddle-shaped coils surround an iron yoke, producing a magnetic field of 4 Tm for tracks of 10 m length (notice that difference parts

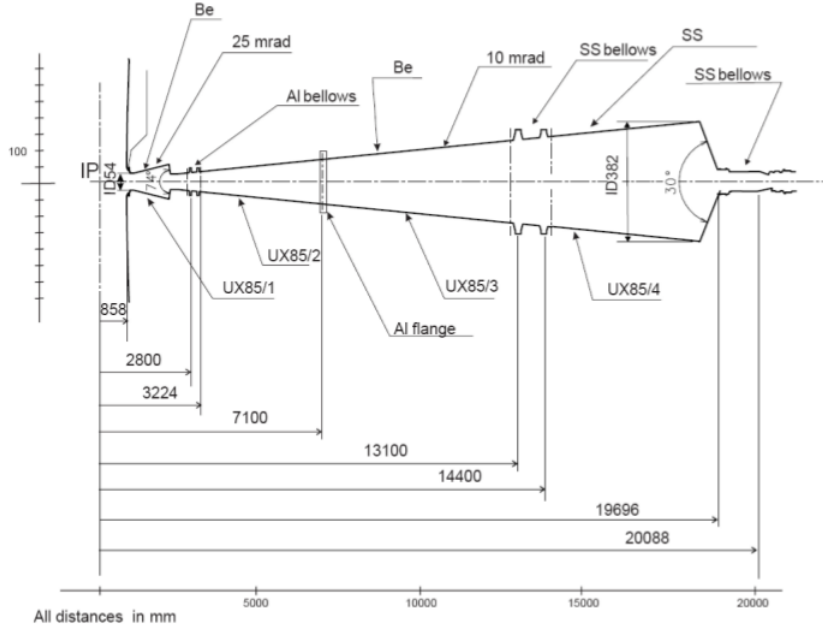


Figure 4.3: LHCb beam pipe

of the detector need for different values of the magnetic field). These coils are made of pure Al-99.7.

The magnet is operated using a Magnet Control System, a well as a Magnet Safety System, that takes care of the security of the magnet performance.

The precision with which the magnetic field of the magnet is measured needs to be of the order of 10^{-4} so as to properly measure the momentum resolution of the charged particles. In order to ensure this, field mapping campaigns in the tracking volume were made and obtained a value of about 4×10^{-4} (4.4). In order to reduce the systematic effects of the detector, especially for CP studies, the polarity of the magnetic field needs to be changed periodically.

4.2.3 Tracking

The tracking system of LHCb consists of two parts: the vertex locator (VELO) and four tracking stations: the *Tracker Turicensis* (TT) upstream of the magnet, and T1-T3 downstream of the magnet. The latter are composed by an Inner Tracker (IT) and an Outer Tracker (OT). Both IT and TT belong to a common project, the *Silicon Tracker* (ST).

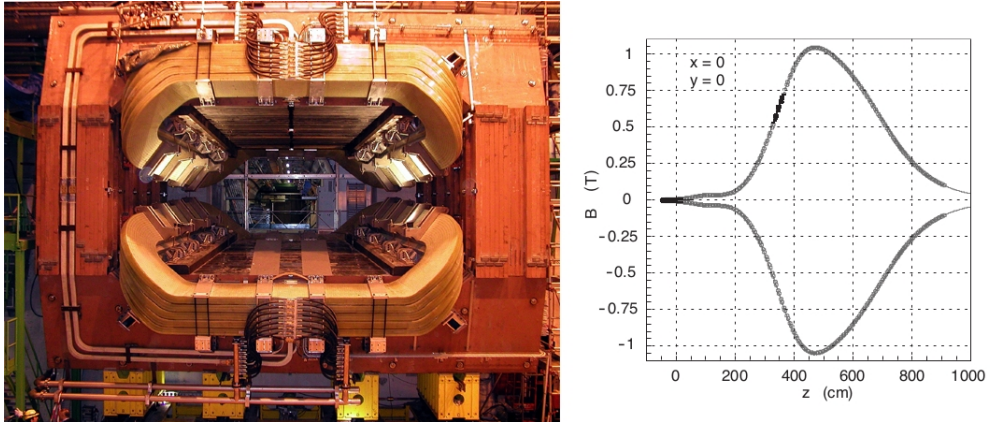


Figure 4.4: LHCb magnet (left) and magnetic field along the z axis (right)

762 4.2.3.1 VELO

763 The ability to reconstruct vertices with a high precision is a key feature of the LHCb
 764 detector. It is vastly used to accurately measure the decay lifetimes, the impact parameter
 765 and the flavour of the particles that are produced. Besides, detached vertices are of crucial
 766 importance for the High Level Trigger (4.2.5).

767 Such reconstruction is done in the VErtex LOcator (VELO), that provides measure-
 768 ments of the track coordinates close to the interaction region. It consists of 20 semicircular
 769 silicon modules located along the beam direction, each one providing measurement of
 770 cylindrical coordinates (r, ϕ) using microstrips, together with two planes perpendicular
 771 to the beam line, the *pile-up veto system*, as it can be seen in 4.5, that are then used to
 772 get rid of high multiplicity events. The minimum pitch at the innermost radius is $38\mu\text{m}$,
 773 increasing linearly to $101.6\mu\text{m}$ at the outer radius of 41.9mm . These sensors must be
 774 retractable, as the distance from them to the beam is smaller than the one required from
 775 LHC during the injection phase. Vacuum inside the VELO is separated from the machine
 776 vacuum by corrugated aluminum foils, *RF-foils*.

777 The VELO was designed in order to fulfill the signal to noise ratio, efficiency, reso-
 778 lution and geometrical requirements. Polar coordinates are used in order to ensure fast
 779 reconstruction of tracks and vertices in the LHCb trigger [55].

780 4.2.3.2 ST

781 As said before, the Silicon Tracker (ST) refers to two different detectors: the Tracker
 782 Turicensis (formerly known as *Trigger Tracker* (TT) and the Inner Tracker (IT) (see 4.6).
 783 Both use silicon microstrip sensors with a strip pitch of about $200\ \mu\text{m}$. The TT is a
 784 $150 \times 130\ \text{cm}^2$ high planar tracking station (covering the full LHCb acceptance), located
 785 upstream of the LHCb dipole magnet. The IT covers a $120 \times 40\ \text{cm}^2$ high cross shaped
 786 region in the centre of the three tracking stations downstream of the magnet.

787 The TT and each of the three IT stations have four detection, organized in an $(x-u-v)$ -

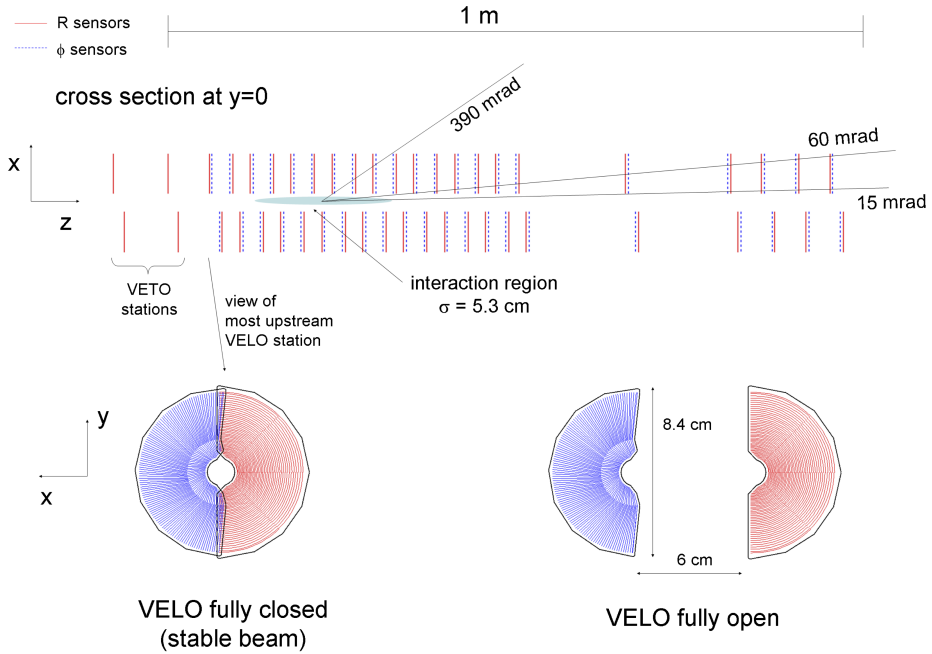


Figure 4.5: Cross section in the (x,z) plane of the VELO silicon sensors, at $y = 0$, with the detector in the fully closed position. The front face of the first modules is also illustrated in both the closed and open positions [55].

788 x) configuration, with vertical strips in the first and the last layer. Strips in the second
 789 and third layer are rotated by a stereo angle of -5° and 5° respectively (so as to get 3D
 790 reconstruction). The pitch is about $200\mu\text{m}$ which gives a single hit resolution of $50\mu\text{m}$.
 791 Momentum resolution is then dominated by multiple scattering. The active area is of
 792 about 8.4m^2 for the TT and of 4.0m^2 for the IT. A temperature below 5°C is maintained
 793 in both cases.

794 4.2.3.3 OT

795 The OT detector is designed for the tracking of charged particles, and the measurement of
 796 their momentum. Excellent momentum resolution and high tracking efficiency are needed
 797 for LHCb analyses. It consists in a drift-time detector, composed of an array of gas-tight
 798 straw-tube modules. For the gas, a mixture of Argon (70%) and CO_2 (30%) is used. This
 799 ensures a fast drift time, as well as a sufficient drift-coordinate resolution.

800 The modules are arranged in three stations, each one consisting of four layers. The
 801 stations are further splitted in two halves, with two independently retractable units of
 802 two half layers (C-frames). Such arrangement can be seen in 4.7.

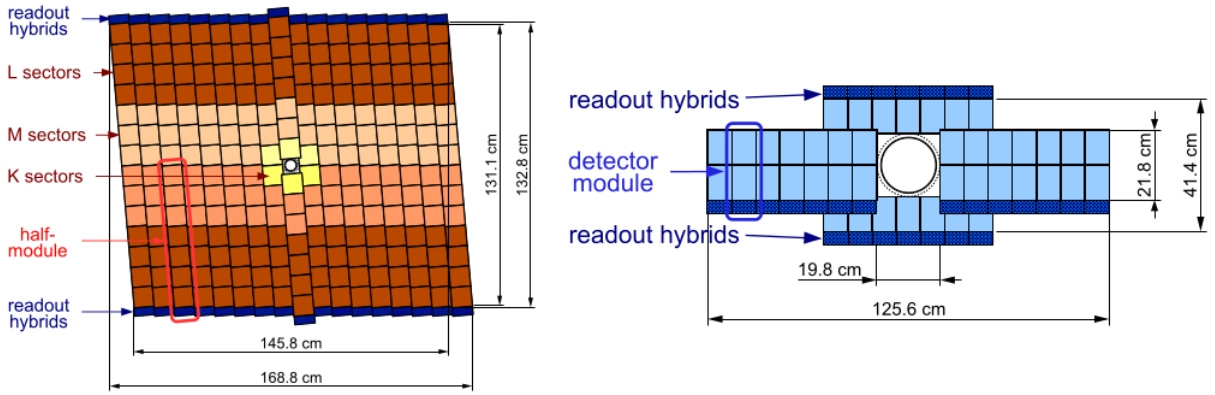


Figure 4.6: Layout of the third TT detection layer (left) and layout of an x detection layer in the second IT station (right) [55].

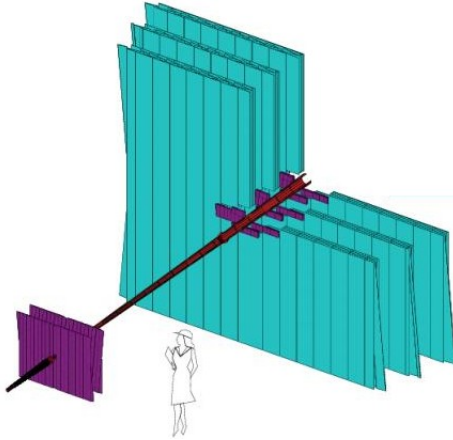


Figure 4.7: Arrangement of OT straw-tube modules in layer and stations [55].

803 4.2.4 PID

804 Particle identification (PID) at LHCb is crucial in order to properly distinguish the dif-
 805 ferent types of particles that are detected. Particularly, it is important to further reduce
 806 backgrounds from different decays, as well as at the trigger level (4.2.5). Three different
 807 subdetectors, described below, are used for PID.

808 4.2.4.1 RICH

809 There are two *Ring Imaging Cherenkov detectors* at LHCb, designed to cover the full
 810 momentum range. RICH1 (4.8 left) covers the low momentum charged particle range
 811 ($\sim 1 - 60\text{GeV}$), while RICH2 (4.8 right) covers the high momentum charged particle
 812 range ($\sim 15\text{GeV}$ up to and beyond $\sim 100\text{GeV}$). In order to do this, RICH1 (located

813 upstream, between the VELO and the Trigger Tracker) uses aerogel and C_4F_{10} radiators,
814 while the downstream detector, RICH2, uses a CF_4 radiator.

815 While RICH1 covers the full LHCb acceptance, from $\pm 25\text{rad}$ to $\pm 300\text{rad}$ horizontal
816 and $\pm 250\text{rad}$ vertical, RICH2 has a more limited angular acceptance (where the high
817 momentum particles are produced), of $\sim \pm 15\text{rad}$ to $\pm 120\text{rad}$ horizontal and $\pm 100\text{rad}$.

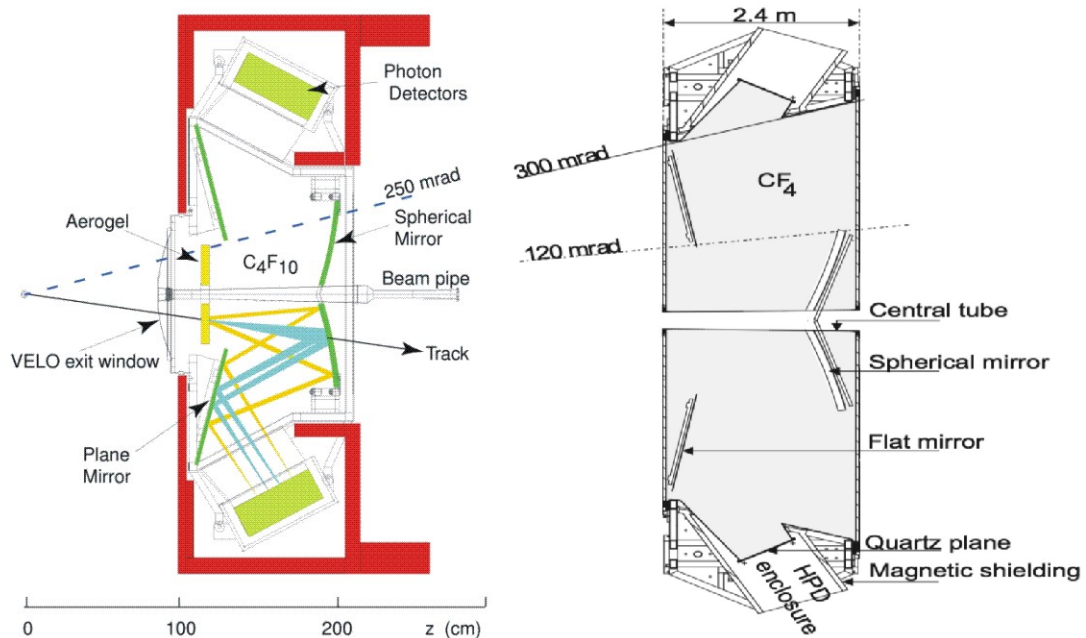


Figure 4.8: Schematic view of RICH1 (left) and RICH2 (right) detectors [55].

818 Both detector use spherical and flat mirrors to focus the Cherenkov light. The optical
819 layout is vertical for RICH1 and horizontal for RICH2. Cherenkov photons in the wave-
820 length range 200-600 nm are detected by Hybrid Photon Detectors (HPDs), which are
821 outside the LHCb acceptnace. These are surrounded by external iron shields that shield
822 tem from the marginal field of the LHCb dipole.

823 4.2.4.2 Calorimeters

824 The transverse energy of hadrons, electrons and photons is measured and selected in the
825 calorimeter for the L0 trigger (4.2.5). The energy and position is also measured for these
826 particles, which are identified in this subdetector, while avoiding the pass of those particles
827 to the muon system. The proper identification of hadrons, electrons and photons is also
828 of great importance for correctly identifying the flavour of the original meson in the decay
829 (*flavour tagging*). This is done taking into account that these particles deposit the energy
830 in the different parts of the calorimeter in a different manner.

831 It consists of two separate parts: an electromagnetic calorimeter (ECAL) followed by
832 a hadron calorimeter (HCAL), to identify electromagnetic and hadronic showers, respec-

tively. A preshower detector (PS) is located before the ECAL, in order to eliminate a large background of charged pions that could be misidentified as electrons. In front of the PS, a scintillator pad detector (SPD), used to select charged particles, is located. For all these parts a variable lateral segmentation is adopted, given that the hit density varies by two orders of magnitude over the calorimeter surface [55]. Because of the dimensions of the hadronic showers, the HCAL is segmented into two zones with larger cell sizes.

In all cases, the same principle of scintillation light transmitted to a Photo-Multiplier (PMT) (that turn this light into an electric signal) by wavelength-shifting (WLS) fibres is adopted. To have a constant transverse energy scale the gain in the ECAL and HCAL phototubes is set in proportion to their distance to the beampipe.

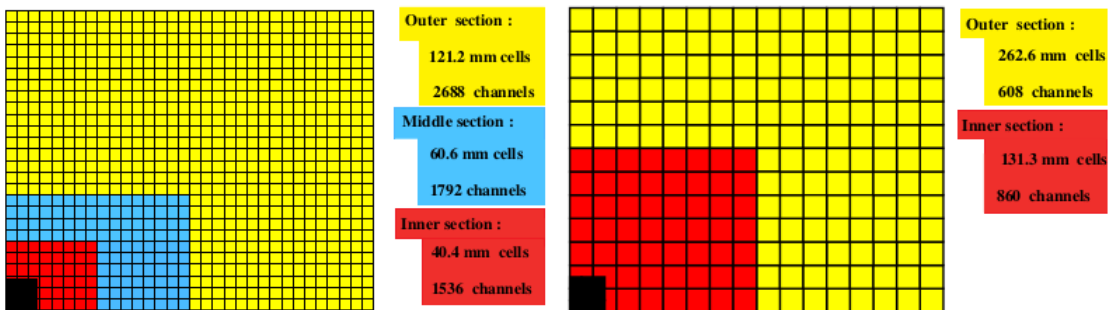


Figure 4.9: Lateral segmentation of the SPD/PS and ECAL (left) and the HCAL (right). One quarter of the detector front face is shown [55].

4.2.4.3 Muon System

The muon system provides fast information for the high- p_T muon trigger at the earliest level (L0) and muon identification for the high-level trigger (HLT) and offline analysis [55]. Given that muons are present in final states of the most relevant channels for LHCb, this is of crucial importance.

It is composed of five rectangular stations (M1-M5), located along the beam axis, with a total of 1380 chambers and 435m² of coverage. The inner and outer angular acceptances are 20(16) mrad and 306(258) mrad in the bending (non-bending) plane respectively [55]. All the stations are divided into 4 regions, R1-R4, with increasing distance from the beam axis. Their dimensions (scaling a factor two from one region to the next) and their geometry provide the same flux and channel occupancy for all of them. Multi-wire proportional chambers (MWPC) are used for all regions except the inner region of station M1, where triple-GEM detectors (consisting of three gas electron multipliers) are used.

Stations M2 to M5 are placed downstream the calorimeters, interleaved with three iron filters. They have a threshold of $\sim 6\text{GeV}/c$ for a muon to cross the five stations. Stations M1-M3 are used to define the track direction and to calculate the p_T of the candidate muon, due to their high spatial resolution along the bending plane. Stations M4 and M5 are focused on identifying penetrating particles. Station M1 is located in front of the

861 calorimeters. Its function is to improve the p_T measurement in the trigger. The geometry
 862 of all the stations is such that all their transverse dimensions scale with the distance from
 863 the interaction point.

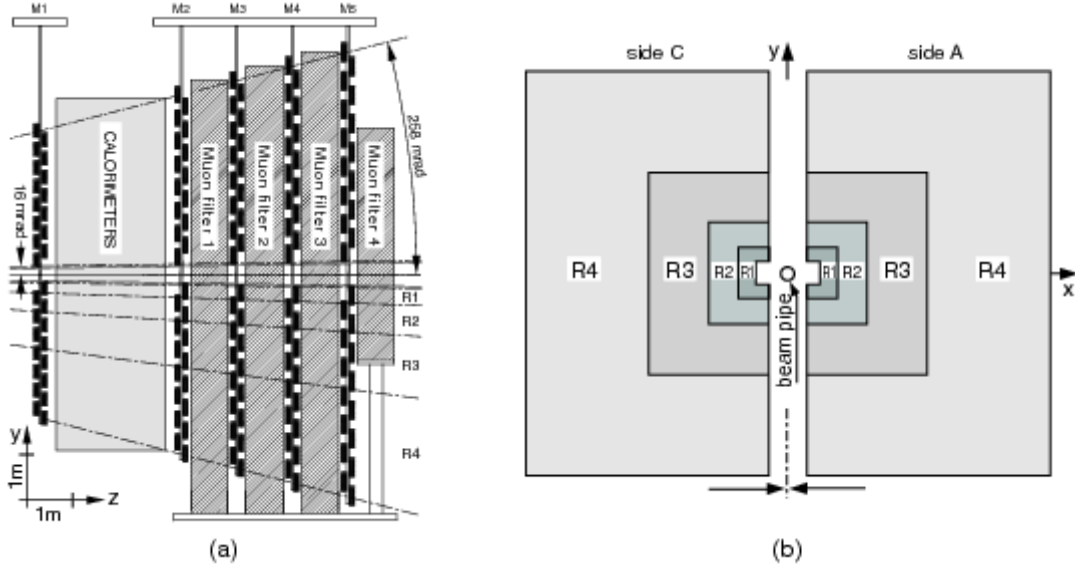


Figure 4.10: (a) Side view of the LHCb Muon Detector. (b) Station layout with the four regions R1-R4 [57].

864 4.2.5 Trigger

865 The LHCb trigger is one of the most important part of its infrastructure, as it allows for
 866 a reduction of the crossing frequency with interactions visible by the spectrometer from
 867 10MHz to about 2 - 5 kHz, at which rate the events are written to storage for further
 868 offline analysis [55]. It is composed by two levels: Level-0 (L0) and the High Level Trigger
 869 (HLT). Both parts are optimised to obtain the highest efficiency for the events selected
 870 in the offline analysis, while avoiding storage of as much background events as possible.

871 4.2.5.1 L0

872 The purpose of this first stage of the trigger is to reduce the LHC beam crossing rate
 873 of 40 MHz to 1MHz, with which the entire detector can be read out [55]. This is done
 874 reconstructing the highest E_T hadron, electron and photon clusters in the calorimeters,
 875 together with the the two highest p_T muons in the muon chambers, as B meson decay
 876 products are expected to have large p_T and E_T . A pile-up system in the VELO estimates
 877 the number of primary pp interactions in each bunch crossing. The calorimeters calculate
 878 the total observed energy and an estimate for the number of tracks, based on the number
 879 of hits in the SPD. With this, unwanted events are discarded.

880 It is composed by three parts, all connected to a different part of the LHCb, and all
881 connected to the L0 DU (see 4.11):

- 882 1. The pile-up system: its purpose is distinguishing crossings with single and multiple
883 visible interactions. For this, it uses four silicon sensors as the ones used in the
884 VELO, that measure the radial position of the tracks. It consists of two silicon
885 planes, situated upstream of the VELO and perpendicular to the beam-line, where
886 the radii of track hits are measured. From this, the position of the track origin on
887 the beam axis (the *vertex*) can be reconstructed.
- 888 2. The L0 calorimeter trigger: its goal is to look for high E_T electrons, photons, neutral
889 pions or hadrons. This is done forming clusters by adding the transverse energy of
890 2x2 cells and selecting the cluster with the highest E_T . This zone is large enough
891 to contain most of the energy, while avoiding overlapping among different particles.
892 Afterwards, such cluster is identified as one of the particle types using information
893 from the SPD, PS, ECAL and HCAL subdetectors.
- 894 3. The L0 muon trigger: in the muon chambers muons are reconstructed with a resolution
895 in p_T of $\sim 20\%$. The L0 muon trigger selects the two muons with the highest p_T
896 for each quadrant of the muon detector. The track finding is performed on the logical
897 pads, searching for hits defining a straight line through the five muon stations
898 and pointing towards the interaction point [55], also enabling the determination of
899 the p_T of the track.

900 Multiplicities are measured by the SPD cells.

901 A L0 Decision Unit (DU) collects all the information and derives the final L0 trigger
902 decision for each bunch crossing to the Readout Supervisor , allowing for overlapping of
903 several trigger conditions, as well as for prescaling. The Readout Supervisor is in charge
904 of the ultimate decision about whether to accept an event or not.

905 The L0 uses custom made electronics, fully synchronous with the 40 MHz bunch
906 crossing signal of the LHC. All L0 electronics uses fully custom-designed boards that use
907 parallelism and pipelining in order to speed up the process. The time passed between a
908 pp interaction and the arrival of the L0 trigger decision is of $4 \mu s$, that leaves $2 \mu s$ for data
909 processing in the L0.

910 4.2.5.2 HLT

911 The High Level Trigger (HLT) reduces the event rate from 1MHz down to 2 - 5 kHz,
912 making use of the full event data. The HLT selected events are then saved on permanent
913 storage. The algorithms that it uses refine candidates found by the L0 and divide them
914 into independent *alleys*, selected from the L0 decision, requiring the candidate tracks to be
915 reconstructed in the VELO and/or the T-tations. With this, the rate is reduced to about
916 30kHz, where it becomes interesting to take into account both inclusive and exclusive
917 criteria. It is further subdivided into HLT1 and HLT2, each with different purposes. The
918 overall flow of all the trigger steps can be seen in 4.12.

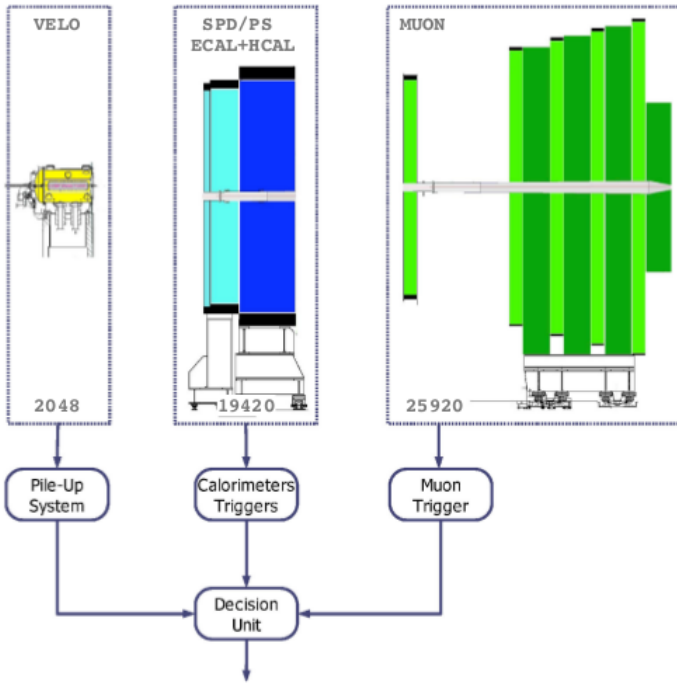


Figure 4.11: Overview of the L0 [55].

919 It consists of a C++ application that runs on over 2000 computing nodes, the Event
 920 Filter Farm (EFF). Even though it can access all data in one event, the purpose is to
 921 discard uninteresting event using part of the full event data. The cuts applied at this stage
 922 are generally very loose compared to the offline analysis, so as to be able to study the
 923 sensitivity of the selections and to profit from refinements due to improved calibration
 924 constants. In order to compute systematic uncertainties and trigger efficiencies, both
 925 levels can be fully emulated on stored data.

926 Both HLT1 and HLT2 summaries, containing the information of all tracks and vertexes
 927 that triggered events, are stored. This allows the study of the trigger performance, as well
 928 as of the trigger source of each event. Furthermore, in order to ensure the traceability of
 929 the trigger conditions in the off-line analysis, the combination of trigger algorithms with
 930 their selection parameters are pre-loaded in the EFF before a fill in a Trigger Configuration
 931 Key (TCK).

932 4.2.5.3 HLT1

933 The main goal of HLT1 is the so-called L0 confirmation, to reconstruct particle in the
 934 VELO and T-stations correspondence to the L0 objects, or for neutral particles to confirm
 935 de absence of a charged particle that could be associated to these same objects. Different
 936 reconstruction sequences (*alleys*) with different algorithms and selection cuts are applied
 937 according to the L0 candidate type. The events can pass by more than one alley, provided

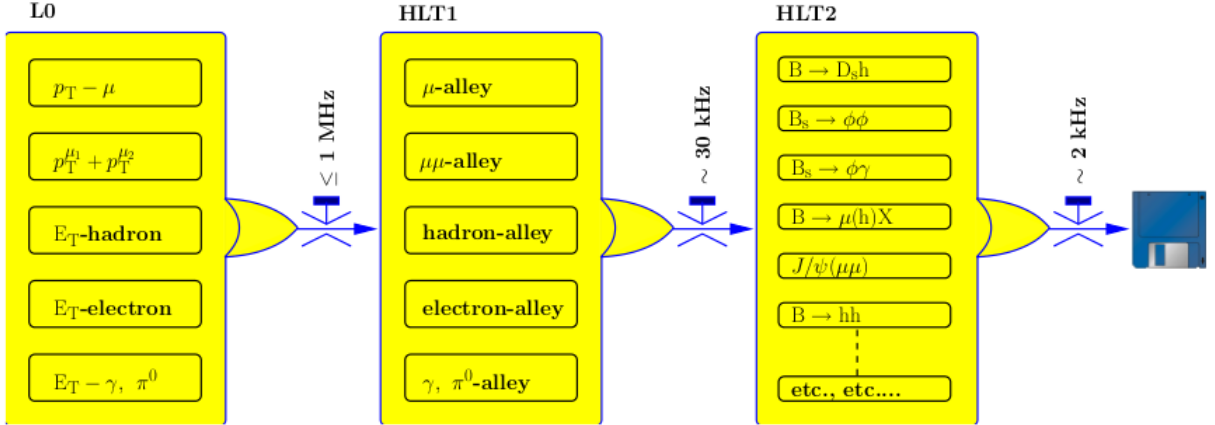


Figure 4.12: Flow-diagram of the different trigger sequences [55].

938 that they are selected by multiple triggers.

939 4.2.5.4 HLT2

940 At this stage of the trigger, a set of tracks is selected with very broad cuts on their
 941 momentum and impact parameter, and used to form composite particles. These are then
 942 used for all selections to avoid duplication in the creation of final states. The selections
 943 can be exclusive or inclusive, depending on whether the full final state is reconstructed
 944 or not. The inclusive triggers are less dependent on the on-line reconstruction, while the
 945 exclusive one produces a smaller rate, thus allowing for a more relaxed set of cuts.

946 4.2.6 Tracking and Vertexing performance

947 In the track reconstruction software the hits in the VELO, the TT, the IT and the OT
 948 detectors are combined to form particle trajectories from the VELO to the calorimeters,
 949 with the purpose of finding all tracks in the event which leave sufficient detector hits.
 950 Depending on the subdetectors used for the reconstruction, offline tracks are classified in
 951 the following categories (see 4.13):

- 952 • **Long tracks:** those that traverse the VELO, the TT and the T-stations, hence
 953 having the most precise momentum determination.
- 954 • **Upstream tracks:** those traversing only the VELO and TT stations. Generally,
 955 they have lower momentum and are bent out of the detector acceptance by the mag-
 956 netic field. Nevertheless, they pass through the RICH1 detector. Hence, they may
 957 generate Cherenkov photons, and can be used to understand backgrounds. Besides,
 958 they can also be used for flavour tagging, albeit their momentum resolution is poor.

- 959 • **Downstream tracks:** traversing only the TT and T stations. The most relevant
 960 cases are the decay products of K_S^0 and Λ that decay outside of the VELO accep-
 961 tance.
- 962 • **VELO tracks:** measured in the VELO only and typically with large angle, or
 963 backward tracks. They are useful for the primary vertex reconstruction.
- 964 • **T tracks:** the ones measured in the T stations, typically produced in secondary
 965 interactions, but useful for the global pattern recognition in RICH2.

966 For K_S^0 reconstruction, only long tracks and downstream tracks are used.

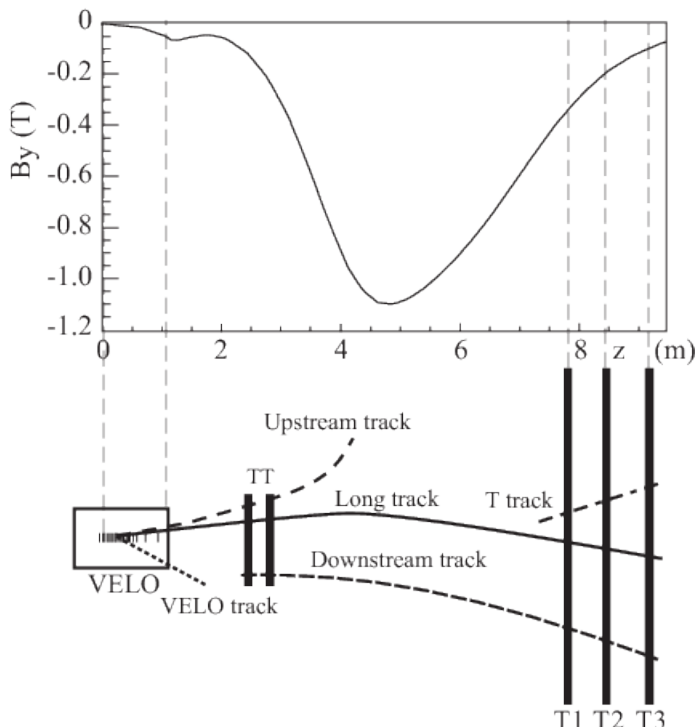


Figure 4.13: Schematic illustration of the various track types. For reference the main B -field component (B_y) os plotted above as a function of the z coordinate [56].

967 For the track reconstruction algorithm, track *seeds* are used as starting points. These
 968 are the initial track candidates in the VELO and T stations, where the magnetic field is
 969 low. Their trajectories are refitted using the Kalman filter [58], that accounts for multiple
 970 scattering and energy loss. The quality os such fitting is monitored using the χ^2 of the fit
 971 and the *pull* distribution for the different parameters.
 972 The pattern recognition performance is evaluated in terms of efficiencies and ghost
 973 rates. The efficiencies are the ratio of successfully reconstructed tracks over the total
 974 amount of reconstructible tracks. A track is considered reconstructible if it has a minimum

number of hits in the relevant subdetector, and *successfully reconstructed* if at least 70% of such hits originate from a single MonteCarlo (simulated) particle. Otherwise, it is considered a *ghost track*.

Figure 4.14 shows this efficiency as a function of two kinetic variables, namely the momentum, p , and the pseudorapidity, η , for 2011 and 2012. The performance in the 2012 data is slightly worse, which is partially due to the higher hit multiplicity at the higher centre-of-mass energy [56]. The average efficiency is above 96% for $5\text{GeV}/c < p < 200\text{GeV}/c$, $2 < \eta < 2$, thus covering the LHCb phase space.

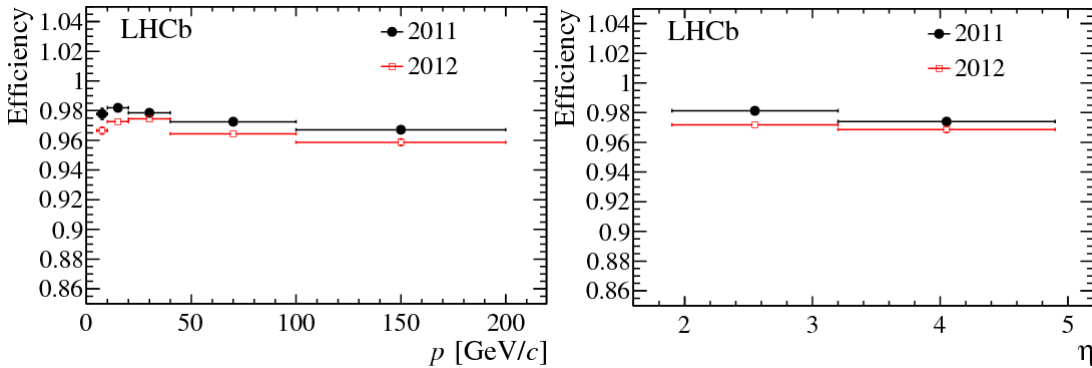


Figure 4.14: Tracking efficiency on muons from J/ψ as a function of momentum (left) and pseudorapidity (right). Black points correspond to 2011 data and red 2012 data [56].

As for the relative momentum resolution, as it is shown in 4.15 for two muons coming from a J/ψ , it is better (about 5 per mille) for low-momentum than for high-momentum (about 8 per mille) ranges. Hence, the best performances in terms of momentum resolution are achieved for long tracks, as said before.

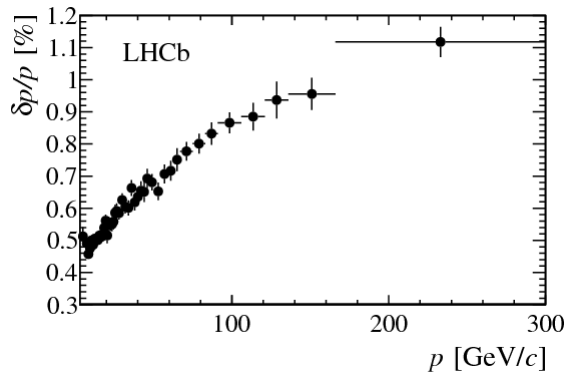


Figure 4.15: Relative momentum resolution versus momentum for long tracks in data obtained using J/ψ decays [56].

987 In order to assess the vertexing performance at LHCb, two main quantities are examined:
 988 the primary vertex (PV) resolution, and the impact parameter. The PV resolution
 989 is measured by comparing two independent measurements of the vertex position in the
 990 same event. This is achieved by randomly splitting the set of tracks in an event into two
 991 and reconstructing the PVs in both sets.

992 The impact parameter (IP) of a track is defined as its distance from the primary vertex
 993 at its point of closest approach to the primary vertex. Particles resulting from the decay
 994 of long lived B or D mesons tend to have larger IP than those of particles produced at
 995 the primary vertex. Selections on IP and the IP χ^2 are extensively used in LHCb analyses
 996 to reduce the contamination from prompt backgrounds. Consequently, an optimal IP
 997 resolution and a good understanding of the effects contributing to the IP resolution are
 998 of prime importance to LHCb performance [56].

999 The IP resolution is governed by three main factors: multiple scattering of particles
 1000 by the detector material; the resolution on the position of hits in the detector from which
 1001 tracks are reconstructed; and the distance of extrapolation of a track between its first hit
 1002 in the detector and the interaction point. The minimisation of these factors is achieved
 1003 in the design of the VELO [56].

1004 The left part of figure 4.16 shows the PV resolution in the x and y direction as a
 1005 function of the number of tracks. It can be seen that in both cases it improves with
 1006 the number of tracks. The right part shows the IP resolution in the x direction as a
 1007 function of the inverse of the transverse momentum. Very good resolution is achieved in
 1008 the VELO, thanks to the silicon strips.

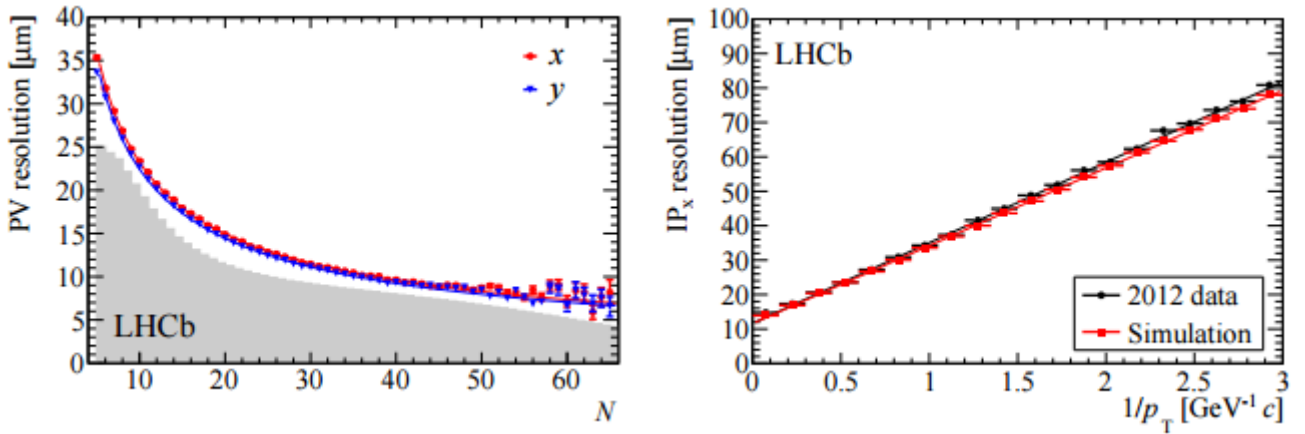


Figure 4.16: The primary vertex resolution (left), for events with one reconstructed primary vertex, as a function of track multiplicity. The x (red) and y (blue) resolutions are separately shown and the superimposed histogram shows the distribution of number of tracks per reconstructed primary vertex for all events that pass the high level trigger. The impact parameter in x resolution as a function of $1/p_T$ (right). Both plots are made using data collected in 2012. [56].

1009 4.2.7 PID performance

1010 As explained in ??, particle identification at LHCb is performed in 4 different subdetectors.
 1011 Each one of them gives a different performance that is then further combined into an
 1012 overall PID performance.

1013 For the calorimeters the main role is to distinguish photons, electrons and neutral
 1014 pions. Electrons are differentiated from photons and π^0 in the fact that they have a track
 1015 associated before the energetic deposit in the calorimeter, as they are charged particles.
 1016 Their associated likelihood is estimated using information from the ECAL, the PS and
 1017 the HCAL. In order to separate photons from π^0 , a neural network classifier is used,
 1018 trained with samples as pure as possible. Non-converted photons are identified using a
 1019 photon hypothesis likelihood, employing variables from the different subdetectors (PS and
 1020 ECAL).

1021 Both for photons and for electrons, the PID performance is assessed using the log-
 1022 likelihood difference between the signal hypothesis (photon or electron) versus the back-
 1023 ground one (hadrons for electrons). In the case of the electrons, this log-likelihood is
 1024 computed as the sum of log likelihoods:

$$\Delta \log \mathcal{L}^{\text{CALO}}(e - h) = \Delta \log \mathcal{L}^{\text{ECAL}}(e - h) + \Delta \log \mathcal{L}^{\text{HCAL}}(e - h) + \Delta \log \mathcal{L}^{\text{PS}}(e - h) \quad (4.1)$$

1025 This is shown in 4.17, for different cuts. As expected, the higher momenta particles
 have higher misidentification rates.

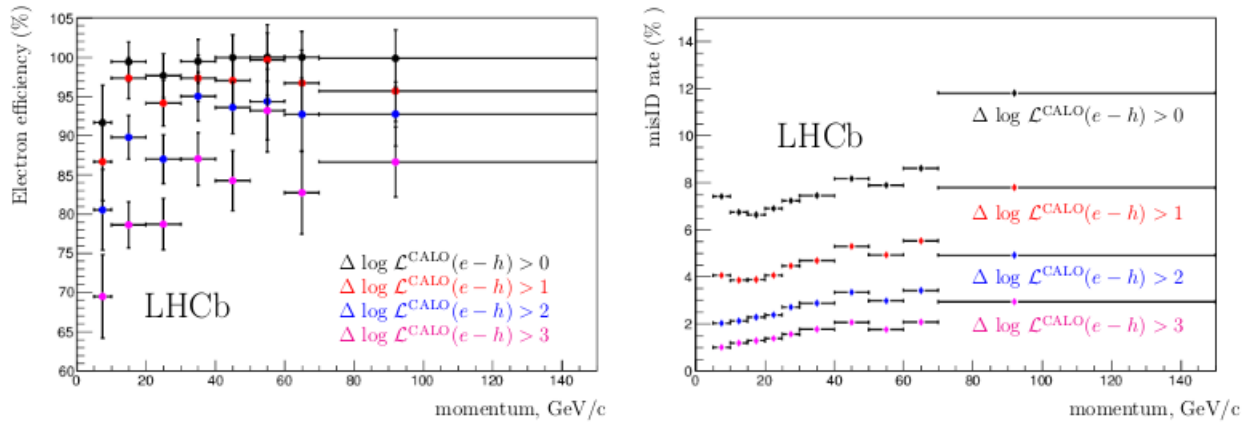


Figure 4.17: Electron identification performances for various $\Delta \log \mathcal{L}^{\text{CALO}}(e - h)$ cut: electron efficiency (left) and misidentification rate (right) as functions of the track momentum [56].

1026
 1027 As for the RICH, its mission is to distinguish charged hadrons (π, K, p). The informa-
 1028 tion thus obtained is used at the final analysis level and as part of the software level of
 1029 the trigger. Complementary information on charged leptons can also be provided by the
 1030 RICH. Its performance is evaluated using two variables:

1031 • The Cherenkov angle resolution, $\theta(\sigma_C)$, defined as the resolution of the Cherenkov
1032 angle with which the emitted photons can be reconstructed.

1033 • The photoelectron yield, defined as the average number of detected photons for each
1034 track traversing the Cherenkov radiator media.

1035 Because of the high average track multiplicity in LHCb events, a reconstructed
1036 Cherenkov ring will generally overlap with several neighbouring rings. Figure 4.18 shows
1037 the Cherenkov angle as a function of particle momentum using information from the ra-
1038 ditor for isolated tracks selected in data. As expected, different bands represent different
1039 masses, hence different particles.

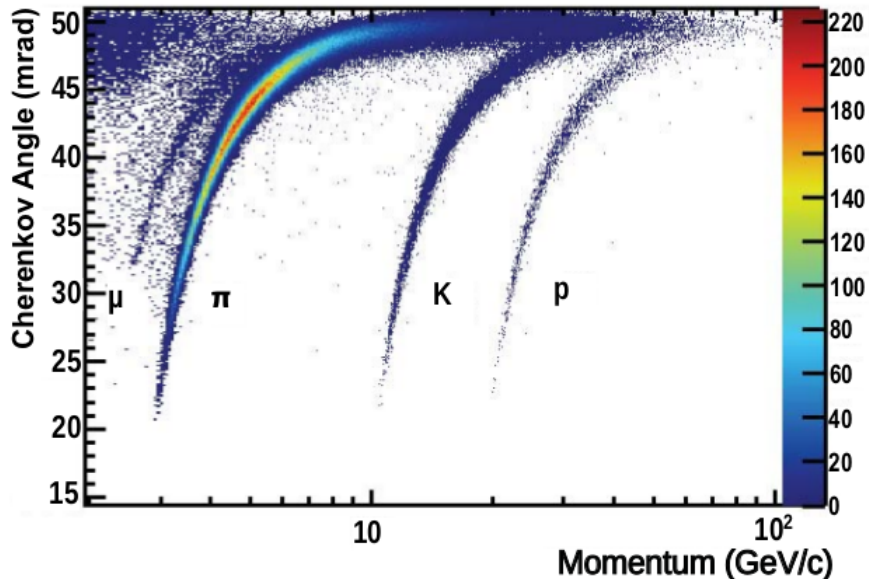


Figure 4.18: Reconstructed Cherenkov angle for *isolated* tracks, as a function of track momentum in the radiator. The Cherenkov bands for muons, pions, kaons and protons are clearly visible [56].

1040 Figure 4.19 shows the kaon efficiency (kaons identified as kaons) and pion misidentifi-
1041 cation (pions misidentified as kaons) fraction achieved in LHCb data and simulation, as a
1042 function of momentum. The results are shown both optimising efficiency and minimising
1043 misidentification rate.

1044 Finally, muons are identified in the muon system. The algorithm is based on the
1045 association of hits around its extrapolated trajectory. In this case, the logarithm of the
1046 ratio between the muon and non-muon (protons, pions and kaons) hypothesis, $\Delta \log \mathcal{L}(\mu)$
1047 is used as discriminating variable. Figure 4.20 shows, as a function of the track momentum
1048 and for different ranges of transverse momentum, the efficiency of the muon candidate
1049 selection, and the probabilities of incorrect identification of protons, pions and kaons as
1050 muons.

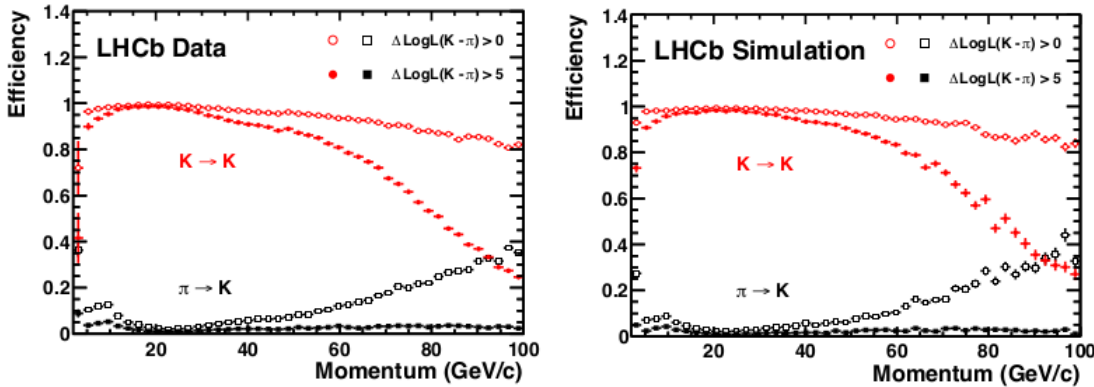


Figure 4.19: Kaon identification efficiency and pion misidentification rate as measured using data (left) and from simulation (right) as a function of track momentum [56]improve.

1051 The combined performance of the different PID subdetectors can be either be com-
 1052 puted as a sum of the different likelihoods, or using multivariate techniques to get a single
 1053 probability value for each particle hypothesis with different informations corresponding to
 1054 each sub-system.

1055 4.2.8 Trigger performance

1056 As discussed in 4.2.5, the LHCb trigger is composed of two parts, in order to reduce the
 1057 input rate to an output rate of 2 -5 kHz. The performance of each part is assessed using
 1058 a data-driven technique with representative samples, to account for inefficiencies due to
 1059 the simplified reconstruction algorithm, possible misalignments and reduced resolution.

1060 In the trigger system, an event is considered to be *Trigger on Signal (TOS)* if the
 1061 trigger objects that are associated with the signal candidate are sufficient to trigger the
 1062 event. On the contrary, if the event has been triggered by trigger objects not associated
 1063 with the signal, it is considered *Trigger Independet of Signal (TIS)*. Notice that events
 1064 can be both TIS and TOS. The TIS and TOS efficiencies are defined as follows:

$$\epsilon^{\text{TIS(TOS)}} = N^{\text{TIS&TOS}} / N^{\text{TOS(TIS)}} \quad (4.2)$$

1065 4.2.8.1 L0 hardware trigger

1066 The L0 trigger consists of three independent nits:

- 1067 • The L0-Calorimeter trigger, that uses information from the SPD, PS, ECAL and
 1068 HCAL to compute E_T that particles deposit in clusters of 2x2 cells. From this, a
 1069 candidate can be L0Hadron, LOPhoton or LOElectron.
- 1070 • The L0-Muon trigger, that looks for the two highest p_T muon tracks in each quad-
 1071 rant, with thresholds on the p_T^{largest} and $p_T^{\text{largest}} \times p_T^{\text{2ndlargest}}$.

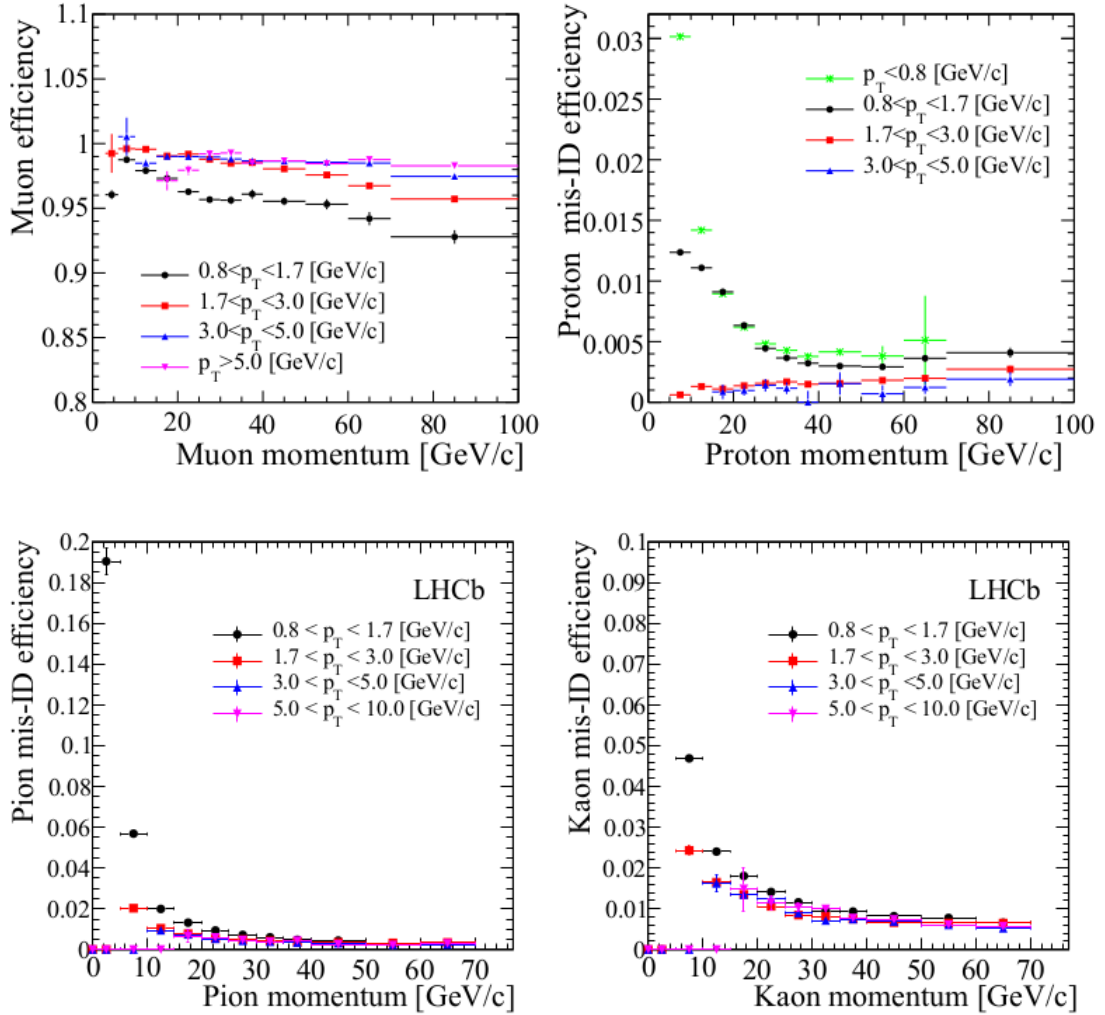


Figure 4.20: Top left: efficiency of the muon candidate selection based on the matching of hits in the muon system to track extrapolation, as a function of momentum for different p_T ranges. Other panels: misidentification probability of protons (top right), pions (bottom left), and kaons (bottom right) as muon candidate as a function of momentum, for different p_T ranges [56].

1072

- The L0-PileUp trigger, used for the computation of the luminosity.

1073

Figure 4.21 shows the L0 hadron efficiency for the representative channels. As expected, it increases with the transverse momentum.

1075

4.2.8.2 High Level Trigger

1076

The HLT has a variety of so-called trigger "lines" that consist of selection parameters for specific classes of events. In HLT1, a partial event reconstruction is performed, while in

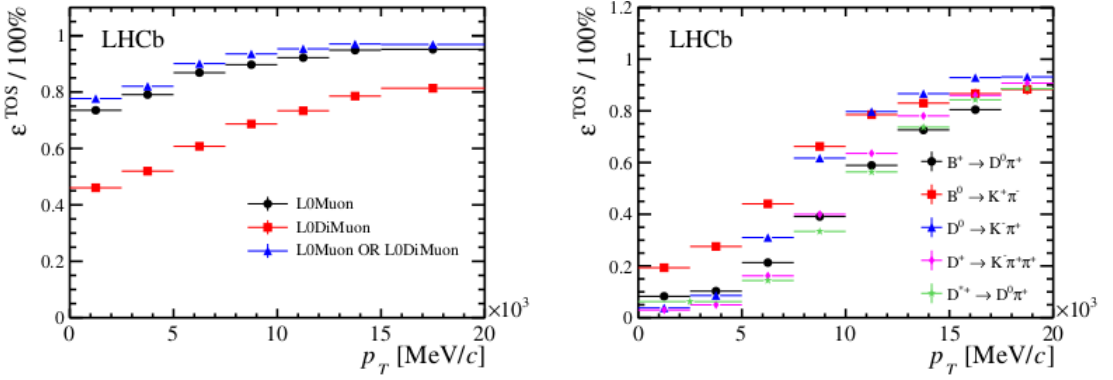


Figure 4.21: (left) L0 muon trigger performance: TOS trigger efficiency for selected $B^+ \rightarrow J/\psi K^+$ candidates. (right) L0 hadron trigger performance: TOS trigger efficiency for different beauty and charm decay modes. [56].

1078 HLT2 the complete event is reconstructed.

1079 In the first level (HLT1), vertices are reconstructed from a minimum of five intersecting
 1080 VELO tracks. Vertices within a radius of $300 \mu\text{m}$ of the mean position of the pp-interaction
 1081 envelope are considered to be primary vertices. During Run 1, the forward track search
 1082 had a minimum momentum requirement that varied between 3 and 6 GeV/c. Dimuon
 1083 candidates are either selected based on their mass without any displacement requirement,
 1084 or based on their displacement without the mass restriction []. The performance of HLT1
 1085 on muonic signatures as a function of p_T of the B^+ parent is shown in 4.22.

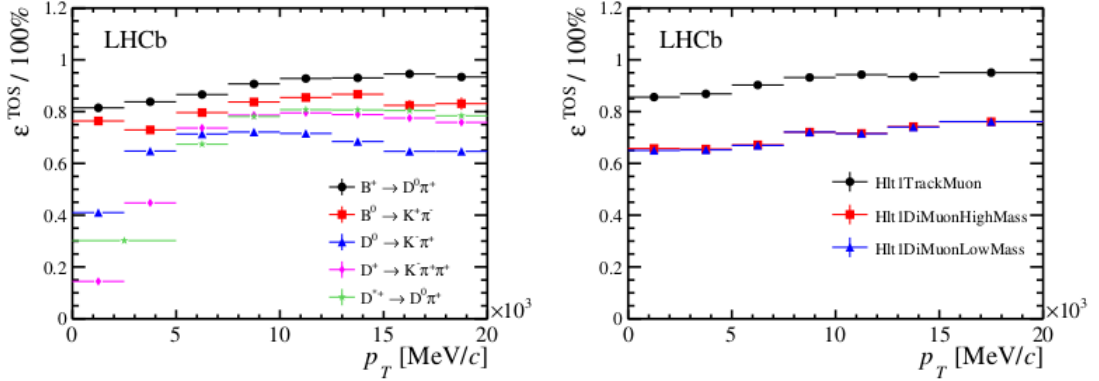


Figure 4.22: HLT1 inclusive track trigger performance: TOS efficiency for various channels as a function of B or D p_T (left) . HLT1 muon trigger performance : TOS efficiency for $B^+ \rightarrow J/\psi K^+$ [56].

1086 In the second level (HLT2), long tracks are searched based on VELO seeds, thus
 1087 simplifying the offline tracking algorithm (because of CPU restrictions). There is a generic
 1088 beauty trigger, for any partially reconstructed b -hadron decay, muon triggers, for decays

1089 with one or two muons, charm triggers and other exclusive and technical lines. Figure
 1090 4.23 shows the performance of the J/ψ triggers.

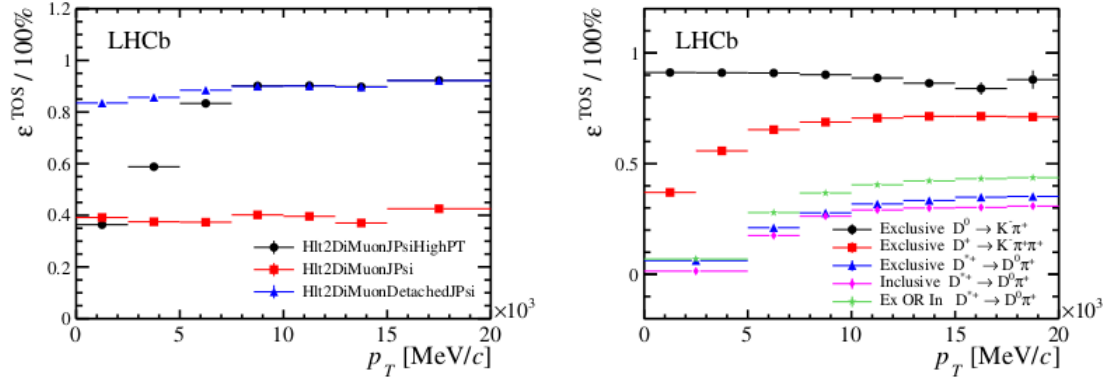


Figure 4.23: HLT2 muon trigger performance for the J/ψ trigger lines (left). HLT2 charm trigger performance for inclusive and exclusive selections (right). [56].

1091 4.2.9 The LHCb Upgrade

1092 The LHCb detector has proven to be an outstanding general-purpose detector in the for-
 1093 ward pseudorapidity region. Nevertheless, some of the measurements are still statistically
 1094 limited. Therefore, in order to fully exploit the potential of LHCb, an increase in the
 1095 luminosity is required. This leads to the need of upgrading some of the subdetectors,
 1096 since the upgraded detector is expected to collect 50 fb^{-1} during 5 years of data-taking,
 1097 with a 40 MHz readout (Phase-I of the Upgrade).

1098 For the sake of this thesis, the changes made during the LHCb Upgrade will greatly
 1099 benefit the sensitivity to rare strange decays, as the trigger limitation will disappear. Also,
 1100 a significant improvement in the ϕ_s measurement is expected. Prospects for the golden
 1101 modes on these fields can be seen in 4.24.

1102 4.2.9.1 Trigger Upgrade

1103 The main change that the LHCb trigger will undergo is the replacement of the L0 stage
 1104 by a software one, the so-called *Low Level Trigger* (LLT), modified to run within the new
 1105 readout architecture. It selects events containing clusters with high transverse energy in
 1106 the calorimeters or tracks with high transverse momentum in the muon detector. A much
 1107 larger LLT rate will be allowed, leading to a much larger rate to storage. Hence, the main
 1108 limits will be processing power and bandwidth. The front-end electronics will be upgraded
 1109 as well to allow reading events at the LHC clock rate. More details can be found in [60].

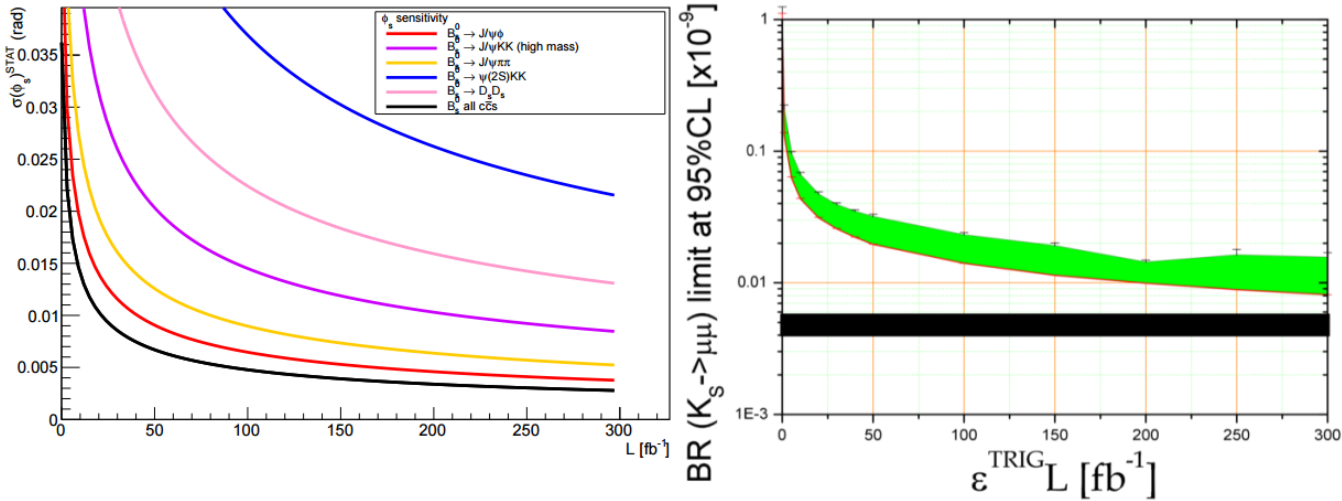


Figure 4.24: Left: expected sensitivity for ϕ_s as a function of the luminosity ref. Right: Expected limit in $\mathcal{B}(K_S^0 \rightarrow \mu^+ \mu^-)$ from LHCb and upgrades, as a function of integrated luminosity times trigger efficiency [59].

1110 4.2.9.2 VELO Upgrade

1111 The LHCb upgrade requires the VELO to have an excellent vertex resolution and two
 1112 track separation, with fast pattern recognition capabilities. Moreover, because of the high
 1113 luminosity, it has to have a sufficient radiation hardness to guarantee the performance
 1114 throughout all the data-taking period. Besides, the upgraded trigger discussed before
 1115 strongly relies on this subdetector.

1116 In order to cope with these requirements, two alternatives were proposed:

- 1117 • A fine-pitched silicon strip detector, similar to the current design, with improved
 1118 cooling and a new ASIC.
- 1119 • A hybrid pixel detector, called *VeloPix*, that uses the Timepix chip [61].

1120 Being the latter the one chosen for the Upgrade. The layout of the upgraded VELO can
 1121 be seen in 4.25.

1122 4.2.9.3 PID Upgrade

1123 As discussed before, the PID performance is crucial for the LHCb physics programme.
 1124 Thus, its upgrade becomes of great importance.

1125 The overall structure of the RICH will remain unchanged. In RICH1, the aerogel will
 1126 be removed, as the efficiency gained by its removal outweighs the improvement on the PID
 1127 provided by it. The HPDs will be replaced by commercial multianode photomultipliers
 1128 (MaPMTs), with external readout electronics. Alternatively a lens system may be used
 1129 there, to re-focus the Cherenkov images onto the 1-inch tubes and thus reduce the number

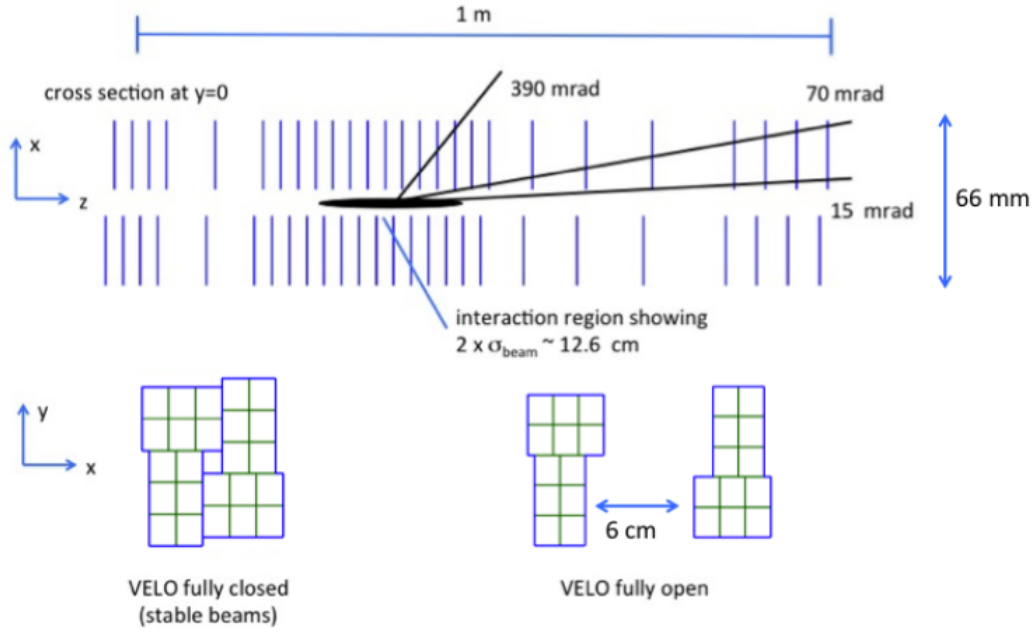


Figure 4.25: Schematic layout of the upgraded VELO.

of tubes required. A new subdetector, still under development, is being considered in order to recover the low momentum particle identification performance. It consists in a time-of-flight system, Time Of internally Reflected Cherenkov Light, TORCH.

As for the calorimeter, the electronics will be upgraded according to the new requirements. Also the PMTs gains will be reduced (and compensated by a gain increase in the electronics) to ensure a longer lifetime. Regarding the radiation hardness, studies have found the calorimeter resistant enough, even though some of the elements (such as the cells in the inner region of the ECAL) will need replacing in the long-term scale. Both the SOD and the PS will be removed, as they mainly contribute to the L0 trigger.

Finally, the muon system will have its first station removed, and additional shielding around the beam pipe in front of station M2. Similarly to the calorimeter, the electronics will be modified to comply with the new conditions.

4.2.9.4 Tracking Upgrade

The TT stations will be replaced by a tracking detector composed of new, high-granularity silicon micro-strip planes with an improved coverage of the LHCb acceptance, the *Upstream Tracker* (UT). Behind the magnet, a *Scintillating Fibre Tracker* (SFT) will be built, which is composed of 2.5m long fibres read out by silicon photomultipliers at the edge of the acceptance, replacing the current OT and IT stations. Both new subdetectors can be seen in 4.26.

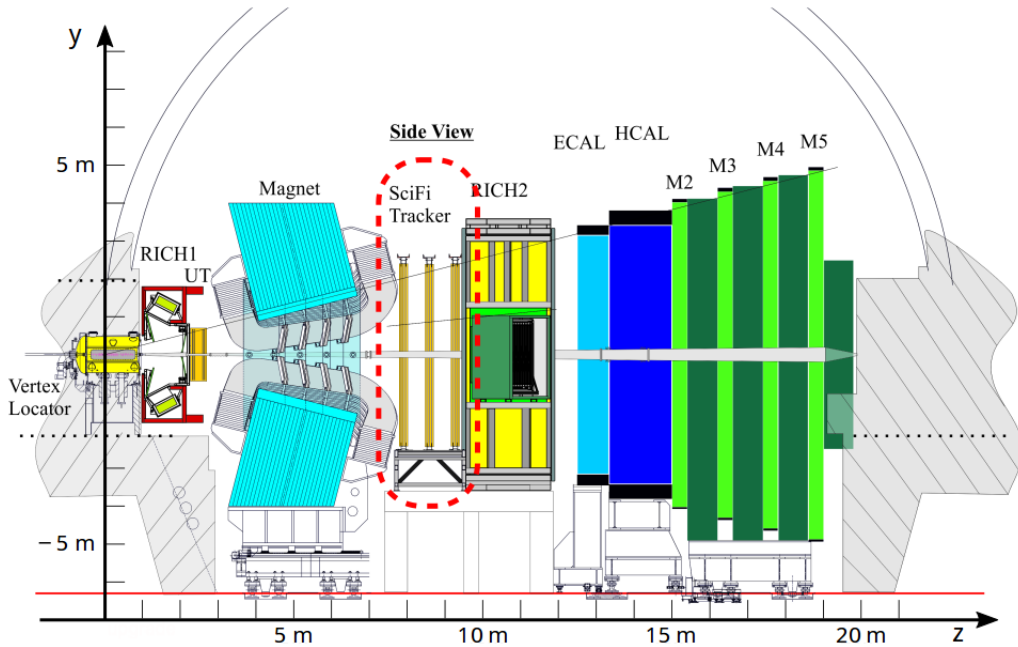


Figure 4.26: Side view of the upgraded LHCb.

1149 4.2.10 Analysis workflow

1150 Raw data from collisions is taken at LHCb at a rate of several million events per second.
1151 A fast, efficient treatment and distribution of such data is thus needed to perform an
1152 offline analysis of a given decay channel. For this, C++ tools and algorithms embedded
1153 inside the Gaudi [62] project are used. The steps that are followed, together with their
1154 correspondance to the different projects inside such framework, are summarised below.

- 1155 1. As explained in 4.2.5, 4.2.8, a first loose selection is applied to the recorded data
1156 with the trigger. The trigger algorithms constitute what is known as the Moore
1157 project [63].
- 1158 2. After data is recorded, it is necessary to convert the electronic signals to track and
1159 vertices. This was discussed in 4.2.3 and 4.2.6. Particle identification (4.2.4, 4.2.7)
1160 is also required to properly assign each of these variables to a given type of particle.
1161 This whole process is called *reconstruction*, and the group of C ++ LHCb libraries
1162 which contain the relevant tools, Brunel [64]. Proper knowledge alignment of each
1163 subdetector is also of great importance at this stage, for which tools under the
1164 Alignment project [65] exist.
- 1165 3. Once all triggered events have been reconstructed, a process is necessary to properly
1166 separate them offline according to their physics content. Such process, called *strip-
1167 ping*, consists on a splitting procedure that selects the different decays according to
1168 their specific features (final state, PV, mother particle, etc.). Each of the selection

1169 criteria are contained in a *stripping line*. The LHCb libraries that take part of this
1170 stage are DaVinci [66] and Erasmus [67].

1171 4. In order to allow the access to the data, while keeping a backup of it, a distributed
1172 system, *Grid* [68] is used by LHCb. Both stripped events and raw data are stored, so
1173 as to have the possibility of performing re-stripping and re-reconstruction if needed.
1174 Such system is of great computational power, and its spread in computing centers
1175 worldwide.

1176 5. Finally, to properly understand the effects from the detector and the steps before on
1177 data, simulation is used. Another important reason for which simulation is crucial
1178 is the need of training analysis tool on well-known states. Simulated Monte Carlo
1179 events (MC) are employed for this, mimicking as much as possible the data. The
1180 C++ libraries at LHCb dedicated to the MC production are contained in Gauss [69],
1181 which is a collection of libraries for physics simulation based on Gaudi and with
1182 specialised algorithms and tools for generators (PYTHIA [70], EvtGen [71] ...) and
1183 detector simulation (Geant4 [72]). The MC events can be further classified as
1184 follows:

- 1185 • Minimum Bias: keep all events generated by PYTHIA: elastic, diffractive,
1186 inelastic.
- 1187 • Inclusive: extract events generated by PYTHIA with at least one b or c hadron
1188 in 400 mrad with respect to the LHCb z axis. If all of these hadrons have
1189 $p_z < 0$, flip the whole event.
- 1190 • Signal: extract events generated by PYTHIA containing at least one specific
1191 particle in 400 mrad. Again, if the candidate has $p_z < 0$, flip the whole event.
1192 In the case of b hadrons and to speed up the generation, if the interaction
1193 contains the b , repeat the hadronisation process of PYTHIA until the interaction
1194 contains the correct particle.

1195 schematic view?

¹¹⁹⁶ Chapter 5

¹¹⁹⁷ $\Delta F=2$

¹¹⁹⁸ 5.1 Introduction

¹¹⁹⁹ The meson-antimeson oscillations are described by the mixing amplitudes [73]

$$M_{12}^{(M)} \equiv \langle M | \mathcal{H}_{\text{eff}}^{\Delta F=2} | \bar{M} \rangle \quad M = K^0, B_{d,s} \quad (5.1)$$

¹²⁰⁰ Where $\mathcal{H}_{\text{eff}}^{\Delta F=2}$ is the *effective* Jamiltonian. Within the MSSM, it has the form:

$$\mathcal{H}_{\text{eff}}^{\Delta F=2} = \sum_{i=1}^5 C_i Q_i + \sum_{i=1}^3 \tilde{C}_i \tilde{Q}_i + \text{h.c.} \quad (5.2)$$

¹²⁰¹ with the operators Q_i given, in the case of B_s mixing, by:

$$\begin{aligned} Q_1 &= (\bar{s}^\alpha \gamma_\mu P_L b^\alpha)(\bar{s}^\beta \gamma^\mu P_L b^\beta) \\ Q_2 &= (\bar{s}^\alpha P_L b^\alpha)(\bar{s}^\beta P_L b^\beta) \\ Q_3 &= (\bar{s}^\alpha P_L b^\beta)(\bar{s}^\beta P_L b^\alpha) \\ Q_4 &= (\bar{s}^\alpha P_L b^\alpha)(\bar{s}^\beta P_R b^\beta) \\ Q_5 &= (\bar{s}^\alpha P_L b^\beta)(\bar{s}^\beta P_R b^\alpha) \end{aligned} \quad (5.3)$$

¹²⁰² where $P_{R,L} = \frac{1}{2}(1 \pm \gamma_5)$ and α, β are colour indices. The operators $\tilde{Q}_{1,2,3}$ are obtained from ¹²⁰³ $Q_{1,2,3}$ by the replacement $L \leftrightarrow R$ [73]. In the case of B_d , the replacement $s \rightarrow d$ needs to ¹²⁰⁴ be done in equation 5.3. Several representative observables can be extracted from these ¹²⁰⁵ amplitudes, such as the mixing phase and the oscillation frequency asl?:

$$\phi_s = \arg(M_{12}), \quad \Delta m_s = |M_{12}| \quad (5.4)$$

¹²⁰⁶ Note that their value strongly depends on NP contributions:

$$M_{12} = M_{12}^{SM} + M_{12}^{NP} \quad (5.5)$$

¹²⁰⁷ The experimental search of the weak mixing angle is discussed in detail in 5.2. Theoretical ¹²⁰⁸ interpretations of this result are reviewed in 5.3, and a MultiNest scan [74] is presented ¹²⁰⁹ in 5.4.

1210 **5.2 ϕ_s experimental**

1211 In the SM, CP -violation originates from a single-phase in the Cabibbo-Kobayashi-
 1212 Maskawa (CKM) quark-mixing matrix [75], as explained in state? REF. There are 3
 1213 different kinds of CP -violation for neutral mesons, e.g. B_s^0 and \bar{B}_s^0 :

- 1214 1. Direct CP -violation: originated by a difference in the amplitudes associated to the
 1215 direct decay of the B_s^0 and \bar{B}_s^0 mesons into the same final state
- 1216 2. CP -violation in the $B_s^0 - \bar{B}_s^0$ oscillation, that arises when the oscillation from B_s^0 to
 1217 \bar{B}_s^0 is different from the oscillation from \bar{B}_s^0 to B_s^0
- 1218 3. CP -violation in the interference between the amplitudes associated to the direct
 1219 decay of a B_s^0 meson into a CP -eigenstate final state and those associated to the
 1220 decay after $B_s^0 - \bar{B}_s^0$ oscillation

1221 This last type of CP -violation is characterized by the CP -violating phase, ϕ_s , defined as:

$$\phi_s^f = -\arg(\lambda_f), \quad \lambda_f = \eta_f \frac{q}{p} \frac{\bar{\mathcal{A}}_f}{\mathcal{A}_f}, \quad (5.6)$$

1222 where f is the final state, η_f is 1(-1) for CP-even(CP-odd) states, $\left| \frac{q}{p} \right|$ determines the
 1223 amount of CP -violation in mixing, and $\mathcal{A}_f(\bar{\mathcal{A}}_f)$ is the amplitude of the $B_s^0(\bar{B}_s^0)$ meson
 1224 decaying into a given final state, f . Precision measurements of this phase are needed in
 1225 order to properly disentangle SM and NP contributions.

1226 In the SM, for $b \rightarrow c\bar{c}s$ transitions and ignoring subleading penguin contributions, this
 1227 phase is predicted to be $-2\beta_s$, where $\beta_s = \arg[-(V_{ts}V_{tb}^*)/(V_{cs}V_{cb}^*)]$ and V_{ij} are elements of
 1228 the CKM quark flavour mixing matrix [?]. The indirect determination via global fits to
 1229 experimental data gives $2\beta_s = 0.0364 \pm 0.0016$ rad ref. This precise indirect determination
 1230 within the SM makes the measurement of ϕ_s interesting since new physics (NP) processes
 1231 could modify the phase if new particles were to contribute to the $B_s^0 - \bar{B}_s^0$ box diagrams [?,
 1232 ?].

The situation after including all Run 1 results from LHCb, and all results from ATLAS,
 CMS, CDF and D0 is shown in Figure 5.1. Current preliminary world averages (and their
 correlations) for the CP violating phase ϕ_s and the decay width difference in the B_s^0
 system, $\Delta\Gamma_s$, are:

$$\begin{aligned} \phi_s &= -0.021 \pm 0.031 \text{ rad} \\ \Delta\Gamma_s &= 0.085 \pm 0.006 \text{ ps}^{-1} \\ \rho(\phi_s, \Delta\Gamma_s) &= -0.0095 \end{aligned}$$

1233 The aim of this analysis is to perform the measurement of ϕ_s in the $B_s^0 \rightarrow J/\psi K^+ K^-$
 1234 channel by adding a further 2fb^{-1} of integrated luminosity collected at 13 TeV in Run 2 of
 1235 LHC in 2015 and 2016. In addition, updated measurements of the decay width difference
 1236 of the light (L) and heavy (H) B_s^0 mass eigenstates, $\Delta\Gamma_s \equiv \Gamma_L - \Gamma_H$, and the ratio between
 1237 the average widths in the B_s^0 and in the B_d^0 systems, Γ_s/Γ_d .

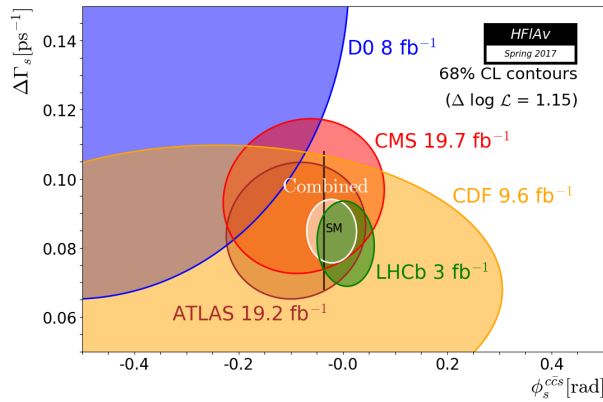


Figure 5.1: Individual 68% confidence-level contours of ATLAS, CMS, CDF, D0 and LHCb in the $(\phi_s^{c\bar{c}s}, \Delta\Gamma_s)$, their combined contour (solid line and shaded area), as well as the SM predictions (thick black rectangle) as performed by the HFLAV [?] averaging group.

1238 5.2.1 Phenomenology

1239 The baseline fit is obtained assuming that direct CP violation caused by penguin diagrams
 1240 is the same for all polarization states, therefore λ_f is considered to be independent of the
 1241 polarization state, f . Checks were made to check this ansatz.

The theoretical differential decay rate for an initial B_s^0 as a function of decay time and angles using polarization dependent $\lambda_f = |\lambda_f|e^{-i\phi_f} \equiv |\lambda_f|e^{-i\phi_f}$ ($f = 0, ||, \perp, S$) is given as [?]

$$\frac{d^4\Gamma(t)}{dm_{KK}^2 d\cos\theta_K d\cos\theta_l d\phi} = \sum_{k=1}^{10} N_k h_k(t) f_k(\theta_K, \theta_l, \phi), \quad (5.7)$$

where the decay-time-dependent functions $h_k(t)$ are given as

$$h_k(t) = \frac{3}{4\pi} e^{-\Gamma t} \left\{ a_k \cosh \frac{\Delta\Gamma t}{2} + b_k \sinh \frac{\Delta\Gamma t}{2} + c_k \cos(\Delta m t) + d_k \sin(\Delta m t) \right\}. \quad (5.8)$$

1242 For an initial \bar{B}_s^0 at production, the signs of c_k and d_k should be reversed. [appendix with](#)
 1243 [coefficients?](#) For the purpose of reducing correlation between fit parameters, it can be
 1244 chosen to fit for $|\lambda_0|$, ϕ_0 and $|\frac{\lambda_f}{\lambda_0}|$, $\phi_f - \phi_0$, for $f \neq 0$.

1245 5.2.2 Samples and event selection

1246 In this section, the data and simulated samples used in this analysis are introduced,
 1247 together with the trigger, stripping and offline selections applied to these samples.

1248 **5.2.2.1 Data sample**

1249 The analysis presented in this report uses a data sample collected at the LHCb experiment
 1250 at the LHC. The dataset corresponded to a total integrated luminosity $\int \mathcal{L} 1.9 \text{fb}^{-1}$. Of
 1251 this, 0.3fb^{-1} were taken in 2015 at a centre-of-mass energy $\sqrt{s} = 13 \text{TeV}$ and 1.6fb^{-1} were
 1252 taken in 2016 at $\sqrt{s} = 13 \text{TeV}$.

1253 Stripping version 26 was used for 2016 data and stripping version 24 was used
 1254 for 2015 data. All stripping versions use exactly the same selection, based on
 1255 the `StrippingBetaSBs2JpsiPhiDetached` `StrippingBetaSBd2JpsiKstDetached` and
 1256 `StrippingBetaSBu2JpsiKDetached` lines in the DIMUON stream. The data samples
 1257 were processed using `DaVinci` version v42r1 and momentum scaling has been applied.

1258 **5.2.2.2 Simulation samples**

1259 In the LHCb simulation, pp collisions are generated using `Pythia` with a specific LHCb
 1260 configuration [?, ?].

Table 5.1: MC samples used in the analysis. SX X indicates the stripping version that
 is used to flag the events. DecProdCut means that all the daughters are required to be
 within LHCb acceptance.

| Event type | Decay mode | Options | Year | Events |
|-----------------|--|--------------------------------|------|--------|
| Signal modes | | | | |
| 13144004 | $B_s^0 \rightarrow J/\psi \phi$ | Update2012,dG=0,DecProdCut,S26 | 2016 | 25M |
| 13144011 | $B_s^0 \rightarrow J/\psi \phi$ | Update2016,DecProdCut,S26 | 2016 | 20M |
| 13144011 | $B_s^0 \rightarrow J/\psi \phi$ | Update2012,DecProdCut,S28 | 2016 | 10M |
| 13144011 | $B_s^0 \rightarrow J/\psi \phi$ | Update2016,DecProdCut,S24 | 2015 | XXM |
| 13144041 | $B_s^0 \rightarrow J/\psi K^+ K^-$ | DecProdCut | 2016 | 7M |
| Backgrounds | | | | |
| 15144001 | $\Lambda_b^0 \rightarrow J/\psi p K^-$ | PHSP, DecProdCut | XXX | XXM |
| 24142001 | Inclusive Jpsi | JpsiInAcc | 2016 | 20M |
| Control samples | | | | |
| 11144001 | $B^0 \rightarrow J/\psi K^{*0}$ | Update2016,DecProdCut,S24 | 2015 | 10M |
| 11144001 | $B^0 \rightarrow J/\psi K^{*0}$ | Update2016,DecProdCut,S26 | 2016 | 10M |
| 12143001 | $B^+ \rightarrow J/\psi K^+$ | Update2016,DecProdCut,S24 | 2015 | 10M |
| 12143001 | $B^+ \rightarrow J/\psi K^+$ | Update2016,DecProdCut,S26 | 2016 | 10M |
| 24142001 | Inclusive Jpsi | JpsiInAcc | 2016 | 20M |
| Generator Level | | | | |

1261 Decays of hadronic particles are described by `EvtGen` [?], in which final state radia-
 1262 tion is generated using `Photos` [?]. The `Geant4` toolkit simulates the interaction of the
 1263 generated particles with the detector, and the detector response [?, ?]. Further details of
 1264 the simulation process can be found in Ref. [?]. The simulated data is processed in a very

similar way to the real data, with the stripping run in flagging mode, with no prescales applied for the trigger. Sim09b was used for the simulated samples. The samples used are listed in Table 5.1.

Simulated signal samples are used to determine the angular acceptance. As will be discussed in Sec. ??, the samples are reweighted to match various distributions observed in data before obtaining the final acceptance. Similarly, the Λ_b^0 and the B^0 samples are used for background studies and decay time acceptance studies, respectively. This is discussed in Sec. ?? and Sec. ??, respectively. The B^+ sample is used for tagging studies as described in Sec. ??.

The main physics parameters used in the main simulation used in this analysis, `Eventtype = 13144011, Bs_Jpsiphi,mm=CPV,update2016,DecProdCut`, are summarized in Table 5.2. For simulated samples a momentum smearing is applied in order to reproduce better the distributions in data.

Table 5.2: Decay model parameters for the Sim09b MC sample used in this analysis, `Eventtype = 13144011, Bs_Jpsiphi,mm=CPV,update2016,DecProdCut`.

| Parameter | Value |
|---------------------------------|-------------------|
| Δm_s | $17.8 ps^{-1}$ |
| $\Delta \Gamma_s$ | $0.08543 ps^{-1}$ |
| Γ_s | $0.6614 ps^{-1}$ |
| ϕ_s | $-0.03 rad$ |
| $ A_0(0) ^2$ | 0.5242 |
| $ A_{\parallel}(0) ^2$ | 0.2256 |
| $ A_{\perp}(0) ^2$ | 0.2500 |
| $\delta_{\parallel} - \delta_0$ | $3.26 rad$ |
| $\delta_{\perp} - \delta_0$ | $3.08 rad$ |

5.2.2.3 Stripping selection

In order to select $B_s^0 \rightarrow J/\psi \phi$ events, in data and MC we start from the stripping line `StrippingBetaSBs2JpsiPhiDetachedLine`, whose selection can be found in Table 5.3. We use Stripping version 26 or 28 for 2016 and Stripping version 24 for 2015. In both cases the selection is the same.

For time resolution studies we use the stripping line `BetaSBs2JpsiPhiPrescaledLine`, which has the same selection as shown in Table 5.3 apart from the cut on the decay time of the B_s^0 candidate.

5.2.2.4 Trigger selection

The following trigger strategy has been identified in order to retain the largest number of signal events while keeping a small number of trigger lines.

Table 5.3: Selection criteria used to identify $B_s^0 \rightarrow J/\psi\phi$ candidates.

| | Variable | Stripping |
|---------------------------------|--|----------------------------------|
| all tracks | $\chi_{\text{track}}^2/\text{nDoF}$ | < 3 |
| $J/\psi \rightarrow \mu^+\mu^-$ | $\Delta\ln\mathcal{L}_{\mu\pi}(\mu^\pm)$ | > 0 |
| | $p_T(\mu^\pm)$ | > 500 MeV/c |
| | χ_{DOCA}^2 | < 20 |
| | $\chi_{\text{vtx}}^2/\text{nDoF}$ | < 16 |
| | $m(\mu^+\mu^-)$ | $\in [3020, 3170]\text{MeV}/c^2$ |
| $\phi \rightarrow K^+K^-$ | χ_{DOCA}^2 | < 30 |
| | $p_T(\phi)$ | > 500 MeV/c |
| | $m(K^+K^-)$ | $\in [980, 1050]\text{MeV}/c^2$ |
| | $\chi_{\text{vtx}}^2/\text{nDoF}$ | < 25 |
| | $\Delta\ln\mathcal{L}_{K\pi}(K^+)$ | > 0 |
| $B_s^0 \rightarrow J/\psi\phi$ | $m(J/\psi K^+K^-)$ | $\in [5150, 5550]\text{MeV}/c^2$ |
| | $\chi_{\text{vtx}}^2/\text{nDoF}$ | < 20 |
| | t | > 0.2 ps |

- 1290 • No L0 requirements
- 1291 • HLT1 selection: `Jpsi_Hlt1DiMuonHighMassDecision_TOS` or
- 1292 `B_Hlt1TrackMuonDecision_TOS` or `B_Hlt1TwoTrackMVADecision_TOS`
- 1293 • HLT2 selection: `Jpsi_Hlt2DiMuonDetachedJPsiDecision_TOS`

1294 5.2.2.5 Corrections

1295 Corrections are applied to the simulated samples to match the distributions obtained from
 1296 data:

- 1297 1. The stripped and triggered $B_s^0 \rightarrow J/\psi K^+K^-$ candidates are taken, with the B_s^0
 1298 decay time restricted to the range [0.3,15] ps.
- 1299 2. The data invariant mass distribution of stripped and triggered $B_s^0 \rightarrow J/\psi K^+K^-$
 1300 candidates is fitted to obtain an sWeighted sample of data that is used in the
 1301 following steps.
- 1302 3. For MC, on top of the selection mentioned before only background categories 0
 1303 (signal) and 50 (radiative events) with true decay time different from 0 are included
 1304 [more details?](#).
- 1305 4. The simulation PID variable distributions are corrected using the `PIDCalib` package.

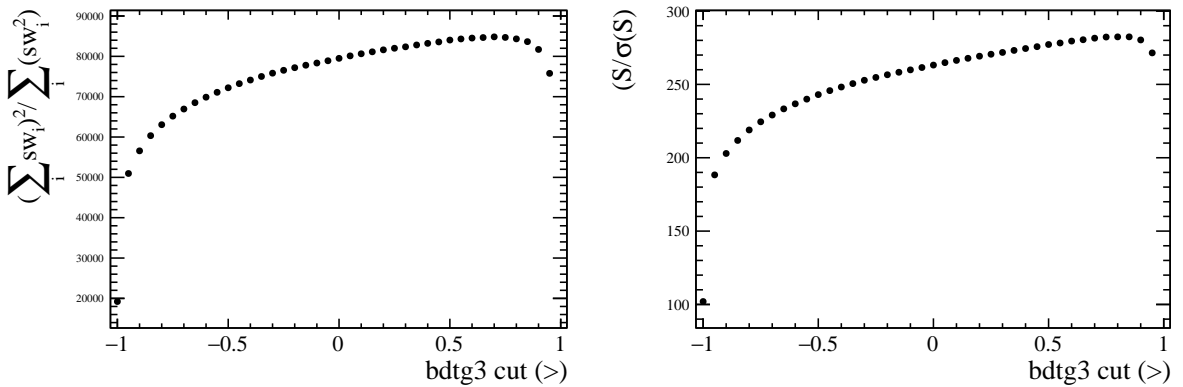


Figure 5.2: Distribution of the figure of merit used to optimise the cut on the BDT response (left) and distribution of signal yield divided by its uncertainty (right).

1306 5. Using the above data sample, the B_s^0 production kinematics, nTracks distribution
1307 and the muon/kaon track ghost probability variables are reweighted.

1308 A BDT is trained to further improve the signal to background ratio. It is trained
1309 with 2016 samples. Namely, the 2016 corrected simulated sample for the signal sample
1310 while 2016 data candidates with $5450\text{MeV}/c^2 < m(J/\psi K^+ K^-) < 5550\text{MeV}/c^2$ are used
1311 for the background sample. Special care was taken to avoid variables that could introduce
1312 angular or decay time efficiencies, like impact parameter χ^2 of final state particles, the
1313 direction angle of the B_s^0 (DIRA) or transverse momentum of final state particles. The
1314 figure of merit used to optimise the BDT response is given by

$$\text{FOM} = \frac{(\sum_i w_i)^2}{\sum_i w_i^2}, \quad (5.9)$$

1315 where the index i runs over all candidates in the sample and w_i are per-candidate weights
1316 that are determined from the invariant mass fit that is performed at each point in the scan
1317 over the BDT response. Figure 5.2 shows on the left how the figure of merit performs and
1318 on the right the number of signal events divided by its uncertainty, both as a function
1319 of the BDT response. A similar distribution is observed. The optimal value is found
1320 to be at > 0.78 . After the BDT requirement has been applied there are approximately
1321 102 000 signal candidates and 26 000 background candidates in the mass window of the
1322 fit, $5320\text{MeV}/c^2 < m(J/\psi K^+ K^-) < 5420\text{MeV}/c^2$ in 2016. The signal to background ratio
1323 is ~ 3.9 . The mass fit used to determine sweights to statistically remove this background
1324 and also the removal of peaking backgrounds for both 2015 and 2016 data samples is
1325 described in detail in the next section.

1326 5.2.3 Mass fit and computation of signal sWeights

1327 The physics parameter of interest are extracted via a log-likelihood fit of the signal PDF
1328 to the unbinned decay time and angular distributions. The events are first weighted

1329 to statistically subtract the background components using the *sPlot* method [?] with
1330 $m(J/\psi K^+ K^-)$ as the discriminating variable.

1331 In order to have an improved resolution, the $m(J/\psi K^+ K^-)$ is determined using both
1332 the J/ψ mass and PV constraints. The combinatorial background is modelled with an
1333 exponential function and the signal distribution with a double-sided *Crystal Ball* (CB)
1334 function. The double-sided CB function uses the per-event mass error as conditional ob-
1335 servable, so that the correlation between $\cos \theta_\mu$ and mass resolution is taken into account.
1336 The full *p.d.f* is the following:

1337

$$p = N_{sig} CB(x; \mu, \alpha_1, \alpha_2, n_1, n_2, s_1, s_2 | \sigma_i) \\ + N_{bkg}((1 - f_{B_d})e^{-\gamma_b x} + f_{B_d} \text{Gauss}(x; \mu_{B_d}, \sigma_{B_d}),$$

1338 where N_{sig} and N_{bkg} is a number of signal and background events correspondingly, μ is the
1339 mean of the distribution, s_1 and s_2 are the scale factors, which accounts for underestima-
1340 tion of the per-event mass error, $\alpha_1, \alpha_2, n_1, n_2$ are the tail parameters, γ_b is the coefficient
1341 in the exponential to describe the background.

1342 The background sources that are considered **consist in**:

- 1343 • $B^0 \rightarrow J/\psi K^{*0}$ peaking background, vetoed using PID cuts.
- 1344 • $\Lambda_b^0 \rightarrow J/\psi p K^-$ peaking background, vetoed using PID cuts. The remaining events
1345 are statistically subtracted by injecting simulated events into the data tuple with a
1346 negative sum of weights equal to the expected number of events.
- 1347 • $B^0 \rightarrow J/\psi K^+ K^-$ peaking background, modelled with a Gaussian in the nominal
1348 mass fit.

1349 For the fit to the $m(J/\psi K^+ K^-)$ distribution, the sample is divided into twenty-four
1350 subsamples, each with an independent signal fraction and different signal mass shapes.
1351 The subsamples correspond to six bins in the $K^+ K^-$ mass, namely [990, 1008, 1016, 1020,
1352 1024, 1032, 1050] MeV/ c^2 , two trigger categories:

- 1353 • “**Biased**”: `B_Hlt1TrackMuonDecision_TOS` or `B_Hlt1TwoTrackMVADecision_TOS`
1354 and not `Jpsi_Hlt1DiMuonHighMassDecision_TOS`
- 1355 • “**Unbiased**”: `Jpsi_Hlt1DiMuonHighMassDecision_TOS`

1356 and two years of the data-taking (2015 and 2016). **plot?**

1357 The event multiplicity (ratio between the number of events containing more than one
1358 candidate and the total number of events) is found to be 1.2% in the full B_s^0 mass region,
1359 but only 0.2% for candidates **in the signal region**. Most of these candidates are due to
1360 cases where the J/ψ is shared and one or two different kaons are added, making these
1361 events truly combinatorial in character. Given the low fraction of multiple events, it is
1362 evaluated as a systematic contribution removed them randomly.

5.2.4 C_{SP} factors

The relative change of the S-wave m_{KK} line shape with respect to that of the P wave has to be considered in the interference terms of the angular expressions, as we are performing the analysis in finite m_{KK} bins (see Ref. [?] for a detailed discussion). This is taken into account by adding a multiplicative correction factor, C_{SP} , to the signal PDF, namely to the S-P-wave interference terms with $k = 8, 9, 10$ in Eq. (5.7), i.e. $N_k \rightarrow C_{SP,i} N_k$. There are in total six C_{SP} factors, one for each m_{KK} bin.

The line shapes of the P and S wave are denoted as $p(m_{KK})$ and $s(m_{KK})$, respectively, where both are normalised to unity over a range $[m_{KK}^L, m_{KK}^U]$. Essentially, the issue is that $\langle p \times s^* \rangle \neq \langle p \rangle \times \langle s^* \rangle$ in each m_{KK} bin. Therefore, the product $p \times s^*$ is integrated, as it appears in the interference terms between the P and S wave. This yields

$$\frac{\int_{m_{KK}^L}^{m_{KK}^H} p \times s^* dm_{KK}}{\sqrt{\int_{m_{KK}^L}^{m_{KK}^H} |p|^2 dm_{KK} \int_{m_{KK}^L}^{m_{KK}^H} |s|^2 dm_{KK}}} = C_{SP} e^{-i\theta_{SP}}, \quad (5.10)$$

where C_{SP} is the correction factor and the phase θ_{SP} is absorbed in the measurement of $\delta_S - \delta_\perp$. The shape of the P wave is a Breit-Wigner distribution, the same as in Eq.(4) of Ref. [?]. The S-wave line shape is an f_0 with pole mass of $0.9499 \text{ GeV}/c^2$ as measured in Ref. [?]. Both the f_0 and ϕ resonance distributions include a phase space factor $\left(\sqrt{\frac{P_B}{m_B} \frac{P_R}{\sqrt{s_{23}}}}\right)$, two Blatt-Weisskopf factors for the B and the K^+K^- resonance, and birth and decay momenta of the f_0, ϕ and B_s^0 , where $L_B = 1, L_R = 0$ for f_0 and $L_B = 0, L_R = 1$ for ϕ . Note that the f_0 mass is considered to be 949 MeV. This value, different from the PDG one (990 ± 30 MeV) [?], is taken from the $B_s^0 \rightarrow J/\psi \pi^+ \pi^-$ measurement [?].

The detector resolution effect on the C_{SP} factors needs to be taken into account. While Eq.5.10 is defined in dependence on the true m_{KK} , the mass bins are defined in dependence on the measured m_{KK} . The resolution effect can be incorporated as an efficiency correction, $\epsilon_i(m_{KK})$, of the C_{SP} factors according to

$$C_{SP} e^{-i\theta_{SP}} = \frac{\int_{2m_K}^{m_{B_s^0}-m_{J/\psi}} p \times s^* \times \epsilon(m_{KK}) dm_{KK}}{\sqrt{\int_{2m_K}^{m_{B_s^0}-m_{J/\psi}} |p|^2 \times \epsilon(m_{KK}) dm_{KK} \int_{2m_K}^{m_{B_s^0}-m_{J/\psi}} |s|^2 \times \epsilon(m_{KK}) dm_{KK}}}, \quad (5.11)$$

where $\epsilon(m_{KK})$ is

$$\epsilon(m_{KK}) = \begin{cases} 1, & \text{if } m_L < m_{KK} < m_H \\ 0 & \text{otherwise.} \end{cases}, \quad (5.12)$$

in the case where we bin in the true m_{KK} mass (or equivalently, have perfect resolution). In reality though, we cut on a measured mass that has a finite resolution, and hence $\epsilon_i(m_{KK})$ will have a non-trivial structure. Note that in this definition we should consider events in the true m_{KK} spectrum up to $2.27 \text{ GeV}/c^2$, which is the value of $m_{B_s^0} - m_{J/\psi}$. However, the ϕ contribution after a certain point in m_{KK} is too small to be modelled

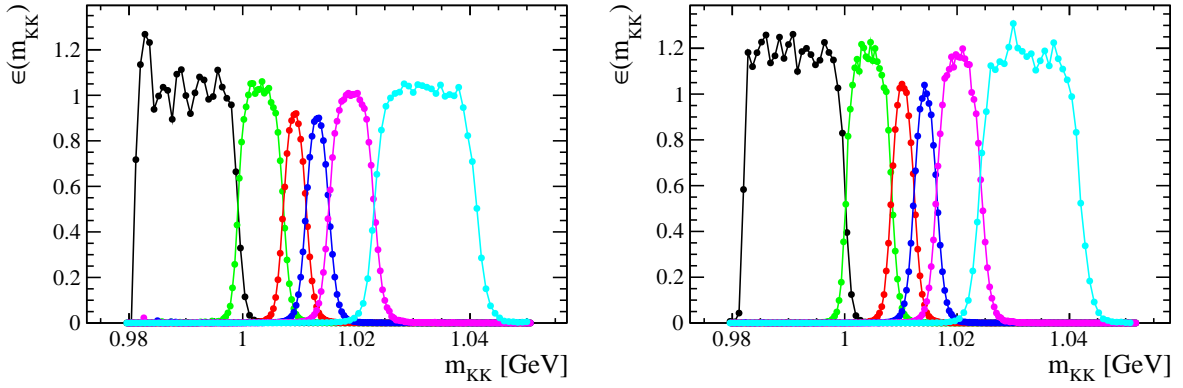


Figure 5.3: Efficiency of each m_{KK} bin selection as a function of MC true m_{KK} using MC without (left) and with (right) S wave.

1394 well in MC, so we apply an upper limit cut at $1.06 \text{ GeV}/c^2$. We use simulated events
 1395 from the 2016 MC sample with and without S wave (see Table 5.1) to determine $\epsilon_i(m_{KK})$
 1396 by dividing the m_{KK} histogram before and after the selection of the events in each bin.
 1397 Fig. 5.3 shows the corresponding distributions. We use the C_{SP} obtained from the MC
 1398 without S wave with exception of the first bin, where the MC with S wave is used. The
 1399 reason for this is that in the region of m_{KK} , the contribution of the S wave is the largest
 1400 and the MC with S wave has more events. With this, we obtain the C_{SP} factors shown in
 1401 Table 5.4.

Table 5.4: C_{SP} factors obtained using Eq. (5.11). The ϕ resonance is parametrized with a relativistic Breit-Wigner.

| m_{KK} bin | S-wave line shape | |
|--------------|-------------------|--------|
| | | f_0 |
| 1 | | 0.8569 |
| 2 | | 0.8768 |
| 3 | | 0.8478 |
| 4 | | 0.8821 |
| 5 | | 0.9406 |
| 6 | | 0.9711 |

1402 5.2.5 Decay time resolution

1403 An effective single-Gaussian model is used to parametrize the decay time resolution. This
 1404 is sufficient to describe the damping effect of the time resolution. It is defined as follows,

$$\mathcal{P}(t) = \mathcal{R}(t) \otimes [f_{\text{prompt}}\delta(t) + f_{\text{ll}}(f_{\text{sl}}e^{-t/\tau_s} + (1-f_{\text{sl}})e^{-t/\tau_l})] + f_{\text{wpv}}W(t), \quad (5.13)$$

1405 Where t is the decay time, δ_t the decay time uncertainty (both calculated from decay tree
 1406 fit in which the PV position is constrained without constraining the J/ψ mass). This
 1407 model is fitted to t in ten bins of δ_t , with $\mathcal{R}(t)$ being:

$$\mathcal{R}(t) \propto \sum_{i=1}^3 f_i \frac{1}{\sqrt{2\pi}\sigma_i} e^{-\frac{1}{2}\left(\frac{t-\mu}{\sigma_i}\right)^2}, \quad (5.14)$$

1408 where $\sum_i f_i = 1$. The three Gaussians have a common mean, different widths and two
 1409 relative fractions, which are allowed to vary in the fit, as are the lifetime and relative
 1410 fractions of the exponential functions. Another component corresponding to events with
 1411 a wrongly-associated PV is added, the fraction of which is allowed to float in the fit. In
 1412 each bin of δ_t , the dilution of the triple Gaussian model is computed as,

$$D = \sum_{i=1}^3 f_i e^{-\sigma_i^2 \Delta m_s^2 / 2}, \quad (5.15)$$

1413 and the effective single Gaussian width as,

$$\sigma_{\text{eff}} = \sqrt{(-2/\Delta m_s^2) \ln D}, \quad (5.16)$$

1414 where $\Delta m_s = 17.77\text{ps}^{-1}$. This converts the resolution into a single-Gaussian function
 1415 with an effective resolution that causes the same damping effect on the magnitude of the
 1416 B_s^0 oscillation. A linear or quadratic calibration curve is then fitted to the variation of
 1417 the effective resolution as a function of $\langle\delta_t\rangle$ to determine the calibration parameters. For
 1418 calibration, simulated $B_s^0 \rightarrow J/\psi\phi$, prompt J/ψ and inclusive J/ψ samples are used, as
 1419 well as prompt J/ψ data. **check** The main source of systematic uncertainty in the calibra-
 1420 tion of the decay time resolution model is the translation from the prompt background
 1421 sample to the signal sample. In addition, there is a systematic arising from the choice to
 1422 include or not the wrong-PV component.

1423 5.2.6 Angular acceptance

1424 The angular acceptance is modelled using *normalization weights*, **ref** obtained from fully
 1425 simulated signal events from the Sim09b production. This simulation sample is iteratively
 1426 weighted to match the distributions of final-state particle kinematics in the real data, as
 1427 well as to match the physics parameters obtained from data, in order to correct for
 1428 imperfections in the detector simulation. In order to do this, a GB reweighting is first
 1429 applied in $p(B_s^0)$, $p_T(B_s^0)$ and $m(K^+K^-)$, together with a reweighting in $p(K^\pm)$, $p_T(K^\pm)$.

1430 The angular normalizations are computed, and the process is repeated until convergence
 1431 is achieved (after 4 iterations).

1432 A total of 10 normalization weights are computed for each year and trigger category,
 1433 as indicated in table 5.5, where the combined weights are shown. The factorization of
 1434 angular acceptance and decay time acceptance is assumed. A systematic effect is assigned
 1435 to such assumption, comparing the final acceptance normalization weights obtained in six
 1436 equal populated decay time bins.

Table 5.5: Angular acceptance weights determined from all available Monte Carlo samples. The f_k are the normalizations of the angular functions (see Equation 5.7) including the acceptance. They are used in the normalization of the *p.d.f.*

| k | f_k/f_1 | | | |
|----------------------------|------------------------|----------------------|------------------------|------------------------|
| | 2015 | | 2016 | |
| | “Unbiased trigger” | “Biased” trigger | “Unbiased trigger” | “Biased trigger” |
| 1 (00) | 1 ± 0 | 1 ± 0 | 1 ± 0 | 1 ± 0 |
| 2 ($\parallel\parallel$) | 1.0297 ± 0.0019 | 1.0278 ± 0.0036 | 1.02637 ± 0.00079 | 1.0181 ± 0.0017 |
| 3 ($\perp\perp$) | 1.0299 ± 0.0019 | 1.0280 ± 0.0035 | 1.02590 ± 0.00078 | 1.0184 ± 0.0017 |
| 4 ($\parallel\perp$) | -0.0007 ± 0.0015 | -0.0071 ± 0.0030 | -0.00029 ± 0.00063 | 0.0017 ± 0.0015 |
| 5 ($0\parallel$) | -0.00013 ± 0.00090 | 0.0038 ± 0.0017 | 0.00115 ± 0.00038 | 0.00260 ± 0.00080 |
| 6 ($0\perp$) | 0.00119 ± 0.00089 | 0.0026 ± 0.0017 | -0.00010 ± 0.00038 | -0.00091 ± 0.00079 |
| 7 (SS) | 1.0076 ± 0.0013 | 1.0123 ± 0.0025 | 1.00618 ± 0.00054 | 1.0112 ± 0.0012 |
| 8 (S \parallel) | -0.0005 ± 0.0012 | -0.0008 ± 0.0023 | 0.00045 ± 0.00048 | -0.0003 ± 0.0010 |
| 9 (S \perp) | -0.0008 ± 0.0012 | 0.0000 ± 0.0023 | -0.00020 ± 0.00049 | -0.0005 ± 0.0010 |
| 10 (S0) | 0.0013 ± 0.0024 | -0.0047 ± 0.0047 | -0.0008 ± 0.0010 | -0.0059 ± 0.0022 |

1437 A cross-check has been performed using a sample of $B^+ \rightarrow J/\psi K^+$ decays in 2016
 1438 data, **yielding a good consistency in the method**.

1439 5.2.7 Decay time acceptance

1440 The reconstruction efficiency is not constant as a function of the B_s^0 decay time due to
 1441 displacement requirements made on signal tracks in the trigger and event selection and to
 1442 a decay-time-dependent efficiency to reconstruct the tracks in the VELO [?]. The overall
 1443 decay-time acceptance is determined using the control channel $B^0 \rightarrow J/\psi K^*(892)^0$, with
 1444 $K^*(892)^0 \rightarrow K^+\pi^-$, which is kinematically very similar to the signal decay and it is
 1445 assumed to have a purely exponential decay-time distribution with a well-known lifetime
 1446 (i.e. the width difference $\Delta\Gamma_d$ is ignored), namely 1.518 ± 0.004 ps [?]. The strategy to
 1447 select $B^0 \rightarrow J/\psi K^*(892)^0$ events and compute the sWeights is similar to the one used for
 1448 $B_s^0 \rightarrow J/\psi K^+K^-$ events. The $K^+\pi^-$ system in the $B^0 \rightarrow J/\psi K^+\pi^-$ decay can be in a
 1449 relative S-wave or P-wave configuration. A $\sim 6\%$ presence of S-wave has been observed
 1450 in data, as described in [?]. However, the simulated $B^0 \rightarrow J/\psi K^*(892)^0$ sample only
 1451 includes the P-wave component. To account for this, an iterative procedure similar to the

one described in 5.2.6 is applied, reweighting the simulation to match the B^0 p and p_T , as well as $m(K^+\pi^-)$ distributions in data. [revisar](#)

The decay time acceptance is defined as

$$\varepsilon_{\text{data}}^{B_s^0}(t) = \varepsilon_{\text{data}}^{B^0}(t) \times \frac{\varepsilon_{\text{sim}}^{B_s^0}(t)}{\varepsilon_{\text{sim}}^{B^0}(t)}, \quad (5.17)$$

where $\varepsilon_{\text{data}}^{B_s^0}(t)$ is the efficiency in data of the fully triggered, selected and weighted events in the B^0 control channel and $r(t) = \varepsilon_{\text{sim}}^{B_s^0}(t)/\varepsilon_{\text{sim}}^{B^0}(t)$ is the ratio of efficiencies of the simulated signal and control modes after the full trigger, selection and MC-data correction chain has been applied. This second term in the acceptance, $r(t)$, accounts for the small differences in the lifetime and kinematics between the signal and control modes. The MC events are reweighted to match the *p.d.f.* of the respective data. [more?](#)

To derive $\varepsilon_{\text{data}}^{B_s^0}(t)$ a simultaneous fit is performed to both the simultaneous samples and the data control channel. This allows to have the overall uncertainties on the B_s^0 data spline coefficients, thus providing an easier control on the associated systematic uncertainty. The decay time acceptance $\varepsilon_{\text{data}}^{B_s^0}(t)$ is then used in the fit to the B_s^0 data signal sample to determine the physics parameters.

For the B^0 and B_s^0 the model used for the fit is composed of the product of a single exponential, convoluted with a single Gaussian resolution, and the respective acceptance function. The latter is modelled using cubic splines with knots at [0.3, 0.58, 0.91, 1.35, 1.96, 3.01, 12.00] ps and the first coefficient is fixed to unity. The knot positions have been chosen according to an exponential distribution between [0.3, 15] ps in order to have six equally populated bins considering $\Gamma = 0.66$ ps. The last knot position is moved from 15 ps to 12 ps in order to have stable fits also for the trigger-year categories which have no decay candidates at these large decay times.

In order to obtain a single spline, $s_{\text{data}}^{B_s^0}$, that represents $\varepsilon_{\text{data}}^{B_s^0}(t)$, combinations of the following three splines are used to describe the acceptance of the three datasets:

- One spline representing the acceptance in B_s^0 MC: $s_{\text{sim}}^{B_s^0}$
- One spline representing the ratio of acceptances in B^0 and B_s^0 MC: $s_{\text{sim}}^{B^0/B_s^0}$
- One spline representing the final acceptance in B_s^0 data: $s_{\text{data}}^{B_s^0}$

These splines are used in the following combinations to describe the acceptances for the three datasets:

- B_s^0 MC: $s_{\text{sim}}^{B_s^0}$
- B^0 MC: $s_{\text{sim}}^{B^0/B_s^0} \times s_{\text{sim}}^{B_s^0}$
- B^0 data: $s_{\text{data}}^{B_s^0} \times s_{\text{sim}}^{B^0/B_s^0}$

1484 A single Gaussian models the resolution, and has a mean of 0ps and a width of
 1485 42fs/39fs/42fs for B_s^0 MC/ B^0 MC/ B^0 data, motivated by the studies in Section ?? and
 1486 the difference of the resolution between B_s^0 and B^0 seen in truth matched MC. The lifetime
 1487 in the fit is fixed to the World average value for data $\tau_{B^0}^{\text{data}} = 1.518$ ps [?], and to the value
 1488 used in the generation of the MC for the simulated samples, namely $\tau_{B^0}^{\text{MC}} = 1.519$ ps and
 1489 $\tau_{B_s^0}^{\text{MC}} = 1.512$ ps.

1490 The decay time acceptance is obtained separately for the data taking periods 2015
 1491 and 2016 and two different trigger paths (“unbiased” and “exclusively biased”). [plots?](#)

1492 The lifetimes $\tau(B^0)$ and $\tau(B^+)$ in $B^0 \rightarrow J/\psi K^{*0}$ and $B^+ \rightarrow J/\psi K^+$ decays are
 1493 measured as a crosscheck of the time acceptance procedure. 2016 data and simulation
 1494 samples for both validation channels are used. The same procedure as for $B_s^0 \rightarrow J/\psi\phi$ is
 1495 used, including the spline knot positions and time resolution (see Sect. ??).

1496 5.2.7.1 Measurement of $\tau(B^0)$

1497 The procedure to determine the decay time efficiency (Sect. ??) is validated by splitting
 1498 the $B^0 \rightarrow J/\psi K^{*0}$ control sample (both data and simulation) into two independent sets.
 1499 One half of the sample is then used as a control while the other is used to measure $\tau(B^0)$.
 1500 Three different criteria are considered for this, namely:

- 1501 • Splitting according to odd/even eventNumber in the original sample, where the
 1502 sample that is used instead of B_s^0 has a cut on $\delta_t < 0.04$ ps.
- 1503 • Splitting according to odd/even eventNumber in the original sample, where the
 1504 sample that is used for fitting has a cut on the opening angle between the kaon
 1505 and the pion that come from the K^{*0} , angle < 0.025 rad. The position of the cut
 1506 is chosen such that the average of the opening angle distribution is close to the
 1507 corresponding one for the $B_s^0 \rightarrow J/\psi\phi$ sample.
- 1508 • Splitting on the K^{*0} mass: events with $m(K^{*0}) < 890$ GeV/c² are used for fitting,
 1509 events with $m(K^{*0}) > 890$ GeV/c² are used as control sample.

1510 For the control samples, the B^0 lifetime is fixed to its input for simulation (1.519 ps)
 1511 and to the world average value for data (1.518 ps) [?]. We obtain the values listed in
 1512 the first column of Table 5.6, where the deviation from the world average [?] is also
 1513 shown. To further improve these results, we also try reweighting the simulated samples
 1514 according such that the B^0 meson p_T distribution matches that in data, as shown in
 1515 Fig. 5.4. The corresponding values for the lifetime (second column of Table 5.6) show a
 1516 better agreement with the PDG value. The fits to the decay time distribution with MC
 1517 reweighting in p_T for the different splittings are shown in Fig. 5.5.

1518 Finally, a reweighting that takes into consideration the S-wave fraction present in data
 1519 (in addition to the aforementioned MC reweighting in $B^0 p_T$) is also considered, using the
 1520 results from Section ???. The splitting that is applied is the one depending on the K^{*0}
 1521 mass. The corresponding fitted lifetime is found to be $\tau(B^0) = 1.519 \pm 0.006$ ps, 0.13σ

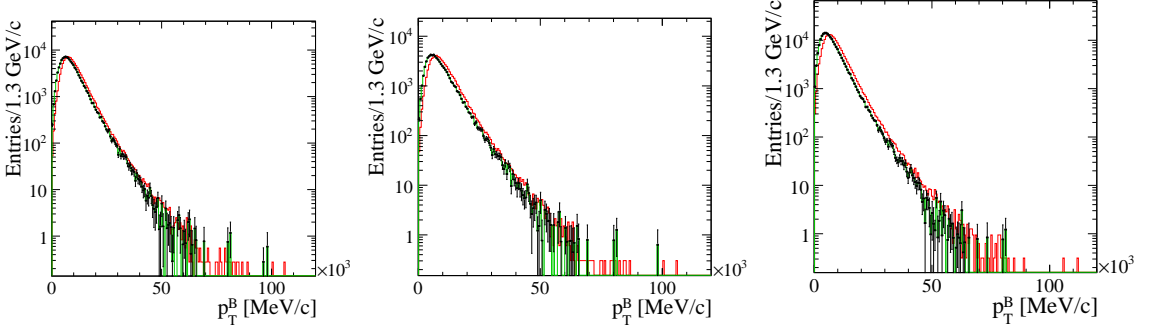


Figure 5.4: Distributions of p_T^B for $B^0 \rightarrow J/\psi K^{*0}$ using splitting according to eventNumber with $\sigma_t < 0.04$ (top left) and angle < 0.025 (top right), and splitting according to $m(K^{*0})$ (bottom). The black dots represent data and the red and green lines the MC before and after the reweighting, respectively.

1522 (0.05%) from the world average [?], thus showing a good agreement. The fitted decay
 1523 time is shown in Fig. 5.5.

Table 5.6: Values of $\tau(B^0)$ obtained for validation of the time acceptance method for the different considered splittings, with (first column) and without reweighting MC in p_T^B .

| Splitting | No $B^0 p_T$ reweighting | $B^0 p_T$ reweighting |
|----------------------------|---|---|
| $\delta_t < 0.04\text{ps}$ | $1.482 \pm 0.007\text{ps} (5.21\sigma, 2.35\%)$ | $1.518 \pm 0.007\text{ps} (0.05\sigma, 0.03\%)$ |
| angle $< 0.025\text{rad}$ | $1.522 \pm 0.008\text{ps} (0.52\sigma, 0.28\%)$ | $1.523 \pm 0.008\text{ps} (0.57\sigma, 0.31\%)$ |
| $m(K^{*0})$ | $1.518 \pm 0.006\text{ps} (0.02\sigma, 0.01\%)$ | $1.518 \pm 0.006\text{ps} (0.03\sigma, 0.01\%)$ |

1524 uncertainties

1525 5.2.8 Flavour tagging

1526 For time-dependent studies the ability of properly identifying the initial flavour of the
 1527 meson (known as *flavour tagging*) is fundamental. To this end, two flavour tagging algo-
 1528 rithms are used: the opposite-side (OS) taggers and the same-side kaon (SSK) taggers,
 1529 which exploit specific features of the incoherent production of $b\bar{b}$ quark pairs in pp colli-
 1530 sions.

1531 Each tagging algorithm gives a tag decision and a mistag probability, the fraction of
 1532 events with the wrong tag decision, $\eta \in [0, 0.5]$. The tag decision takes values +1, 1, or 0,
 1533 if the signal meson is tagged as B_s^0 , \bar{B}_s^0 or untagged, respectively. The fraction of events
 1534 in the sample with a nonzero tagging decision gives the efficiency of the tagger, ε . The
 1535 mistag probability is then calibrated to obtain the corrected per-event mistag probability,
 1536 ω . This is used to determine the dilution factor, $\mathcal{D} = (1 - 2\omega)$, that rescales the efficiency
 1537 of the tagger to quantify the fraction of the sample equivalent to perfectly tagged events.
 1538 This effective efficiency is called tagging power, given by the product of the efficiency and
 1539 the square dilution, $\varepsilon\mathcal{D}^2$.

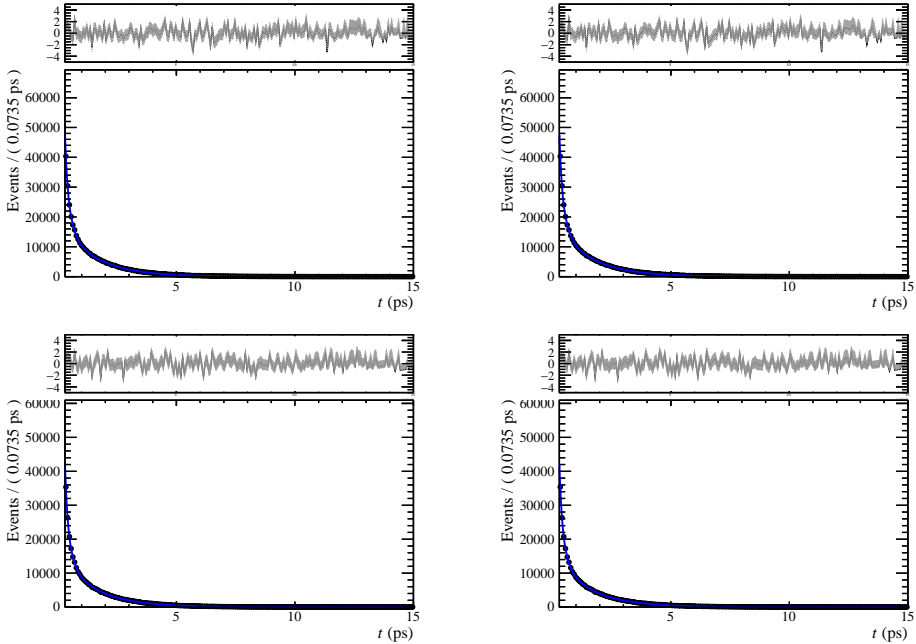


Figure 5.5: Decay time distribution of $B^0 \rightarrow J/\psi K^{*0}$ decays and the corresponding likelihood fit result, splitting according to eventNumber with $\sigma_t < 0.04$ (top left) and angle < 0.025 (top right), and splitting according to $m(K^{*0})$ without (bottom left) and with S-wave consideration.

1540 In this analysis the taggers have been optimised for Run 1 data but here their calibra-
 1541 tion is determined using Run 2 data. **update if necessary** A linear dependence of ω with
 1542 η is assumed,

$$\omega = p_0 + p_1(\eta - \langle \eta \rangle) \quad (5.18)$$

1543 where p_0, p_1 are calibration parameters and $\langle \eta \rangle$ is the average predicted mistag probabili-
 1544 ties for the calibration samples. When using OS and SSK algorithms, the calibration
 1545 model become:

1546

$$1547 \omega^{\text{alg}} = (p_0^{\text{alg}} + \frac{\Delta p_0^{\text{alg}}}{2}) + (p_1^{\text{alg}} + \frac{\Delta p_1^{\text{alg}}}{2})(\eta^{\text{alg}} - \langle \eta^{\text{alg}} \rangle) \text{ for an initial } B_s^0 \text{ event}$$

$$1548 \omega^{\text{alg}} = (p_0^{\text{alg}} - \frac{\Delta p_0^{\text{alg}}}{2}) + (p_1^{\text{alg}} - \frac{\Delta p_1^{\text{alg}}}{2})(\eta^{\text{alg}} - \langle \eta^{\text{alg}} \rangle) \text{ for an initial } \bar{B}_s^0 \text{ event}$$

1549 where $r\text{malg} = \text{OS}, \text{SSK}$ and Δp_i^{alg} are mistag asymmetries.

1550 The calibration of the opposite-side tagger is made using $B^+ \rightarrow J/\psi K^+$ decays,
 1551 while for the same-side kaon tagger $B_s^0 \rightarrow D_s^- \pi^+$ decays are used. The overall tagging
 1552 performance is summarised in table 5.7.

Table 5.7: Tagging performance

| Category | Fraction(%) | $\varepsilon(\%)$ | \mathcal{D}^2 | $\varepsilon\mathcal{D}^2(\%)$ |
|----------|-------------|-------------------|-----------------|--------------------------------|
| OS-only | 14.44 | 10.26 | 0.087 | 0.90 ± 0.03 |
| SSK-only | 59.48 | 42.28 | 0.030 | 1.29 ± 0.31 |
| OS&SSK | 26.09 | 18.54 | 0.099 | 1.84 ± 0.12 |
| Total | 100 | 71.09 | 0.057 | 4.02 ± 0.34 |

1553 5.2.9 Data fitting

1554 The fitting procedure uses the sFit technique for background subtraction, as described
 1555 in Section 5.2.3. The full PDF, based on Eq. (5.7) and taking into account all detector
 1556 response effects, is given by

$$\begin{aligned} \mathcal{P}(t, \Omega | q^{\text{OS}}, q^{\text{SSK}}, \eta^{\text{OS}}, \eta^{\text{SSK}}, \sigma_t) &= \sum_{y=2015}^{2016} \sum_{g=b,ub} \sum_{i=1}^6 \sum_{k=1}^{10} \frac{1}{\mathcal{N}_{y,g}} \mathcal{P}_{i,k}(t, \Omega | q^{\text{OS}}, q^{\text{SSK}}, \eta^{\text{OS}}, \eta^{\text{SSK}}, \sigma_t) \\ &= \sum_{y=2015}^{2016} \sum_{g=b,ub} \sum_{i=1}^6 \sum_{k=1}^{10} \frac{1}{\mathcal{N}_{y,g}} \tilde{N}_{i,k} f_{g,y,k}(\Omega) \varepsilon_{g,y}(t) \\ &\quad \cdot \{ [(1 + q^{\text{OS}}(1 - 2\omega^{\text{OS}}(\eta^{\text{OS}}))) (1 + q^{\text{SSK}}(1 - 2\omega^{\text{SSK}}(\eta^{\text{SSK}}))) \\ &\quad \cdot h_k(t|B_s^0) \\ &\quad + (1 - q^{\text{OS}}(1 - 2\bar{\omega}^{\text{OS}}(\eta^{\text{OS}}))) (1 - q^{\text{SSK}}(1 - 2\bar{\omega}^{\text{SSK}}(\eta^{\text{SSK}}))) \\ &\quad \cdot h_k(t|\bar{B}_s^0)] \otimes G(t|\sigma_t) \}, \end{aligned} \quad (5.19)$$

1557 where i is the m_{KK} bin; y is the year of data taking; g is the trigger line (biased and unbiased);
 1558 q^{OS} and q^{SSK} are the OS and SSK tag decisions, η^{OS} and η^{SSK} the measured mistag probabilities,
 1559 ω and $\bar{\omega}$ the mistag probability calibration for B_s^0 and \bar{B}_s^0 (see Section ??); $\varepsilon(t)$ is the decay time
 1560 acceptance (see Section ??); $G(t|\sigma_t)$ is the decay time resolution with decay time uncertainty
 1561 σ_t (see Section ??); $\tilde{N}_{i,k} = N_k$ for $k < 8$ and $\tilde{N}_{i,k} = C_{\text{SP},i} N_k$ for $k = 8, 9, 10$ (see Section 5.2.4);
 1562 $\mathcal{N}_{y,g}$ is the normalisation given by

$$\mathcal{N}_{y,g}(t, \Omega | q^{\text{OS}}, q^{\text{SSK}}, \eta^{\text{OS}}, \eta^{\text{SSK}}, \sigma_t) = \int_{t=0.3\text{ps}}^{15\text{ps}} \int_{\Omega} \sum_{i=1}^6 \sum_{k=1}^{10} w_k \mathcal{P}_{i,k}(t, \Omega | q^{\text{OS}}, q^{\text{SSK}}, \eta^{\text{OS}}, \eta^{\text{SSK}}, \sigma_t) dt d\Omega, \quad (5.20)$$

1563 where w_k are the angular acceptance weights (see Section ??).

1564 The values of ϕ_s and $\Delta\Gamma_s$ were kept blinded during the full analysis.
rephrase

1565 5.2.10 Baseline fit

1566 $\Delta\Lambda_d^s = \Lambda_s - \Lambda_d$ is fitted instead of Λ_s , given that it can be measured with a higher precision
 1567 (independently of the value of Λ_d used in the determination of the time acceptance). Events

1568 with negative mistag probability are manually assigned $\omega = 0$. As said before, λ and ϕ_s are
 1569 assumed to be common to all polarisation states. Checks of this assumption are made, where
 1570 polarisation dependence is instead considered. These are in agreement with the baseline fit.
 1571 Several fitters were independently developed, including the baseline one, based on the usage of
 1572 graphics processing units (GPUs). These are optimized for parallel calculations that allow a
 1573 faster computation. A good agreement is found between the fit results provided by the different
 1574 fitters.

1575 The fit result is given in Table ?? and the corresponding correlation matrix in Table ??.
 1576 The statistical uncertainties reported are the symmetric uncertainties from Hesse^{ref}. The
 1577 background subtracted projection plots are shown in Figures ?? and ???. One-dimensional
 1578 likelihood profiles of the fit parameters are shown in Figures ??-???. ^{update} A summary of the
 1579 systematic uncertainties is shown in ^{reference}. ??

1580 5.2.11 Coverage of the uncertainty with the sFit

1581 To check the reliability of the uncertainties on the physics parameters in the data fit to the
 1582 time and helicity angles, the method of bootstrapping is applied to both data and simulation.
 1583 For this, a set of pseudo-samples is created by randomly selecting events from the simulation or
 1584 data sample. The number of events in each pseudo-sample is the same as the number of events
 1585 of the original one. After creating the samples, they are fitted, and the central value and pull
 1586 distributions for each fit parameter are plotted (see figures in Appendix B). The correspond-
 1587 ing bootstrapping uncertainty (and the uncertainty on the uncertainty) for each parameter is
 1588 obtained from the RMS of the distribution of its central values.

1589 5.2.11.1 Simulation

1590 The results for bootstrapping using simulation are shown in Table 5.8. For this study a simula-
 1591 tion sample from 2016 has been used, with S26 applied. Good agreement is found between the
 1592 errors provided by the fit and the ones computed using bootstrapping.

Table 5.8: Variation in the statistical uncertainties for the fit parameters using the errors provided by the fit and the ones obtained with bootstrapping for simulation.

| Parameter | Fit | Bootstrapping |
|----------------------------------|--------|---------------------------|
| f_L | 0.0006 | 0.0005819 ± 0.000002 |
| f_\perp | 0.0008 | 0.000796 ± 0.0000126 |
| ϕ_s [rad] * | 0.0016 | 0.0016091 ± 0.0000256 |
| δ_\perp [rad] | 0.006 | 0.0063273 ± 0.0001005 |
| δ_\parallel [rad] | 0.007 | 0.006711 ± 0.0001066 |
| $ \lambda $ | 0.001 | 0.0010967 ± 0.0000174 |
| $\Delta\Gamma_d^s$ [ps^{-1}] | 0.0005 | 0.00057 ± 0.0000091 |
| $\Delta\Gamma_s$ [ps^{-1}] * | 0.0016 | 0.0015527 ± 0.0000247 |
| Δm_s [ps^{-1}] | 0.0021 | 0.0021915 ± 0.0000348 |

1593 **5.2.11.2 Signal and background simulation**

1594 A sample composed by signal and background is used for the bootstrapping studies. It is
 1595 obtained using a S28, 2016 simulation sample, combined with background that is generated
 1596 from 2016 data's sidebands. The preliminary results are shown in Table 5.9. Results for the
 1597 nominal fit are shown in Table 5.10, together with the corresponding inputs used for MC. As
 1598 for the test with pure signal MC (see Sec. 5.2.11.1), good agreement is found between the errors
 1599 obtained using bootstrapping and the ones provided by the fit.

Table 5.9: Variation in the statistical uncertainties for the fit parameters using the errors provided by the fit and the ones obtained with bootstrapping for signal and background simulation.

| Parameter | Fit | Bootstrapping |
|----------------------------------|-----------|---------------------------|
| f_L | 0.0008834 | 0.0008598 ± 0.0000118 |
| f_\perp | 0.001239 | 0.0012018 ± 0.0000165 |
| ϕ_s [rad] * | 0.009296 | 0.0094382 ± 0.0001296 |
| δ_\perp [rad] | 0.03491 | 0.036471 ± 0.0005006 |
| δ_\parallel [rad] | 0.0289 | 0.0239876 ± 0.0003292 |
| $ \lambda $ | 0.006291 | 0.0062407 ± 0.0000857 |
| $\Delta\Gamma_d^s$ [ps^{-1}] | 0.0007465 | 0.0007257 ± 0.000010 |
| $\Delta\Gamma_s$ [ps^{-1}] * | 0.002395 | 0.0022637 ± 0.0000311 |
| Δm_s [ps^{-1}] | 0.01379 | 0.0144994 ± 0.000199 |

Table 5.10: Fit results for signal and background simulation

| Parameter | Fit | Input |
|----------------------------------|--------------------------|---------|
| f_L | 0.5288 ± 0.0008834 | 0.5241 |
| f_\perp | 0.247 ± 0.001239 | 0.25 |
| ϕ_s [rad] * | -0.04027 ± 0.009296 | -0.03 |
| δ_\perp [rad] | 3.042 ± 0.03491 | 3.08 |
| δ_\parallel [rad] | 3.23 ± 0.0289 | 3.26 |
| $ \lambda $ | 0.9988 ± 0.006291 | 1.0 |
| $\Delta\Gamma_d^s$ [ps^{-1}] | 0.005276 ± 0.0007465 | 0.00601 |
| $\Delta\Gamma_s$ [ps^{-1}] * | 0.08673 ± 0.002395 | 0.0854 |
| Δm_s [ps^{-1}] | 17.8 ± 0.01379 | 17.8 |

1600 **5.2.11.3 Data**

1601 The results for bootstrapping using 2016 data can be seen in Table 5.11. In this case, sWeighted
 1602 2016 data has been used, with Stripping version 26. Contrary to simulation, discrepancies are
 1603 found between bootstrapping and fit errors, especially in the strong phases and the S wave fit
 1604 fractions. There could be a couple of possible explanations for this. First, the sWeights used for
 1605 the fit are not recalculated for each randomly drawn sample, which can lead to differences in the
 1606 uncertainties. However, this doesn't seem to affect the MC and so is probably only a secondary
 1607 effect. Second, the bootstrapping test shows two minima for $\delta_S^1 - \delta_\perp$. A likelihood profile
 1608 test on the data confirmed this. A reliable error estimation for the lower minimum is impossible
 1609 because it merges with the higher minimum before the likelihood changes by a significance of 1σ .
 1610 Last but not least, the likelihoods of some parameters show an asymmetric and non-Gaussian
 1611 behaviour. This is especially true for the S wave parameters, where the fit fractions are low and
 1612 we lack the statistical power to determine their uncertainties. In these cases, the fit errors are
 1613 not an apt estimate of the uncertainties. Instead, for the final result the uncertainties will be
 1614 taken from the parameter likelihood profiles.

Table 5.11: Variation in the statistical uncertainties for the fit parameters using the errors provided by the fit and the ones obtained with bootstrapping for 2016 data.

| Parameter | Fit | Bootstrapping |
|---------------------------------|----------|---------------------------|
| f_L | 0.003124 | 0.0032169 ± 0.0000474 |
| f_\perp | 0.0043 | 0.0043788 ± 0.0000645 |
| ϕ_s [rad] * | 0.04637 | 0.0474420 ± 0.0006984 |
| δ_\perp [rad] | 0.1304 | 0.1492076 ± 0.0021966 |
| δ_\parallel [rad] | 0.07729 | 0.0414571 ± 0.0006103 |
| $ \lambda $ | 0.01579 | 0.0191426 ± 0.0002818 |
| Γ_s [ps^{-1}] | 0.002529 | 0.0025023 ± 0.0000368 |
| $\Delta\Gamma_s$ [ps^{-1}]* | 0.008355 | 0.0082595 ± 0.0001216 |
| Δm_s [ps^{-1}] | 0.05667 | 0.0733526 ± 0.0010799 |
| $\delta_S^1 - \delta_\perp$ | 0.3492 | 0.6728437 ± 0.0099055 |
| $\delta_S^2 - \delta_\perp$ | 0.3653 | 0.3101728 ± 0.0045663 |
| $\delta_S^3 - \delta_\perp$ | 0.4979 | 0.4256790 ± 0.0062668 |
| $\delta_S^4 - \delta_\perp$ | 0.1823 | 1.6134152 ± 0.0237524 |
| $\delta_S^5 - \delta_\perp$ | 0.1006 | 0.4099490 ± 0.0060352 |
| $\delta_S^6 - \delta_\perp$ | 0.1935 | 0.2751857 ± 0.0040512 |
| F_S^1 | 0.04565 | 0.0477817 ± 0.0007034 |
| F_S^2 | 0.00963 | 0.0094324 ± 0.0001389 |
| F_S^3 | 0.002055 | 0.0020870 ± 0.0000307 |
| F_S^4 | 0.005845 | 0.0054945 ± 0.0000809 |
| F_S^5 | 0.01386 | 0.0144309 ± 0.0002124 |
| F_S^6 | 0.02029 | 0.0201681 ± 0.0002969 |

Table 5.12: Physics observables constraints imposed in this study.

| Observable | Constraint |
|---|---|
| $\Delta M_s^{\text{EXP/SM}}$ | 0.968 ± 0.078 TK: 0.887(59)[1712.06572] |
| $\phi_s - \phi_s^{\text{SM}}$ | 0.0154 ± 0.031 |
| $\mathcal{B}(B_s^0 \rightarrow \mu^+ \mu^-)^{\text{EXP/SM}}$ | $0.9 \pm 0.2(\text{EXP}) \pm 0.1(\text{TH})$ |
| $\mathcal{B}(B_d^0 \rightarrow \mu^+ \mu^-)^{\text{EXP/SM}}$ | $4.0 \pm 2.0(\text{EXP}) \pm 0.4(\text{TH})$ |
| $\Delta m_s A_{SL} / \Delta \Gamma_s - (\Delta m_s A_{SL} / \Delta \Gamma_s)^{\text{SM}}$ | -0.1258 ± 0.5651 |
| $\mathcal{B}(B^+ \rightarrow \tau^+ \nu_\tau)^{\text{EXP/SM}}$ | 0.91 ± 0.22 [?] |
| ΔC_7 | -0.02 ± 0.02 [?] |
| m_H | 125.09 ± 20 [GeV] [2016 PDG] |
| $\tan \beta$: M_A plane | ATLAS limits for hMSSM scenario [?] |
| LSP | Lightest neutralino |

1615 combination with run 1?

1616 5.3 ϕ_s pheno

1617

1618 1. Introduction

1619 2. WCs

1620 3. Plots

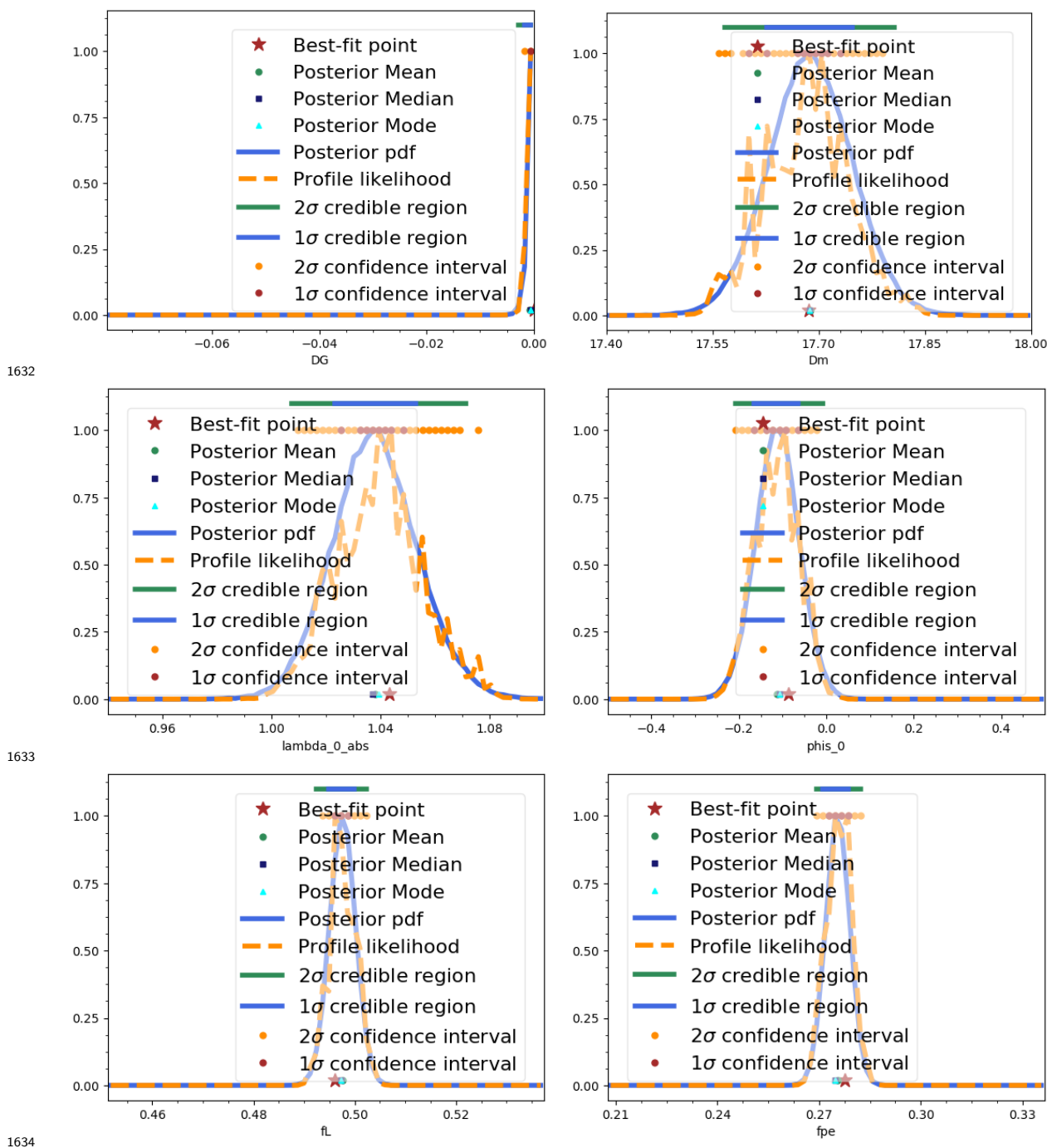
1621 4. Scan ranges

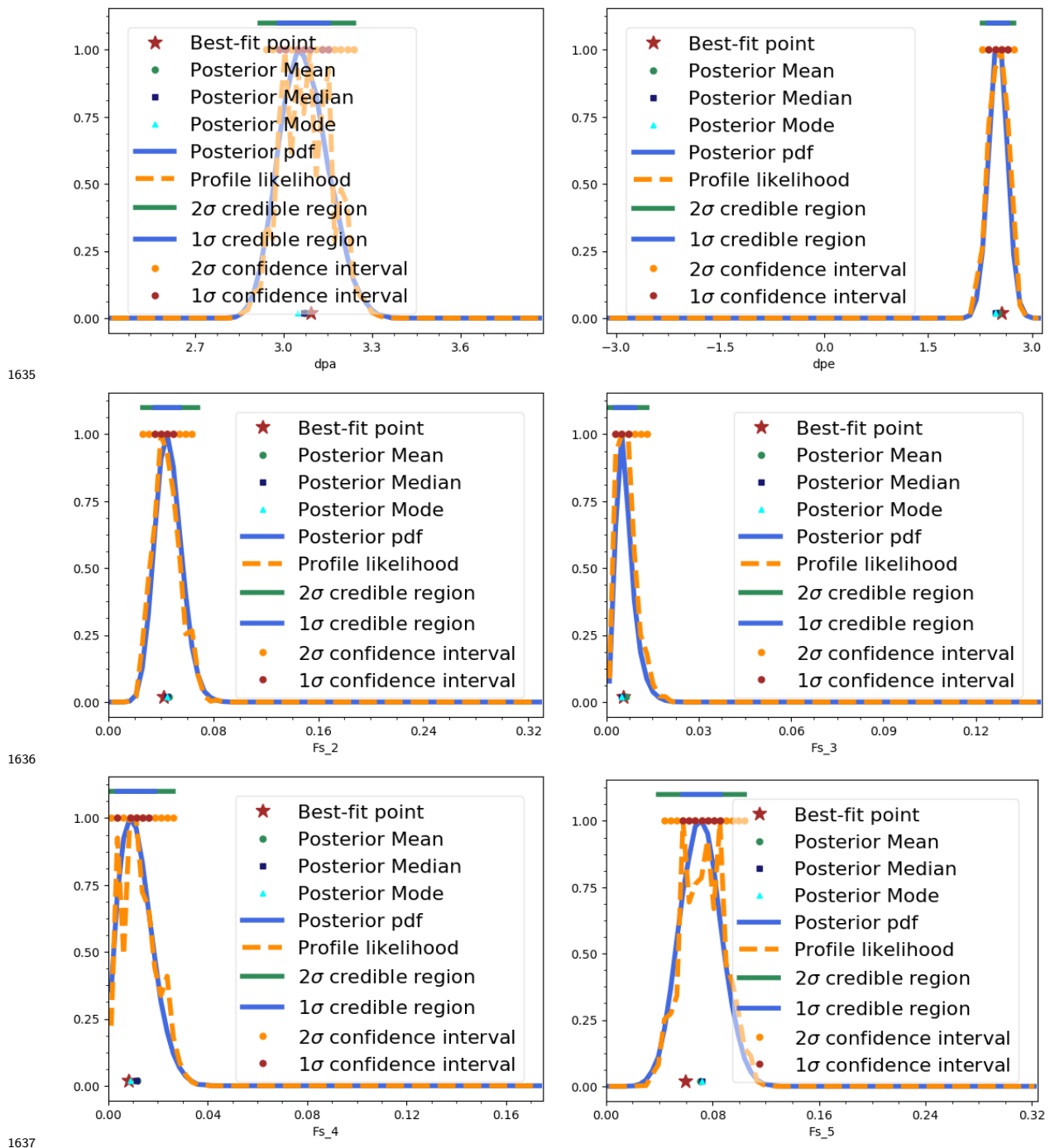
1622 5. Interpretation

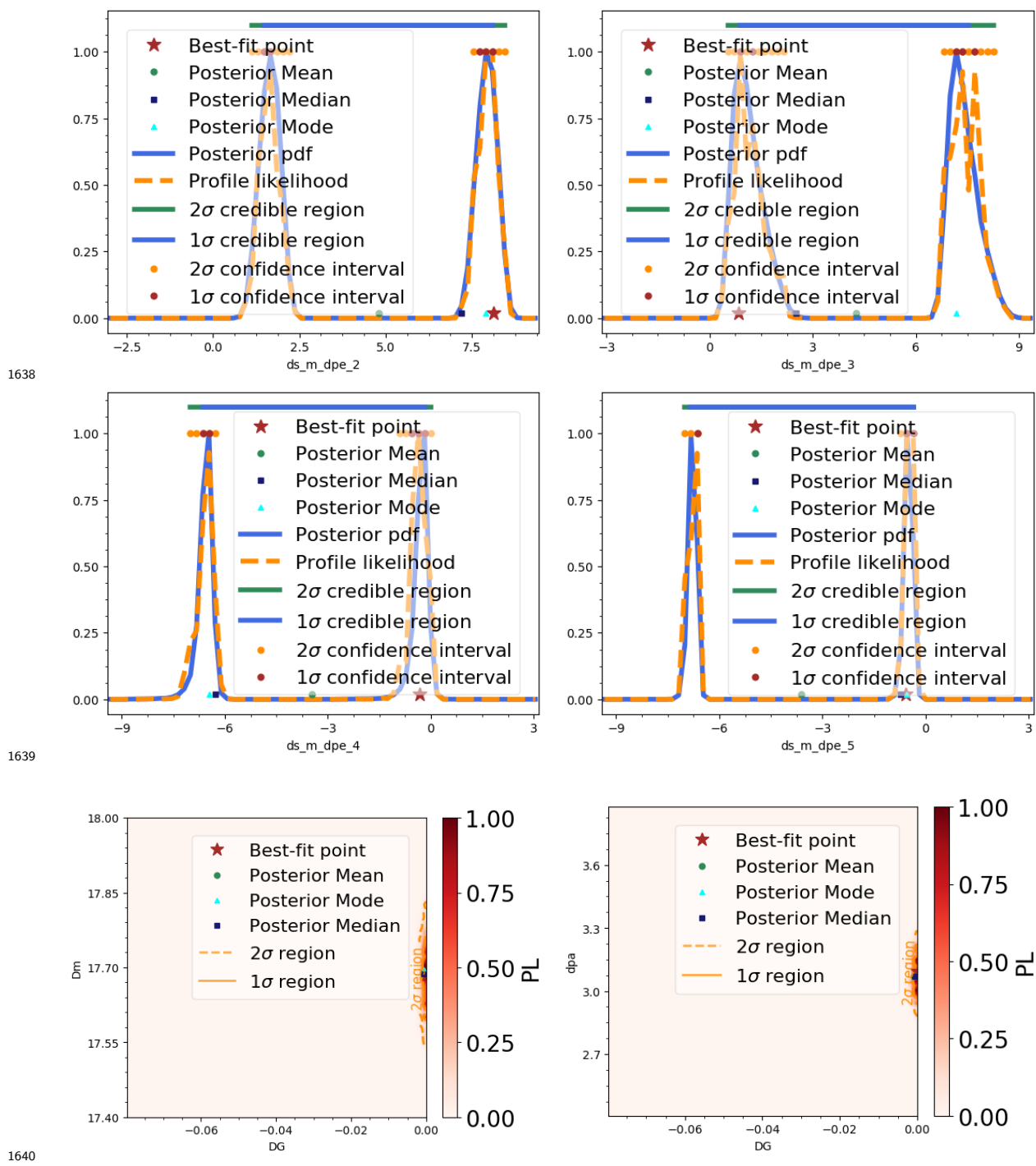
1623 5.3.1 Observables

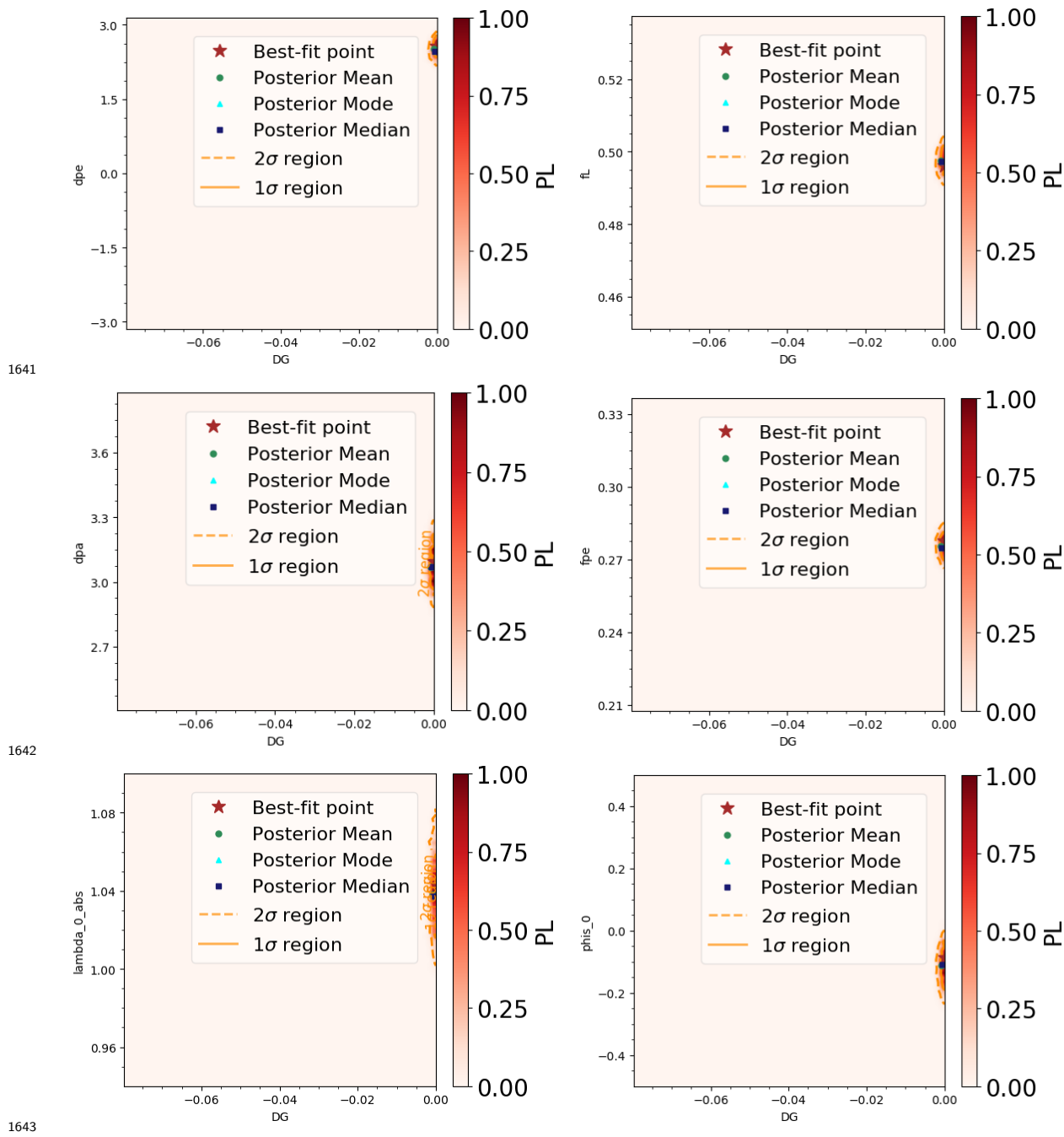
1624 5.4 ϕ_s MultiNest

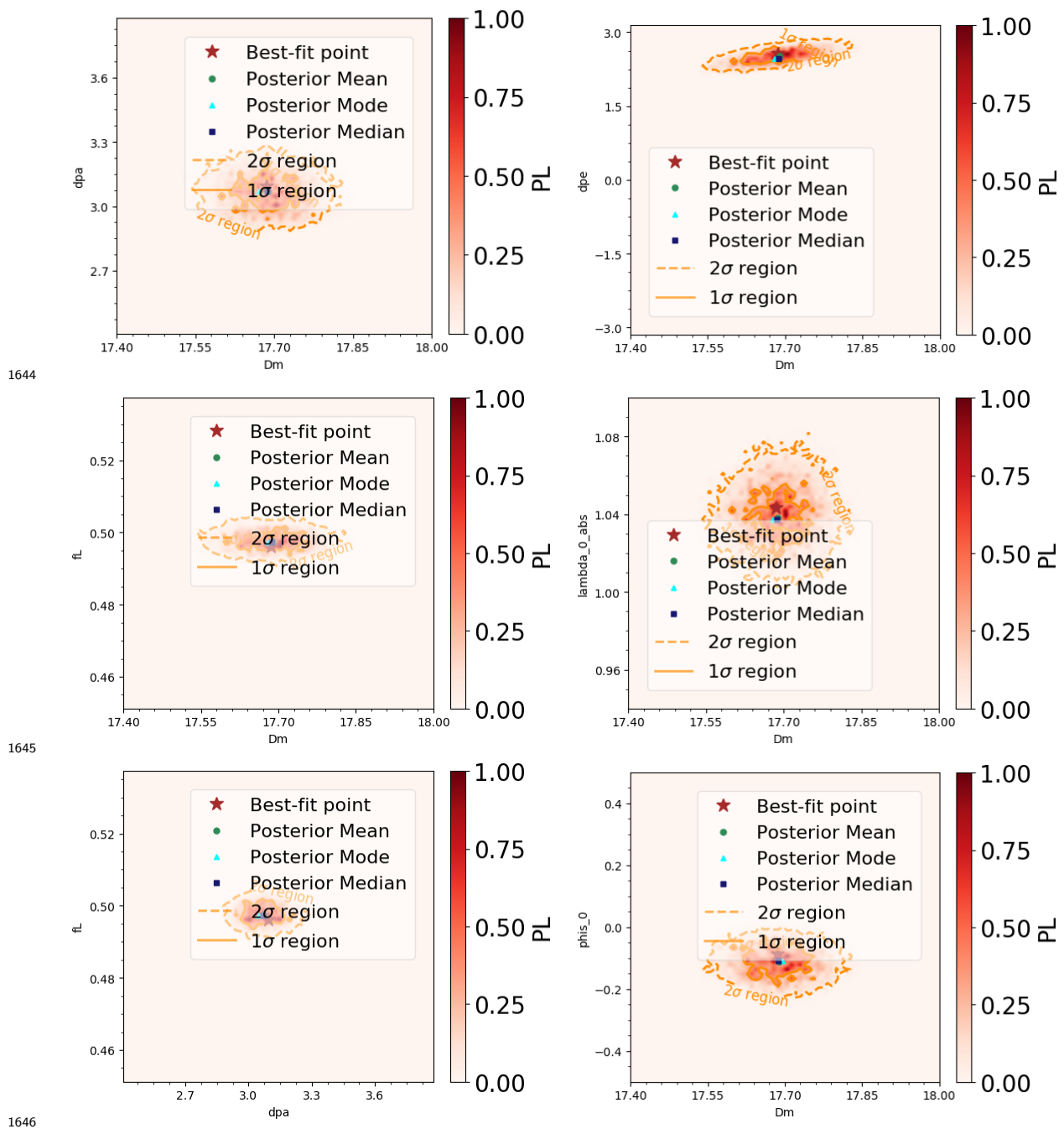
1625 A scan is performed using the `MultiNest` Bayesian inference tool [\[74\]](#), with [2016 LHCb data](#).
1626 More details on the `MultiNest` algorithm are given in the following subsection. The lower and
1627 upper bins are removed from the scan, as they represent a high computational cost and they
1628 don't have much statistics. Therefore, only 4 m_{KK} bins are used. To this same end, $\Gamma_s - \Gamma_d$
1629 is fixed to its [PDG value](#), $-0.002678 \text{ ps}^{-1}$. The results are shown in figures [5.4](#) and [5.4](#). As it
1630 can be seen from these, the scan results are in agreement with the fit results. Moreover, two
1631 minimas for positive and negative $\Delta \Gamma_s$ are shown. ...

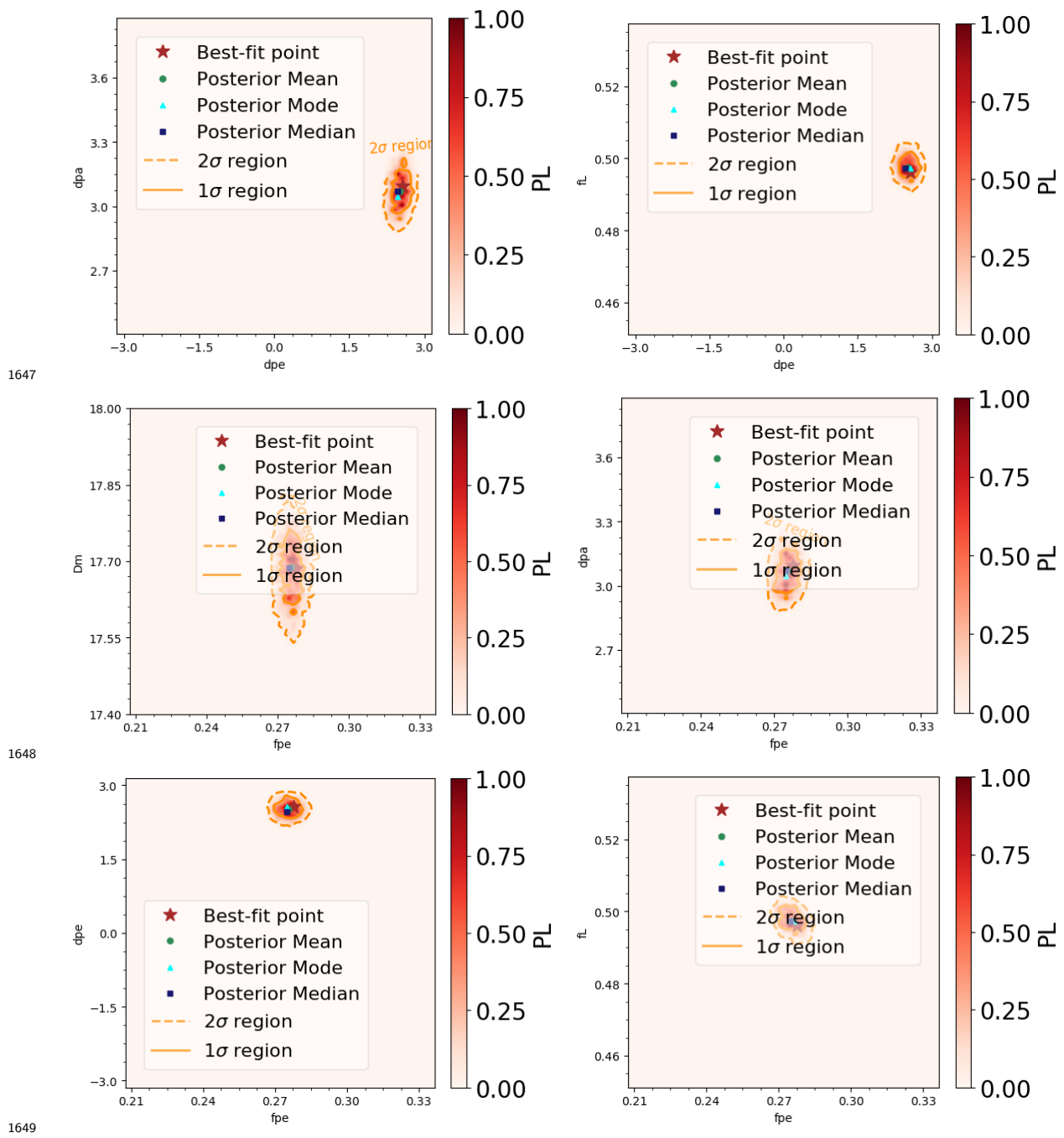


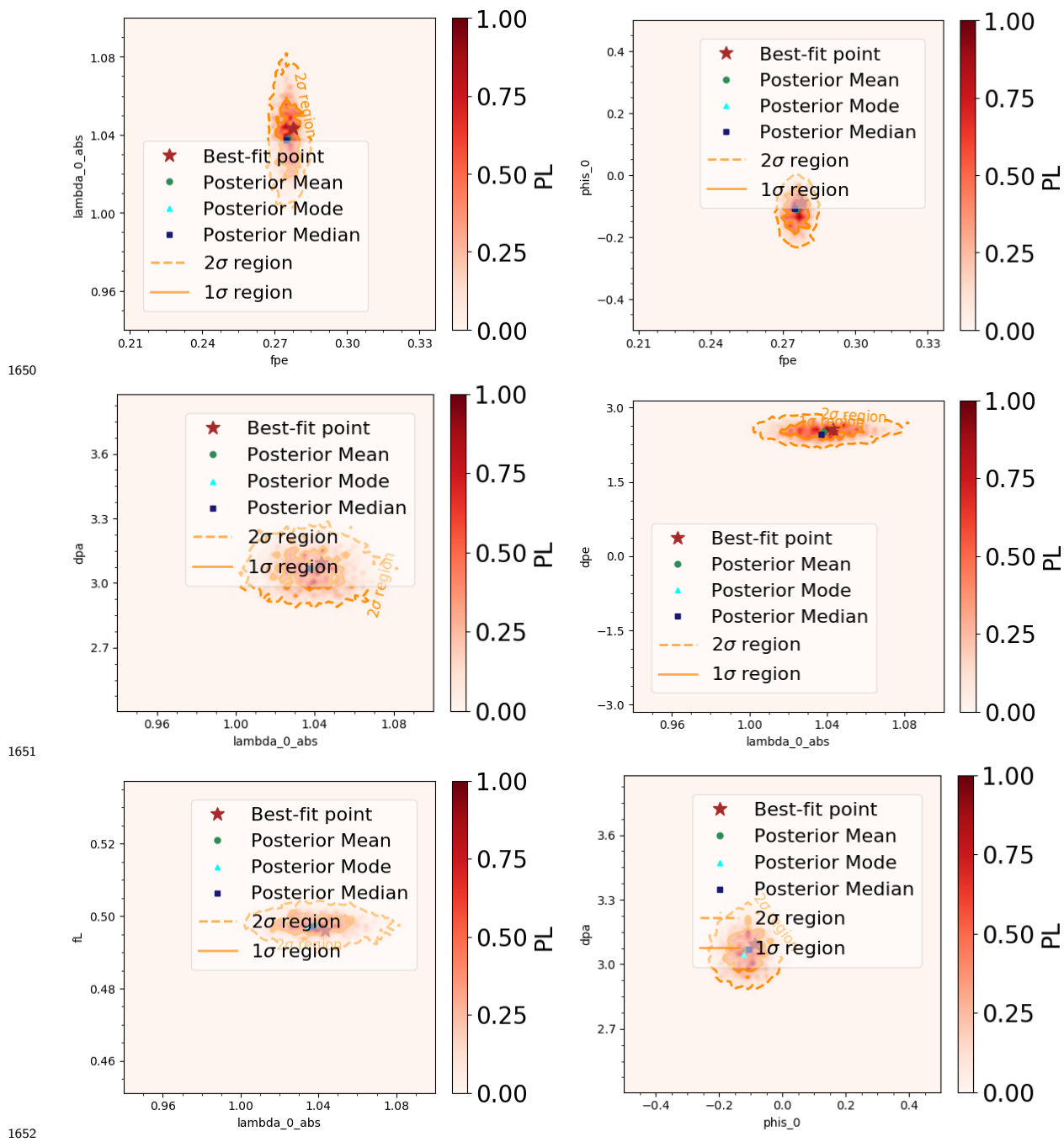


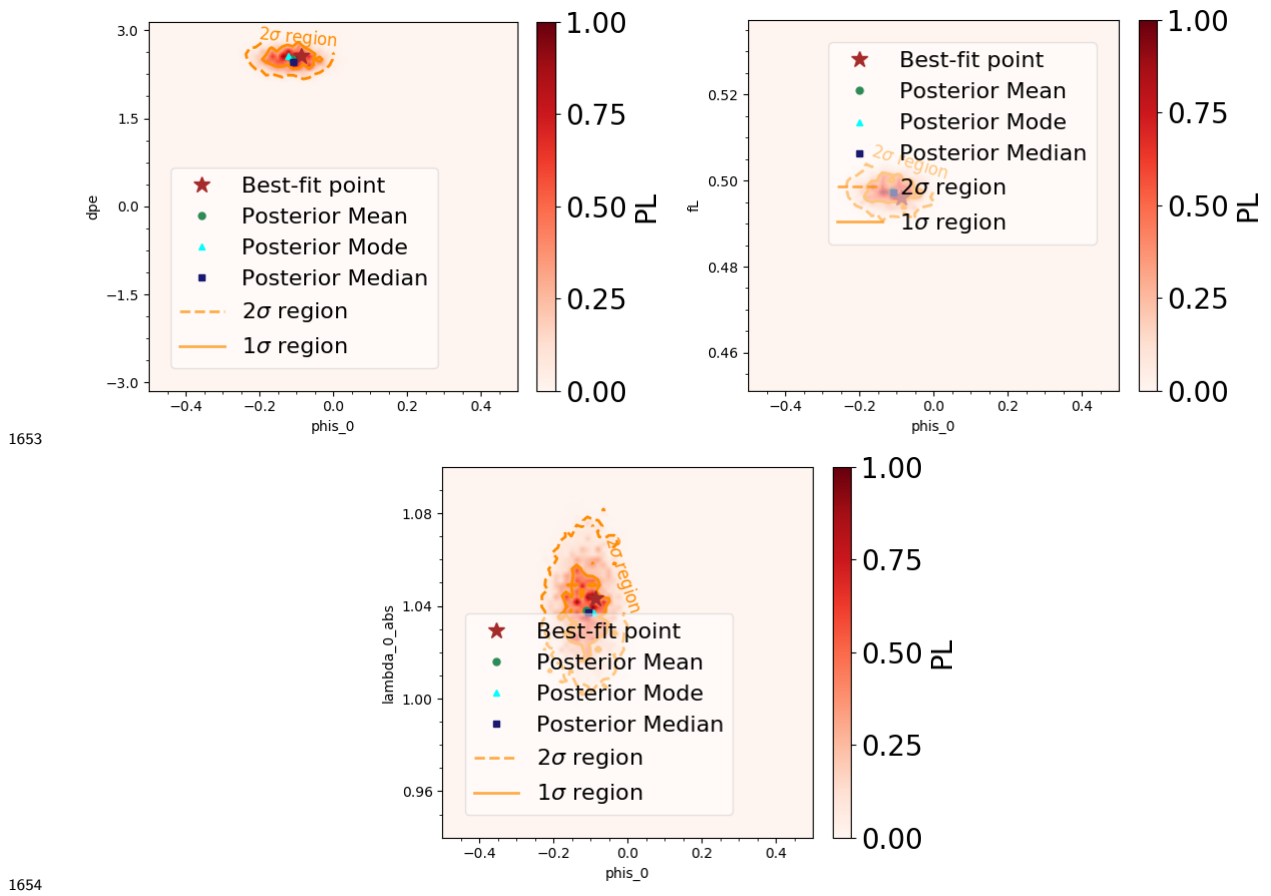












1655

- 1656 1. Description of the tool
- 1657 2. Description of the plots + Methodology
- 1658 3. Conclusions from the plots

1659 **5.4.1 MultiNest**

1660 ?? MultiNest is a multimodal, parallelizable nested sampling algorithm.

1661 It calculates the evidence, with an associated error estimate, and produces posterior samples
 1662 from distributions that may contain multiple modes and/or pronounced (curving) degeneracies
 1663 in high dimensions. The algorithm also naturally identifies individual modes of a distribution,
 1664 allowing for the evaluation of the 'local' evidence and parameter constraints associated with
 1665 each mode separately.

1666 **5.4.1.1 Bayesian inference**

1667 Bayesian inference provides a consistent approach to the estimation of a set of parameters Θ in
 1668 a model or hypothesis H , for the data, D , $Pr(\Theta|D, H)$, according to Bayes' theorem ref. The

1669 Bayesian evidence, $Pr(D|H) \equiv \mathcal{Z}$, usually ignored in parameter estimation problems, plays a
 1670 central role in model selection. It is the factor required to normalize the posterior over Θ .

$$\mathcal{Z} = \int \mathcal{L}(\Theta)\pi(\Theta)d^D\Theta \quad (5.21)$$

1671 Where D is the dimensionality of the parameter space. The evaluation of this integral is a
 1672 challenging numerical task.

1673 5.4.1.2 Nested sampling

1674 Nested sampling is a MC technique aimed at efficient evaluation of the Bayesian evidence, but
 1675 also produces posterior inferences as a by-product. It exploits the relation between the likelihood
 1676 and prior volumeeta ($dX = \pi(\Theta)d^D\Theta$) to transform the multidimensional evidence integral into
 1677 a one-dimensional integral:

$$\mathcal{Z} = \int_0^1 \mathcal{L}(X)dX \quad (5.22)$$

1678 $\mathcal{L}(X)$ is a monotonically decreasing function of X. Thus:

$$\mathcal{Z} = \sum_{i=1}^M \mathcal{L}_i w_i dX \quad (5.23)$$

1679 • i=0 and N 'active' or 'live' samples are drawn from the full prior $\pi(\Theta)$, so that the initial
 1680 prior volume is $X_0 = 1$.

1681 • Samples are sorted in order of their likelihood and the smallest (\mathcal{L}_0) is discarded, becoming
 1682 'inactive', and replaced by a point drawn from the prior subject to the constraint $\mathcal{L} > \mathcal{L}_0$.
 1683 $X_1 = t_1 X_0$, $Pr(t) = Nt^{N-1}$

1684 • Repeat previous tep, until the entire prior volume has been traversed. The algorithm thus
 1685 travels through nested shells of likelihood as the prior volume is reduced.

1686 • $X_i = \exp(-i/N)$

1687 • Algorithm is terminated on determining the evidence to some specified precision: $\Delta\mathcal{Z} =$
 1688 $\sum_{i=1}^N \mathcal{L}_j w_{M+j}$, $w_{M+j} = X_M/N$ where N are the active points.

1689 Once the evidence is found, posterior inferences can be easily generated using inactive and active
 1690 points generated in the nested sampling process. Each point is assigned the weight:

$$p_j = \frac{\mathcal{L}_j w_j}{\mathcal{Z}} \quad (5.24)$$

1691 **5.4.1.3 Ellipsoidal nested sampling**

1692 The most challenging task in implementing the nested sampling algorithm is drawing samples
1693 from the prior within the hard constraint $\mathcal{L} > \mathcal{L}_i$ at each iteration i . Ellipsoidal nested sam-
1694 ple tries to overcome this problem by approximating the iso-likelihood contour $\mathcal{L} = \mathcal{L}_i$ by a
1695 D-dimensional ellipsoid, determined from the covariance matrix of the current set of active
1696 points. New points are selected from the prior within this ellipsoidal bound until one fulfills
1697 the aforementioned condition. This method is not well suited to multimodal distribution. Its
1698 efficiency is improved by identifying distinct *clusters* of active points that are well separated and
1699 constructing an individual (enlarged) ellipsoid bound for each cluster.

1700 **5.4.1.4 The MultiNest algorithm**

1701 The clusters in which the set of active points are partitioned are then enclosed in ellipsoids and
1702 a new point is drawn from the set of these 'overlapping' ellipsoids (properly taking into account
1703 the overlaps. For highly multimodal problems, the nested sampling algorithm would require
1704 a large number of active points to ensure that all the modes are detected, resulting in a slow
1705 convergence.

1706 The MultiNest algorithm is controlled by two parameters:

- 1707 • The number of active points, N . It should be large enough that, in the initial sampling
1708 from the full prior space, there is a high probability that at least one point lies in the
1709 'basin of attraction' of each mode of the posterior. Also sufficiently large so that all the
1710 regions of the parameter space are sampled adequately, bigger than the dimensionality of
1711 the parameter space.
- 1712 • The maximum efficiency, e , that controls the sampling volume at each iteration, which is
1713 equal to the sum of the volumes of the ellipsoids enclosing the active point set.

¹⁷¹⁴ Chapter 6

¹⁷¹⁵ Kaon Physics

¹⁷¹⁶ 6.1 Introduction

¹⁷¹⁷ Kaons play a major role in particle physics, both for Standard Model (SM) and for New Physics
¹⁷¹⁸ (NP) searches. Their rare decays proceed mainly via flavour-changing neutral currents (FCNC),
¹⁷¹⁹ thus forbidden at loop level within the SM. This makes their branching fraction highly suppressed
¹⁷²⁰ in the SM. Therefore, they constitute an excellent probe for New Physics manifesting in new
¹⁷²¹ particles entering the process.

¹⁷²² Of all the possible kaon decays, the processes involving a $s \rightarrow d$ transition (see Fig. 6.1) have
¹⁷²³ the strongest CKM suppression factor ($\propto V_{td}V_{ts} \sim 10^{-4}$). Hence, they are particularly sensitive
¹⁷²⁴ to sources of flavour violation different from those of the Standard Model (SM). Indeed, flavour
¹⁷²⁵ violation can induce detectable effects at accessible energy in flavour-changing processes even if
¹⁷²⁶ the scale of the new dynamics is heavy and well above their direct production at accelerators.
¹⁷²⁷ Among these transitions, the decay $K_L^0 \rightarrow \pi^0\mu^+\mu^-$ has been shown to be sensitive to, for
¹⁷²⁸ example, models with extra dimensions [?]. However, the potential for this decay to constrain
¹⁷²⁹ scenarios beyond the Standard Model is limited by the large SM uncertainty on its branching
¹⁷³⁰ fraction prediction [?],

$$\mathcal{B}(K_L^0 \rightarrow \pi^0\mu^+\mu^-)_{\text{SM}} = \{1.4 \pm 0.3; 0.9 \pm 0.2\} \times 10^{-11}. \quad (6.1)$$

¹⁷³¹ The two numbers in the brackets correspond to two theoretical solutions, depending on whether
¹⁷³² constructive or destructive interference between the contributing waves is present. The reason
¹⁷³³ for the large theoretical uncertainty on $\mathcal{B}(K_L^0 \rightarrow \pi^0\mu^+\mu^-)_{\text{SM}}$ is the limited precision on the
¹⁷³⁴ chiral-perturbation-theory parameter $|a_S|$. An improved measurement of $\mathcal{B}(K_S^0 \rightarrow \pi^0\mu^+\mu^-)$ will
¹⁷³⁵ reduce this uncertainty. The most precise measurement of $\mathcal{B}(K_S^0 \rightarrow \pi^0\mu^+\mu^-)$ was performed by
¹⁷³⁶ the NA48 experiment at CERN [?], which obtained

$$\mathcal{B}(K_S^0 \rightarrow \pi^0\mu^+\mu^-) = (2.9^{+1.5}_{-1.2}(\text{stat}) \pm 0.2(\text{syst})) \times 10^{-9}. \quad (6.2)$$

¹⁷³⁷ Missing connector

¹⁷³⁸ Leptonic decays of pseudoscalar mesons with down-type quarks are known to be very sensitive
¹⁷³⁹ to the Higgs sector of the Minimal Supersymmetric Standard Model (MSSM), due to, among
¹⁷⁴⁰ others, enhancement factors proportional to $(\tan^6 \beta/M_A^4)$.¹ This factor comes from the so-

¹Note that this enhancement factor is not present in the up-type quark case.

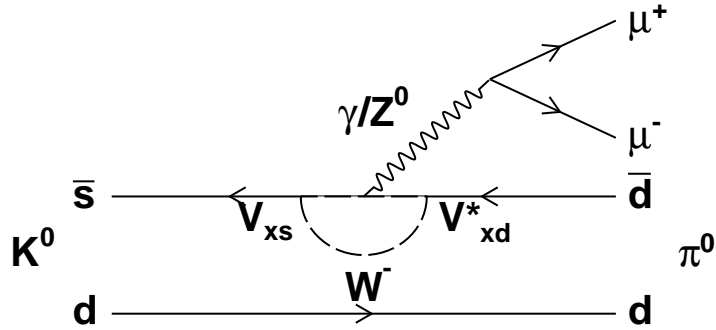


Figure 6.1: Feynman diagram of the process $K^0 \rightarrow \pi^0 \mu^+ \mu^-$.

1741 called non-holomorphic Yukawa terms at large $\tan \beta$ [?, ?, ?, ?, ?, ?],² which are triggered by
1742 the supersymmetric (SUSY) μ term, and hence the non-SUSY two-Higgs-doublet model cannot
1743 produce this enhancement [?]. The best known example is $B_s^0 \rightarrow \mu^+ \mu^-$ [?, ?, ?, ?, ?, ?, ?, ?, ?, ?, ?, ?, ?, ?, ?, ?, ?, ?, ?].
1744

1745 If Minimal Flavour Violation (MFV) is imposed, then $B_s^0 \rightarrow \mu^+ \mu^-$ is the dominant constraint
1746 in $P \rightarrow \mu^+ \mu^-$ decays. This is due to the stronger Yukawa coupling of the b -quark compared to
1747 the s -quark, and to the better experimental precision in $B_s^0 \rightarrow \mu^+ \mu^-$ compared to $B_d^0 \rightarrow \mu^+ \mu^-$.
1748 However, in the presence of new sources of flavour violation, the sensitivity of each mode depends
1749 on the flavour and CP structures of the corresponding terms.

1750 Hence, a priori, $B_s^0 \rightarrow \mu^+ \mu^-$, $B_d^0 \rightarrow \mu^+ \mu^-$, $K_S^0 \rightarrow \mu^+ \mu^-$, and $K_L^0 \rightarrow \mu^+ \mu^-$ are all separate
1751 constraints that carry complementary information in the general MSSM. The observables related
1752 to these decay modes are typically branching fractions and CP asymmetries. Even though
1753 the muon polarization could carry interesting information, it cannot be observed by current
1754 experiments.

1755 Even though the LHCb experiment ref was not initially designed to study these particles,
1756 the large amount of kaons produced at LHCb ref makes them a rich area to study. moreIt
1757 has demonstrated very good performance in the search for rare leptonic K_S^0 decays [?]. In
1758 the following sections, we evaluate the potential sensitivity of LHCb to $\mathcal{B}(K_S^0 \rightarrow \pi^0 \mu^+ \mu^-)$
1759 considering the data to be collected with the LHCb detector before and after its upgrade in
1760 2018, as well as supersymmetric contributions to the decay $K_S^0 \rightarrow \mu^+ \mu^-$ in light of current
1761 experimental data.

1762 6.2 $K_S^0 \rightarrow \pi^0 \mu^+ \mu^-$ Sensitivity study

1763 ??

1764

² The higher-order contributions have been derived up to two-loop level in refs. [?, ?, ?].

1765 6.2.1 Analysis strategy

1766 Decays of the K_s^0 in LHCb are characterized by decay vertices separated from the interaction
 1767 point³, and with tracks having an average transverse momentum significantly lower than those
 1768 from b and c decays. The transverse momentum range is similar to typical tracks generated in
 1769 the proton-proton collision and hence has almost no discriminating power.

1770 Muon candidates are combined into $\mu^+\mu^-$ pairs. Then a π^0 can be added to the dimuon pair
 1771 to make a fully reconstructed K_s^0 decay. However, since the reconstruction efficiency of the π^0
 1772 is limited, events in which no π^0 is found are also considered, based only on the dimuon information.
 1773 This leads to two independent analyses: one for the events in which all decay products
 1774 are considered (hereafter FULL) and one in which only the dimuon pair is used (hereafter PAR-
 1775 TIAL). The reconstructed candidates are then passed through a selection algorithm followed by
 1776 a *Boosted Decision Tree* (BDT) classification, to reduce the high level of background.

1777 The properties of the $K_s^0 \rightarrow \pi^0\mu^+\mu^-$ decays are studied using simulated samples with a
 1778 differential decay rate modeled according to Ref. [?]. The corresponding $\mu\mu$ mass distribution,
 1779 $m_{\mu\mu}$, as well as the dependence of the (cosine of the) dimuon helicity angle, $\cos\theta_\mu$ (see the angle
 1780 definitions in Fig. 6.2), on $m_{\mu\mu}$ are shown in Fig. 6.3.

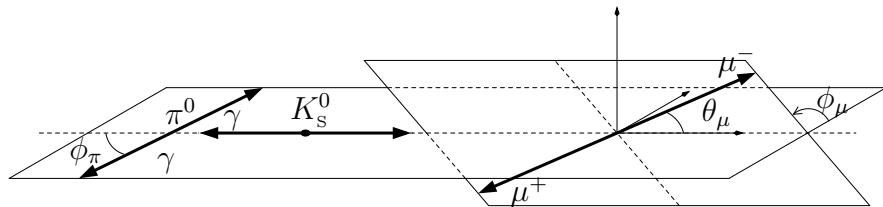


Figure 6.2: Definition of the helicity angles in the K_s^0 rest frame.

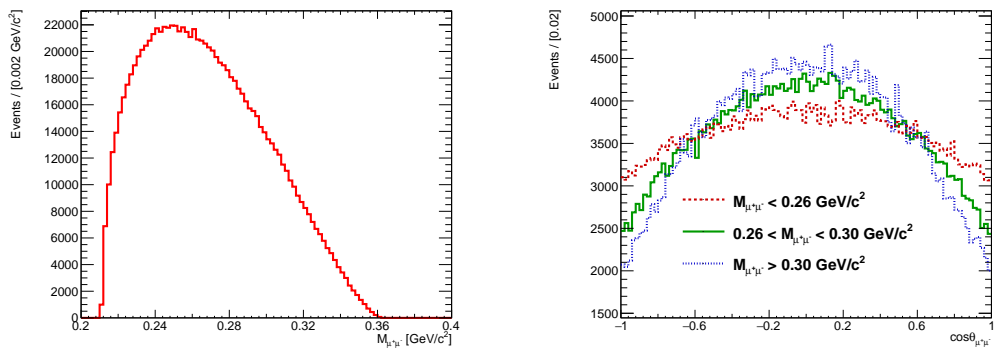


Figure 6.3: $m_{\mu\mu}$ distribution (left), and the dimuon helicity angle depending on $m_{\mu\mu}$ (right).

³The K_s^0 at LHC typically decays after traversing tens of centimeters to even several meters.

1781 The BDT is trained with simulated signal events and combinatorial background events from
 1782 the existing LHCb data. Since the main goal of this study is to evaluate the sensitivity for
 1783 the LHCb upgrade, where the trigger efficiency is expected to be very high, trigger unbiased
 1784 data samples are preferred. Therefore, the events are obtained from the *Trigger Independent of*
 1785 *Signal* (TIS) [?] category of the LHCb trigger. This means that the tracks and clusters of the
 1786 reconstructed candidate are not needed to fire the trigger at any level, because another object
 1787 in the underlying event already fired it. This ensures an almost trigger unbiased data set, while
 1788 still providing a sample much larger than random selection triggers.

1789 The expected signal yield is obtained assuming the NA48 central value for $\mathcal{B}(K_s^0 \rightarrow \pi^0 \mu^+ \mu^-)$,
 1790 normalizing the signal yield with respect to $K_s^0 \rightarrow \pi^+ \pi^-$ as

$$\frac{N(K_s^0 \rightarrow \pi^0 \mu^+ \mu^-)}{N(K_s^0 \rightarrow \pi^+ \pi^-)} = \frac{\mathcal{B}(K_s^0 \rightarrow \pi^0 \mu^+ \mu^-) \epsilon_{K_s^0 \rightarrow \pi^0 \mu^+ \mu^-}}{\mathcal{B}(K_s^0 \rightarrow \pi^+ \pi^-) \epsilon_{K_s^0 \rightarrow \pi^+ \pi^-}}, \quad (6.3)$$

1791 where the observed $K_s^0 \rightarrow \pi^+ \pi^-$ yield is extracted from data and the efficiency ratio, $\frac{\epsilon_{K_s^0 \rightarrow \pi^0 \mu^+ \mu^-}}{\epsilon_{K_s^0 \rightarrow \pi^+ \pi^-}}$,
 1792 is obtained from simulation.

1793 The $\mathcal{B}(K_s^0 \rightarrow \pi^0 \mu^+ \mu^-)$ sensitivity is measured in a pseudo-experiment study. First, the
 1794 signal and background yields are extrapolated for a desired expected luminosity and trigger effi-
 1795 ciency, then pseudo-experiments are generated according to those yields. The $\mathcal{B}(K_s^0 \rightarrow \pi^0 \mu^+ \mu^-)$
 1796 uncertainty is obtained from a fit to the K_s^0 mass distribution of the pseudo-experiments, using
 1797 the signal and background models obtained from MC and the fit to the available LHCb data,
 1798 respectively. The mass fit range is [420, 580] MeV/ c^2 .

1799 6.2.2 Reconstruction and selection

1800 Pairs of muon candidates are reconstructed combining opposite-charged tracks with hits in the
 1801 vertex locator (VELO), trigger tracker, tracker stations, and muon chambers. In addition, the
 1802 tracks are required to be separated by at least 6σ from any $p - p$ collision point in the event.
 1803 Tracks with transverse momentum lower than 80 MeV/ c are ignored. A dimuon candidate pair
 1804 can be combined with a π^0 candidate to build a K_s^0 candidate. The events in which the entire
 1805 decay chain is used are classified as FULL. When only the dimuon information is used, they are
 1806 clasified as PARTIAL.

1807 Neutral pion candidates are reconstructed from γ candidate pairs that correspond to two
 1808 independent clusters in the calorimeter. Each photon candidate is required to have a transverse
 1809 momentum of at least 200 MeV/ c and the pion candidate a mass within 30 MeV/ c^2 of the world
 1810 average π^0 mass. The mass resolution is then improved by constraining the π^0 candidate mass
 1811 to the world average π^0 mass, and by constraining the three-momentum vector of the K_s^0 to
 1812 point back to the production vertex. For the PARTIAL candidates, a momentum vector with an
 1813 absolute value of ≈ 10 GeV/ c is used as a representative of the π^0 momentum when calculating
 1814 the invariant mass. As a consequence of these kinematic constraints, the K_s^0 candidate mass
 1815 resolution depends only weakly on the π^0 momentum.

1816 Additional selection requirements are applied to reduce the amount of data to analyze, fulfil
 1817 the rate requirements for LHCb offline processing and reduce the amount of background. These
 1818 include a K_s^0 candidate lifetime of at least 1 ps and removing events in the kinematic region of
 1819 $\Lambda \rightarrow p\pi$ and $K_s^0 \rightarrow \pi^+ \pi^-$ in the Armenteros-Podolski plane [?]. The total reconstruction and
 1820 selection efficiency for the FULL channel is 5.47×10^{-4} .

Requiring a well-reconstructed π^0 implies an inefficiency penalty of a factor ten. Thus, a complementary strategy for the PARTIAL candidates is also investigated. Indeed, the constraints on the π^0 mass and the K_s^0 momentum are sufficient to create a peaking distribution if there is an estimate of the typical value of the π^0 momentum ($\approx 10 \text{ GeV}/c$), as shown in Fig. 6.4. A comparison of the reconstructed mass resolution between FULL and PARTIAL is difficult due to the asymmetric and non-Gaussian distribution of the PARTIAL case. To get an estimate, the corresponding FWHM values are calculated. In the FULL case, it is $23.3 \text{ MeV}/c^2$ and in the PARTIAL $40.6 \text{ MeV}/c^2$.

The PARTIAL selection does not require any information about a reconstructed π^0 . Some requirements had to be tightened in order to keep the background at a manageable level. These include a lower distance of closest approach between the two muon tracks; a minimum requirement on the K_s^0 vertex quality, $\chi^2/ndof = 9$; a higher minimum requirement on the K_s^0 vertex detachment from the interaction point; and minimum radial, z - and absolute distance requirements between the K_s^0 vertex and the interaction point. The total reconstruction and selection efficiency for the PARTIAL analysis is 3.0×10^{-3} , well above that of the FULL, but at a cost of an increased background yield.

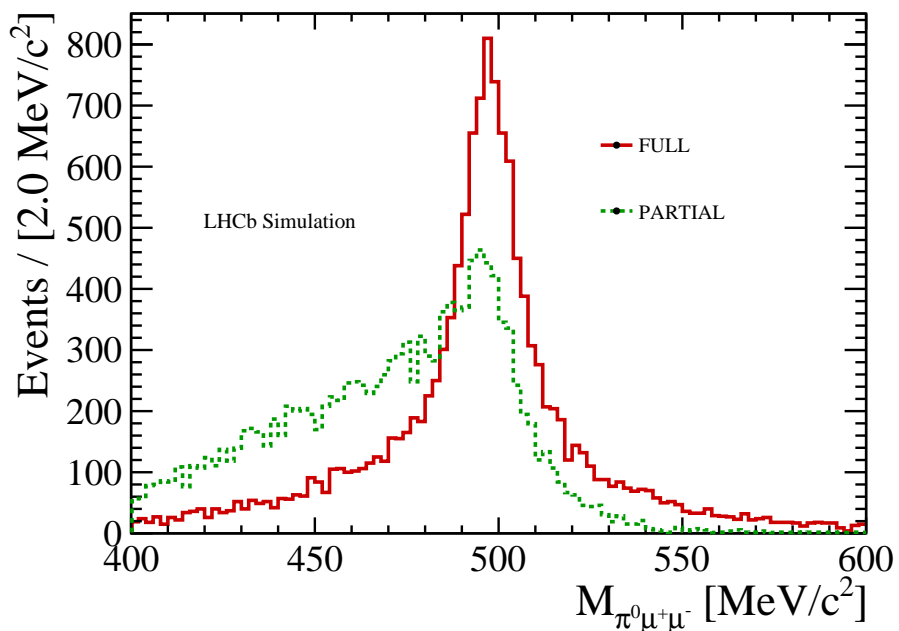


Figure 6.4: Comparison between the FULL (solid red) and PARTIAL (dashed green) kaon candidate mass distributions.

A BDT is used to separate signal from combinatorial background. It is trained with MC events (signal class) and a part of the data that is not used in the fit (combinatorial background class). The BDT uses information about the geometrical properties of the events, kinematics, track quality, and muon identification quality. The BDT response for signal and background for both FULL and PARTIAL is shown in Fig. 6.5.

The events are classified in four bins of the BDT response. The signal yields are obtained

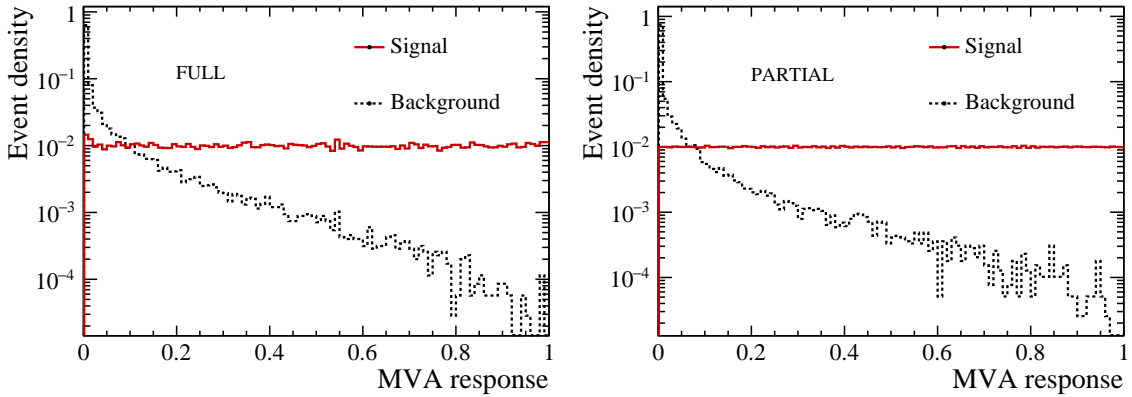


Figure 6.5: BDT response both for signal (solid red) and background (dashed black). Right: FULL channel. Left: PARTIAL channel. Signal and background are normalized to the same area.

1843 in a simultaneous fit of the mass distribution in each BDT bin, as described in the following
 1844 sections.

1845 6.2.3 Background sources

1846 Several sources of background are investigated to assess their relevance for a measurement of
 1847 $\mathcal{B}(K_s^0 \rightarrow \pi^0 \mu^+ \mu^-)$:

- 1848 • $K_s^0 \rightarrow \pi^+ \pi^-$ decays, where both pions are misidentified as muons, and in the case of
 1849 the FULL category, combined with a random π^0 from the underlying event. These decays
 1850 have a mass larger than that of the K_s^0 and do not enter the fit region, except for potential
 1851 residual tails that effectively add up to the combinatorial background. No evidence for
 1852 $K_s^0 \rightarrow \pi^+ \pi^-$ background is seen for the BDT region being fitted.
- 1853 • $K^0 \rightarrow \mu^+ \mu^- \gamma\gamma$ decays. This background was considered in the NA48 analysis [?], How-
 1854 ever, its contribution at LHCb is found to be negligible: In the case of the K_L^0 decay (with
 1855 a branching fraction of $1.0_{-0.6}^{+0.8} \times 10^{-8}$ [1]) the upper decay time acceptance introduces
 1856 an effective 10^{-3} reduction with respect to K_s^0 and hence the effective $\mathcal{B}(K_L^0 \rightarrow \mu^+ \mu^- \gamma\gamma)$
 1857 becomes as low as 10^{-11} . There is no experimental measurement of $\mathcal{B}(K_s^0 \rightarrow \mu^+ \mu^- \gamma\gamma)$,
 1858 however, since the process is dominated by the two-photon exchange⁴, it can be estimated
 1859 as:

$$\mathcal{B}(K_s^0 \rightarrow \mu^+ \mu^- \gamma\gamma) = \frac{\mathcal{B}(K_s^0 \rightarrow \gamma\gamma)}{\mathcal{B}(K_L^0 \rightarrow \gamma\gamma)} \mathcal{B}(K_L^0 \rightarrow \mu^+ \mu^- \gamma\gamma) \sim 4.8 \times 10^{-11} \quad (6.4)$$

1860 and is thus negligible.

- 1861 • $K_L^0 \rightarrow \pi^0 \pi^+ \pi^-$ decays. The mass distribution of these decays is shown in Fig. 6.6 as
 1862 obtained in simulation. Since there is no evidence of this background in the data, it is

⁴Isidori and D'Ambrosio, private communication.

neglected. Including a $K_L^0 \rightarrow \pi^0\pi^+\pi^-$ component to the observed background does not change significantly the sensitivity estimates. The K_S^0 counterpart has a branching fraction of 3.5×10^{-7} and thus is about four orders of magnitude smaller than $K_L^0 \rightarrow \pi^0\pi^+\pi^-$. In general, no sign of a resonant structure in the $\pi^+\pi^-\pi^0$ is seen on data.

- Combinatorial background. Combinatorial background is considered to be composed by random combination of tracks, including those generated by pseudo-random combinations of hits during the pattern recognition. It has a monotonic shape across the studied invariant mass range.

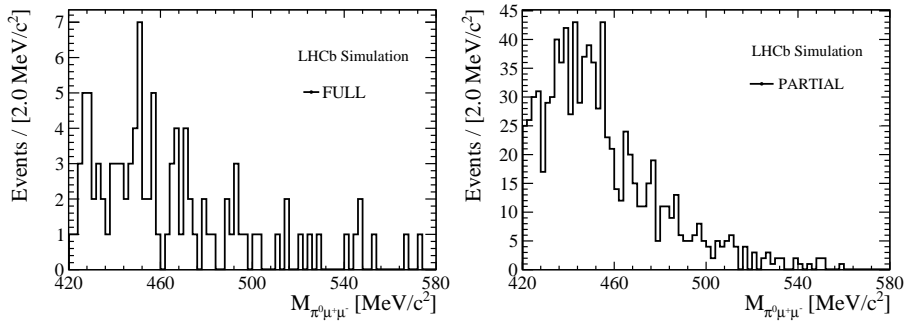


Figure 6.6: Invariant mass distribution of simulated $K^0 \rightarrow \pi^+\pi^-\pi^0$ decays selected in the FULL (left) and PARTIAL (right) categories.

6.2.4 Fit model

Only events in the BDT range [0.6,1] are considered in the fit to the data. A simultaneous fit to the mass distribution across four equally-sized independent bins of the BDT response is performed. The combinatorial background is described with an exponential PDF for both FULL and PARTIAL analysis, with independent floating yields and decay constants in each BDT bin. The signal model is an Hypathia distribution [?] with different configurations for FULL and PARTIAL (see Fig. 6.7). The signal model parameters are independent in each BDT bin and are obtained from simulation. The fractions of signal events allotted to each BDT bin are also fixed from values obtained from simulation, with a total signal yield remaining as the sole free parameter describing signal in the simultaneous fit. The signal yield is floated in the fit to the data. It is measured to be compatible with zero within one to two sigma. The fit projections to the FULL and PARTIAL data are shown in Fig. 6.8.

6.2.5 Expected sensitivity

The expected statistical precision on $\mathcal{B}(K_S^0 \rightarrow \pi^0\mu^+\mu^-)$ for multiple values of the integrated luminosity up to 100 fb^{-1} is estimated in this section. The TIS samples used are equivalent to a 100% trigger efficiency sample with an integrated luminosity of 4.9 and 0.77 pb^{-1} for the FULL and PARTIAL samples, respectively. The expected background yield is extrapolated from the

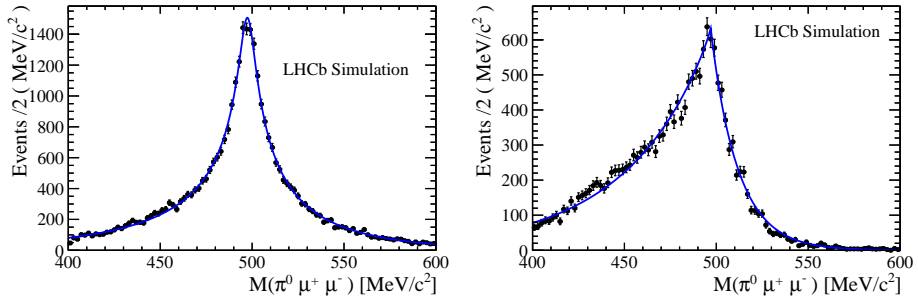


Figure 6.7: Signal fit using the Hypathia function for FULL (left) and PARTIAL (right) categories.

1888 current data fit result, where the signal yield is consistent with zero. The background yield is
 1889 scaled linearly for larger integrated luminosities.

1890 For each integrated luminosity in the studied range, sets of pseudo-experiments are generated
 1891 with the above background expectations, and with a signal yield expectation of

$$N_{sig} = \frac{\mathcal{B}(K_s^0 \rightarrow \pi^0 \mu^+ \mu^-)}{\mathcal{B}(K_s^0 \rightarrow \pi^+ \pi^-)} \frac{\epsilon_{K_s^0 \rightarrow \pi^0 \mu^+ \mu^-}}{\epsilon_{K_s^0 \rightarrow \pi^+ \pi^-}} N(K_s^0 \rightarrow \pi^+ \pi^-) \times \frac{L_{fut}}{L_{curr}}, \quad (6.5)$$

1892 where L_{fut} and L_{curr} are the future and current luminosities, respectively. The models de-
 1893 scribed in Sect. 6.2.4 are fit to each pseudo-experiment with a floating $\mathcal{B}(K_s^0 \rightarrow \pi^0 \mu^+ \mu^-)$. The
 1894 background model parameters used are the ones obtained from the fit to the data Sect. 6.2.4.
 1895 The statistical uncertainties are obtained as the variations of $\mathcal{B}(K_s^0 \rightarrow \pi^0 \mu^+ \mu^-)$ that deviate
 1896 from the minimum of the log-likelihood profile by half a unit. Finally, the uncertainties are
 1897 averaged across the set of pseudo-experiments for a given integrated luminosity. The uncer-
 1898 tainties on the background extrapolation are large and translate into large uncertainties on the
 1899 luminosity needed for achieving a given sensitivity. The resulting sensitivity curves are shown
 1900 in Fig. 6.9. It can be seen that the analyses of both PARTIAL and FULL categories can lead
 1901 to a precision better than NA48 for the LHCb upgrade if a trigger efficiency above $\approx 50\%$ can
 1902 be maintained. The K_s^0 production cross-section increases by $\approx 20\%$ at 14 TeV compared to 8
 1903 TeV, but this increase is cancelled by a larger fraction of K_s^0 decaying outside of the VELO vol-
 1904 ume. For this reason, no energy correction has been applied to the sensitivity estimate. Studies
 1905 of $K_s^0 \rightarrow \pi^0 \mu^+ \mu^-$ and minimum bias samples simulated with the LHCb upgrade detector and
 1906 conditions show that the High Level Trigger rate can be kept low enough for a 100 % efficiency.
 1907 Further timing studies are currently ongoing.

1908 6.2.6 Conclusions

1909 A precise measurement of the $K_s^0 \rightarrow \pi^0 \mu^+ \mu^-$ branching fraction is crucial for a precise $\mathcal{B}(K_L^0 \rightarrow$
 1910 $\pi^0 \mu^+ \mu^-)$ SM theoretical prediction and the search for physics beyond the SM in $K_L^0 \rightarrow \pi^0 \mu^+ \mu^-$.
 1911 The sensitivity of the LHCb experiment to $\mathcal{B}(K_s^0 \rightarrow \pi^0 \mu^+ \mu^-)$ was studied based on 3 fb^{-1} of data
 1912 recorded at 7 and 8 TeV center-of-mass energy during 2011 and 2012, and on 0.3 fb^{-1} of data
 1913 recorded at 13 TeV center-of-mass energy during 2016. Full and partial decay reconstruction

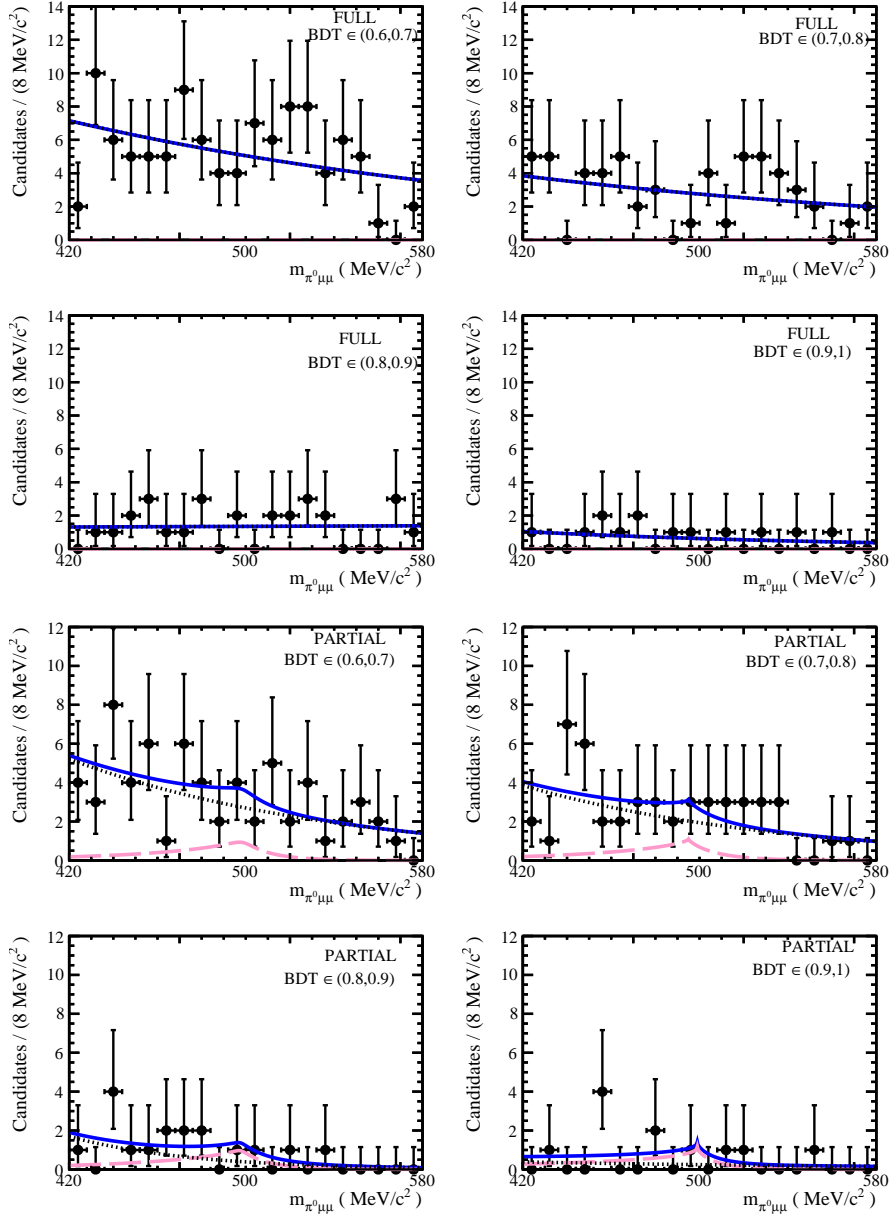


Figure 6.8: Fit to data for FULL (top) and PARTIAL (bottom) categories. The magenta dashed line shows the signal contribution, the dotted black line the background, and the solid blue line the prediction from the total fit model.

algorithms were considered, aiming at a high reconstruction efficiency. The sensitivity study was performed using pseudo-experiments by extrapolating signal yield results based on the currently available data to expected future integrated luminosities. If a trigger efficiency of at least 50% can be assured in the future, LHCb can determine $\mathcal{B}(K_S^0 \rightarrow \pi^0 \mu^+ \mu^-)$ with a precision significantly better than that of NA48.

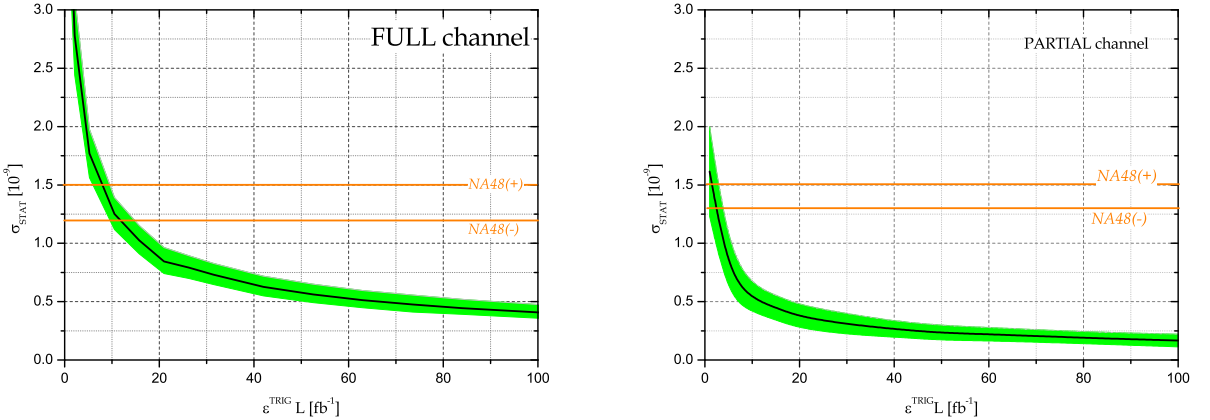


Figure 6.9: Expected precision on $\mathcal{B}(K_s^0 \rightarrow \pi^0 \mu^+ \mu^-)$ for the FULL (top) and PARTIAL (bottom) channels, as a function of the integrated luminosity times trigger efficiency, $L \times \varepsilon^{TRIG}/SEL$.

1919 6.3 Probing SUSY effects in $K_s^0 \rightarrow \mu^+ \mu^-$

1920 In this section, the MSSM effects in the $K_s^0 \rightarrow \mu^+ \mu^-$ decay are explored. The Standard Model
 1921 (SM) expectation is $(5.18 \pm 1.50_{LD} \pm 0.02_{SD}) \times 10^{-12}$ [?, ?, ?], where the first uncertainty comes
 1922 from the long-distance (LD) contribution and the second one comes from the short-distance (SD)
 1923 contribution. On the other hand, the current experimental upper bound is 8×10^{-10} at 90% C.L.,
 1924 using 3 fb^{-1} of LHCb data [?]. The LHCb upgrade could reach sensitivities at the level of about
 1925 1×10^{-11} or even below, approaching the SM prediction [?]. The branching ratio $\mathcal{B}(K_s^0 \rightarrow \mu^+ \mu^-)$
 1926 is predicted taking into account the relevant experimental constraints on the branching fractions
 1927 $\mathcal{B}(K_L^0 \rightarrow \mu^+ \mu^-)$, $\mathcal{B}(B^+ \rightarrow \tau^+ \nu_\tau)$ and $\mathcal{B}(K^+ \rightarrow \mu^+ \nu_\mu)$, the CP violation parameters $\varepsilon'_K/\varepsilon_K$ and
 1928 ε_K , the $K_L^0 - K_S^0$ mass difference, $\Delta M_K \equiv M_{K_L^0} - M_{K_S^0} > 0$, and the Wilson coefficient C_7 from
 1929 $b \rightarrow s\gamma$. For this, the Mass Insertion Approximation (hereafter MIA) [?] is used, treating the
 1930 corresponding terms as phenomenological parameters at the SUSY scale. The details of the
 1931 formalism are given in subsection 6.3.1. The subsets of the MSSM parameter space are studied
 1932 in scans performed on Graphics Processing Units (GPU), as detailed in section 6.3.2. The results
 1933 are shown in section ?? and conclusions are drawn in section 6.2.6.

1934 6.3.1 Formalism

1935 The followed notation is the one of refs. [?, 73]. The right-handed down and up squarks are
 1936 denoted as D and U , respectively. Because of the $SU(2)_L$ doublet, the two left-handed squarks
 1937 are **degenerate**, and are denoted as Q . The average of the Q , D , and U -squark masses squared
 1938 are denoted by \tilde{m}_Q^2 , \tilde{m}_d^2 , \tilde{m}_u^2 , respectively.

1939 The mass insertions (hereafter MIs) are defined as:

$$(\delta_d^{LL})_{ij} = \frac{[(\mathcal{M}_D^2)_{LL}]_{ij}}{\tilde{m}_Q^2} = \frac{(m_Q^2)_{ji}}{\tilde{m}_Q^2}, \quad (6.6)$$

$$(\delta_u^{LL})_{ij} = \frac{[(\mathcal{M}_U^2)_{LL}]_{ij}}{\tilde{m}_Q^2} = \frac{(V m_Q^2 V^\dagger)_{ji}}{\tilde{m}_Q^2}, \quad (6.7)$$

$$(\delta_d^{RR})_{ij} = \frac{[(\mathcal{M}_D^2)_{RR}]_{ij}}{\tilde{m}_d^2} = \frac{(m_D^2)_{ij}}{\tilde{m}_d^2}, \quad (6.8)$$

1940 where V is the Cabibbo–Kobayashi–Maskawa (CKM) matrix and $\mathcal{M}_{D,U}^2$ are the 6×6 squark
 1941 mass matrices. Note that the indices ij are inverted for LL . Comparison with the SUSY Les
 1942 Houches Accord 2 convention [?] is given in the appendix of ref. [73].

1943 The running coupling constants α_1 , α_2 , and α_3 are defined as

$$\alpha_1 = \frac{g_1^2}{4\pi} = \frac{5}{3} \frac{g'^2}{4\pi}, \quad (6.9)$$

$$\alpha_2 = \frac{g_2^2}{4\pi} = \frac{g^2}{4\pi}, \quad (6.10)$$

$$\alpha_3 = \frac{g_3^2}{4\pi} = \frac{g_s^2}{4\pi}, \quad (6.11)$$

1944 where g' , g , and g_s are the $U(1)_Y$, $SU(2)_L$, and $SU(3)_C$ group coupling constants, respectively.
 1945 In the following, these couplings are evaluated at the μ^{SUSY} scale, defined as $\mu^{\text{SUSY}} = \sqrt{\tilde{m}_Q M_3}$.

1946 6.3.1.1 Observables

1947 As will be shown in the next subsections, the main MSSM contribution to $\mathcal{B}(K_S^0 \rightarrow \mu^+ \mu^-)$ is
 1948 proportional to $\left[(\delta_d^{LL(RR)})_{12} \mu \tan^3 \beta M_3 / M_A^2 \right]^2$. In order to constrain those parameters, the
 1949 following observables are calculated in addition to $\mathcal{B}(K_S^0 \rightarrow \mu^+ \mu^-)$:

- 1950 • Observables sensitive, among others, to the off-diagonal mass insertion terms $(\delta_d^{LL(RR)})_{12}$:
 1951 $\mathcal{B}(K_L^0 \rightarrow \mu^+ \mu^-)$, $\varepsilon'_K / \varepsilon_K$, ε_K , and ΔM_K .⁵
- 1952 • Observables sensitive to $\tan \beta$ and the heavy Higgs mass: $\mathcal{B}(B^+ \rightarrow \tau^+ \nu_\tau)$, $\mathcal{B}(K^+ \rightarrow \mu^+ \nu_\mu)$,
 1953 ΔC_7 .

1954 The definitions of $\mathcal{B}(B^+ \rightarrow \tau^+ \nu_\tau)$, $\mathcal{B}(K^+ \rightarrow \mu^+ \nu_\mu)$, and C_7 are given in ref. [73] and
 1955 the remaining observables are defined in the following subsections. The CKM matrix is fitted
 1956 excluding measurements with potential sensitivity to MSSM contributions.

1957 The constraints that are imposed on physics observables sensitive to the MSSM same pa-
 1958 rameters as $\mathcal{B}(K_S^0 \rightarrow \mu^+ \mu^-)$ are listed in table 6.1, where the EXP/SM represents the measured
 1959 value over the SM prediction with their uncertainties. Due to the poor theoretical knowledge
 1960 of ΔM_K , it is assigned a 100% theoretical uncertainty; thus, the constraint imposed on this

⁵ The contributions to $\mathcal{B}(K \rightarrow \pi \nu \bar{\nu})$ are controlled by an additional free parameter, the slepton mass, and $\mathcal{O}(1)$ effects are possible in this scenario [?].

Table 6.1: Physics observables constraints imposed in this study. The two different constraints on $\mathcal{B}(K_L^0 \rightarrow \mu^+ \mu^-)^{\text{EXP/SM}}$ arise from an unknown sign of $A_{L\gamma\gamma}^\mu$ in eq. (6.21) (see refs. [?, ?]).

| Observable | Constraint |
|--|--|
| $\mathcal{B}(K_S^0 \rightarrow \mu^+ \mu^-)^{\text{EXP/SM}}$ | unconstrained |
| $\mathcal{B}(K_L^0 \rightarrow \mu^+ \mu^-)^{\text{EXP/SM}}$ | $1.00 \pm 0.12 (+)$ [?, ?, ?] $0.84 \pm 0.16 (-)$ [?, ?, ?] |
| $\Delta M_K^{\text{EXP/SM}}$ | 1 ± 1 |
| $\varepsilon_K^{\text{EXP/SM}}$ | 1.05 ± 0.10 [?, ?, ?] |
| $\Delta(\varepsilon'_K/\varepsilon_K)^{\text{EXP-SM}}$ | $[15.5 \pm 2.3(\text{EXP}) \pm 5.07(\text{TH})] \times 10^{-4}$ [?, ?] |
| $\mathcal{B}(B^+ \rightarrow \tau^+ \nu_\tau)^{\text{EXP/SM}}$ | 0.91 ± 0.22 [?] |
| $\mathcal{B}(K^+ \rightarrow \mu^+ \nu_\mu)^{\text{EXP/SM}}$ | 1.0004 ± 0.0095 [?] |
| ΔC_7 | -0.02 ± 0.02 [?] |
| $\tan \beta : M_A$ plane | ATLAS limits for hMSSM scenario [?] |
| LSP | Lightest neutralino |
| B_G | $1 \pm 3(\text{TH})$ [?, ?] |

observable penalizes only $\mathcal{O}(1)$ effects. It is not counted as a degree of freedom in the χ^2 tests, so that the ΔM_K constraint can only make the bounds tighter, but never looser.

Remaining constraints can in principle be satisfied by adjusting the other parameters of the model. In particular, B physics constraints not included in the list can be satisfied by parameters unspecified in the scan (e.g. setting $\delta_{13} \approx \delta_{23} \approx 0$ and small A_t). The relation of eq. (6.7) may induce non-zero up-type MIIs in the B sector and hence modify $B_{s(d)}^0 \rightarrow \mu^+ \mu^-$. These effects were checked and found to be negligible in the considered scenarios. The large SUSY masses in our scan are typically beyond the reach of LHC.

The lattice values for $(\varepsilon'_K/\varepsilon_K)^{\text{SM}}$ used are from refs. [?, ?, ?, ?], although the conclusions extracted from this study remain largely unchanged if the χ_{PT} value from refs. [?, ?, ?] is used instead. Both $\varepsilon_K^{\text{EXP/SM}}$ and $\Delta(\varepsilon'_K/\varepsilon_K)^{\text{EXP-SM}}$ are discussed in more detail in the following subsections.

6.3.1.2 $K_s^0 \rightarrow \mu^+ \mu^-$

The $|\Delta S| = 1$ effective Hamiltonian relevant for the $K^0 \rightarrow \ell\bar{\ell}$ transition at the Z boson mass scale is

$$\mathcal{H}_{\text{eff}} = -C_A Q_A - \tilde{C}_A \tilde{Q}_A - C_S Q_S - \tilde{C}_S \tilde{Q}_S - C_P Q_P - \tilde{C}_P \tilde{Q}_P + \text{H.c.}, \quad (6.12)$$

where C_A , C_S and C_P are the axial, scalar and pseudoscalar Wilson coefficients. The right-handed and left-handed axial (\tilde{Q}_A , Q_A), scalar (Q_S , \tilde{Q}_S) and pseudoscalar (Q_P , \tilde{Q}_P) operators

1978 are given by:

$$\begin{aligned} Q_A &= (\bar{s}\gamma^\mu P_L d)(\bar{\ell}\gamma_\mu\gamma_5\ell), & \tilde{Q}_A &= (\bar{s}\gamma^\mu P_R d)(\bar{\ell}\gamma_\mu\gamma_5\ell), \\ Q_S &= m_s(\bar{s}P_R d)(\bar{\ell}\ell), & \tilde{Q}_S &= m_s(\bar{s}P_L d)(\bar{\ell}\ell), \\ Q_P &= m_s(\bar{s}P_R d)(\bar{\ell}\gamma_5\ell), & \tilde{Q}_P &= m_s(\bar{s}P_L d)(\bar{\ell}\gamma_5\ell), \end{aligned} \quad (6.13)$$

1979 where $P_{L,R}$ are the left and right-handed projection operators. For $\mathcal{B}(K_{S,L}^0 \rightarrow \mu^+\mu^-)$ ⁶, there
1980 are two contributions from S-wave ($A_{S,L}$) and P-wave transitions ($B_{S,L}$), resulting in:⁷

$$\mathcal{B}(K_{S,L}^0 \rightarrow \mu^+\mu^-) = \tau_{S,L}\Gamma(K_{S,L}^0 \rightarrow \mu^+\mu^-) = \tau_{S,L} \frac{f_K^2 M_K^3 \beta_\mu}{16\pi} (|A_{S,L}|^2 + \beta_\mu^2 |B_{S,L}|^2), \quad (6.14)$$

1981 with

$$A_S = \frac{m_s M_K}{m_s + m_d} \text{Im}(C_P - \tilde{C}_P) + \frac{2m_\mu}{M_K} \text{Im}(C_A - \tilde{C}_A), \quad (6.15)$$

$$B_S = \frac{2G_F^2 M_W^2 m_\mu}{\pi^2 M_K} B_{S\gamma\gamma}^\mu - \frac{m_s M_K}{m_s + m_d} \text{Re}(C_S - \tilde{C}_S), \quad (6.16)$$

1982 and

$$A_L = \frac{2G_F^2 M_W^2 m_\mu}{\pi^2 M_K} A_{L\gamma\gamma}^\mu - \frac{m_s M_K}{m_s + m_d} \text{Re}(C_P - \tilde{C}_P) - \frac{2m_\mu}{M_K} \text{Re}(C_A - \tilde{C}_A), \quad (6.17)$$

$$B_L = \frac{m_s M_K}{m_s + m_d} \text{Im}(C_S - \tilde{C}_S), \quad (6.18)$$

1983 where

$$\beta_\mu = \sqrt{1 - \frac{4m_\mu^2}{M_K^2}}. \quad (6.19)$$

1984 The long-distance contributions are [?, ?, ?, ?]:

$$\frac{2G_F^2 M_W^2 m_\mu}{\pi^2 M_K} B_{S\gamma\gamma}^\mu = (-2.65 + 1.14i) \times 10^{-11} (\text{GeV})^{-2}, \quad (6.20)$$

$$\frac{2G_F^2 M_W^2 m_\mu}{\pi^2 M_K} A_{L\gamma\gamma}^\mu = \pm(0.54 - 3.96i) \times 10^{-11} (\text{GeV})^{-2}, \quad (6.21)$$

1985 with⁸

$$B_{S\gamma\gamma}^\mu = \frac{\pi\alpha_0}{G_F^2 M_W^2 f_K M_K |H(0)|} \mathcal{I} \left(\frac{m_\mu^2}{M_K^2}, \frac{m_{\pi^\pm}^2}{M_K^2} \right) \sqrt{\frac{2\pi}{M_K} \frac{\mathcal{B}(K_S^0 \rightarrow \gamma\gamma)^{\text{EXP}}}{\tau_S}}, \quad (6.22)$$

$$A_{L\gamma\gamma}^\mu = \frac{\pm 2\pi\alpha_0}{G_F^2 M_W^2 f_K M_K} \mathcal{A}(M_K^2) \sqrt{\frac{2\pi}{M_K} \frac{\mathcal{B}(K_L^0 \rightarrow \gamma\gamma)^{\text{EXP}}}{\tau_L}}, \quad (6.23)$$

⁶ The electron modes are suppressed by m_e^2/m_μ^2 , and we do not consider them in this paper.

⁷ Our result agrees with refs. [?, ?, ?, ?]. However, it disagrees with notable literature [?, 73] after discarding the long-distance contributions. We found that C_{10}^{SM} should be $-C_{10}^{\text{SM}}$ in eq. (3.45) of ref. [73], and $(C_P - C'_P)$ should be $(C'_P - C_P)$ in eq. (2.4) of ref. [?].

⁸ Note that $B_{S\gamma\gamma}^\mu$ is denoted by $A_{S\gamma\gamma}^\mu$ in refs. [?, ?].

where a two-loop function $\mathcal{I}(a, b)$ from the $2\pi^\pm 2\gamma$ intermediate state is given in refs. [?, ?], a pion one-loop contribution with two external on-shell photons is represented as $H(0) = 0.331 + i0.583$ [?], and a one-loop function $\mathcal{A}(s)$ from the 2γ intermediate state is given in refs. [?, ?].

Here, $\alpha_0 = 1/137.04$, $f_K = (155.9 \pm 0.4)$ MeV [?], and $\tau_{S,L}$ are the $K_{S,L}^0$ lifetimes. Note that there is a theoretically and experimentally unknown sign in $A_{L\gamma\gamma}^\mu$, which is determined by higher chiral orders than $\mathcal{O}(p^4)$ contributions [?, ?], and they provide two different constraints on $\mathcal{B}(K_L^0 \rightarrow \mu^+ \mu^-)^{\text{EXP/SM}}$ in table 6.1. This sign can be determined by a precise measurement of the interference between $K_L^0 \rightarrow \mu^+ \mu^-$ and $K_S^0 \rightarrow \mu^+ \mu^-$ [?]. In addition, in the MSSM, the correlation between $\mathcal{B}(K_S^0 \rightarrow \mu^+ \mu^-)$ and $\mathcal{B}(K_L^0 \rightarrow \mu^+ \mu^-)$ depends on the unknown sign of $A_{L\gamma\gamma}^\mu$.

In the case in which new physics enters only in \tilde{C}_S and $\tilde{C}_P = \tilde{C}_S$ (pure left-handed MSSM scenario), the following relations between the branching fractions of K_S^0 and K_L^0 decaying into $\mu^+ \mu^-$ can be established:

$$\begin{aligned} \mathcal{B}(K_S^0 \rightarrow \mu^+ \mu^-) &\propto \beta_\mu^2 |N_S^{\text{LD}}|^2 + (A_{S,\text{SM}}^{\text{SD}})^2 - 2M_K \left[A_{S,\text{SM}}^{\text{SD}} \text{Im}(\tilde{C}_S) - \beta_\mu^2 \text{Re}(N_S^{\text{LD}}) \text{Re}(\tilde{C}_S) \right] \\ &\quad + M_K^2 \left\{ [\text{Im}(\tilde{C}_S)]^2 + \beta_\mu^2 [\text{Re}(\tilde{C}_S)]^2 \right\}, \end{aligned} \quad (6.24)$$

$$\begin{aligned} \mathcal{B}(K_L^0 \rightarrow \mu^+ \mu^-) &\propto |N_L^{\text{LD}}|^2 + (A_{L,\text{SM}}^{\text{SD}})^2 - 2M_K \text{Re}(\tilde{C}_S) [A_{L,\text{SM}}^{\text{SD}} - \text{Re}(N_L^{\text{LD}})] \\ &\quad + M_K^2 \left\{ [\text{Re}(\tilde{C}_S)]^2 + \beta_\mu^2 [\text{Im}(\tilde{C}_S)]^2 \right\} - 2A_{L,\text{SM}}^{\text{SD}} \text{Re}(N_L^{\text{LD}}), \end{aligned} \quad (6.25)$$

with

$$A_{S,\text{SM}}^{\text{SD}} = \frac{2m_\mu}{M_K} \text{Im}(C_{A,\text{SM}}), \quad A_{L,\text{SM}}^{\text{SD}} = \frac{2m_\mu}{M_K} \text{Re}(C_{A,\text{SM}}), \quad (6.26)$$

and

$$N_S^{\text{LD}} = \frac{2G_F^2 M_W^2 m_\mu}{\pi^2 M_K} B_{S\gamma\gamma}^\mu, \quad N_L^{\text{LD}} = \frac{2G_F^2 M_W^2 m_\mu}{\pi^2 M_K} A_{L\gamma\gamma}^\mu, \quad (6.27)$$

where m_d terms are discarded for simplicity.

The long-distance term $\text{Re}(N_L^{\text{LD}})$ holds the unknown sign from $A_{L\gamma\gamma}^\mu$, which changes the correlation significantly, as will be shown.

On the other hand, if new physics produces only C_S and $C_P = -C_S$ (pure right-handed MSSM), the two branching fractions are

$$\begin{aligned} \mathcal{B}(K_S^0 \rightarrow \mu^+ \mu^-) &\propto \beta_\mu^2 |N_S^{\text{LD}}|^2 + (A_{S,\text{SM}}^{\text{SD}})^2 - 2M_K \left[A_{S,\text{SM}}^{\text{SD}} \text{Im}(C_S) + \beta_\mu^2 \text{Re}(N_S^{\text{LD}}) \text{Re}(C_S) \right] \\ &\quad + M_K^2 \left\{ [\text{Im}(C_S)]^2 + \beta_\mu^2 [\text{Re}(C_S)]^2 \right\}, \end{aligned} \quad (6.28)$$

$$\begin{aligned} \mathcal{B}(K_L^0 \rightarrow \mu^+ \mu^-) &\propto |N_L^{\text{LD}}|^2 + (A_{L,\text{SM}}^{\text{SD}})^2 - 2M_K \text{Re}(C_S) [A_{L,\text{SM}}^{\text{SD}} - \text{Re}(N_L^{\text{LD}})] \\ &\quad + M_K^2 \left\{ [\text{Re}(C_S)]^2 + \beta_\mu^2 [\text{Im}(C_S)]^2 \right\} - 2A_{L,\text{SM}}^{\text{SD}} \text{Re}(N_L^{\text{LD}}). \end{aligned} \quad (6.29)$$

It is shown that $\mathcal{B}(K_L^0 \rightarrow \mu^+ \mu^-)$ is the same as the pure left-handed one by a replacement of $C_S \rightarrow \tilde{C}_S$, while $\mathcal{B}(K_S^0 \rightarrow \mu^+ \mu^-)$ is not; the final terms of the first line have opposite sign. Hence, the relations between the two branching fractions are different for left-handed and right-handed new physics scenarios.

2010 For those cases, the experimental measurement of $\mathcal{B}(K_L^0 \rightarrow \mu^+ \mu^-)$ [?],

$$\mathcal{B}(K_L^0 \rightarrow \mu^+ \mu^-)^{\text{EXP}} = (6.84 \pm 0.11) \times 10^{-9}, \quad (6.30)$$

2011 imposes an upper bound on $\mathcal{B}(K_S^0 \rightarrow \mu^+ \mu^-)$. This bound can be alleviated if $|C_S| \neq |C_P|$ or if
2012 new physics is present simultaneously in the left-handed and right-handed Wilson coefficients.

2013 Experimentally, an *effective* branching ratio of $K_S^0 \rightarrow \mu^+ \mu^-$ [?] can also be accessed. This
2014 includes an interference contribution with $K_L^0 \rightarrow \mu^+ \mu^-$ in the neutral kaon sample,

$$\begin{aligned} \mathcal{B}(K_S^0 \rightarrow \mu^+ \mu^-)_{\text{eff}} &= \tau_S \left(\int_{t_{\min}}^{t_{\max}} dt e^{-\Gamma_S t} \varepsilon(t) \right)^{-1} \left[\int_{t_{\min}}^{t_{\max}} dt \left\{ \Gamma(K_S^0 \rightarrow \mu^+ \mu^-) e^{-\Gamma_S t} \right. \right. \\ &\quad \left. \left. + \frac{D f_K^2 M_K^3 \beta_\mu}{8\pi} \text{Re} [i (A_S A_L - \beta_\mu^2 B_S^* B_L) e^{-i\Delta M_K t}] e^{-\frac{\Gamma_S + \Gamma_L}{2} t} \right\} \varepsilon(t) \right], \end{aligned} \quad (6.31)$$

2015 where the dilution factor D is a measure of the initial ($t = 0$) $K^0 - \bar{K}^0$ asymmetry,

$$D = \frac{K^0 - \bar{K}^0}{K^0 + \bar{K}^0}, \quad (6.32)$$

2016 and $\varepsilon(t)$ is the decay-time acceptance of the detector. The second line of eq. (6.31) corresponds
2017 to an interference effect between K_L^0 and K_S^0 , and for $D = 0$, $\mathcal{B}(K_S^0 \rightarrow \mu^+ \mu^-)_{\text{eff}}$ corresponds to
2018 $\mathcal{B}(K_S^0 \rightarrow \mu^+ \mu^-)$. The current experimental bound [?],

$$\mathcal{B}(K_S^0 \rightarrow \mu^+ \mu^-)^{\text{EXP}} < 8 \times 10^{-10} \text{ [90% C.L.],} \quad (6.33)$$

2019 uses untagged K^0 and \bar{K}^0 mesons produced in almost equal amounts, and hence $D = 0$ is
2020 assumed. A pure $K_L^0 \rightarrow \mu^+ \mu^-$ background can be subtracted by a combination of **simultaneous**
2021 **measurement of $K_S^0 \rightarrow \pi^+ \pi^-$ events** and knowledge of the observed value of $\mathcal{B}(K_L^0 \rightarrow \mu^+ \mu^-)$
2022 in eq. (6.30) [?]. The decay-time acceptance of the LHCb detector is parametrized by $\varepsilon(t) =$
2023 $\exp(-\beta t)$ with $\beta \simeq 86 \text{ ns}^{-1}$, and the range of the detector for selecting $K^0 \rightarrow \mu^+ \mu^-$ is $t_{\min} =$
2024 $8.95 \text{ ps} = 0.1\tau_S$ and $t_{\max} = 130 \text{ ps} = 1.45\tau_S$.

2025 Given the potential measurement of an effective branching ratio by different dilution factors
2026 $D > 0$ and $D' < 0$ using K^- tagging and K^+ tagging [?], respectively, the direct CP asymmetry
2027 can be measured using the difference $\mathcal{B}(K_S^0 \rightarrow \mu^+ \mu^-)_{\text{eff}}(D) - \mathcal{B}(K_S^0 \rightarrow \mu^+ \mu^-)_{\text{eff}}(D')$, which is a
2028 theoretically clean quantity that emerges from a genuine direct CP violation. Here, the charged
2029 kaon is accompanied by the neutral kaon beam as, for instance, $pp \rightarrow K^0 K^- X$ or $pp \rightarrow \bar{K}^0 K^+ X$.
2030 Note that a definition of D' is the same as D in eq. (6.32) but charged kaons of opposite sign
2031 are required in the event selection. Therefore, following direct CP asymmetry in $K_S^0 \rightarrow \mu^+ \mu^-$
2032 can be defined:

$$A_{CP}(K_S^0 \rightarrow \mu^+ \mu^-)_{D,D'} = \frac{\mathcal{B}(K_S^0 \rightarrow \mu^+ \mu^-)_{\text{eff}}(D) - \mathcal{B}(K_S^0 \rightarrow \mu^+ \mu^-)_{\text{eff}}(D')}{\mathcal{B}(K_S^0 \rightarrow \mu^+ \mu^-)_{\text{eff}}(D) + \mathcal{B}(K_S^0 \rightarrow \mu^+ \mu^-)_{\text{eff}}(D')} \quad (6.34)$$

2033 The indirect CP -violating contributions, numerically negligible when compared to the CP -
2034 conserving and the direct CP -violating contributions [?], were discarded. Within the SM, the
2035 Wilson coefficients are,

$$C_{A,\text{SM}} = -\frac{[\alpha_2(M_Z)]^2}{2M_W^2} (V_{ts}^* V_{td} Y_t + V_{cs}^* V_{cd} Y_c), \quad (6.35)$$

$$\tilde{C}_{A,\text{SM}} = C_{S,\text{SM}} = \tilde{C}_{S,\text{SM}} = C_{P,\text{SM}} = \tilde{C}_{P,\text{SM}} \simeq 0, \quad (6.36)$$

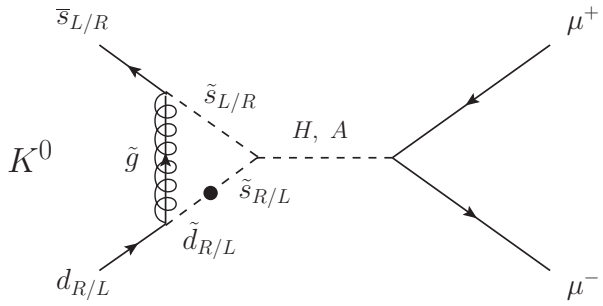


Figure 6.10: Feynman diagram of the leading (pseudo-)scalar MSSM contributions to $K_S^0 \rightarrow \mu^+ \mu^-$ and $K_L^0 \rightarrow \mu^+ \mu^-$, which include a gluino and a heavy Higgs boson. The black dot is the corresponding mass insertion term.

where $Y_t = 0.950 \pm 0.049$ and $Y_c = (2.95 \pm 0.46) \times 10^{-4}$ [?]. Using the CKM matrix tailored for probing the MSSM contributions, we obtain the SM prediction of A_{CP} ,

$$A_{CP}(K_S^0 \rightarrow \mu^+ \mu^-)_{D,D'}^{\text{SM}} = \begin{cases} -\frac{3.71(D-D')}{(10.53 \pm 3.01) - 3.71(D+D')}, & (+) \\ \frac{3.98(D-D')}{(10.53 \pm 3.01) + 3.98(D+D')}, & (-) \end{cases} \quad (6.37)$$

where (+) and (-) correspond to the unknown sign of $A_{L\gamma\gamma}^\mu$ in eq. (6.21). The uncertainty is totally dominated by $B_{S\gamma\gamma}^\mu$ [?] and it will be sharpened by the dispersive treatment of $K_S^0 \rightarrow \gamma^{(*)}\gamma^{(*)}$ [?].

In the case where $D' = -D$, achieved by the accompanying opposite-charged-kaon tagging, the SM prediction of A_{CP} is simplified:

$$A_{CP}(K_S^0 \rightarrow \mu^+ \mu^-)_{D,-D}^{\text{SM}} = \begin{cases} (-0.704_{-0.281}^{+0.156}) \times D, & (+) \\ (+0.756_{-0.168}^{+0.302}) \times D. & (-) \end{cases} \quad (6.38)$$

In the MSSM, the leading contribution to C_A , induced by terms of second order in the expansion of the squark mass matrix of the chargino Z -penguin, is [?, ?],

$$C_A = -\frac{(\alpha_2)^2}{16M_W^2} \frac{[(\mathcal{M}_U^2)_{LR}]_{23}^* [(\mathcal{M}_U^2)_{LR}]_{13}}{M_2^4} l(x_2^Q, x_2^u), \quad (6.39)$$

$$\tilde{C}_A = 0, \quad (6.40)$$

where $x_2^Q = \tilde{m}_Q^2/M_2^2$ and $x_2^u = \tilde{m}_u^2/M_2^2$. The loop function $l(x, y)$ [?] is defined in appendix ???. Here, contributions from the Wino-Higgsino mixing are omitted. Setting $\tilde{m}_Q^2 = \tilde{m}_u^2$ gives the MIA result of refs. [?, ?].

The leading MSSM contributions to $C_{S(P)}$ and $\tilde{C}_{S(P)}$ in $K_S^0 \rightarrow \mu^+ \mu^-$ and $K_L^0 \rightarrow \mu^+ \mu^-$ are

2049 shown in figure 6.10. For C_S and \tilde{C}_S , it is obtained

$$C_S = -\frac{2}{3} \frac{\alpha_s \alpha_2 m_\mu}{M_W^2} \frac{\mu M_3}{M_A^2 \tilde{m}_d^2} (\delta_d^{RR})_{12} \frac{\tan^3 \beta}{(1 + \epsilon_g \tan \beta)^2 (1 + \epsilon_\ell \tan \beta)} G(x_d^3, x_d^Q) \\ -\frac{2}{3} \frac{\alpha_s \alpha_2 m_\mu}{M_W^2} \frac{m_b}{m_s} \frac{\mu M_3 \tilde{m}_Q^2}{M_A^2 \tilde{m}_d^4} (\delta_d^{RR})_{13} (\delta_d^{LL})_{32} \\ \times \frac{\tan^3 \beta}{(1 + \epsilon_g \tan \beta)[1 + (\epsilon_g + \epsilon_Y y_t^2) \tan \beta](1 + \epsilon_\ell \tan \beta)} H(x_d^3, x_d^Q), \quad (6.41)$$

$$\tilde{C}_S = -\frac{2}{3} \frac{\alpha_s \alpha_2 m_\mu}{M_W^2} \frac{\mu M_3}{M_A^2 \tilde{m}_Q^2} (\delta_d^{LL})_{12} \frac{\tan^3 \beta}{(1 + \epsilon_g \tan \beta)^2 (1 + \epsilon_\ell \tan \beta)} G(x_Q^3, x_Q^d) \\ -\frac{2}{3} \frac{\alpha_s \alpha_2 m_\mu}{M_W^2} \frac{m_b}{m_s} \frac{\mu M_3 \tilde{m}_d^2}{M_A^2 \tilde{m}_Q^4} (\delta_d^{LL})_{13} (\delta_d^{RR})_{32} \\ \times \frac{\tan^3 \beta}{(1 + \epsilon_g \tan \beta)[1 + (\epsilon_g + \epsilon_Y y_t^2) \tan \beta](1 + \epsilon_\ell \tan \beta)} H(x_Q^3, x_Q^d) \\ + \frac{(\alpha_2)^2 m_\mu m_t^2}{8 M_W^4} \frac{\mu A_t}{M_A^2 \tilde{m}_Q^2} V_{ts}^* V_{td} \frac{\tan^3 \beta [1 + (\epsilon_g + \epsilon_Y y_t^2) \tan \beta]^2}{(1 + \epsilon_g \tan \beta)^4 (1 + \epsilon_\ell \tan \beta)} F(x_Q^\mu, x_Q^u) \\ + \frac{(\alpha_2)^2 m_\mu}{4 M_W^2} \frac{\mu M_2}{M_A^2 \tilde{m}_Q^2} (\delta_u^{LL})_{12} \frac{\tan^3 \beta}{(1 + \epsilon_g \tan \beta)^2 (1 + \epsilon_\ell \tan \beta)} G(x_Q^2, x_Q^\mu), \quad (6.42)$$

2050 with

$$\epsilon_g = \frac{2 \alpha_s}{3 \pi} \frac{\mu M_3}{\tilde{m}_Q^2} F(x_Q^3, x_Q^d), \quad (6.43)$$

$$\epsilon_Y = \frac{1}{16 \pi} \frac{\mu A_t}{\tilde{m}_Q^2} F(x_Q^\mu, x_Q^u), \quad (6.44)$$

$$\epsilon_\ell \simeq -\frac{3 \alpha_2}{16 \pi}, \quad (6.45)$$

2051 where $x_d^3 = M_3^2 / \tilde{m}_d^2$, $x_d^Q = \tilde{m}_Q^2 / \tilde{m}_d^2$, $x_Q^3 = M_3^2 / \tilde{m}_Q^2$, $x_Q^d = \tilde{m}_d^2 / \tilde{m}_Q^2$, $x_Q^\mu = \mu^2 / \tilde{m}_Q^2$, $x_Q^u = \tilde{m}_u^2 / \tilde{m}_Q^2$,
2052 $x_Q^2 = M_2^2 / \tilde{m}_Q^2$, and $x_Q^\mu = \mu^2 / \tilde{m}_Q^2$. The loop functions $F(x, y)$, $G(x, y)$, and $H(x, y)$ are defined
2053 in appendix ???. These results are consistent with ref. [73] in the universal squark mass limit
2054 after changing the flavour and its chirality for B_s^0 decay. Here, the following approximation is
2055 used

$$\alpha \simeq \beta - \frac{\pi}{2}, \quad M_H \simeq M_A, \quad (6.46)$$

2056 where α is an angle of the orthogonal rotation matrix for the CP -even Higgs mass, and M_H
2057 (M_A) is a CP -even (odd) heavy Higgs mass. On the other hand, the contributions to C_P and
2058 \tilde{C}_P are

$$C_P = -C_S, \quad \tilde{C}_P = \tilde{C}_S. \quad (6.47)$$

2059 Note that the Wilson coefficients in the MSSM are given at the μ^{SUSY} scale, and there is no
2060 QCD correction from the renormalization-group (RG) evolution at the leading order.

2061 **6.3.1.3 $\varepsilon'_K/\varepsilon_K$**

2062 New physics models affecting $\varepsilon'_K/\varepsilon_K$ have recently attracted some attention, since lattice results
 2063 from the RBC and UKQCD collaborations [?, ?, ?, ?] have been reporting 2–3 σ below [?, ?] the
 2064 experimental world average of $\text{Re}(\varepsilon'_K/\varepsilon_K)$ [?]. This is consistent with the recent calculations in
 2065 the large- N_c analyses [?, ?]. Although the lattice simulation [?] includes final-state interactions
 2066 partially along the line of ref. [?], final-state interactions have to be still fully included in the
 2067 calculations in light of a discrepancy of a strong phase shift δ_0 [?, ?, ?]. Conversely, combining
 2068 large- N_c methods with chiral loop corrections can bring the value of $\varepsilon'_K/\varepsilon_K$ in agreement with
 2069 the experiment [?, ?, ?].

2070 The hadronic matrix elements used in this paper come from lattice simulations. For the χ^2
 2071 test, the following constraint is used,

$$\Delta \left(\frac{\varepsilon'_K}{\varepsilon_K} \right)^{\text{EXP-SM}} \equiv \text{Re} \left(\frac{\varepsilon'_K}{\varepsilon_K} \right)^{\text{EXP}} - \left(\frac{\varepsilon'_K}{\varepsilon_K} \right)^{\text{SM}} = [15.5 \pm 2.3(\text{EXP}) \pm 5.07(\text{TH})] \times 10^{-4}, \quad (6.48)$$

2072 with

$$\left(\frac{\varepsilon'_K}{\varepsilon_K} \right)^{\text{SM}} \rightarrow \left(\frac{\varepsilon'_K}{\varepsilon_K} \right)^{\text{SM}} + \left(\frac{\varepsilon'_K}{\varepsilon_K} \right)^{\text{SUSY}}, \quad (6.49)$$

2073 where the SM prediction at the next-to-leading order in ref. [?] is used. The experimental value
 2074 of ε_K is used in the calculation of the ratio.

2075 Within the MSSM, the SUSY contributions to $\varepsilon'_K/\varepsilon_K$ are dominated by gluino box, chargino-
 2076 mediated Z -penguin, and chromomagnetic dipole contributions. The first two contributions are
 2077 represented by the same $|\Delta S| = 1$ four-quark effective Hamiltonian at the μ^{SUSY} scale, which
 2078 is:

$$\mathcal{H}_{\text{eff}} = \frac{G_F}{\sqrt{2}} \sum_q \sum_{i=1}^4 \left[C_i^q Q_i^q + \tilde{C}_i^q \tilde{Q}_i^q \right] + \text{H.c.}, \quad (6.50)$$

2079 with

$$\begin{aligned} Q_1^q &= (\bar{s}d)_{V-A} (\bar{q}q)_{V+A}, & \tilde{Q}_1^q &= (\bar{s}d)_{V+A} (\bar{q}q)_{V-A}, \\ Q_2^q &= (\bar{s}_\alpha d_\beta)_{V-A} (\bar{q}_\beta q_\alpha)_{V+A}, & \tilde{Q}_2^q &= (\bar{s}_\alpha d_\beta)_{V+A} (\bar{q}_\beta q_\alpha)_{V-A}, \\ Q_3^q &= (\bar{s}d)_{V-A} (\bar{q}q)_{V-A}, & \tilde{Q}_3^q &= (\bar{s}d)_{V+A} (\bar{q}q)_{V+A}, \\ Q_4^q &= (\bar{s}_\alpha d_\beta)_{V-A} (\bar{q}_\beta q_\alpha)_{V-A}, & \tilde{Q}_4^q &= (\bar{s}_\alpha d_\beta)_{V+A} (\bar{q}_\beta q_\alpha)_{V+A}, \end{aligned} \quad (6.51)$$

2080 where $(V \mp A)$ refers to $\gamma_\mu(1 \mp \gamma_5)$, and α and β are color indices.

2081 The Wilson coefficients from the gluino box contributions are leading contributions when
 2082 the mass difference between right-handed squarks exists [?, ?]. They are shown in appendix ??
 2083 with their corresponding loop functions defined in appendix ???. Here, $(\delta_d)_{13}(\delta_d)_{32}$ terms are
 2084 discarded for simplicity.

2085 The Wilson coefficients of the chargino-mediated Z -penguin are induced by terms of second
 2086 order in the expansion of MIA. These ones are shown in appendix ??, where the loop function
 2087 $l(x, y)$ is given by eq. (??).

2088 The matching conditions to the standard four-quark Wilson coefficients [?] are

$$\begin{aligned}
s_1 &= 0, & s_2 &= 0, \\
s_3 &= \frac{1}{3} (C_3^u + 2C_3^d), & s_4 &= \frac{1}{3} (C_4^u + 2C_4^d), \\
s_5 &= \frac{1}{3} (C_1^u + 2C_1^d), & s_6 &= \frac{1}{3} (C_2^u + 2C_2^d), \\
s_7 &= \frac{2}{3} (C_1^u - C_1^d), & s_8 &= \frac{2}{3} (C_2^u - C_2^d), \\
s_9 &= \frac{2}{3} (C_3^u - C_3^d), & s_{10} &= \frac{2}{3} (C_4^u - C_4^d).
\end{aligned} \tag{6.52}$$

2090 The coefficients for the opposite-chirality operators, $\tilde{s}_{1,\dots,10}$, are trivially found from the previous
2091 ones by replacing $C_{1,2,3,4}^q \rightarrow \tilde{C}_{1,2,3,4}^q$. Using the Wilson coefficients $\vec{s} = (s_1, s_2, \dots, s_{10})^T$ and
2092 $\tilde{\vec{s}} = (\tilde{s}_1, \tilde{s}_2, \dots, \tilde{s}_{10})^T$ at the μ^{SUSY} scale, the dominant box and penguin contributions to $\varepsilon'_K/\varepsilon_K$
2093 are given by [?]

$$\left. \frac{\varepsilon'_K}{\varepsilon_K} \right|_{\text{box+pen}} = \frac{G_F \omega_+}{2|\varepsilon_K^{\text{EXP}}| \text{Re} A_0^{\text{EXP}}} \langle \vec{Q}_{\varepsilon'}(\mu)^T \hat{U}(\mu, \mu^{\text{SUSY}}) \text{Im} [\vec{s} - \tilde{\vec{s}}] \rangle, \tag{6.53}$$

2094 with

$$\omega_+ = (4.53 \pm 0.02) \times 10^{-2}, \tag{6.54}$$

$$|\varepsilon_K^{\text{EXP}}| = (2.228 \pm 0.011) \times 10^{-3}, \tag{6.55}$$

$$\text{Re} A_0^{\text{EXP}} = (3.3201 \pm 0.0018) \times 10^{-7} \text{ GeV}. \tag{6.56}$$

2095 The hadronic matrix elements at $\mu = 1.3$ GeV, including $I = 0$ and $I = 2$ parts, are [?]

$$\langle \vec{Q}_{\varepsilon'}(\mu)^T \rangle = \left(0.345, 0.133, 0.034, -0.179, 0.152, 0.288, 2.653, 17.305, 0.526, 0.281 \right) (\text{GeV})^3, \tag{6.57}$$

2096 and the approximate function of the RG evolution matrix $\hat{U}(\mu, \mu^{\text{SUSY}})$ is given in ref. [?].

2097 Next, the $|\Delta S| = 1$ chromomagnetic-dipole operator that contributes to $\varepsilon'_K/\varepsilon_K$ is

$$\mathcal{H}_{\text{eff}} = C_g^- Q_g^- + \text{H.c.}, \tag{6.58}$$

2098 with

$$Q_g^- = -\frac{g_s}{(4\pi)^2} (\bar{s} \sigma^{\mu\nu} T^A \gamma_5 d) G_{\mu\nu}^A. \tag{6.59}$$

2099 The complete expression for the Wilson coefficient C_g^- at the μ^{SUSY} scale is shown in ap-
2100 pendix ??, where $(\delta_d)_{13}(\delta_d)_{32}$ terms are discarded for simplicity. The corresponding loop func-
2101 tions $I(x, y)$, $J(x, y)$, $K(x, y)$, $L(x, y)$, $M_3(x)$, and $M_4(x)$ are defined in appendix ??.

2102 The chromomagnetic-dipole contribution to $\varepsilon'_K/\varepsilon_K$ is [?]

$$\left. \frac{\varepsilon'_K}{\varepsilon_K} \right|_{\text{chromo}} = \frac{\omega_+}{|\varepsilon_K^{\text{EXP}}| \text{Re} A_0^{\text{EXP}}} \left(1 - \hat{\Omega}_{\text{eff}} \right) \frac{11\sqrt{3}}{64\pi^2} \frac{M_\pi^2 M_K^2}{f_\pi(m_s + m_d)} \eta_s B_G \text{Im} C_g^-, \tag{6.60}$$

2103 where $f_\pi = (130.2 \pm 1.7)$ MeV [?], and [?, ?, ?]

$$\hat{\Omega}_{\text{eff}} = 0.148 \pm 0.080, \quad (6.61)$$

$$\eta_s = \left[\frac{\alpha_s(m_b)}{\alpha_s(1.3 \text{ GeV})} \right]^{\frac{2}{25}} \left[\frac{\alpha_s(m_t)}{\alpha_s(m_b)} \right]^{\frac{2}{23}} \left[\frac{\alpha_s(\mu^{\text{SUSY}})}{\alpha_s(m_t)} \right]^{\frac{2}{21}}. \quad (6.62)$$

2104 According to refs. [?, ?], the hadronic matrix element for the chromomagnetic-dipole operator
 2105 into two pions, B_G , is enhanced by $1/N_c \cdot M_K^2/M_\pi^2$ from the large next-to-leading-order corrections
 2106 that it receives. Therefore, the leading order in the chiral quark model, $B_G = 1$, is implausible.
 2107 In the following analyses, it is considered $B_G = 1 \pm 3$.

2108 The other contributions are negligible [?]. Note that the sub-leading contributions which
 2109 come from the gluino-mediated photon-penguin and the chargino-mediated Z -penguins induced
 2110 by terms of first order in the expansion of the squark mass matrix, have opposite sign and
 2111 practically cancel each other [?].

2112 Finally, the SUSY contributions to $\varepsilon'_K/\varepsilon_K$ are given as

$$\left(\frac{\varepsilon'_K}{\varepsilon_K} \right)^{\text{SUSY}} \simeq \left. \frac{\varepsilon'_K}{\varepsilon_K} \right|_{\text{box+pen}} + \left. \frac{\varepsilon'_K}{\varepsilon_K} \right|_{\text{chromo}}. \quad (6.63)$$

2113 Note that the contributions to $\varepsilon'_K/\varepsilon_K$ from the heavy Higgs exchanges were discarded, although
 2114 they give the strong isospin-violating contribution naturally: the contribution is enhanced by
 2115 $\tan^3 \beta$ for only down-type four-fermion scalar operators. These contributions must be propor-
 2116 tional to $m_d m_s$ which cannot be compensated by $\tan^3 \beta$, so that they should be the higher-order
 2117 contributions for $\varepsilon'_K/\varepsilon_K$.

2118 6.3.1.4 ε_K and ΔM_K

2119 Although ε_K is one of the most sensitive quantities to new physics, the SM prediction is still
 2120 controversial. Especially, the leading short-distance contribution to ε_K in the SM is proportional
 2121 to $|V_{cb}|^4$ (cf., ref. [?]), whose measured values from inclusive semileptonic B decays ($\bar{B} \rightarrow X_c \ell^- \bar{\nu}$)
 2122 and from exclusive decays ($\bar{B} \rightarrow D^{(*)} \ell^- \bar{\nu}$ and $\Lambda_b \rightarrow \Lambda_c \ell^- \bar{\nu}$) are inconsistent at a 4.1σ level [?, ?].
 2123 A recent discussion about the exclusive $|V_{cb}|$ is given in refs. [?, ?, ?].

2124 In this paper, for the SM prediction, we use [?]

$$\varepsilon_K^{\text{SM}} = (2.12 \pm 0.18) \times 10^{-3}, \quad (6.64)$$

2125 with

$$\varepsilon_K = e^{i\varphi_\varepsilon} \varepsilon_K^{\text{SM}}, \quad (6.65)$$

2126 where $\varphi_\varepsilon = \tan^{-1}(2\Delta M_K/\Delta\Gamma_K) = (43.51 \pm 0.05)^\circ$ [?]. This value and the uncertainty are based
 2127 on the inclusive $|V_{cb}|$ [?], the Wolfenstein parameters in the angle-only-fit method [?], and the
 2128 long-distance contribution obtained by the lattice simulation [?]. Combining the measured value
 2129 in eq. (6.55)

$$\varepsilon_K^{\text{EXP/SM}} = 1.05 \pm 0.10(\text{TH}), \quad (6.66)$$

2130 on the χ^2 test, with

$$\varepsilon_K^{\text{SM}} \rightarrow \varepsilon_K^{\text{SM}} + \varepsilon_K^{\text{SUSY}}. \quad (6.67)$$

2131 Note that it is also imposed that $\text{Re}(\varepsilon_K) > 0$ from $\text{Re}(\varepsilon_K) = (1.596 \pm 0.013) \times 10^{-3}$ [?].

2132 Within the MSSM, the SUSY contributions to ε_K are dominated by gluino box diagrams. In
2133 this paper, however, we will focus on their suppressed region. The crossed and uncrossed gluino-
2134 box diagrams give opposite sign contributions and there is a certain cancellation region [?, ?],
2135 and/or simultaneous mixings of (δ_d^{LL}) and (δ_d^{RR}) can also produce the cancellation. Therefore,
2136 we also consider the sub-dominant contributions which come from Wino and Higgsino boxes.
2137 The $|\Delta S| = 2$ four-quark effective Hamiltonian at the μ^{SUSY} scale is [?]

$$\mathcal{H}_{\text{eff}} = \sum_{i=1}^5 C_i Q_i + \sum_{i=1}^3 \tilde{C}_i \tilde{Q}_i + \text{H.c.}, \quad (6.68)$$

2138 with

$$\begin{aligned} Q_1 &= (\bar{d}\gamma_\mu P_L s) (\bar{d}\gamma^\mu P_L s), & Q_2 &= (\bar{d}P_L s) (\bar{d}P_L s), & Q_3 &= (\bar{d}_\alpha P_L s_\beta) (\bar{d}_\beta P_L s_\alpha), \\ Q_4 &= (\bar{d}P_L s) (\bar{d}P_R s), & Q_5 &= (\bar{d}_\alpha P_L s_\beta) (\bar{d}_\beta P_R s_\alpha), \\ \tilde{Q}_1 &= (\bar{d}\gamma_\mu P_R s) (\bar{d}\gamma^\mu P_R s), & \tilde{Q}_2 &= (\bar{d}P_R s) (\bar{d}P_R s), & \tilde{Q}_3 &= (\bar{d}_\alpha P_R s_\beta) (\bar{d}_\beta P_R s_\alpha). \end{aligned} \quad (6.69)$$

2139 The kaon mixing amplitude $M_{12}^{(K)}$, ΔM_K and ε_K are given by

$$M_{12}^{(K)} = \frac{\langle K^0 | \mathcal{H}_{\text{eff}} | \bar{K}^0 \rangle}{2M_K}, \quad (6.70)$$

$$\Delta M_K = 2\text{Re}[M_{12}^{(K)}], \quad (6.71)$$

$$\varepsilon_K = \kappa_\varepsilon \frac{e^{i\varphi_\varepsilon}}{\sqrt{2}} \frac{\text{Im}[M_{12}^{(K)}]}{\Delta M_K^{\text{EXP}}} = e^{i\varphi_\varepsilon} \varepsilon_K^{\text{SUSY}}, \quad (6.72)$$

2140 where $\kappa_\varepsilon = 0.94 \pm 0.02$ [?]. Using the latest lattice result [?], for the hadronic matrix elements

$$\langle K^0 | \vec{Q}(\mu) | \bar{K}^0 \rangle = (0.00211, -0.04231, 0.01288, 0.09571, 0.02452) \text{ (GeV)}^4, \quad (6.73)$$

2141 with $\langle K^0 | \tilde{Q}_{1,2,3}(\mu) | \bar{K}^0 \rangle = \langle K^0 | Q_{1,2,3}(\mu) | \bar{K}^0 \rangle$, where $\mu = 3$ GeV and it was used $m_s(\mu) =$
2142 (81.64 ± 1.17) MeV and $m_d(\mu) = (2.997 \pm 0.049)$ MeV [?].

2143 The leading-order QCD RG corrections are given by [?]

$$C_1(\mu) = \eta_1^K C_1(\mu^{\text{SUSY}}), \quad (6.74)$$

$$\begin{pmatrix} C_2(\mu) \\ C_3(\mu) \end{pmatrix} = X_{23} \eta_{23}^K X_{23}^{-1} \begin{pmatrix} C_2(\mu^{\text{SUSY}}) \\ C_3(\mu^{\text{SUSY}}) \end{pmatrix}, \quad (6.75)$$

$$\begin{pmatrix} C_4(\mu) \\ C_5(\mu) \end{pmatrix} = \begin{pmatrix} (\eta_1^K)^{-4} & \frac{1}{3} \left[(\eta_1^K)^{-4} - (\eta_1^K)^{\frac{1}{2}} \right] \\ 0 & (\eta_1^K)^{\frac{1}{2}} \end{pmatrix} \begin{pmatrix} C_4(\mu^{\text{SUSY}}) \\ C_5(\mu^{\text{SUSY}}) \end{pmatrix}, \quad (6.76)$$

2144 with

$$\eta_1^K = \left[\frac{\alpha_s(m_b)}{\alpha_s(\mu)} \right]^{\frac{6}{25}} \left[\frac{\alpha_s(m_t)}{\alpha_s(m_b)} \right]^{\frac{6}{23}} \left[\frac{\alpha_s(\mu^{\text{SUSY}})}{\alpha_s(m_t)} \right]^{\frac{6}{21}}, \quad (6.77)$$

$$\eta_{23}^K = \begin{pmatrix} (\eta_1^K)^{\frac{1}{6}(1-\sqrt{241})} & 0 \\ 0 & (\eta_1^K)^{\frac{1}{6}(1+\sqrt{241})} \end{pmatrix}, \quad (6.78)$$

$$X_{23} = \begin{pmatrix} \frac{1}{2}(-15 - \sqrt{241}) & \frac{1}{2}(-15 + \sqrt{241}) \\ 1 & 1 \end{pmatrix}. \quad (6.79)$$

2145 The QCD corrections to $\tilde{C}_{1,2,3}$ are the same as $C_{1,2,3}$.

2146 The Wilson coefficients from the $|\Delta S| = 2$ gluino boxes are shown in appendix ?? with their
2147 corresponding loop functions defined in appendix ???. In the universal squark mass limit, these
2148 results are consistent with ref. [73]. Here, the terms proportional to $[(\mathcal{M}_D^2)_{LR}]_{12}$ or $(\delta_d)_{13}(\delta_d)_{32}$
2149 are discarded for simplicity.

2150 The Wilson coefficients and their corresponding loop functions for the sub-leading contribu-
2151 tions to ε_K are given in appendix ?? and ??, respectively.

2152 6.3.2 Parameter scan

2153 The MSSM parameter scan is performed with the framework **Ipanema- β** [?] using a GPU of the
2154 model GeForce GTX 1080. The samples are a combination of flat scans plus scans based on
2155 genetic algorithms [?]. The cost function used by the genetic algorithm is the likelihood function
2156 with the observable constrains. In addition, aiming to get a dense population in regions with
2157 $\mathcal{B}(K_S^0 \rightarrow \mu^+ \mu^-)$ significantly different from the SM prediction, specific penalty contributions are
2158 added to the total cost function. Specific scans at $\tan \beta \approx 50$ and $M_A \approx 1.6$ TeV are performed,
2159 as for those values the chances to get sizable MSSM effects are larger. Three different scenarios
2160 are studied (for the ranges of the scanned parameters see table 6.2):

- 2161 • **Scenario A:** A generic scan with universal gaugino masses. No constraint on the Dark
2162 Matter relic density is applied in this case, other than the requirement of neutralino
2163 Lightest Supersymmetric Particle (LSP). The LSP is Bino-like in most cases, although
2164 some points with Higgsino LSP are also found.
- 2165 • **Scenario B:** A scan motivated by scenarios with Higgsino Dark Matter. In this scenario,
2166 the relic density is mostly function of the LSP mass, which fulfills the measured density [?]
2167 at $m_{\chi_1^0} \approx 1$ TeV [?, 30, 40, 41]. Thus, a scan is performed with $|\mu| = 1$ TeV $< M_1$. **Universal
2168 gaugino masses** are assumed in this scenario, which then implies that $M_3 > 4.5$ TeV.
- 2169 • **Scenario C:** A scan motivated by scenarios with Wino Dark Matter, which is possible
2170 in mAMSB or pMSSM, although it is under pressure by γ -rays and antiprotons data [?].
2171 In those scenarios, the relic density is mostly function of the LSP mass, which fulfills the
2172 experimental value [?] at $m_{\chi_1^0} \approx 3$ TeV [?, 30]. Thus, a scan is made with $M_2 = 3$ TeV
2173 $< |\mu|, M_{1,3}$. The Bino mass M_1 is set to 5 TeV for simplicity. Since it is only necessary
2174 in order to ensure that the LSP is Wino-like, any other value above 3 TeV (such as,
2175 e.g., an mAMSB-like relation $M_1 \approx 9.7$ TeV) could also be used without changing the
2176 obtained results. The lightest neutralino and the lightest chargino are nearly degenerate,

Table 6.2: Scan ranges for scenario A, B (motivated by Higgsino Dark Matter) and C (motivated by Wino Dark Matter). All masses are in TeV. The nuisance parameter B_G appears in the chromomagnetic-dipole contribution to $\varepsilon'_K/\varepsilon_K$.

| Parameter | Scenario A | Scenario B | Scenario C |
|---|---|---|-------------|
| \tilde{m}_Q | [2, 10] | [2, 10] | [4, 10] |
| $\tilde{m}_Q^2/\tilde{m}_d^2$ | [0.25, 4] | [0.25, 4] | [0.25, 4] |
| M_3 | [2, 10] | [4.5, 15] | [4, 15] |
| $\tan \beta$ | [10, 50] | [10, 50] | [10, 50] |
| M_A | [1, 2] | [1, 2] | [1, 2] |
| $ \mu $ | [1, 10] | 1 | [5, 20] |
| M_1 | $\frac{\alpha_1(\mu^{SUSY})}{\alpha_3(\mu^{SUSY})} M_3$ | $\frac{\alpha_1(\mu^{SUSY})}{\alpha_3(\mu^{SUSY})} M_3$ | 5 |
| M_2 | $\frac{\alpha_2(\mu^{SUSY})}{\alpha_3(\mu^{SUSY})} M_3$ | $\frac{\alpha_2(\mu^{SUSY})}{\alpha_3(\mu^{SUSY})} M_3$ | 3 |
| B_G | [-2, 4] | [-2, 4] | [-2, 4] |
| $\text{Re} \left[(\delta_d^{LL(RR)})_{12} \right]$ | [-0.2, 0.2] | [-0.2, 0.2] | [-0.2, 0.2] |
| $\text{Im} \left[(\delta_d^{LL(RR)})_{12} \right]$ | [-0.2, 0.2] | [-0.2, 0.2] | [-0.2, 0.2] |

and radiative corrections are expected to bring the chargino mass to be ≈ 160 MeV heavier than the lightest neutralino [?].

For simplicity, in all cases the trilinear couplings and the mass insertions (other than $(\delta_d^{LL(RR)})_{12}$ and $(\delta_u^{LL})_{12}$) are set to zero, and μ is treated as a real parameter, with both signs allowed a priori.

Further studies were also performed at the MFV limit, using RG equations induced MIs in CMSSM. As expected, no significant effect is found in this case.

For the squark masses, it is considered that $\tilde{m}_Q = \tilde{m}_u \neq \tilde{m}_d$. This set up is motivated by the SUSY SU(5) grand unified theory, where Q and U -squark are contained in **10** representation matter multiplet while D -squark is in **5** representation one. In general, their soft-SUSY breaking masses are different and depend on couplings between the matter multiplets and the SUSY breaking spurion field.

6.3.3 Results

In this subsection, the main results of the performed scans are showed. The points with $\chi^2 < 12.5$, corresponding to 95% C.L. for six degrees of freedom, are considered experimentally viable. The number of degrees of freedom has been calculated as the number of observables, not counting the nuisance parameter B_G , the rigid bound on the $\tan \beta:M_A$ plane, and ΔM_K , which are not Gaussian distributed. Therefore, the χ^2 requirement corresponds to a 95% C.L. or tighter.

Similar plots are obtained applying a looser bound on the absolute χ^2 accompanied with a $\Delta \chi^2 < 5.99$ across the plane being plotted. Due to the large theory uncertainty, $\mathcal{B}(K_L^0 \rightarrow \mu^+ \mu^-)$ can go up to $\approx 1 \times 10^{-8}$ at 2σ level. Values slightly above that limit can still be allowed if they reduce the χ^2 contribution in other observables. The allowed regions are separated by the sign

2199 of $A_{L\gamma\gamma}^\mu$ in eq. (6.21). Results for A_{CP} are also shown, which could be experimentally accessed
2200 by means of a tagged analysis.

2201 6.3.3.1 Effects from $(\delta_d^{LL(RR)})_{12}$ separately

2202 The effects of pure left-handed(right-handed) MIs are studied separately, to determine the re-
2203 gions of the MSSM parameter space in which either *LL* MIs or *RR* MIs dominate⁹. The obtained
2204 scatter plots for $\mathcal{B}(K_L^0 \rightarrow \mu^+ \mu^-)$ vs $\mathcal{B}(K_S^0 \rightarrow \mu^+ \mu^-)$ and $\mathcal{B}(K_S^0 \rightarrow \mu^+ \mu^-)$ vs $\varepsilon'_K/\varepsilon_K$ are shown
2205 in figure 6.11 and figure 6.12 for Scenario A, figure 6.13 and figure 6.14 for Scenario B, and
2206 figure 6.15 and figure 6.16 for Scenario C. The points in the planes correspond to predictions
2207 from different values of the input parameters. It should be noted that in such cases, the SUSY
2208 contributions to ε_K can be suppressed naturally in a heavy gluino region ($M_3 \gtrsim 1.5\tilde{m}_Q$) [?, ?].

2209 In Scenario A (see figure 6.11) and Scenario C (see figure 6.15), we can see that the 95% C.L.
2210 allowed regions for $\mathcal{B}(K_S^0 \rightarrow \mu^+ \mu^-)$ in light of the constraints listed in table 6.1 are approximately
2211 $[0.78, 14] \times 10^{-12}$ for *LL*-only contributions, and $[1.5, 35] \times 10^{-12}$ for *RR*-only contributions,
2212 without any need of fine-tuning the parameters to avoid constraints from $\mathcal{B}(K_L^0 \rightarrow \mu^+ \mu^-)$. The
2213 MSSM contributions are similar for *RR* and *LL*, and the differences on the allowed ranges for
2214 $\mathcal{B}(K_S^0 \rightarrow \mu^+ \mu^-)$ arise from the interference with the SM amplitudes in $K_{S(L)}^0 \rightarrow \mu^+ \mu^-$, which
2215 are shown in section ??.

2216 The allowed regions for scenarios A and C are very similar to each other, although marginally
2217 larger on A. It can also be seen that, in Scenario B (see figure 6.13) the maximum departure of
2218 $\mathcal{B}(K_S^0 \rightarrow \mu^+ \mu^-)$ from the SM is smaller than in the other scenarios, since $C_{S,P} \propto \mu$ and μ is small
2219 relative to squark and gluino masses. In the contributions to $(\varepsilon'_K/\varepsilon_K)^{\text{SUSY}}$, the chromomagnetic-
2220 dipole contribution can be significant in both *LL*-only and *RR*-only cases when $\mu \tan \beta$ and B_G
2221 have large values, while the box contributions can be significant only via *LL* MIs [?]. Note that
2222 the penguin contributions to $(\varepsilon'_K/\varepsilon_K)^{\text{SUSY}}$ are neglected in the parameter scan.

2223 The effective branching fraction and *CP* asymmetry are shown in figure 6.17 for Scenario
2224 A. Note that the negative value of $\mathcal{B}(K_S^0 \rightarrow \mu^+ \mu^-)_{\text{eff}}$ is compensated in data by inclusion of
2225 the background events from $K_L^0 \rightarrow \mu^+ \mu^-$, so that the overall $K^0 \rightarrow \mu^+ \mu^-$ is always positive.
2226 Correlation patterns of A_{CP} with other observables can be seen in figure 6.18, where $D' = -D$
2227 and $D = 0.5$ are chosen for simplicity. It is found that *CP* asymmetries can be up to ≈ 6
2228 (at $D = 1$), approximately eight times bigger than in the SM. The largest effects are found in
2229 left-handed scenarios.

2230 6.3.3.2 Floating *LL* and *RR* MIs simultaneously

2231 A priori, one possibility to avoid the constraint from $\mathcal{B}(K_L^0 \rightarrow \mu^+ \mu^-)$ is to allow simultaneously
2232 for non-zero *LL* and *RR* mass insertions. This way both $C_{S(P)}$ and $\tilde{C}_{S(P)}$ are non zero and
2233 eqs. (6.24)–(6.29) do not hold. Tuning the values of the MIs, regions in which the MSSM
2234 contributions to $\mathcal{B}(K_S^0 \rightarrow \mu^+ \mu^-)$ do not alter $\mathcal{B}(K_L^0 \rightarrow \mu^+ \mu^-)$ significantly (thus satisfying the
2235 experimental bound) can be found. Choosing for example

$$\text{Re} [(\delta_d^{LL})_{12}] = -\text{Re} [(\delta_d^{RR})_{12}], \quad \text{Im} [(\delta_d^{LL})_{12}] = \text{Im} [(\delta_d^{RR})_{12}], \quad (6.80)$$

⁹As an example, MFV models the *LL* MIs can become non-zero after RGE, which does not happen for *RR* MIs.

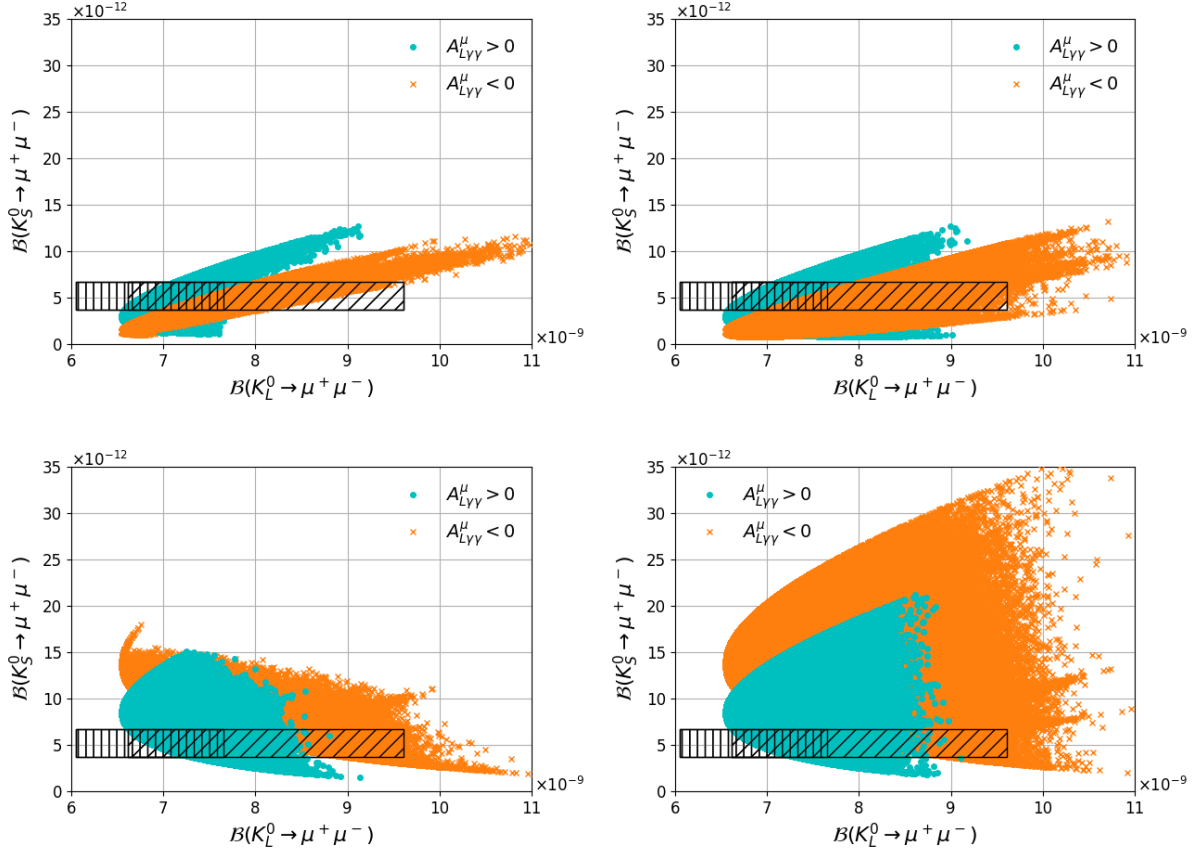


Figure 6.11: Scenario A $\mathcal{B}(K_S^0 \rightarrow \mu^+\mu^-)$ vs $\mathcal{B}(K_L^0 \rightarrow \mu^+\mu^-)$ for $(\delta_d^{LL})_{12} \neq 0$ and $(M_3 \cdot \mu) > 0$ (upper left), $(\delta_d^{LL})_{12} \neq 0$ and $(M_3 \cdot \mu) < 0$ (upper right), $(\delta_d^{RR})_{12} \neq 0$ and $(M_3 \cdot \mu) > 0$ (lower left), and $(\delta_d^{RR})_{12} \neq 0$ and $(M_3 \cdot \mu) < 0$ (lower right). The cyan dots correspond to $A_{L\gamma\gamma}^\mu > 0$ and the orange crosses to $A_{L\gamma\gamma}^\mu < 0$. The vertically hatched area corresponds to the SM prediction for $A_{L\gamma\gamma}^\mu > 0$ and the inclined hatched area corresponds to the SM prediction for $A_{L\gamma\gamma}^\mu < 0$.

then the SUSY contributions to $\mathcal{B}(K_L^0 \rightarrow \mu^+\mu^-)$ are canceled, while the SUSY contributions to $\mathcal{B}(K_S^0 \rightarrow \mu^+\mu^-)$ are maximized (see eqs. (6.14)–(6.18)). However, it is known that in those cases the bounds from ΔM_K and ε_K are very stringent. Fine-tuned regions with $\mathcal{B}(K_S^0 \rightarrow \mu^+\mu^-) > 10^{-10}$, or even at the level of the current experimental bound of 8×10^{-10} at 90% C.L. [?] (consistent with all the listed constraints ref?) while targetting large values of $\mathcal{B}(K_S^0 \rightarrow \mu^+\mu^-)$, can be found using genetic algorithms with cost functions.

These points are located along very narrow strips in the $(\delta_d^{LL})_{12}$ vs $(\delta_d^{RR})_{12}$ planes, as shown in figure 6.19. The figure corresponds to Scenario C as it is the one with higher density of points at large values of $\mathcal{B}(K_S^0 \rightarrow \mu^+\mu^-)$ and the pattern observed in Scenario A is nearly identical. A particularly favorable region corresponds to $|(\delta_d^{LL})_{12}| \approx 2|(\delta_d^{RR})_{12}| \sim 0.03$ and $\arg[(\delta_d^{LL})_{12}] \approx -\arg[(\delta_d^{RR})_{12}] + \pi$, which is in the vicinity of eq. (6.80), and with δ_u^{LL} given by the symmetry relation of eq. (6.7). They also favor narrow regions in the squark vs gluino

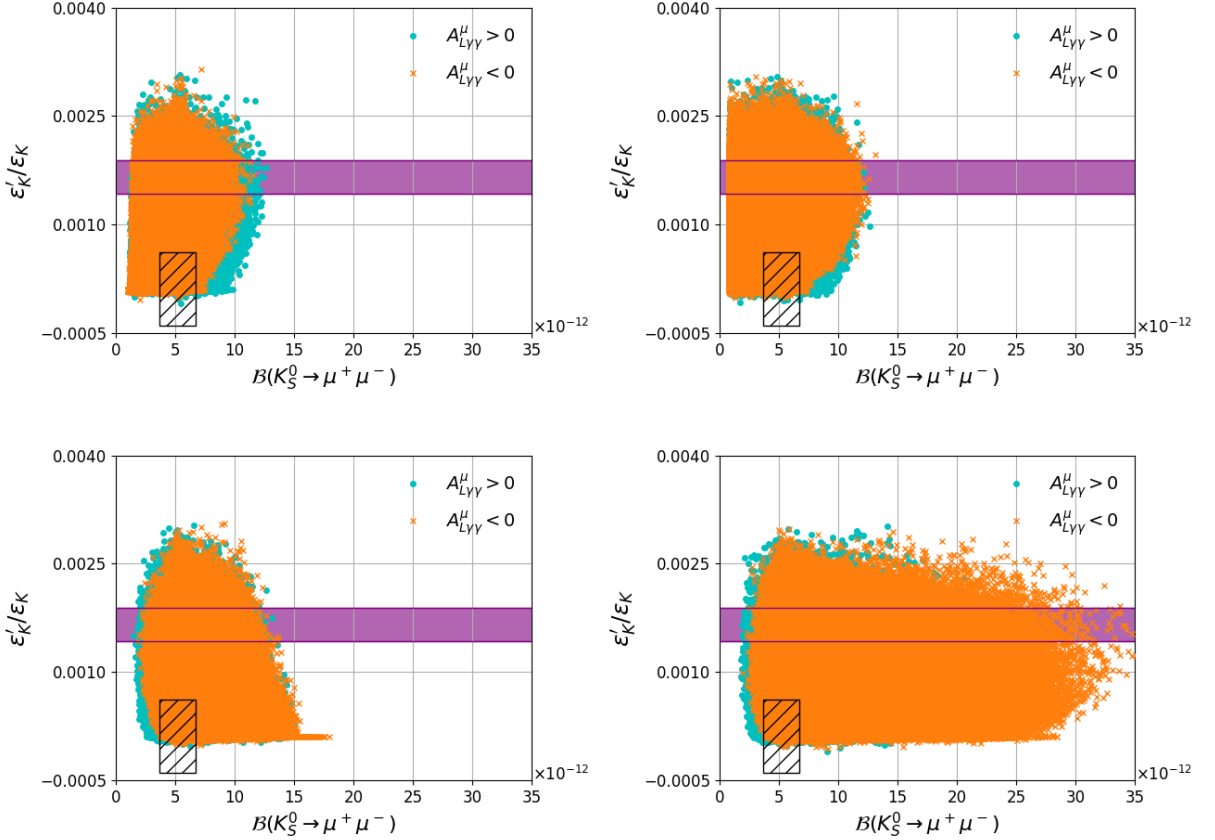


Figure 6.12: Scenario A $\frac{\varepsilon'_K}{\varepsilon_K}$ vs $\mathcal{B}(K_S^0 \rightarrow \mu^+ \mu^-)$ for $(\delta_d^{LL})_{12} \neq 0$ and $(M_3 \cdot \mu) > 0$ (upper left), $(\delta_d^{LL})_{12} \neq 0$ and $(M_3 \cdot \mu) < 0$ (upper right), $(\delta_d^{RR})_{12} \neq 0$ and $(M_3 \cdot \mu) > 0$ (lower left), and $(\delta_d^{RR})_{12} \neq 0$ and $(M_3 \cdot \mu) < 0$ (lower right). The cyan dots correspond to $A_{L\gamma\gamma}^\mu > 0$ and the orange crosses to $A_{L\gamma\gamma}^\mu < 0$. The deep purple band corresponds to the experimental results and the hatched area to the SM prediction.

masses planes as shown in figure 6.20. The values close to the experimental upper bound can still be obtained even if the constraint on ΔM_K is significantly tightened.

Using the SM prediction for ε_K provided in ref. [?]:

$$\varepsilon_K^{\text{EXP/SM}} = 1.41 \pm 0.16(\text{TH}), \quad (6.81)$$

It is found that it is easier to accommodate *LL* and *RR* MIs of similar sizes, and fine-tuned regions with $\mathcal{B}(K_S^0 \rightarrow \mu^+ \mu^-) > 10^{-10}$ are found with higher chances. The shapes of the strips in the mass insertion planes do not change substantially. Notice however that this prediction, that is obtained using $|V_{cb}|$ from exclusive decays, is less consistent with data than the one that was used previously.

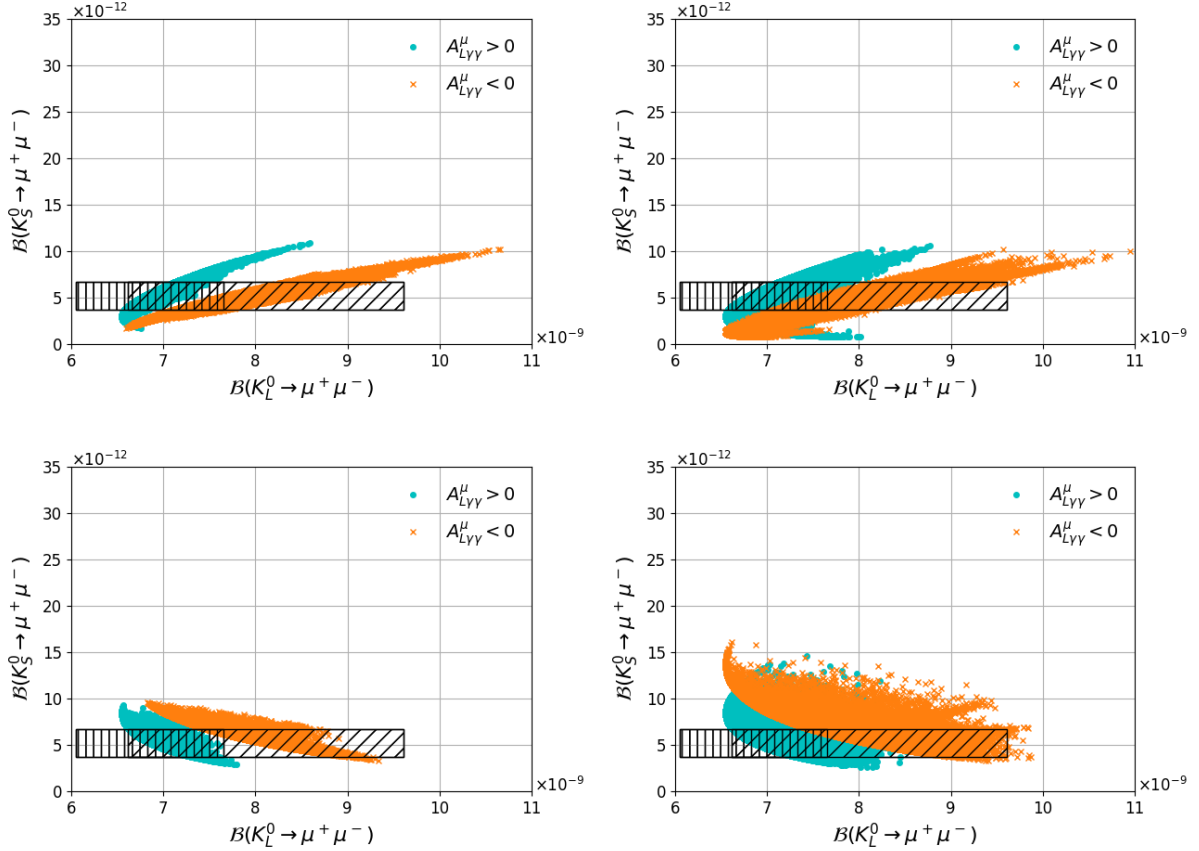


Figure 6.13: Scenario B, motivated by Higgsino Dark Matter with universal gaugino masses, $\mathcal{B}(K_S^0 \rightarrow \mu^+ \mu^-)$ vs $\mathcal{B}(K_L^0 \rightarrow \mu^+ \mu^-)$ for $(\delta_d^{LL})_{12} \neq 0$ and $(M_3 \cdot \mu) > 0$ (upper left), $(\delta_d^{LL})_{12} \neq 0$ and $(M_3 \cdot \mu) < 0$ (upper right), $(\delta_d^{RR})_{12} \neq 0$ and $(M_3 \cdot \mu) > 0$ (lower left), and $(\delta_d^{RR})_{12} \neq 0$ and $(M_3 \cdot \mu) < 0$ (lower right). The cyan dots correspond to $A_{L\gamma\gamma}^\mu > 0$ and the orange crosses to $A_{L\gamma\gamma}^\mu < 0$. The vertically hatched area corresponds to the SM prediction for $A_{L\gamma\gamma}^\mu > 0$ and the inclined hatched area corresponds to the SM prediction for $A_{L\gamma\gamma}^\mu < 0$.

2256 6.3.3.3 Non degenerate Higgs masses

2257 The results so far have been obtained in the MSSM framework, in which $|C_S| \approx |C_P|$, due to the
 2258 mass degeneracy $M_H \approx M_A$. In models in which such degeneracy can be broken, the constraint
 2259 that $\mathcal{B}(K_L^0 \rightarrow \mu^+ \mu^-)$ imposes to $\mathcal{B}(K_S^0 \rightarrow \mu^+ \mu^-)$ becomes looser the more those two masses
 2260 differ. This happens for example at low values of M_A in the MSSM, and requiring $\tan \beta$ to be
 2261 small to avoid constraints from $\tan \beta : M_A$ planes from LHC. Those regions are more difficult to
 2262 study, since it would require a detailed specification of the MSSM and test it against bounds of
 2263 the Higgs sector. The mass degeneracy is also broken in extensions such as NMSSM. According
 2264 to the scans performed, on those cases values of $\mathcal{B}(K_S^0 \rightarrow \mu^+ \mu^-) > 10^{-10}$ could be reached for
 2265 mass differences of $\mathcal{O}(33\%)$ or larger without fine-tuning the MIs.

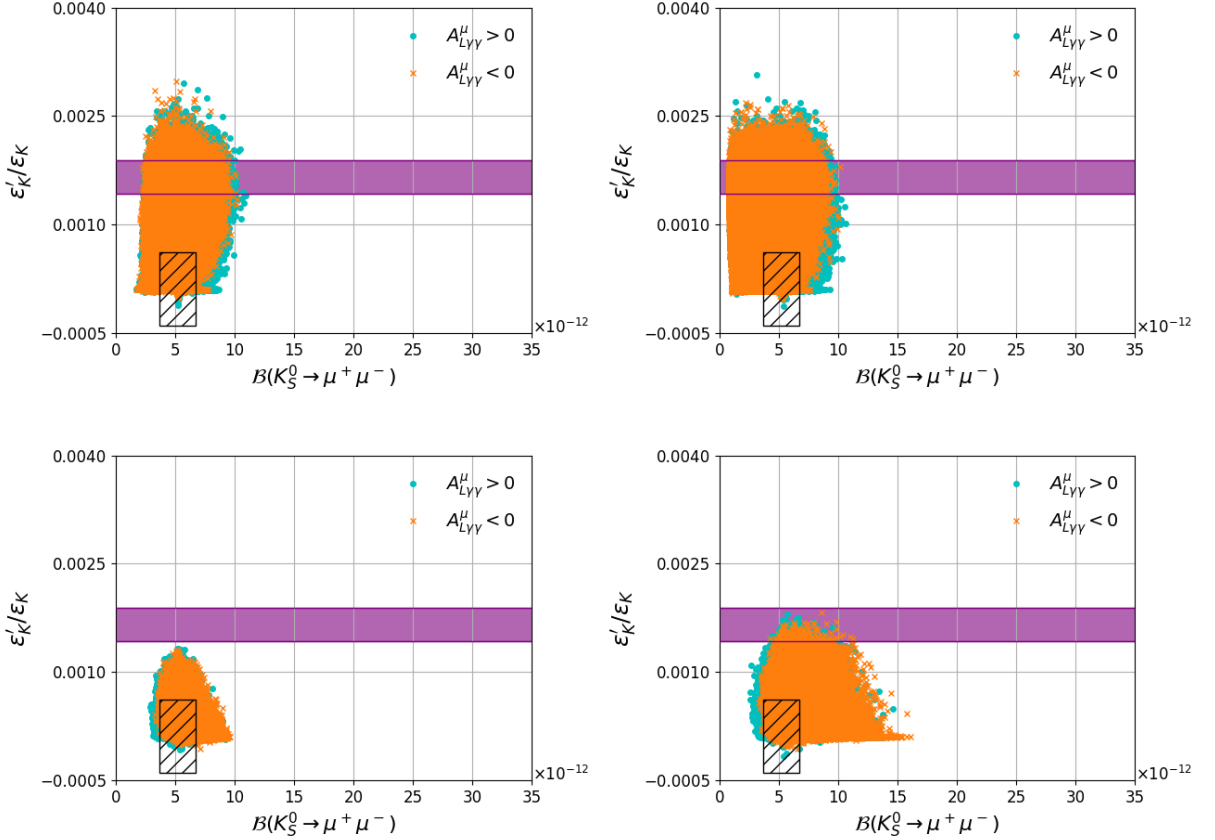


Figure 6.14: Scenario B, motivated by Higgsino Dark Matter and universal gaugino masses, $\frac{\varepsilon'_K}{\varepsilon_K}$ vs $\mathcal{B}(K_S^0 \rightarrow \mu^+\mu^-)$ for $(\delta_d^{LL})_{12} \neq 0$ and $(M_3 \cdot \mu) > 0$ (upper left), $(\delta_d^{LL})_{12} \neq 0$ and $(M_3 \cdot \mu) < 0$ (upper right), $(\delta_d^{RR})_{12} \neq 0$ and $(M_3 \cdot \mu) > 0$ (lower left), and $(\delta_d^{RR})_{12} \neq 0$ and $(M_3 \cdot \mu) < 0$ (lower right). The cyan dots correspond to $A_{L\gamma\gamma}^\mu < 0$ and the orange crosses to $A_{L\gamma\gamma}^\mu > 0$. The deep purple band corresponds to the experimental results and the hatched area to the SM prediction.

6.3.4 Conclusions

The MSSM contribution to $\mathcal{B}(K_S^0 \rightarrow \mu^+\mu^-)$ for non-zero $(\delta_d^{LL})_{12}$ and $(\delta_d^{RR})_{12}$ mass insertions has been studied, motivated by the experimental value of $\varepsilon'_K/\varepsilon_K$, and in the large $\tan\beta$ regime. It is found that MSSM contributions to $\mathcal{B}(K_S^0 \rightarrow \mu^+\mu^-)$ can surpass the SM contributions [$\mathcal{B}(K_S^0 \rightarrow \mu^+\mu^-)^{\text{SM}} = 5.18 \times 10^{-12}$] by up to a factor of seven (see figure 6.11), reaching the level of 3.5×10^{-11} even for large SUSY masses, with no conflict with existing experimental data, and are detectable by LHCb. This is also the case even if $\varepsilon'_K/\varepsilon_K$ turns out to be SM-like as predicted by refs. [?, ?, ?]. Figures of correlations between $\mathcal{B}(K_S^0 \rightarrow \mu^+\mu^-)$ and other observables have been provided for different regions of the MSSM parameter space, and can be used to understand which scenarios are more or less favoured, depending on the experimental outcomes. The 3.5×10^{-11} bound is due to the combined effect of $\Delta M_K, \varepsilon_K$, and $K_L^0 \rightarrow \mu^+\mu^-$

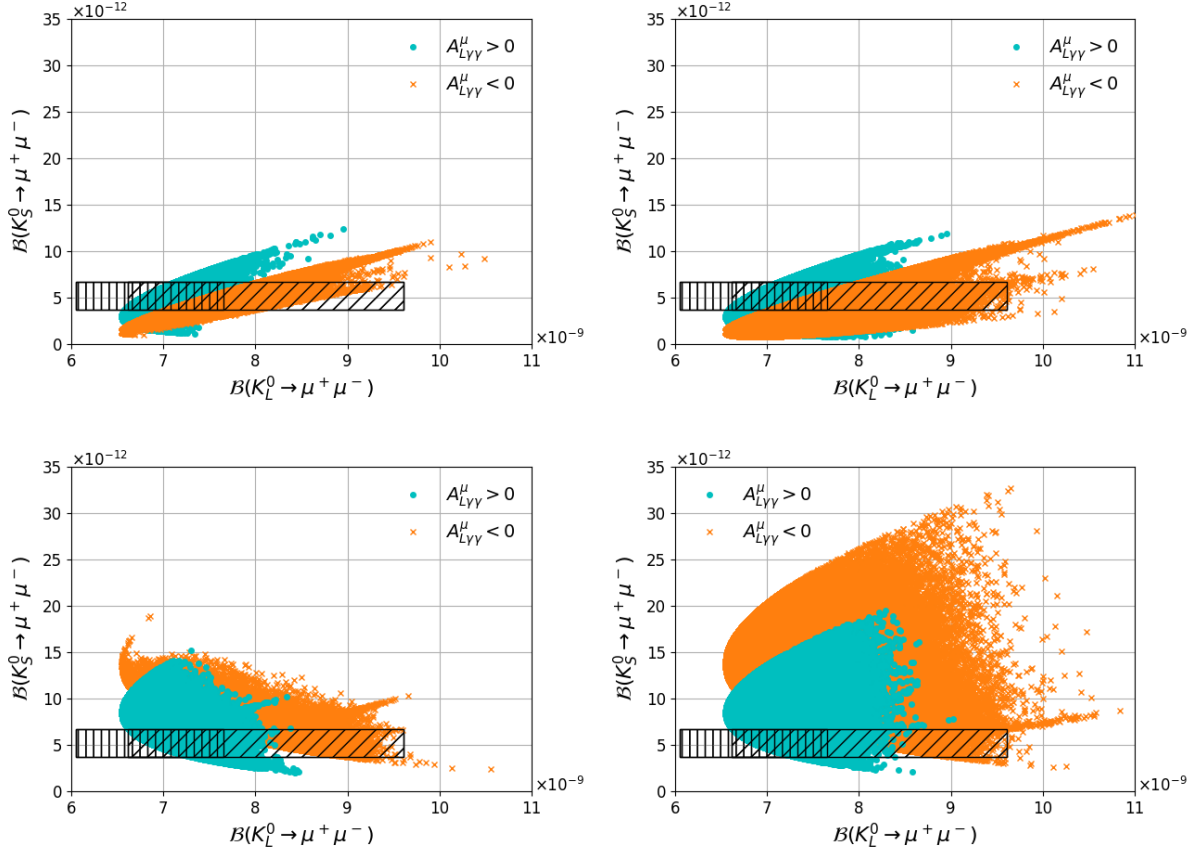


Figure 6.15: Scenario C (motivated by Wino Dark Matter) $\mathcal{B}(K_S^0 \rightarrow \mu^+ \mu^-)$ vs $\mathcal{B}(K_L^0 \rightarrow \mu^+ \mu^-)$ for $(\delta_d^{LL})_{12} \neq 0$ and $(M_3 \cdot \mu) > 0$ (upper left), $(\delta_d^{LL})_{12} \neq 0$ and $(M_3 \cdot \mu) < 0$ (upper right), $(\delta_d^{RR})_{12} \neq 0$ and $(M_3 \cdot \mu) > 0$ (lower left), and $(\delta_d^{RR})_{12} \neq 0$ and $(M_3 \cdot \mu) < 0$ (lower right). The cyan dots correspond to $A_{L\gamma\gamma}^\mu > 0$ and the orange crosses to $A_{L\gamma\gamma}^\mu < 0$. The vertically hatched area corresponds to the SM prediction for $A_{L\gamma\gamma}^\mu > 0$ and the inclined hatched area corresponds to the SM prediction for $A_{L\gamma\gamma}^\mu < 0$.

constraints. Such bound is not rigid, and fine-tuned regions can bring the branching fraction above the 10^{-10} level, even up to the current experimental bound; the largest deviations from SM are found at $|(\delta_d^{LL})_{12}| \approx 2|(\delta_d^{RR})_{12}| \sim 0.03$ and $\arg[(\delta_d^{LL})_{12}] \approx -\arg[(\delta_d^{RR})_{12}] + \pi$ for large squark and gluino masses. The the CP asymmetry of $K^0 \rightarrow \mu^+ \mu^-$ can be significantly modified by MSSM contributions, being up to eight times bigger than the SM prediction in the pure LL case. It should be noted that, for simplicity, only the main contributions in the large $\tan \beta$ regime have been considered. Discarded terms could, in principle, provide even more flexibility to the allowed regions.

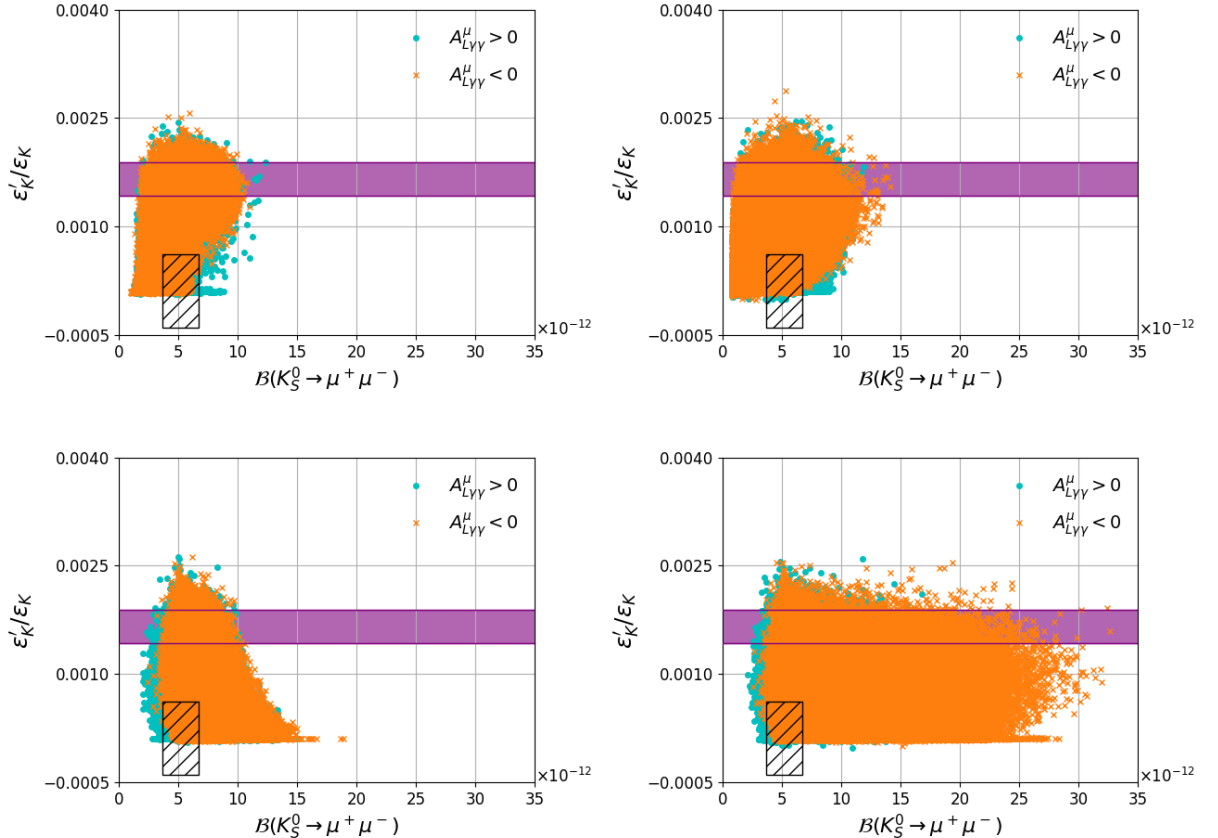


Figure 6.16: Scenario C, motivated by Wino Dark Matter, $\frac{\varepsilon'_K}{\varepsilon_K}$ vs $\mathcal{B}(K_S^0 \rightarrow \mu^+ \mu^-)$ for $(\delta_d^{LL})_{12} \neq 0$ and $(M_3 \cdot \mu) > 0$ (upper left), $(\delta_d^{LL})_{12} \neq 0$ and $(M_3 \cdot \mu) < 0$ (upper right), $(\delta_d^{RR})_{12} \neq 0$ and $(M_3 \cdot \mu) > 0$ (lower left), and $(\delta_d^{RR})_{12} \neq 0$ and $(M_3 \cdot \mu) < 0$ (lower right). The cyan dots correspond to $A_{L\gamma\gamma}^\mu > 0$ and the orange crosses to $A_{L\gamma\gamma}^\mu < 0$. The deep purple band corresponds to the experimental results and the hatched area to the SM prediction.

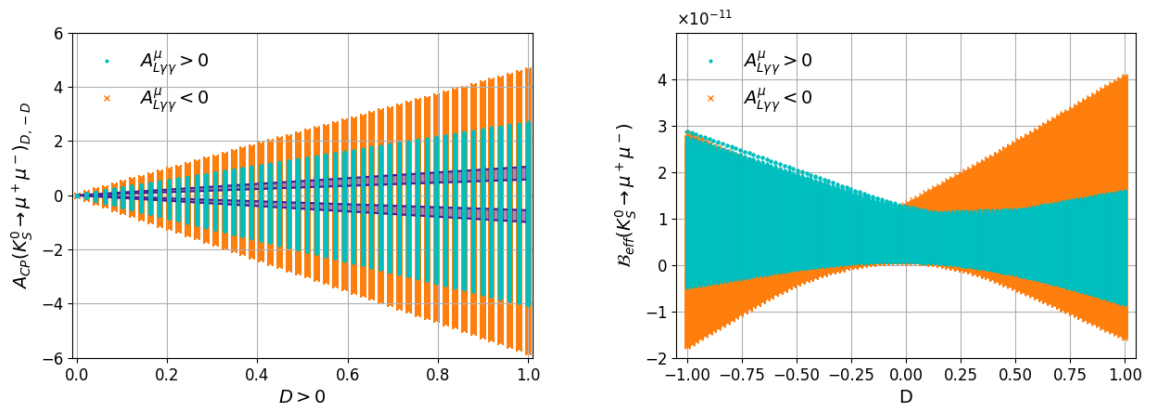


Figure 6.17: Scenario A, $(\delta_d^{LL})_{12} \neq 0$ and $(M_3 \cdot \mu) < 0$. Plots of $A_{CP}(K_S^0 \rightarrow \mu^+ \mu^-)$ vs D (left) for the case $D = -D'$ ($D > 0$) where the cyan dots correspond to $A_{L\gamma\gamma}^\mu > 0$, the orange crosses to $A_{L\gamma\gamma}^\mu < 0$, and the deep purple bands correspond to the SM predictions in eq. (6.38). $\mathcal{B}(K_S^0 \rightarrow \mu^+ \mu^-)_{\text{eff}}$ vs D (right).

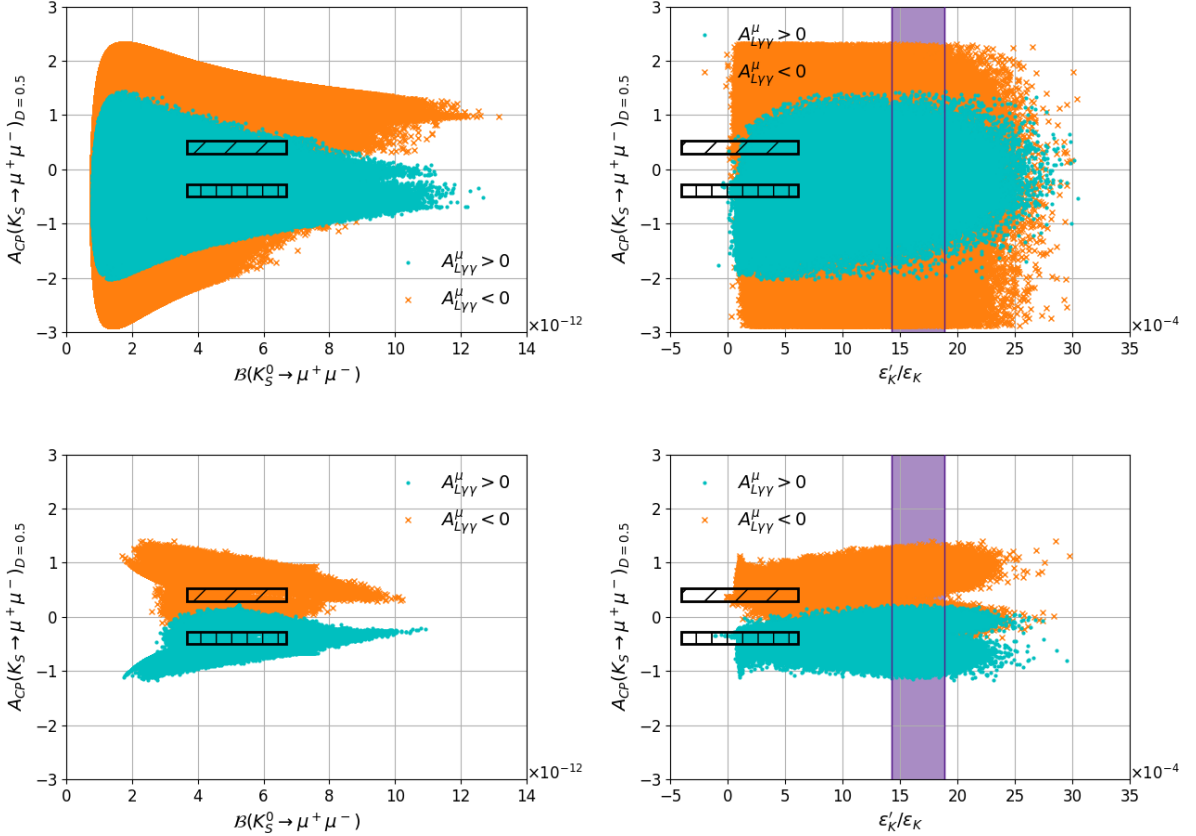


Figure 6.18: A_{CP} vs $\mathcal{B}(K_S^0 \rightarrow \mu^+ \mu^-)$ (left) and vs $\varepsilon'_K / \varepsilon_K$ (right). The top panels correspond to Scenario A, $(\delta_d^{LL})_{12} \neq 0$ and $(M_3 \cdot \mu) < 0$. The bottom panels correspond to Scenario B, $(\delta_d^{LL})_{12} \neq 0$ and $(M_3 \cdot \mu) > 0$. The plots are done for $D = -D' = 0.5$. The cyan dots correspond to $A_{L\gamma\gamma}^\mu > 0$ and the orange crosses to $A_{L\gamma\gamma}^\mu < 0$. The deep purple bands correspond to the experimental value of $\varepsilon'_K / \varepsilon_K$, the vertically hatched areas correspond to the SM prediction for $A_{L\gamma\gamma}^\mu > 0$ and the inclined hatched areas to the SM prediction for $A_{L\gamma\gamma}^\mu < 0$.

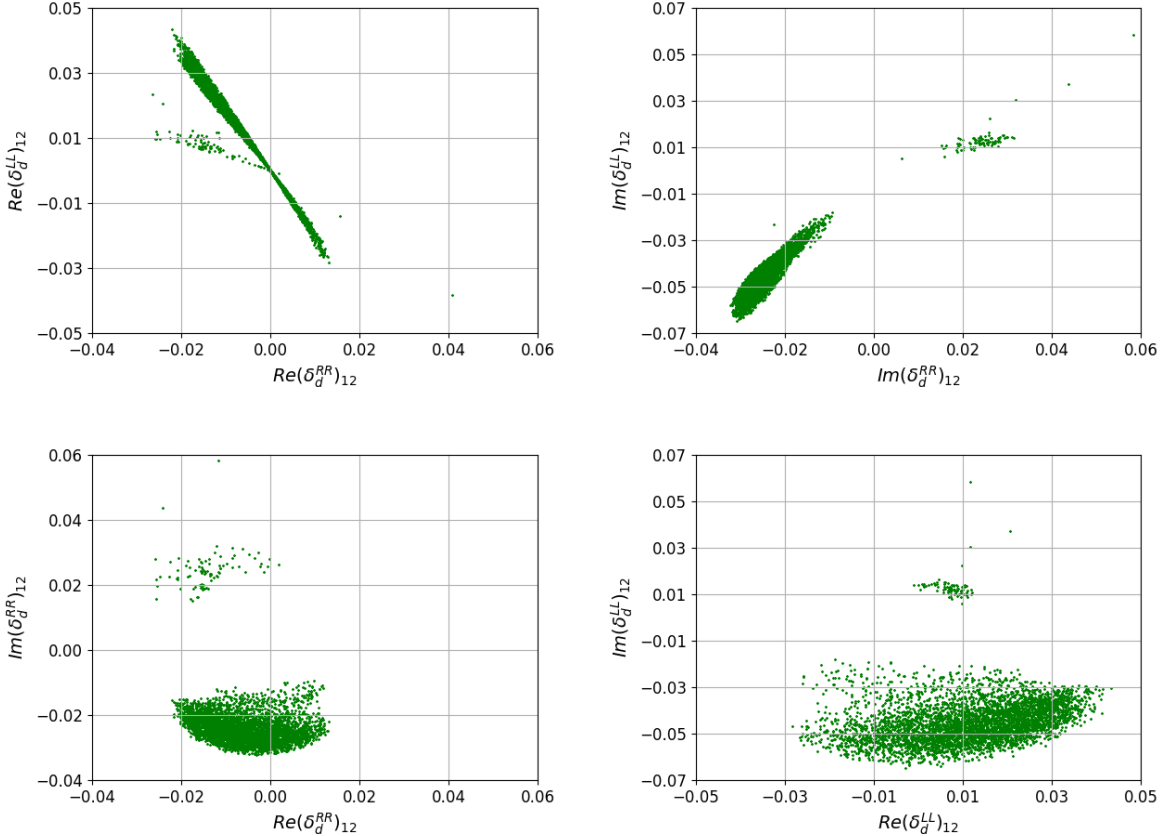


Figure 6.19: Scatter plots of the real (upper left) and the imaginary (upper right) parts of the mass insertions $(\delta_d^{RR})_{12}$ and $(\delta_d^{LL})_{12}$ for $\mathcal{B}(K_S^0 \rightarrow \mu^+ \mu^-) > 2 \times 10^{-10}$, of the real vs imaginary $(\delta_d^{RR})_{12}$ (lower left) and of the real vs imaginary $(\delta_d^{LL})_{12}$ (lower right). All points in the plane pass the experimental constraints defined in section ???. The up-type MI $(\delta_u^{LL})_{12}$ is given by eq. (6.7). The plots correspond to Scenario C, with a sample of 4378 points with $\mathcal{B}(K_S^0 \rightarrow \mu^+ \mu^-) > 2 \times 10^{-10}$ and $\chi^2 < 12.5$, produced after 6M generations of $200k$ points each. The pattern observed in Scenario A is very similar.

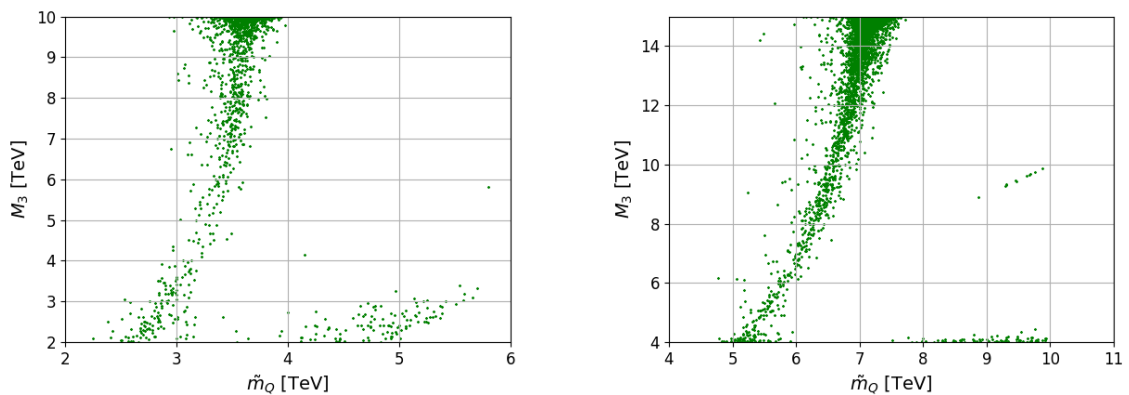


Figure 6.20: Scatter plot of the squark and gluino masses for $\mathcal{B}(K_S^0 \rightarrow \mu^+ \mu^-) > 2 \times 10^{-10}$ taking into account the constraints defined in section ???. Left: Scenario A, Right: Scenario C. The χ^2 cut in Scenario A has been relaxed to 14 to increase the density of points.

2285 **Chapter 7**

2286 **CMSSM**

2287 **7.1 MasterCode framework**

2288 The **MasterCode** framework performs global fits following a frequentist approach. Its core con-
2289 sists of tools to compute the different the SUSY observables, tools to calculate the χ^2 (that
2290 will be discussed in more details in [ref](#)) and the interface to an appropriate sampling algorithm,
2291 **MultiNest** [ref](#). So as to compute the SUSY observables, the full MSSM spectrum for **electroweak**
2292 **observables** (including masses, mixing matrices and couplings) is computed by **SoftSUSY 3.7.2**.
2293 The Higgs sector of this spectrum is further refined using calculations from **FeynHiggs 2.10.0**.
2294 This spectrum (in a format compliant with SUSY Les Houches Accord [ref](#)) is then used as input
2295 for other codes to compute more observables and constraints, summarised in [7.1](#). From this,
2296 a global likelihood function is constructed, including contributions from electroweak precision
2297 observables, flavour measurements, the cosmological dark matter density and direct searches for
2298 dark matter, as well as the LHC Higgs mass measurement and E_T searches.

Table 7.1: Codes used to calculate SUSY observables in the **MasterCode** framework.

| Code | Reference | Observables |
|---|---|--|
| SoftSUSY 3.7.2 | ref | SUSY spectrum |
| FeynHiggs-2.10.0 | ref | Higgs sector, $(g - 2)_\mu$ |
| micrOMEGAs-3.2 SSARD | ref | $\Omega_{\text{CDM}} h^2$ |
| SuFla, SuperIso v3.5 FeynWZ | ref ref | $\sigma_p^{\text{SI}}, \Delta\sigma_p^{\text{SI}}$ Flavour physics M_W, Z -pole |
| HiggsSignals-1.3.1 HiggsBounds-4.2.0 SDECAY-1.3b | ref ref ref | Constraints Higgs signal-strengths Constraints $H/A \rightarrow \tau^+\tau^-$ decay Decay tables |

2299 7.2 Sampling algorithm

2300 The main goal of the `MasterCode` framework is establishing confidence intervals for parameters
2301 and observables. In order to do this, the desired region is sampled and the likelihood function is
2302 inspected by means of the `MultiNest` algorithm ref. Even though it was designed as a Bayesian
2303 inference tool, it has proven to be very sucessful in computing profile likelihood functions ref.

2304 The likelihood is computed iteratively based on the so-called ellipsoidal neted sample. In
2305 this mechanism, ellipsoidal bounds are constructed in the unit cube based on clustering of N
2306 *active* points. For each iteration, the point with the lowest likelihood amongst a set of points
2307 (*live* or active) is discarded, and another one with higher likelihood is searched. When found, it
2308 replaces the former, that turns into an *inactive* point. This is done until the Bayesian evidence
2309 has reaches a value controled by the *tolerance*.

2310 Apart from its robustness and efficiency, this algorithm was specifically designed to deal
2311 with multiple local maxima and elongated curving degeneracies, thus fulfilling `MasterCode`'s
2312 requirements. A special feature of `MultiNest` is that once a point becomes active, it forms a
2313 basin of attraction, so that proximal points will be sampled. This ensures the coverage of small
2314 volumes, provided one of their points becomes active.

2315 In order to ensure a good coverage of the parameter space, this is divided into segments.
2316 The "cross-product" of these segments constitute *boxes*. For each of these boxes, the number
2317 of active points is $N = 1000$. Priors are defined in order to convert the input parameters into
2318 physical quantities computable by the likelihood. Usually soft flat priors are used (an example of
2319 this distribution can be seen in 7.1). With this, 80% of the distribution lies within the nominal
2320 segment range, with the rest 20 % lies outside these bounds. This allows for some overlap
2321 between boxes, hence avoiding edge effects between neighbouring parameter segments.

2322 7.3 Scan Ranges

2323 The scan ranges are chosen such that they include a full coverage of parameter space, paying
2324 spacial attention to the mass scales relevant for LHC, while maintaining the Yukawa couplings
2325 perturbatively small (hence $1.2 \leq \tan \beta \geq 65$). The input parameters and the nuisance param-
2326 eters are sampled using soft flat and Gaussian priors, respectively. The ranges, the number of
2327 segments and the resulting number of boxes that are used in the scan are given in 7.2.

Table 7.2: Sampling ranges and segment definitions in the MODEL.

| Parameter | Range | # Segments |
|-----------|---------|------------|
| MISSING | MISSING | MISSING |

2328 7.4 Method

2329 So as to explore the different models within the `MasterCode` framework, frequentist confidence
2330 intervals and regins for the model parameters and corresponding predictions for physical ob-

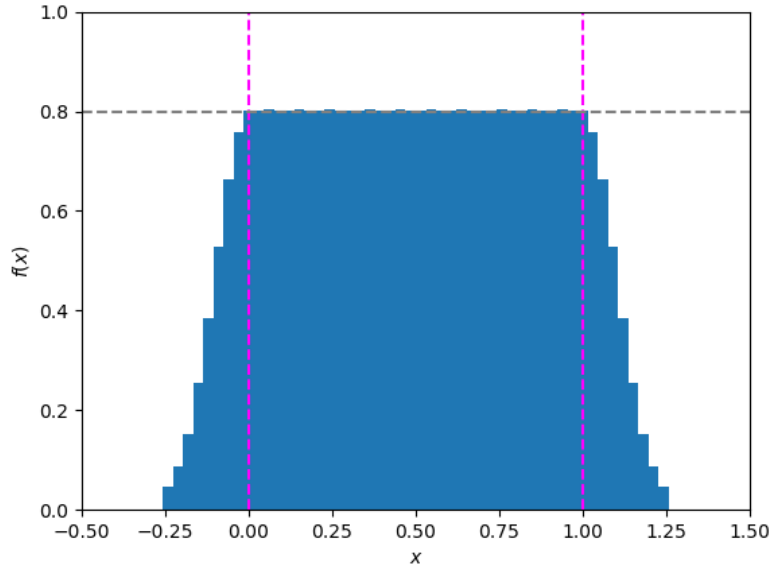


Figure 7.1: Illustration of soft flat prior, for which 80% is flat and lies within the nominal range of the segment ($[0,1]$]), while 20% of the distribution lies outside the nominal range, and is normally distributed.

servables are established. In order to do this, a χ^2 function is constructed from the likelihood function using Wilks' theorem, $\chi^2 \approx -2 \ln(\theta) + \text{const.}$, being this normalisation constant irrelevant. **For the sake of this study**. The χ^2 function is given by

$$\chi^2(\theta) \equiv \sum_i \left(\frac{O_{i,\text{meas.}} - O_{i,\text{pred.}}}{\sigma(O_i)} \right)^2 + \sum_j \left(\frac{\theta_{j,\text{meas.}}^{\text{SM}} - \theta_{j,\text{nuis.}}^{\text{SM}}}{\sigma(\theta_{j,\text{meas.}}^{\text{SM}})} \right)^2 + \sum_k \chi_{k,\text{non-Gaussian}}^2 \quad (7.1)$$

where $O_{i,\text{pred.}}(\theta)$ ($O_{i,\text{meas.}}(\theta)$) are the predicted (measured) values for the observables, $\theta(O_i)$ is the total uncertainty, obtained adding the experimental and theoretical uncertainties in quadrature, and $\theta_{k,\text{nuis.}}$ are the SM nuisance parameters m_t , $\Delta\alpha_{\text{had}}^{(5)}(M_Z)$, M_Z that are allowed to vary in the fit while being constrained according to their measured values and uncertainties. The first two terms in 7.1 correspond to a normal distribution of the likelihood, thus being "Gaussian" constraints, while the third term is "non-Gaussian" and a more refined treatment is needed. The confidence intervals for n parameters and/or physical observables of interest at a confidence level α are thus given by the condition $\Delta\chi^2 \leq \Delta\chi^2(\alpha, n)$. Some typical values are given in 7.3. Therefore, 68% CL intervals (regions) correspond to $\Delta\chi^2 < 1$ ($\Delta\chi^2 < 2.30$), while 95% CL intervals (regions) correspond to $\Delta\chi^2 < 4$ ($\Delta\chi^2 < 5.99$) for one- (two-)dimensional profile likelihood functions.

7.4.1 Gaussian Constraints

The following Gaussian Constraints are used in the study:

Table 7.3: Sampling ranges and segment definitions in the MODEL.

| $\alpha(\%)$ | $\Delta\chi^2(\alpha, 1)$ | $\Delta\chi^2(\alpha, 2)$ |
|--------------|---------------------------|---------------------------|
| 68 | 0.99 | 2.27 |
| 68.3 | 1 | 2.30 |
| 95 | 3.84 | 5.99 |
| 95.4 | 4 | 6.18 |
| 99 | 6.63 | 9.21 |
| 99.7 | 9 | 11.82 |

- 2347 • 95% CL lower limits on the masses of SUSY particles from ALEPH, DELPHI, L3, OPAL
2348 experiments [ref](#).
- 2349 • Top Mass, $m_t = 173.34 \pm 0.76$ GeV[ref](#), treated as a nuisance parameter.
- 2350 • Light Higgs Boson, with a measured mass[ref](#) of $M_h = 125.09 \pm 0.24_{\text{EXP}} \pm 1.5_{\text{SUSY}}$ GeV.
2351 The assumed theoretical uncertainty for the lightest Higgs mass within MSSM (computed
2352 using **FeynHiggs-2.10.0**) is a conservative but accurate estimate of the point-by-point
2353 uncertainty that can be calculated with such [code](#). Further constraints on the Higgs decays
2354 are incorporated using **HiggsSignals-1.3.1**.
- 2355 • Dark Matter Relic Density, determined from anisotropies in the Cosmic Microwave Back-
2356 ground and satellite measurements, $\Omega_{\text{CDM}}h^2 = 0.1186 \pm 0.0022_{\text{EXP}} \pm 0.012_{\text{TH}}$, from [ref](#).
2357 The SUSY prediction is taken from **micrOMEGAs-3.2**. Given the high sensitivity of such
2358 prediction to the given spectrum, a theoretical uncertainty of $\sim 10\%$ is assumed.
- 2359 • The Anomalous Dipole Moment of the Muon, $(g - 2)_\mu^{\text{EXP}} - (g - 2)_\mu^{\text{SM}} = (30.2 \pm 5.4_{\text{stat}} \pm$
2360 $3.3_{\text{sys}} \pm 6.1_{\text{SM}} \pm 2.0_{\text{SUSY}}) \times 10^{-10}$, from [refs](#). The anomalous dipole moment is computed
2361 within MSSM using **FeynHiggs-2.10.0**.
- 2362 • Electroweak Precision Observables, M_W and the Z -pole observables. These are computed
2363 using **FeynWZ**. Its inputs, $\Delta\alpha_{\text{had}}^{(5)}(M_Z)$ and M_Z , are treated as nuisance parameters in the
2364 fit.
- 2365 • Flavour Physics Observables, such as branching fractions from rare B decays, rare K
2366 decays, $B - \bar{B}$ mixing and ϵ_K . The SUSY predictions for flavour physics observables are
2367 calculated using **SuFla** [update](#).

2368 7.4.2 Non-Gaussian Constraints

2369 Contributions from non-Gaussian constraints include:

- 2370 • Searches for Squarks and Gluinos by ATLAS and CMS [ref](#), that strongly constraint the
2371 parameter space of the models. A χ^2 is extrapolated from the provided contour plots. [ref](#)
2372 [38 en Higgs](#)

- 2373 ● Production of heavy neutral Higgs bosons decaying into taus, $H/A \rightarrow \tau^+ \tau^-$. As before,
2374 a χ^2 is constructed from the exclusion contours from ATLAS [ref](#) and CMS [ref](#) using
2375 [HiggsBounds-4.2.0](#).
- 2376 ● Spin-independent cross-section of neutralino-nucleus elastic scattering, taking into account
2377 results from LUX, XENON and PICO [check](#), [refs](#) and theor experimental uncertainties in
2378 the theoretical calculation [ref 79](#) Kees.
- 2379 ● [reinterpretation of searches?](#)

Appendices

Appendix A

MasterCode observables

A.1 Mass Spectrum

The electroweak symmetry breaking of the MSSM leads to 4 physical Higgs particles: a CP -odd scalar (A), two CP -even neutral scalars (h^0 and H^0) and two charged scalars (H^\pm), with masses given by

$$\begin{aligned} M_A^2 &= |\mu|^2 + m_{H_u}^2 + m_{H_d}^2 \\ M_{h^0, H^0}^2 &= \frac{1}{2} \left[M_A^2 + M_Z^2 \mp \sqrt{(M_A^2 + M_Z^2)^2 - 4M_Z^2 M_A^2 \cos 2\beta^2} \right] \\ M_{H^\pm}^2 &= M_A^2 + M_W^2 \end{aligned} \quad (\text{A.1})$$

As for the neutralinos, its mass matrix is given by

$$\mathbf{Y} = \begin{pmatrix} M_1 & 0 & -c_\beta s_W M_Z & s_\beta s_W M_Z \\ 0 & M_2 & c_\beta c_W M_Z & -s_\beta c_W M_Z \\ -c_\beta s_W M_Z & c_\beta c_W M_Z & 0 & -\mu \\ s_\beta s_W M_Z & -s_\beta c_W M_Z & -\mu & 0 \end{pmatrix} \quad (\text{A.2})$$

where $s_\beta = \sin \beta$, $c_\beta = \cos \beta$, $c_W = \cos W$, $s_W = \sin W$. The four neutralino masses are obtained diagonalising [A.2](#), $\mathbf{N} \mathbf{Y} \mathbf{N}^{-1} = \text{diag}(m_{\tilde{\chi}_1^0}, m_{\tilde{\chi}_2^0}, m_{\tilde{\chi}_3^0}, m_{\tilde{\chi}_4^0})$, where $m_{\tilde{\chi}_1^0} < m_{\tilde{\chi}_2^0} < m_{\tilde{\chi}_3^0} < m_{\tilde{\chi}_4^0}$.

In the case of the charginos, its mass matrix is:

$$\mathbf{X} = \begin{pmatrix} M_2 & \sqrt{2}s_\beta M_W \\ \sqrt{2}c_\beta M_W & \mu \end{pmatrix} \quad (\text{A.3})$$

It is diagonalised by two unitary matrices, \mathbf{U} , \mathbf{V} as $\mathbf{U}^* \mathbf{X} \mathbf{V}^{-1} = \text{diag}(m_{\tilde{\chi}_1^\pm}, m_{\tilde{\chi}_2^\pm})$, where

$$m_{\tilde{\chi}_1^\pm}^2, m_{\tilde{\chi}_2^\pm}^2 = \frac{1}{2} \left\{ |M_2|^2 + |\mu|^2 + M_W^2 \mp \sqrt{(|M_2|^2 + |\mu|^2 + 2M_W^2)^2 - 4|\mu M_2 - M_W \sin 2\beta|^2} \right\} \quad (\text{A.4})$$

For the sfermion, the mass terms are given in the MSSM Lagrangian by <https://arxiv.org/pdf/hep-ph/0604147.pdf>:

$$\mathcal{L} = -\frac{1}{2}(\tilde{f}_L^\dagger, \tilde{f}_R^\dagger) \begin{pmatrix} M_L^2 + m_f^2 & m_f X_f^* \\ m_f X_f & M_R^2 + m_f^2 \end{pmatrix} \begin{pmatrix} \tilde{f}_L \\ \tilde{f}_R \end{pmatrix} \quad (\text{A.5})$$

2394 where

$$\begin{aligned} M_L^2 &= M_{\tilde{F}}^2 + M_Z^2 \cos 2\beta (I_3^f - Q_f s_W^2), \\ M_R^2 &= M_{\tilde{F}'}^2 + M_Z^2 \cos 2\beta Q_f s_W^2, \\ X_f &= A_f - \mu * \cot \beta, \tan \beta \end{aligned} \quad (\text{A.6})$$

2395 $\cot \beta$ and $I_3^f = \frac{1}{2}$ ($\tan \beta$ and $I_3^f = -\frac{1}{2}$) correspond to up-type squarks (down-type squarks
2396 and sleptons) and $M_{\tilde{F}, \tilde{F}'}$ denote the left-handed and right-handed soft SUSY breaking mass
2397 parameters respecitvely, and Q_f is the electromagnetic charge. The sfermion mass eigenstate
2398 can be obtained with unitary matrix, $\mathbf{U}_{\tilde{\mathbf{f}}}$, giving the eigenvalues:

$$m_{\tilde{f}_{1,2}}^2 = m_f^2 + \frac{1}{2} [(M_L^2 - M_R^2)^2 + 4m_f^2 |X_f|^2] \quad (\text{A.7})$$

2399 **sneutrino masses?**

2400 A.2 Dark Matter Relic Density

2401 The cosmological dark matter density is one of two most important dark matter constraints. Its
2402 value is measured by Planck to be $\Omega_{\text{CDM}} h^2 = 0.1186 \pm 0.0020_{\text{EXP}} \pm 0.0024_{\text{TH}}$ ref, where h is
2403 the reduced Hubble constant. Assuming the neutralino to be the supersymmetric DM candidate
2404 and the only responsible for the DM relic density, different (co)annihilation mechanisms are
2405 suggested to bring the obtained density into the observed range. Some of these mechanisms
2406 (hereafter, DM mechanisms) are:

- 2407 1. Bulk region: in the case where the neutralino is mostly Bino-like and at least one of the
2408 sfermions is not too heavy, the neutralino annihilates to a pair of SM particles (e.g., a pair
2409 of fermions) via t-channel exchange of a sfermion. [plot?](#)
- 2410 2. Sfermion coannihilation: it takes place when sfermions have nearly degenerate masses and
2411 the LSP is mostly Bino-like. The condition for stau and stop coannihilation (\tilde{f}) is:

$$\left(\frac{m_{\tilde{f}}}{m_{\tilde{\chi}_1^0}} - 1 \right) < 0.15 \quad (\text{A.8})$$

- 2412 3. A/H , h and Z Funnels: in this mechanism, the neutralino is mostly Bino-like and
2413 $\left| \frac{M_{A,H,h}}{m_{\tilde{\chi}_1^0}} - 2 \right| < 0.1$
- 2414 4. *Hybrid* regions: where more than one of the aforementioned DM mechanism dominate.
2415 [more?](#)
- 2416 5. Chargino coannihilation: fulfilled when the lightest chargino and neutralino are nearly
2417 degenerate: $\left(\frac{m_{\tilde{\chi}_1^\pm}}{m_{\tilde{\chi}_1^0}} - 2 \right) < 0.25$, being the LSP either Higgsino-like (with very heavy
2418 neutralinos) or Bino-like.

2419 6. Focus-point region: fulfilled when the LSP has an enhanced Higgsino component as a
 2420 result of a near-degeneracy in the neutralino mass matrix, $\left(\frac{\mu}{m_{\tilde{\chi}_1^0}} - 1 < 0.3\right)$

2421 7. Your model here

2422 A.3 Neutralino Scattering off Nuclei

2423 One of the most powerful ways in which to search for DM is to look for its scattering on nuclei
 2424 in low-background underground experiments ref, both in direct (**XENON1T**, **LUX**, **PandaX-II**
 2425 ...) and indirect (**IceCube**, **PICO**) dark matter detection experiments, that include searches
 2426 for **γ -rays**, **neutrinos**, **positrons or antiprotons** from DM annihilations near the Galactic Center,
 2427 Galactic Halo and in dwarf galaxies, and for highly energetic neutrinos produced by the annihi-
 2428 lations of DM particles inside the Sun ref or Earth ref. In both cases, the signals are proportional
 2429 to the local density of dark matter and the χ -nucleon cross-section. Within MSSM, four ob-
 2430 servables can contribute to this scattering: the spin-independent and dependent cross sections
 2431 of neutralinos on protons and nucleons. These contributions appear in non velocity dependent
 2432 part of the MSSM Lagrangian that addresses the χ -nucleon scattering:

$$\mathcal{L} = \alpha_{2i} \bar{\chi} \gamma^\mu \gamma^5 \bar{q}_i \gamma_\mu \gamma^5 q_i + \alpha_{3i} \bar{\chi} \chi \bar{q}_i q_i \quad (\text{A.9})$$

2433 where the coefficients sum over the quark generations, denoting i up-type ($i = 1$) and down-type
 2434 ($i = 2$) quarks. The first term is spin-dependent, while the second part is spin-dependent. The
 2435 cross-sections for these two parts are obtained from α_{3i} and α_{2i} , respectively.

2436 A.3.1 Spin-Independent Term

2437 The scalar or spin-independent (SI) part of the cross-section can be written in the zero-
 2438 momentum-transfer limit as

$$\sigma_{\text{SI}} = \frac{4m_r^2}{\pi} [Z f_p + (A - Z) f_n]^2 \quad (\text{A.10})$$

2439 where m_r is the χ -nuclear reduced mass, Z the atomic number, A the atomic weight, and for
 2440 $N = n$ or p

$$\frac{f_N}{m_N} = \sum_{q=u,d,s} f_{T_q}^{(N)} \frac{\alpha_{3q}}{m_q} + \frac{2}{27} f_{TG}^{(N)} \sum_{q=c,b,t} \frac{\alpha_{3q}}{m_q} \quad (\text{A.11})$$

2441 and

$$m_N f_{T_q}^{(N)} \equiv \langle N | m_q \bar{q} q \rangle \equiv m_q B_q^{(N)}, \quad f_{TG}^{(N)} = 1 - \sum_{q=u,d,s} f_{T_q}^{(N)} \quad (\text{A.12})$$

2442 The π -nucleon sigma term, $\Sigma_{\pi n}$, may be written as

$$\Sigma_{\pi n} \equiv \frac{1}{2} (m_u + m_d) \times (B_u^{(N)} + B_d^{(N)}) \quad (\text{A.13})$$

2443 It is related to the strange scalar density in the nucleon, y , by

$$y = 1 - \sigma_0 / \Sigma_{\pi N} \quad (\text{A.14})$$

A.3.2 Spin-Dependent Term

The scalar or spin-dependent (SD) part of the cross-section can be written in the zero-momentum-transfer limit as

$$\sigma_{\text{SD}} = \frac{32}{\pi} G_F^2 m_r^2 \Lambda^2 J(J+1) \quad (\text{A.15})$$

where J is the spin of the nucleus and

$$\Lambda \equiv \frac{1}{J} (a_p \langle S_p \rangle + a_n \langle S_n \rangle) \quad (\text{A.16})$$

and

$$a_p = \sum_q \frac{\alpha_{2q}}{\sqrt{2}G_f} \Delta_q^{(p)}, \quad a_n = \sum_i \frac{\alpha_{2q}}{\sqrt{2}G_f} \Delta_q^{(n)} \quad (\text{A.17})$$

The factors $\Delta_q^{(N)}$ parametrize the quark spin content of the nucleon and are only significant for the light (u,d,s) quarks.

The biggest uncertainty in spin-independent scattering is due to the poor knowledge of the $\langle N|q\bar{q}|N\rangle$ matrix elements linked to the π -nucleon σ term, $\Sigma_{\pi N}$, followed by uncertainties in the SU(3) octet symmetry-breaking contribution to the nucleon mass, σ_0 . The treatment of the spin-independent nuclear scattering matrix element within `MasterCode` is performed with `SSARD`.

Given the expressions in A.10 and A.15, experiments with heavy elements such as Ge and Xe are more sensitive to σ_{SI} (proportional to Z^2) than to σ_{SD} . The SD cross sections are on the other hand nearly independent on the quark masses ref.

A.4 Anomalous Magnetic Moment of the Muon

The magnetic moment for a given lepton, l , is related to its intrinsic spin, \vec{S} , through the Dirac equation:

$$\vec{M} = g_l \frac{e}{2m_l} \vec{S} \quad (\text{A.18})$$

Where m_l is the lepton mass and g_l is the gyromagnetic ratio. Quantum loop effects to the Dirac prediction are parameterized by the anomalous magnetic moment

$$a_l \equiv \frac{g_l - 2}{2} \quad (\text{A.19})$$

While for the electron this quantity is the most precisely measured ref and calculated ref quantity in Nature, this is not the case for the muon. For this particle, $g_\mu = 2$, while

$$a_\mu^{\text{SM}} = a_\mu^{\text{QED}} + a_\mu^{\text{EW}} + a_\mu^{\text{Had}} \quad (\text{A.20})$$

where photonic and leptonic contributions are embedded inside a_μ^{QED} , W^\pm , Z or Higgs loops are accounted for in a_μ^{EW} and a_μ^{Had} contain hadronic (quark and gluon) loop contributions:

$$a_\mu^{\text{QED}} = 116584718.95(0.08) \times 10^{-11} \quad (\text{A.21})$$

2468 where the main contribution to the uncertainty comes from the fine structure constant, α ref

$$a_\mu^{\text{EW}} = a_\mu^{\text{EW}}[1 - \text{loop}] + a_\mu^{\text{EW}}[2 - \text{loop}] = 153.6(1.0) \times 10^{-11} \quad (\text{A.22})$$

2469 and

$$a_\mu^{\text{Had}}[\text{LO}] = 6931(33)(7) \times 10^{-11}, \quad a_\mu^{\text{Had}}[\text{N(N)LO}] = 19(26) \times 10^{-11} \quad (\text{A.23})$$

2470 where the error is dominated by systematic uncertainties and perturbative QCD for Lead-
2471 ing Order (LO), and by hadronic light-by-light uncertainty in (Next-to-)Next-Leading Order
2472 (N(N)NLO). Summing all these contributions give rise to the SM prediction:

$$a_\mu^{\text{SM}} = 116591823(1)(34)(26) \times 10^{-11} \quad (\text{A.24})$$

2473 being the errors due to the electroweak, lowest-order hadronic and higher-order hadronic contri-
2474 butions, respectively. As it can be seen, the hadronic contribution to the anomalous magnetic
2475 moment dominates the uncertainty. The most precise measurement of this quantity has been
2476 made studying the precession of μ^+ and μ^- in a constant external magnetic field inside a con-
2477 fining storage ring by the E821 experiment at Brookhaven National Lab (BNL), yielding:

$$a_\mu^{\text{exp}} = 11659209.1(5.4)(3.3) \times 10^{-10} \quad (\text{A.25})$$

2478 where the first error is statistic and the second systematic. Therefore

$$\Delta a_\mu = a_\mu^{\text{exp}} - a_\mu^{\text{SM}} = 268(63)(43) \times 10^{-11} \quad (\text{A.26})$$

2479 where the first error is experimental and the second theoretical. Hence, there is a 3.5σ discrep-
2480 ancy between the experimental and SM results. Possible explanations for such difference arise
2481 in a Supersymmetric scenario, where there is an additional contribution:

$$a_\mu^{\text{SUSY}} \simeq \pm 130 \times 10^{-11} \left(\frac{100 \text{GeV}}{m_\Lambda} \right)^2 \tan \beta \quad (\text{A.27})$$

2482 An alternative scenario that can give explanation to this disagreement is that with a *dark photon*,
2483 a relatively light vector boson from the dark matter sector that couples to the SM sector through
2484 mixing with the ordinary photon. refs

2485 A.5 Electroweak Precision Observables

2486 Electroweak precision observables (henceforth, EWPO), are known with high accuracy. There-
2487 fore, they serve as useful constraints in NP models. The EWPO that are used within the
2488 **MasterCode** framework are the following: **Inclusive Quantities: Cross-Sections and Par-**
2489 **tial Widths:**

- 2490 • Z mass, M_Z
- 2491 • Total decay width, Γ_Z
- 2492 • Hadronic pole cross-section $\sigma_{\text{had}}^0 \equiv \frac{12\pi}{M_Z^2} \frac{\Gamma_{ee}\Gamma_{\text{had}}}{\Gamma_Z^2}$

- 2493 • Ratio of hadronic to leptonic decay $R_l^0 \equiv \Gamma_{\text{had}}/\Gamma_{ll}$
 2494 • Ratio of partial decay width into $q\bar{q}$ ($q = b, c$) to the total hadronic width $R_q^0 = \Gamma_{q\bar{q}}/\Gamma_{rmhad}$

2495 **Asymmetries and Effective Fermionic Weak Mixing Angle:**

- 2496 • Asymmetry parameters, $\mathcal{A}_f \equiv 2 \frac{\text{Re}(g_{Vf} g_{Af})}{1 + \text{Re}(g_{Vf}/g_{Af})^2}$, where g_{Vf} and g_{Af} are the effective vector
 2497 and axial couplings
 2498 • Forward backward asymmetries, $A_{FB}^{0,f} = \frac{3}{4} \mathcal{A}_e \mathcal{A}_f$
 2499 • Effective fermionic weak mixing angle, $\sin \theta_{\text{eff}}^f$

2500 Observables with the superscript 0 are *pseudo-observables*, derived from measured quantities to
 2501 facilitate the theoretical interpretation.

2502 **A.6 Flavour Physics Observables**

2503 Flavour Physics Observables (hereafter, FPO) are also included within the `MasterCode` frame-
 2504 work, as their observables are also affected by NP. The B -meson decays $B_{s,d} \rightarrow \mu^+ \mu^-$, $B \rightarrow X_s \gamma$,
 2505 $B \rightarrow \tau \nu$, $B \rightarrow X_s ll$, the K -mesond decays $K \rightarrow \mu \nu$, $K \rightarrow \pi \nu \bar{\nu}$, observables related to $B - \bar{B}$
 2506 mixing ΔM_{B_s} , $\frac{\Delta M_{B_s}^{\text{EXP/SM}}}{\Delta M_{B_d}^{\text{EXP/SM}}}$ and $\Delta \epsilon_K$ are included. [ref](#)

2507 **Appendix B**

2508 **Coverage of the uncertainty with the
2509 sFit**

2510 Figures below show the distributions of the parameters from the fit, together with their cor-
2511 responding pull distributions, obtained when performing the bootstrapping test, for both sim-
2512 ulation (Fig. B.2 and Fig. B.1), data (Fig. B.4 and Fig. B.3), and simulation of signal and
2513 background (Fig. B.6 and Fig. B.5).

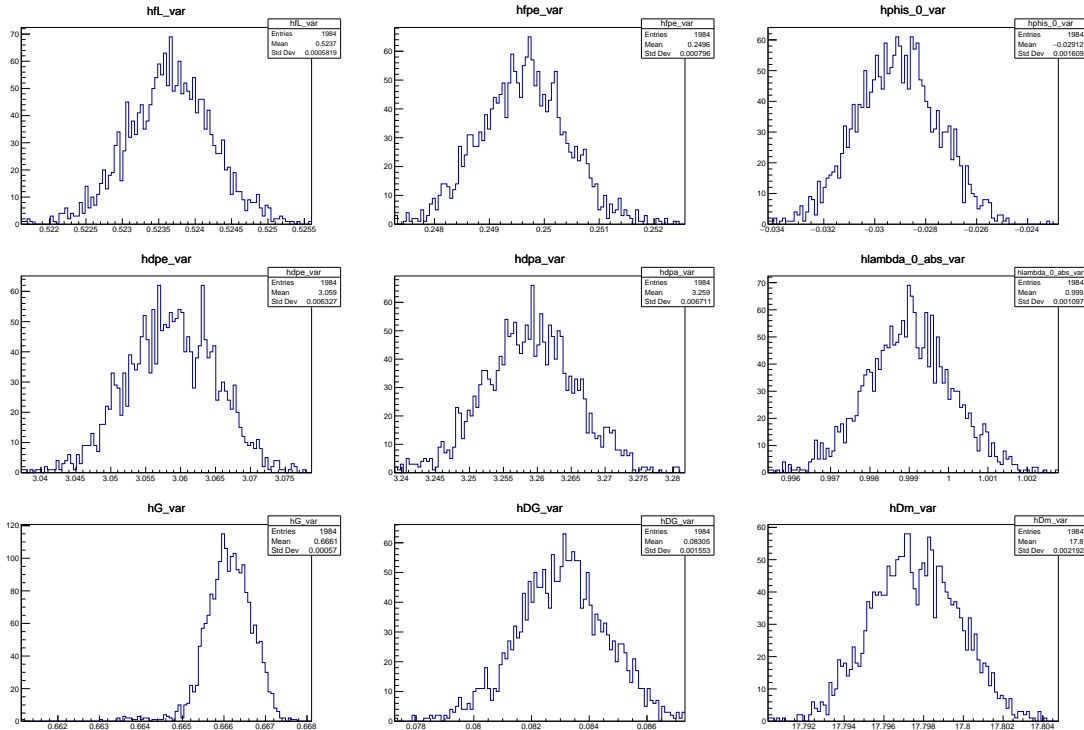


Figure B.1: Distributions of the fit parameters using bootstrapping (MC).

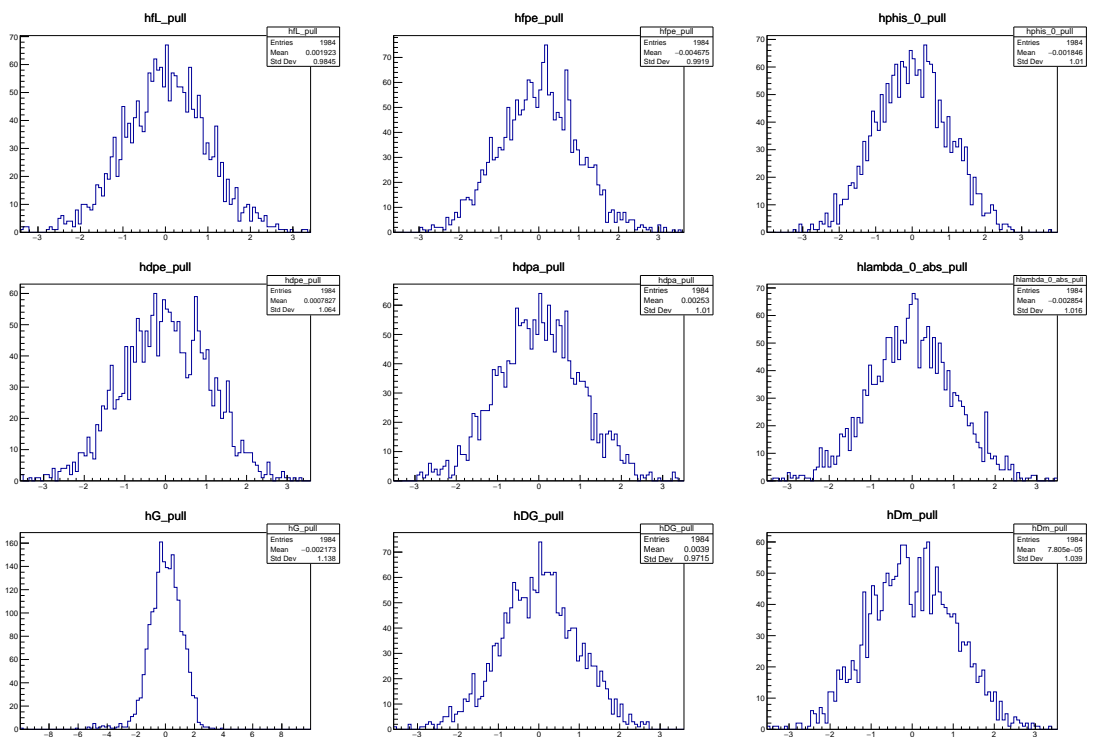


Figure B.2: Pull distributions of the fit parameters using bootstrapping (MC). Pulls are computed relative to MC generation values.

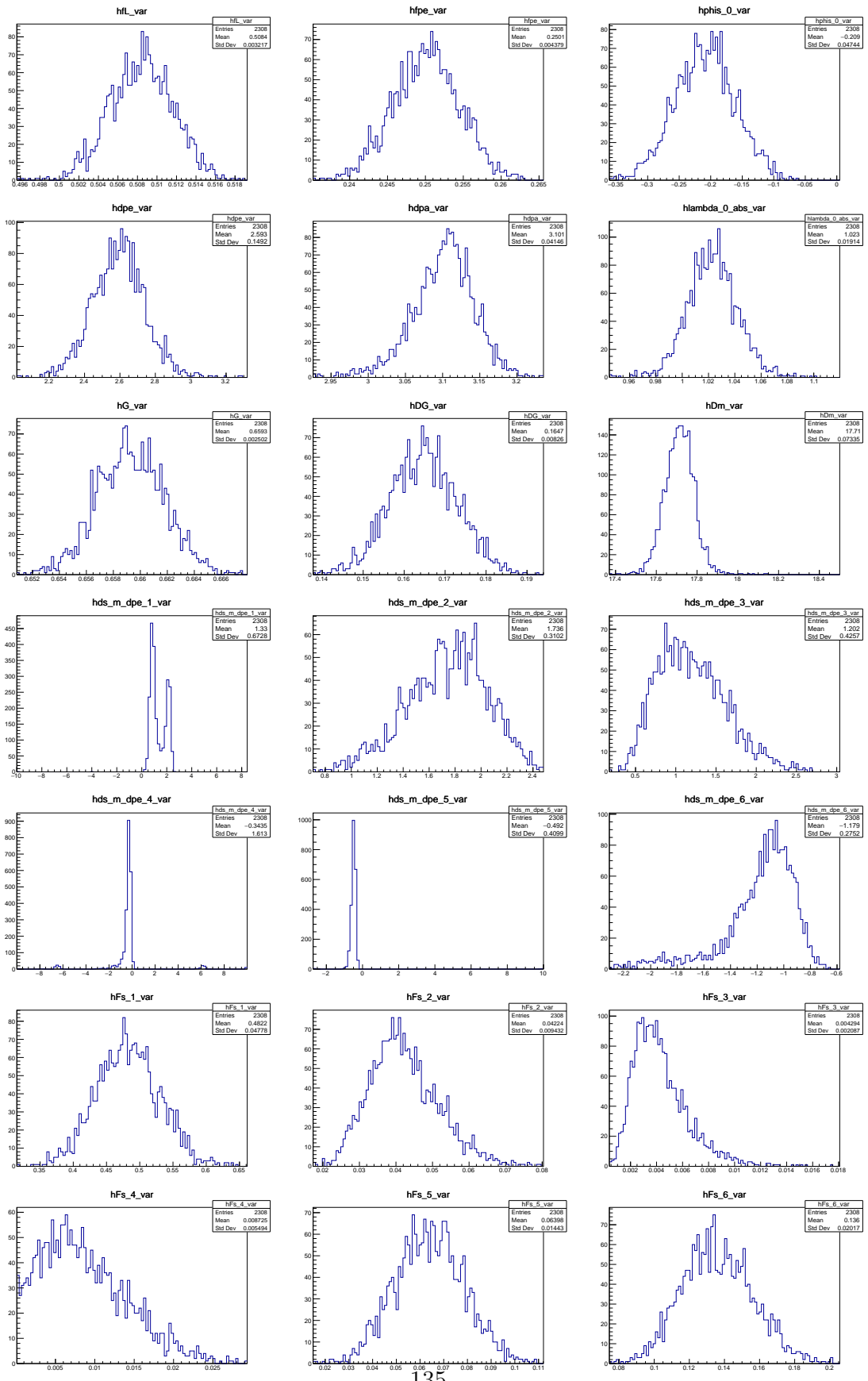


Figure B.3: Distributions of the fit parameters using bootstrapping (data).

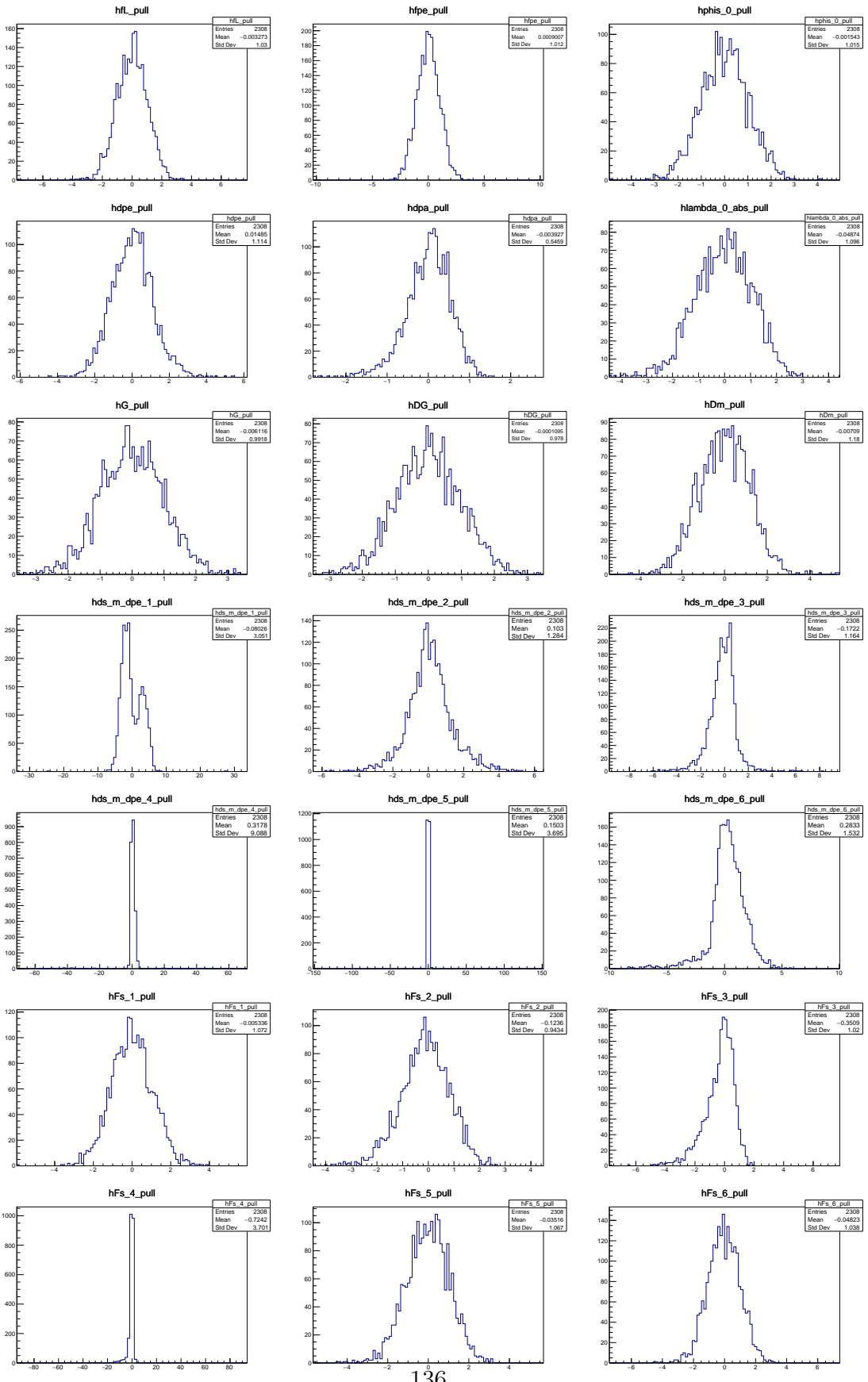


Figure B.4: Pull distributions of the fit parameters using bootstrapping (data). Pulls are computed relative to data central values.

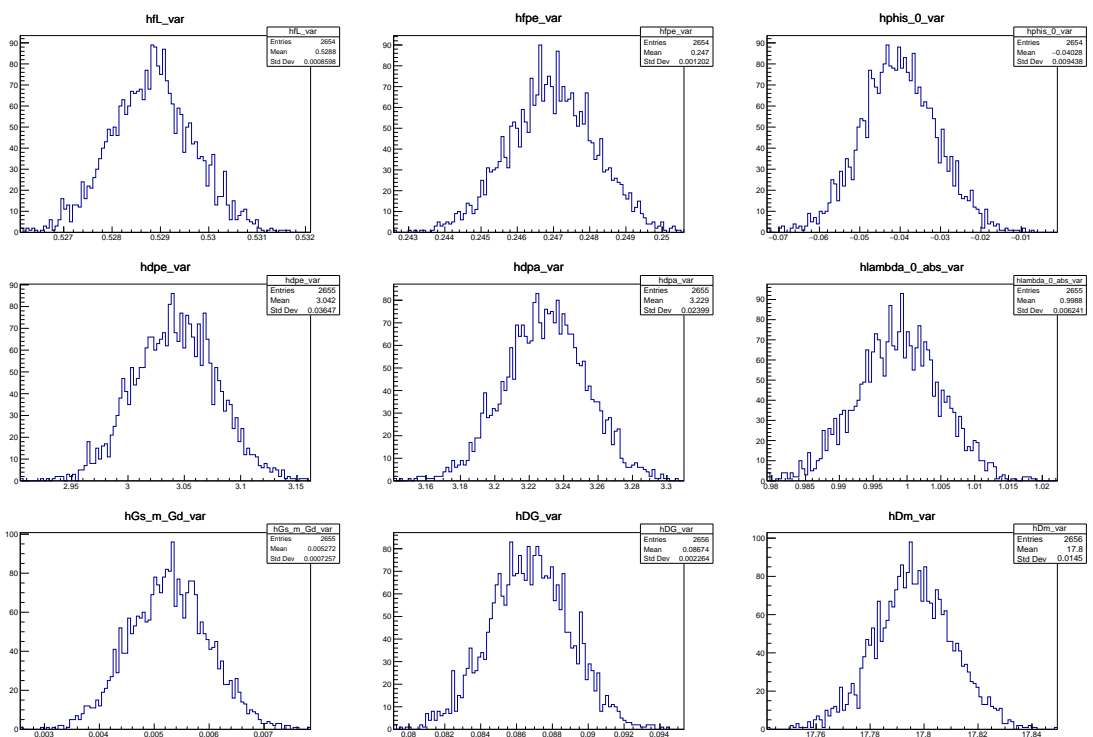


Figure B.5: Distributions of the fit parameters using bootstrapping (simulation and background simulation).

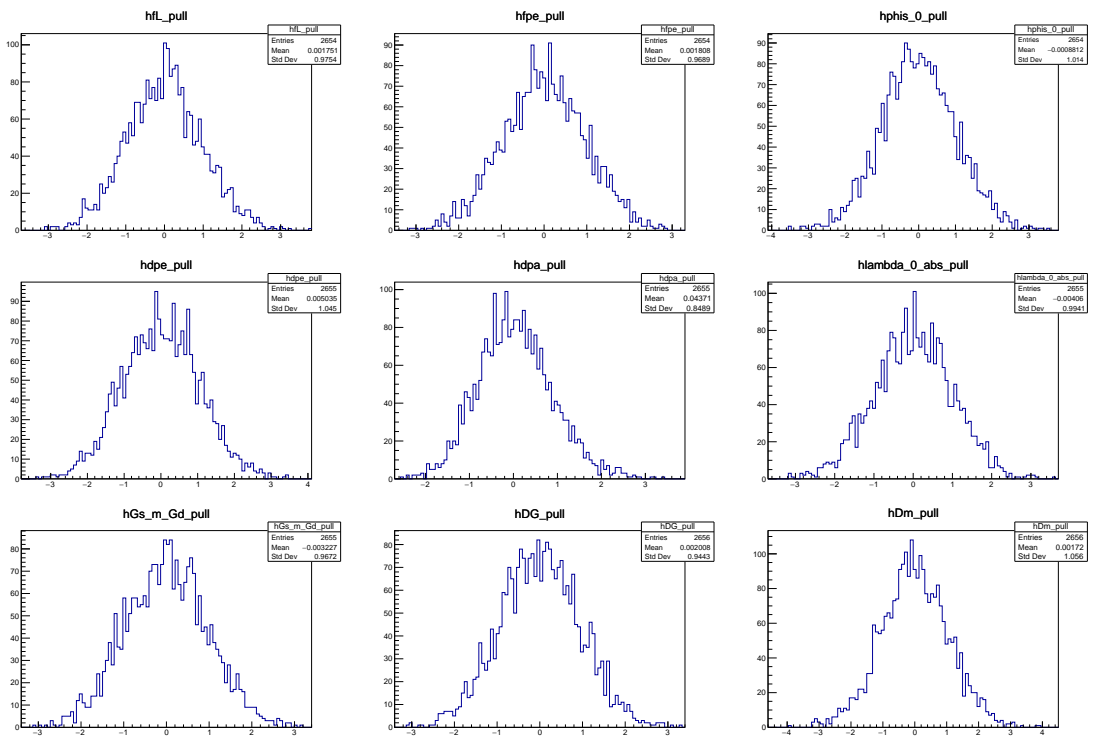


Figure B.6: Pull distributions of the fit parameters using bootstrapping (signal and background simulation).

2514

Bibliography

- 2515 [1] Particle Data Group, C. Patrignani *et al.*, *Review of Particle Physics*, Chin. Phys. **C40**
2516 (2016), no. 10 100001.
- 2517 [2] P. W. Higgs, *Broken symmetries and the masses of gauge bosons*, Phys. Rev. Lett. **13** (1964)
2518 508.
- 2519 [3] ATLAS, G. Aad *et al.*, *Observation of a new particle in the search for the Standard
2520 Model Higgs boson with the ATLAS detector at the LHC*, Phys. Lett. **B716** (2012) 1,
2521 [arXiv:1207.7214](https://arxiv.org/abs/1207.7214).
- 2522 [4] CMS, S. Chatrchyan *et al.*, *Observation of a new boson at a mass of 125 GeV with the
2523 CMS experiment at the LHC*, Phys. Lett. **B716** (2012) 30, [arXiv:1207.7235](https://arxiv.org/abs/1207.7235).
- 2524 [5] M. Maltoni, T. Schwetz, M. A. Tortola, and J. W. F. Valle, *Status of global fits to neutrino
2525 oscillations*, New J. Phys. **6** (2004) 122, [arXiv:hep-ph/0405172](https://arxiv.org/abs/hep-ph/0405172).
- 2526 [6] M. Drewes, *The Phenomenology of Right Handed Neutrinos*, Int. J. Mod. Phys. **E22** (2013)
2527 1330019, [arXiv:1303.6912](https://arxiv.org/abs/1303.6912).
- 2528 [7] P. Kooijman and N. Tuning, *Lectures on CP Violation*, 2015.
- 2529 [8] J. M. Cline, *Baryogenesis*, in *Les Houches Summer School - Session 86: Particle Physics
2530 and Cosmology: The Fabric of Spacetime Les Houches, France, July 31-August 25, 2006*,
2531 2006. [arXiv:hep-ph/0609145](https://arxiv.org/abs/hep-ph/0609145).
- 2532 [9] N. P. Vogt, M. P. Haynes, T. Herter, and R. Giovanelli, *M/L, H-alpha rotation curves, and
2533 HI measurements for 329 nearby cluster and field spirals. 1. Data*, Astron. J. **127** (2004)
2534 3273, [arXiv:astro-ph/0402649](https://arxiv.org/abs/astro-ph/0402649).
- 2535 [10] R. Massey, T. Kitching, and J. Richard, *The dark matter of gravitational lensing*, Rept.
2536 Prog. Phys. **73** (2010) 086901, [arXiv:1001.1739](https://arxiv.org/abs/1001.1739).
- 2537 [11] R. D. Peccei and H. R. Quinn, *Constraints imposed by CP conservation in the presence of
2538 pseudoparticles*, Phys. Rev. D **16** (1977) 1791.
- 2539 [12] S. Weinberg, *A new light boson?*, Phys. Rev. Lett. **40** (1978) 223.
- 2540 [13] F. Wilczek, *Problem of strong p and t invariance in the presence of instantons*, Phys. Rev.
2541 Lett. **40** (1978) 279.
- 2542 [14] <http://www.theo-physik.uni-kiel.de/~bonitz/public/nobel04/public.html>.

- 2543 [15] J. R. Ellis, J. Hisano, M. Raidal, and Y. Shimizu, *A New parametrization of the seesaw*
 2544 *mechanism and applications in supersymmetric models*, Phys. Rev. **D66** (2002) 115013,
 2545 [arXiv:hep-ph/0206110](https://arxiv.org/abs/hep-ph/0206110).
- 2546 [16] F. Jegerlehner and A. Nyffeler, *The Muon g-2*, Phys. Rept. **477** (2009) 1, [arXiv:0902.3360](https://arxiv.org/abs/0902.3360).
- 2547 [17] KamLAND-Zen, A. Gando *et al.*, *Search for Majorana Neutrinos near the Inverted Mass*
 2548 *Hierarchy Region with KamLAND-Zen*, Phys. Rev. Lett. **117** (2016), no. 8 082503,
 2549 [arXiv:1605.02889](https://arxiv.org/abs/1605.02889), [Addendum: Phys. Rev. Lett.117,no.10,109903(2016)].
- 2550 [18] GERDA, M. Agostini *et al.*, *Improved Limit on Neutrinoless Double- β Decay of ^{76}Ge from*
 2551 *GERDA Phase II*, Phys. Rev. Lett. **120** (2018), no. 13 132503, [arXiv:1803.11100](https://arxiv.org/abs/1803.11100).
- 2552 [19] R. D. Peccei, *The Strong CP problem and axions*, Lect. Notes Phys. **741** (2008) 3,
 2553 [arXiv:hep-ph/0607268](https://arxiv.org/abs/hep-ph/0607268), [3(2006)].
- 2554 [20] T. Kaluza, *On the Unification Problem in Physics*, Sitzungsber. Preuss. Akad. Wiss. Berlin
 2555 (Math. Phys.) **1921** (1921) 966, [arXiv:1803.08616](https://arxiv.org/abs/1803.08616).
- 2556 [21] O. Klein, *Quantentheorie und fünfdimensionale relativitätstheorie*, Zeitschrift für Physik **37**
 2557 (1926) 895.
- 2558 [22] L. Randall and R. Sundrum, *Large mass hierarchy from a small extra dimension*, Phys.
 2559 Rev. Lett. **83** (1999) 3370.
- 2560 [23] A. Lenz, *Constraints on a fourth generation of fermions from Higgs Boson searches*, Adv.
 2561 High Energy Phys. **2013** (2013) 910275.
- 2562 [24] V. Sanz and J. Setford, *Composite Higgs Models after Run 2*, Adv. High Energy Phys.
 2563 **2018** (2018) 7168480, [arXiv:1703.10190](https://arxiv.org/abs/1703.10190).
- 2564 [25] S. Coleman and J. Mandula, *All possible symmetries of the s matrix*, Phys. Rev. **159** (1967)
 2565 1251.
- 2566 [26] S. S. AbdusSalam *et al.*, *Benchmark Models, Planes, Lines and Points for Future SUSY*
 2567 *Searches at the LHC*, Eur. Phys. J. **C71** (2011) 1835, [arXiv:1109.3859](https://arxiv.org/abs/1109.3859).
- 2568 [27] D. Z. Freedman, P. van Nieuwenhuizen, and S. Ferrara, *Progress Toward a Theory of Su-*
 2569 *pergravity*, Phys. Rev. **D13** (1976) 3214.
- 2570 [28] J. R. Ellis, K. A. Olive, and Y. Santoso, *The MSSM parameter space with nonuniversal*
 2571 *Higgs masses*, Phys. Lett. **B539** (2002) 107, [arXiv:hep-ph/0204192](https://arxiv.org/abs/hep-ph/0204192).
- 2572 [29] A. Datta, A. Kundu, and A. Samanta, *New bounds on slepton and Wino masses*
 2573 *in anomaly mediated supersymmetry breaking models*, Phys. Rev. **D64** (2001) 095016,
 2574 [arXiv:hep-ph/0101034](https://arxiv.org/abs/hep-ph/0101034).
- 2575 [30] E. Bagnaschi *et al.*, *Likelihood Analysis of the Minimal AMSB Model*, Eur. Phys. J. **C77**
 2576 (2017), no. 4 268, [arXiv:1612.05210](https://arxiv.org/abs/1612.05210).
- 2577 [31] S. P. Martin, *A Supersymmetry primer*, [arXiv:hep-ph/9709356](https://arxiv.org/abs/hep-ph/9709356), [Adv. Ser. Direct. High
 2578 Energy Phys.18,1(1998)].

- 2579 [32] Super-Kamiokande, H. Nishino *et al.*, *Search for Proton Decay via $p \rightarrow e^+ \pi^0$ and $p \rightarrow \mu^+ \pi^0$ in a Large Water Cherenkov Detector*, *Phys. Rev. Lett.* **102** (2009) 141801, [arXiv:0903.0676](#).
- 2580
2581
- 2582 [33] A. Masiero and J. W. F. Valle, *A model for spontaneous r parity breaking*, *Physics Letters B* **251** (1990), no. 2 273 .
- 2583
2584
- 2585 [34] J. C. Romão, C. A. Santos, and J. W. F. Valle, *How to spontaneously break r parity*, *Physics Letters B* **288** (1992), no. 3 311 .
- 2586
2587
- 2588 [35] D. K. Ghosh, G. Senjanovic, and Y. Zhang, *Naturally Light Sterile Neutrinos from Theory of R-parity*, *Phys. Lett. B* **698** (2011) 420, [arXiv:1010.3968](#).
- 2589
2590
- 2591 [36] GAMBIT, P. Athron *et al.*, *Combined collider constraints on neutralinos and charginos*, [arXiv:1809.02097](#).
- 2592
2593
- 2594 [37] GAMBIT, P. Athron *et al.*, *A global fit of the MSSM with GAMBIT*, *Eur. Phys. J. C* **77** (2017), no. 12 879, [arXiv:1705.07917](#).
- 2595
2596
- 2597 [38] GAMBIT, P. Athron *et al.*, *Global fits of GUT-scale SUSY models with GAMBIT*, *Eur. Phys. J. C* **77** (2017), no. 12 824, [arXiv:1705.07935](#).
- 2598
2599
- 2600 [39] E. Bagnaschi *et al.*, *Likelihood Analysis of Supersymmetric SU(5) GUTs*, *Eur. Phys. J. C* **77** (2017), no. 2 104, [arXiv:1610.10084](#).
- 2601
2602
- 2603 [40] E. Bagnaschi *et al.*, *Likelihood Analysis of the pMSSM11 in Light of LHC 13-TeV Data*, *Eur. Phys. J. C* **78** (2018), no. 3 256, [arXiv:1710.11091](#).
- 2604
2605
- 2606 [41] J. C. Costa *et al.*, *Likelihood Analysis of the Sub-GUT MSSM in Light of LHC 13-TeV Data*, *Eur. Phys. J. C* **78** (2018), no. 2 158, [arXiv:1711.00458](#).
- 2607
2608
- 2609 [42] P. Paradisi and D. M. Straub, *The SUSY CP Problem and the MFV Principle*, *Phys. Lett. B* **684** (2010) 147, [arXiv:0906.4551](#).
- 2610
2611
- 2612 [43] W. Altmannshofer, A. J. Buras, and D. Guadagnoli, *The MFV limit of the MSSM for low tan(beta): Meson mixings revisited*, *JHEP* **11** (2007) 065, [arXiv:hep-ph/0703200](#).
- 2613
2614
- 2615 [44] G. D'Ambrosio, G. F. Giudice, G. Isidori, and A. Strumia, *Minimal flavor violation: An Effective field theory approach*, *Nucl. Phys. B* **645** (2002) 155, [arXiv:hep-ph/0207036](#).
- 2616
2617
- 2618 [45] C. Csaki, Y. Grossman, and B. Heidenreich, *MFV SUSY: A Natural Theory for R-Parity Violation*, *Phys. Rev. D* **85** (2012) 095009, [arXiv:1111.1239](#).
- 2619
2620
- 2621 [46] D. M. Straub, *MFV and the SUSY CP Problem*, *AIP Conf. Proc.* **1200** (2010) 904, [arXiv:0909.3296](#).
- 2622
2623
- 2624 [47] A. J. Buras *et al.*, *Universal unitarity triangle and physics beyond the standard model*, *Phys. Lett. B* **500** (2001) 161, [arXiv:hep-ph/0007085](#).
- 2625
2626
- 2627 [48] CKMfitter Group, J. Charles *et al.*, *CP violation and the CKM matrix: Assessing the impact of the asymmetric B factories*, *Eur. Phys. J. C* **41** (2005), no. 1 1, [arXiv:hep-ph/0406184](#).
- 2628
2629

- 2614 [49] CMS, S. Chatrchyan *et al.*, *Observation of a new boson at a mass of 125 GeV with the*
 2615 *CMS experiment at the LHC*, Phys. Lett. **B716** (2012) 30, [arXiv:1207.7235](https://arxiv.org/abs/1207.7235).
- 2616 [50] ATLAS, G. Aad *et al.*, *Observation of a new particle in the search for the Standard*
 2617 *Model Higgs boson with the ATLAS detector at the LHC*, Phys. Lett. **B716** (2012) 1,
 2618 [arXiv:1207.7214](https://arxiv.org/abs/1207.7214).
- 2619 [51] ATLAS, W. W. Armstrong *et al.*, *ATLAS: Technical proposal for a general-purpose p p*
 2620 *experiment at the Large Hadron Collider at CERN*, .
- 2621 [52] CMS, *CMS, the Compact Muon Solenoid: Technical proposal*, .
- 2622 [53] *ALICE: Technical proposal for a large ion collider experiment at the CERN LHC*, .
- 2623 [54] LHCb, S. Amato *et al.*, *LHCb technical proposal*, .
- 2624 [55] LHCb collaboration, A. A. Alves Jr. *et al.*, *The LHCb detector at the LHC*, JINST **3** (2008)
 2625 [S08005](https://arxiv.org/abs/S08005).
- 2626 [56] LHCb, R. Aaij *et al.*, *LHCb Detector Performance*, Int. J. Mod. Phys. **A30** (2015), no. 07
 2627 [1530022](https://arxiv.org/abs/1412.6352), [arXiv:1412.6352](https://arxiv.org/abs/1412.6352).
- 2628 [57] A. A. Alves, Jr. *et al.*, *Performance of the LHCb muon system*, JINST **8** (2013) P02022,
 2629 [arXiv:1211.1346](https://arxiv.org/abs/1211.1346).
- 2630 [58] R. Fruhwirth, *Application of Kalman filtering to track and vertex fitting*, Nucl. Instrum.
 2631 Meth. **A262** (1987) 444.
- 2632 [59] LHCb, D. M. Santos, *A strange program for LHCb*, EPJ Web Conf. **179** (2018) 01013.
- 2633 [60] L. Collaboration, *LHCb Trigger and Online Upgrade Technical Design Report*, .
- 2634 [61] X. Llopert *et al.*, *Timepix, a 65k programmable pixel readout chip for arrival time, energy*
 2635 *and/or photon counting measurements*, Nuclear Instruments and Methods in Physics Re-
 2636 *search Section A: Accelerators, Spectrometers, Detectors and Associated Equipment* **581**
 2637 *(2007)*, no. 1 485 , VCI 2007.
- 2638 [62] P. Mato, *Gaudi-architecture design document*, Tech. Rep. LHCb-98-064, CERN, Geneva,
 2639 Nov, 1998.
- 2640 [63] *The MOORE project*, [http://lhcb-release-area.web.cern.ch/LHCb-release-area/
 2641 DOC/moore/](http://lhcb-release-area.web.cern.ch/LHCb-release-area/DOC/moore/).
- 2642 [64] *The BRUNEL project*, <http://lhcbdoc.web.cern.ch/lhcbdoc/brunel/>.
- 2643 [65] *The ALIGNMENT project*, <http://lhcbdoc.web.cern.ch/lhcbdoc/alignment/>.
- 2644 [66] <https://twiki.cern.ch/twiki/bin/view/LHCb/DaVinci>.
- 2645 [67] <https://gitlab.cern.ch/lhcb/Erasmus>.
- 2646 [68] C. Eck *et al.*, *LHC computing Grid: Technical Design Report. Version 1.06 (20 Jun 2005)*,
 2647 Technical Design Report LCG, CERN, Geneva, 2005.

- 2648 [69] <http://lhcbdoc.web.cern.ch/lhcbdoc/gauss/>.
- 2649 [70] T. Sjostrand, S. Mrenna, and P. Z. Skands, *A Brief Introduction to PYTHIA 8.1*, *Comput.*
2650 *Phys. Commun.* **178** (2008) 852, [arXiv:0710.3820](https://arxiv.org/abs/0710.3820).
- 2651 [71] A. Ryd *et al.*, *EvtGen: A Monte Carlo Generator for B-Physics*, .
- 2652 [72] S. Agostinelli *et al.*, *Geant4 simulation toolkit*, *Nuclear Instruments and Methods in Physics*
2653 *Research Section A: Accelerators, Spectrometers, Detectors and Associated Equipment* **506**
2654 (2003), no. 3 250 .
- 2655 [73] W. Altmannshofer *et al.*, *Anatomy and Phenomenology of FCNC and CPV Effects in SUSY*
2656 *Theories*, *Nucl. Phys.* **B830** (2010) 17, [arXiv:0909.1333](https://arxiv.org/abs/0909.1333).
- 2657 [74] F. Feroz, M. P. Hobson, and M. Bridges, *MultiNest: an efficient and robust Bayesian*
2658 *inference tool for cosmology and particle physics*, *Mon. Not. Roy. Astron. Soc.* **398** (2009)
2659 1601, [arXiv:0809.3437](https://arxiv.org/abs/0809.3437).
- 2660 [75] J. Charles *et al.*, *Predictions of selected flavour observables within the Standard Model*,
2661 *Phys. Rev.* **D84** (2011) 033005, [arXiv:1106.4041](https://arxiv.org/abs/1106.4041).